Protonation and Reduction Dynamics in [FeFe]-Hydrogenases

im Fachbereich Physik der Freien Universität Berlin eingereichte

Dissertation zur Erlangung des Grades eines Doktors der

Naturwissenschaften (Dr. rer. nat.)

vorgelegt von
Moritz Senger

Berlin 2017

Erster Gutachter: Prof. Dr. Joachim Heberle

Zweiter Gutachter: Priv.-Doz. Dr. Michael Haumann

Tag der Disputation: 06.02.2018

Abstract

Hydrogenases are metalloenzymes that catalyze uptake and release of molecular hydrogen. Redox chemistry takes place at a Ni- or Fe-metallic cofactors characteristic for hydrogenases. [FeFe]-hydrogenases are of special interest due to high H_2 turnover rates at low overpotential and serve as an inspiring model for the design of synthetic catalysts. The active site, called "H-cluster", consists of a canonical [4Fe-4S] cluster linked to the eponymous diiron site. The two Fe ions proximal (Fe_p) and distal (Fe_d) to the [4Fe-4S] cluster are ligated by one CN and CO ligand, respectively. Both Fe ions are bridged by a CO ligand (μCO) and by an azadithiolate (adt) group that serves as lewis base to Fe_d where turnover takes place. The molecular proceedings of hydrogen turnover are under debate. Besides the oxidized, active-ready state (Hox) two increasingly reduced states have been proposed. Two states reduced by one electron are reported, either reduced at the diiron site (Hred) or at the [4Fe-4S] cluster (Hred'). The two-electron reduced species Hsred resembles Hred with an additional reduction of the [4Fe-4S] cluster. Hhyd, a formally two-electron reduced redox species is supposed to be key intermediate in hydrogen turnover, featuring a terminal bound hydride ideal to interact with a proton shared via adt group and the proton transfer path. However the interplay of protein and cofactor, protons and electrons and the role of active site geometry in hydrogen turnover is still not fully understood. Infrared spectroscopy is particularly sensitive to the CO- and CN ligands of the diiron site and enables monitoring even small changes in electron density as for example protonation in the vicinity of the active site. A protocol for specific isotopic editing of individual CO ligands at the diiron site was developed. Correlation with DFT calculations offered the possibility to reveal alterations in cofactor arrangement. Hereby, a bridging hydride geometry was confirmed for Hred and Hsred that features an apical CO ligand at Fe_d. The enhanced stability of this cofactor arrangement disfavors their catalytic relevance. In contrast, the bridging CO geometry identified for Hred' preserves the apical vacancy preferred for turnover. Protonation at the [4Fe-4S] cluster was found to stabilize this geometry and level the redox potential for a second reduction step. H/D exchange experiments confirmed the enrichment of Hhyd in native enzyme that was accompanied by protonation at the [4Fe-4S] as well. A catalytic cycle for hydrogen turnover is proposed that exclusively consists of states with conserved geometry (Hox, Hred' and Hhyd). Concerted protonation and reduction at the [4Fe-4S] cluster appear to maintain this geometry. Efficient catalysis is not restricted to the diiron site but also influenced by the protein environment that offers a remote protonation site. Synthetic catalysts should exploit the regulative effects offered by protonable redox ligands.

Zusammenfassung

Hydrogenasen katalysieren die Aufnahme und Abgabe von molekularem Wasserstoff (H_2). Die Redoxchemie dieser Metalloenzyme findet an Nickel- oder Eisen-Kofaktoren statt. [FeFe]-Hydrogenasen zeigen hohe H_2-Abgaberaten und dienen als inspirierendes Modell für das Design synthetischer Katalysatoren. Das aktive Zentrum, der sogenannte "H-cluster", besteht aus einem klassischem [4Fe-4S] Zentrum, verbunden mit einem in der Natur einzigartigen Eisen-Eisen-Komplex ([FeFe]). Die zwei Eisen-Ionen proximal (Fe_p) und distal (Fe_d) zum [4Fe-4S] Zentrum binden jeweils einen CO- und einen CN-Liganden. Beide Eisen-Ionen werden durch einen dritten CO-Liganden verbrückt und binden zusätzlich eine Azadithiolat-Gruppe (adt), deren sekundäres Amin mit Fe_d ein frustriertes Lewis-Paar bildet. Die molekularen Details der Wasserstoffkatalyse werden in der Literatur kontrovers diskutiert.
Neben dem oxidierten Grundzustand (Hox) sind vier zunehmend reduzierte Intermediate vorgeschlagen worden, darunter zwei einfach reduzierte Zustände, Hred und Hred'. Dabei ist Hred durch eine Reduktion des [FeFe] Zentrum charakterisiert worden, während Hred' durch Reduktion des [4Fe-4S] Zentrum gekennzeichnet ist. Der zweifach reduzierte Zustand Hsred ähnelt Hred, zeigt aber ein zusätzlich reduziertes [4Fe-4S] Zentrum. Hhyd, ein formal zweifach reduzierter Zustand, wurde als wichtiges Intermediat in der Wasserstoffkatalyse vorgeschlagen. Terminal an Fe_d bindet der H-cluster hier eine hydridische Spezies, die mit dem Proton der adt-Gruppe instantan zu H_2 reagieren kann. Die adt-Gruppe ist der Schnittpunkt von H-cluster und Protonentransferpfad. Das genaue Zusammenspiel von Protein und Kofaktor, Protonen und Elektronen und die Rolle der Struktur des aktiven Zentrums sind bisher nicht hinreichend verstanden.
Infrarotspektroskopie eigent sich ideal für die Analyse von Hydrogenasen. Die CO- und CN-Liganden des [FeFe] Zentrums absorbieren intensiv im mittleren Infrarot und überlappen nicht mit den Absorptionsbanden von Protein oder flüssigem Wasser. Dadurch können auch kleinste Änderungen in der Elektronendichteverteilung detektieren werden, beispielsweise die Bindung eines Protons in der Nähe des H-clusters. Es wurde ein photochemisches Protokoll entwickelt, um die natürlichen ^{12}CO-Liganden den [FeFe] Zentrums selektiv gegen ^{13}CO auszutauschen (Isotopenmarkierung). In Korrelation mit DFT Rechnungen war es möglich, die Kofaktorgeometrie mit hoher Präzision aufzulösen, so dass auch subtile Unterschiede, die in der Proteinkristallographie verloren gehen, enhüllt werden konnten. Erstmals wurde so zum Beispiel eine Kofaktorgeometrie mit einem verbrückenden Hydrid für Hred und Hsred bestätigt. Ein daraus resultierender apikaler CO Ligand und die erhöhte Stabilität des verbrückenden Hydrides machen eine katalytische Relevanz dieser Zustände unwahrscheinlich. Im Gegensatz dazu wurde für Hred' ein verbrückender CO Ligand und damit die apikale Vakanz am distalen Eisen-Ion bestätigt. Die Beibehaltung dieser, von Hox bekannten, „konservativen" Struktur ist von zentraler Bedeutung für eine effiziente Wasserstoffkatalyse. Eine Protonierung am [4Fe-4S] Zentrum stabilisiert die konservative Geometrie in Hred' und dämpft das Redoxpotential für den zweiten Reduktionsschritt. H/D-Austauschexperimente bestätigten die Anreicherung von Hhyd in nativem Enzym. DFT Rechnungen suggerieren auch für Hhyd ein Protonierung am [4Fe-4S] Zentrum.
Ein katalytischer Zyklus, der nur Zustände mit konservativer Geometrie berücksichtig konnte formuliert werden (Hox, Hred', und Hhyd). Eine aufeinander abgestimmte Protonierung und Reduktion am [4Fe-4S] Zentrum scheinen die Geometrieerhaltung zu unterstützen. Für die Entwicklung synthetischer Katalysatoren sollten diese regulatorischen Effekte in Betracht gezogen werden, zum Beispiel durch protonierbare Redoxliganden, die eine vorzeigtige Reduktion und Bildung verbrückender Hydride am bimetallischen Zentrum verhindern.

Publications:

[I] M. Senger, S. Mebs, J. Duan, F. Wittkamp, U. P. Apfel, J. Heberle, M. Haumann and S. T. Stripp
Stepwise isotope editing of [FeFe]-hydrogenases exposes cofactor dynamics.
Proceedings of the National Academy of Sciences of the United States of America
vol.113, no.30, pp 8454-9, 2016

[II] M. Winkler, M. Senger, J. F. Duan, J. Esselborn, F. Wittkamp, E. Hofmann, U. P. Apfel, S. T. Stripp and T. Happe
Accumulating the hydride state in the catalytic cycle of [FeFe]-hydrogenases.
Nature Communications
vol.8:16115, 2017

[III] S. Mebs, M. Senger, J. Duan, F. Wittkamp, U.-P. Apfel, T. Happe, M. Winkler, S. T. Stripp and M. Haumann
Bridging Hydride at Reduced H-Cluster Species in [FeFe]-Hydrogenases Revealed by Infrared Spectroscopy, Isotope Editing, and Quantum Chemistry.
Journal of the American Chemical Society
vol.139, no.35, pp 12157-12160, 2017

[IV] M. Senger, S. Mebs, J. Duan, O. Shulenina, K. Laun, L. Kertess, F. Wittkamp, U.-P. Apfel, T. Happe, M. Winkler, M. Haumann and S. T. Stripp
Protonation/Reduction Dynamics at the [4Fe-4S] Subsite of the Hydrogen-forming Cofactor in [FeFe]-Hydrogenases.
Physical Chemistry Chemical Physics
in press

[V] S. Mebs, R. Kositzki, J. Duan, M. Senger, F. Wittkamp, U. P. Apfel, T. Happe, S. T. Stripp, M. Winkler and M. Haumann
Hydrogen and oxygen trapping at the H-cluster of [FeFe]hydrogenase revealed by site-selective spectroscopy and QM/MM calculations.
Biochim Biophys Acta
in press

[VI] M. Senger, K. Laun, F. Wittkamp, J. Duan, T. Happe, M. Winkler, U. P. Apfel and S. T. Stripp
Reduction of the Catalytic [4Fe-4S] Cluster in [FeFe]-hydrogenases is coupled to Proton Transfer
in revision

[VII] M. Senger and S. T. Stripp
Wasserstoffkatalyse in Mikroalgen.
Nachrichten aus der Chemie
vol.65, no.2, pp 109-215, 2017

[VIII] M. Senger, S. T. Stripp and B. Soboh
Proteolytic cleavage orchestrates cofactor insertion and protein assembly in [NiFe]-hydrogenase biosynthesis.
Journal of Biological Chemistry
vol.292, no.28, pp 11670-11681, 2017

List of Abbrevations

adt azadithiolate

ATR Attenuated Total Reflection

BSA Bovine serum albumin protein

CN cyanide

dCN distal cyanide ligand

CO carbonyl

dCO distal carbonyl ligand

pCO proximal carbonyl ligand

d_1CO first distal carbonyl ligand

d_2CO second distal carbonyl ligand

DFT Density functional theory

DT sodium dithionite

Em midpoint potential

Fe_d distal iron ion

Fe_p proximal iron ion

FTIR Fourier Transform Infrared Spectroscopy

IR Infrared

Hox oxidized state

HoxH protonated oxidized state

Hred diiron site reduced state

Hred' [4Fe-4S] reduced state

Hred'H protonated [4Fe-4S reduced state

Hsred super reduced state

Hox-CO oxidized CO inhibited state

HoxH-CO oxidized protonated CO inhibited state

Hhyd hydride state

PCET proton coupled electron transfer

PTP proton transfer pathway

MFC mass flow controller

RMSD root mean square deviation

SHE standard hydrogen electrode

Tris tris(hydroxymethyl)aminomethane

Contents

1 Introduction **1**

1.1 Hydrogen as an energy source 2

1.2 Hydrogenases 3

1.3 Redox states of [FeFe]-Hydrogenase 5

1.4 Scope of the thesis 7

2 Materials and Methods **9**

2.1 Vibrational Spectroscopy 10

2.1.1 Molecular Vibrations 10

2.1.2 IR Spectroscopy 11

2.1.3 Fourier Transform Infrared Spectroscopy 11

2.1.4 Attenuated Total Reflection 12

2.1.5 ATR-FTIR Spectroscopy 15

2.1.6 Spectrometer and Experimental Environment 15

2.1.7 Aerosol FTIR-ATR Setup 15

2.1.8 Spectro-electrochemistry using ATR-FTIR spectroscopy 17

2.2 Density Functional Theory 19

2.3 Enzyme Expression, Purification and Maturation 19

3 Results **21**

3.1 ATR-FTIR Spectroscopy on [FeFe]-Hydrogenase 22

3.1.1 Hydration and Dehydration of Enzyme Films 23

3.1.2 Temporal Stability of Enzyme Films 25

3.1.3 Overview of Hydrogenase interaction with gases 26

3.2 Isotopic editing of Carbonyl ligands 31

3.3 pH Titrations . . . 37
3.3.1 Hox and HoxH . . . 37
3.3.2 Hox-CO and HoxH-CO . . . 40
3.3.3 Sulfur/Selenium exchange . . . 40
3.3.4 H/D exchange . . . 43
3.3.5 Hred' and Hred . . . 45
3.3.6 Hred' and Hred'H . . . 46
3.4 Hred and Hsred . . . 50
3.5 The hydride state (Hhyd) . . . 52
3.6 O_2 inactivation (Hox-O_2) . . . 54
3.7 CpI, Cofactor Variants and Amino Acid Variants . . . 55
3.8 Correlation to DFT model structures and frequency calculations . . . 58
3.8.1 Hox and Hox-CO . . . 58
3.8.2 Hox and HoxH . . . 62
3.8.3 Hred' and Hred'H . . . 64
3.8.4 Hred and Hsred . . . 65
3.8.5 Hox-O_2 and Hhyd . . . 67

4 Discussion **69**
4.1 Hox-CO and Hox . . . 70
4.2 Hred and Hsred . . . 73
4.3 HoxH . . . 74
4.4 Hred' and Hred'H . . . 78
4.5 The hydride state Hhyd . . . 81
4.6 Hox-O_2 . . . 82
4.7 The catalytic cycle . . . 83

5 Conclusion **87**

A Selbstständigkeitserklärung **99**

B Supporting Information **100**
B.1 Isotopic editing . . . 100
B.2 pH . . . 102

B.3 Hred and Hsred 105
B.4 Hydride State 106
B.5 DFT 108
B.6 CpI 113
B.7 HydA1 Cofactor Variants 118
B.8 Proton Path Variants 123
B.9 Time-resolved Studies 137

Chapter 1

Introduction

The increasing energy demand on earth forces mankind to search for new ways to convert energy. Energy conversion by burning fossil resources is accompanied with multiple challenges. For example fossil resources like oil or natural gas will be exhausted at some point. The product of combustion, carbon dioxide contributes to the greenhouse effect and enhances the climate problem.[1] Nuclear energy can not cover the worlds demand and comes along with the unsolved nuclear waste problem.[2]

1.1 Hydrogen as an energy source

The oxidation of molecular hydrogen (H_2) by molecular oxygen (O_2) (Knallgas reaction) is a highly exergonic reaction ($\frac{240kJ}{mol/H_2}$) that has the potential to deliver the energy needed and that establishes the bases for a "hydrogen economy".

$$2H_2 + O_2 \rightarrow 2H_2O \tag{1.1}$$

Molecular oxygen is present to ca. 21% in the lower atmosphere and water as product is not as climate active as CO_2.[3] The challenge remains to gain sufficient amounts of molecular hydrogen. Albeit Hydrogen is the most abundant element in the known universe, hydrogen gas is nearly not present in our atmosphere. Due to its low specific density it easily escapes into space. Di-hydrogen is produced mainly by steam reformation of fossil resources and electrolysis (water splitting). Steam reformation requires high temperature and thereby high energy. Furthermore, in this process, CO_2 is produced thus contributes to the greenhouse effect. Electrolysis of water into O_2 and H_2 has a negative energy balance but can be an option to "store" energy produced by green seasonal fluctuating energy converters like wind power stations or solar cells that would be otherwise wasted.

Hydrogen has been deemed the "fuel of the future". Constant supply with molecular hydrogen demands for efficient production. Nature's catalyst for the reduction of protons to molecular hydrogen with low electrochemical overpotential are macromolecules called hydrogenases.

1.2 Hydrogenases

Hydrogenases can be found in archaea, bacteria, fungi, and algae.[4] There are three major classes of hydrogenases [NiFe]-Hydrogenase,[5] Iron-only Hydrogenase[6] and [FeFe]-Hydrogenase[7–9] differentiated by the metal ion content of the active site. Hydrogenases are metalloenzymes that catalyze H_2 uptake and release.

$$2H^+ + 2e^- \leftrightarrow H_2 \tag{1.2}$$

The product/educt ratio determines the direction the reaction proceeds. Either H_2 will be consumed if the protons can leave the enzyme and a suitable electron acceptor is available (uptake) or hydrogen release will take place when excess protons and electrons are present. The [FeFe]-hydrogenase is mainly catalyzing proton reduction and the turnover rates up to 1000 molecules H_2 per second are significantly higher than in [NiFe]-hydrogenases.[10,11]

[NiFe]-Hydrogenases

[NiFe]-hydrogenase typically consists of 2 subunits. The NiFe-active site is harbored by the large subunit and the small subunit hosts additional FeS-clusters that facilitate electron transfer to the active site. Four cysteines ligate the nickel ion and two ligate the iron ion as well. Additional ligands of the iron ion are two cyanide (CN) and one carbonyl (CO) ligand.[4,8] [NiFe]-hydrogenases mainly oxidize H_2 and are not biased to show high hydrogen release activity. Oxygen is inhibiting most [NiFe]-Hydrogenases but some are even oxygen tolerant like membrane bound hydrogenase and soluble hydrogenase from *Ralstonia eutropha* H16.[7,12,13]

[FeFe]-Hydrogenases

[FeFe]-hydrogenases are mostly monomeric enzymes that harbor at least one [4Fe-4S]-cluster covalently linked via a cysteine to an unusual diiron site forming the so called H-cluster.[14] The iron ion closer to the [4Fe-4S]-cluster is named the proximal iron ion (Fe_p) and the more distant one the distal iron ion (Fe_d). Every iron ion of the diiron site is ligated by one CO and one CN ligand. An additional CO ligand is bound in between

the two iron ions in bridging position (μCO). The iron ions are connected by a amine-dithiolate group (adt).[15,16] The nitrogen atom of adt group acts as a hangman group and is part of a frustrated Lewis acid-base pair formed with the open coordination site at Fe_d.[16] It functions as the relay to a proton transfer pathway (PTP) formed by conserved amino acids and water molecules that connect the H-cluster with the bulk medium.[17–22] Di-Hydrogen and other gases can access the H-cluster via a hydrophobic channel formed by the enzyme. [FeFe]-hydrogenases are inactivated by oxygen that lead to the destruction of the H-cluster.[23] Exposed to CO the enzyme is inhibited by a additional CO molecule bound to the open coordination site of the F_d.[24] For this reason, H_2 turnover is abolished and the enzyme is protected against O_2. In the active form (with open coordination site at Fe_d) absorption of visible light leads to cleavage of the iron carbonyl bands. Several H-clusters are destroyed while others are inhibited by the free CO molecules produced in this process.[25]

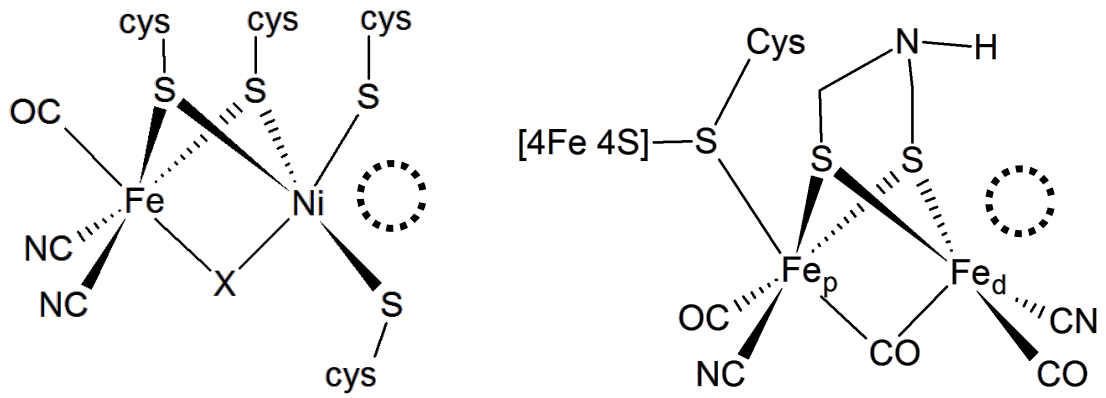

Figure 1.1: Chemical representation of the [NiFe] active site (left) and the H-cluster of [FeFe]-hydrogenase (right). Dashed circles indicate the open coordination site.

Most [FeFe]-hydrogenases harbor additional [Fe-S]-clusters that are used for electron transport to the H-cluster. In CpI from *Clostridium pasteurianum* three [4Fe-4S]- and one [2Fe-2S] cluster were identified[9] in addition to the H-cluster. DdH from *Desulvovibrio desulfuricans* contains two accessory [4Fe-4S] clusters. HydA1 from the green alga *Chlamydomonas reinhardtii* is considered as the minimal version of [FeFe]-hydrogenase. It exclusively contains the H-cluster. All three types of [FeFe]-hydrogenase can be expressed in *E. coli* as "apo" protein that lacks the diiron site and subsequently artificial maturated with a synthetic cofactor to yield active enzyme.[26–28] By this approach alternated diiron sites can be implemented into otherwise native enzyme.[27] The H-cluster is covalently bound by four cysteines that ligate the Fe ions of the [4Fe-4S] cluster. One

of these cysteines connects additionally the [4Fe-4S] cluster to the diiron site. Besides this bonds no covalent interactions with the protein fold are reported.[19] The CO- and CN ligand arrangement was modeled by possible hydrogen-bond interactions of the CN ligands to the protein fold according to X-ray crystallography data.[9,29]

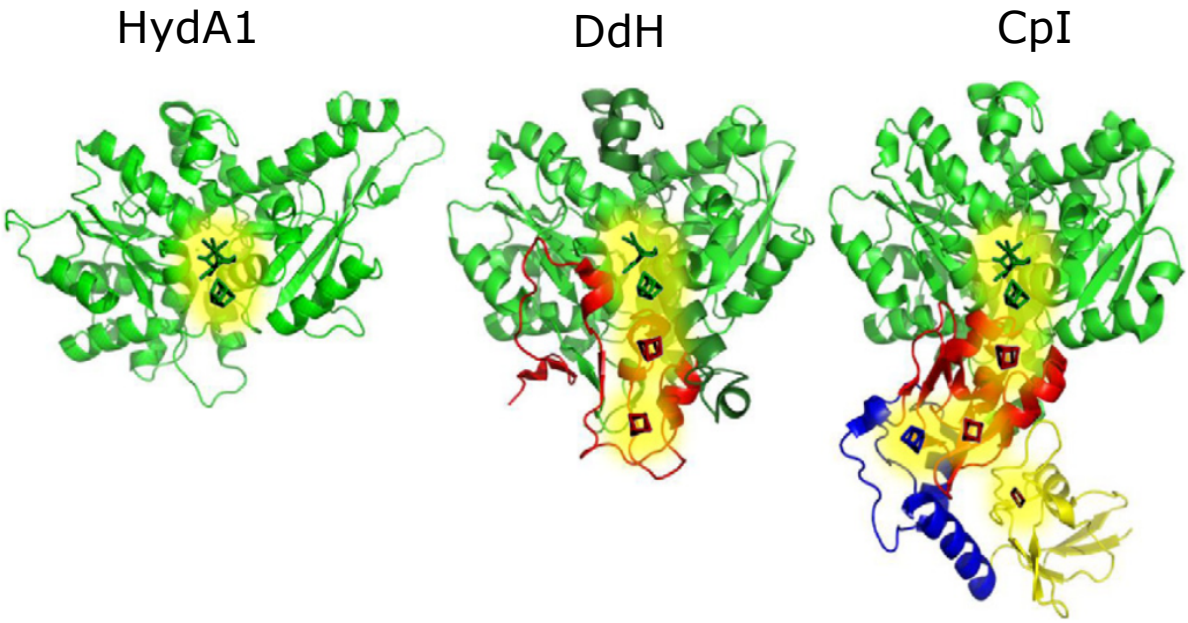

Figure 1.2: Overview on the different [FeFe]-Hydrogenases used in this work. HydA1 as minimal subunit of hydrogen turnover comprises only the H-cluster. DdH and CpI contain additional protein domains (red for DdD and red, blue, yellow for CpI) that harbor accessory Fe-S clusters. Figure adapted from.[19]

Besides crystal structure analysis [FeFe]-hydrogenases are investigated by X-ray absorption spectroscopy,[23] EPR spectroscopy,[24] Mössbauer spectroscopy,[30] IR spectroscopy[25] and protein film electrochemistry.[12] This combined research lead to characterization of several redox states for the H-cluster.

1.3 Redox states of [FeFe]-Hydrogenase

The H-cluster of [FeFe]-hydrogenases has to undergo two reduction steps in order to provide the electrons needed for hydrogen release. The oxidized state (Hox) is characterized by a oxidized [4Fe-4S] cluster (+2) and an oxidized diiron site (+3). Hox represents the active-ready "resting state" featuring an vacancy at Fe_d.[24,31,32] Two redox states reduced by one electron are known. Reduction of the diiron site leads to formation of Hred. The [4Fe-4S] cluster remains oxidized while structure and ligand arrangement of the diiron

Table 1.1: Electronic configuration and alternative annotations of redox states. δe^- reports on reduction compared to Hox.

redox state	Δe^-	[4Fe-4S]	diiron site	alternative notation	reference
Hox	0	+2	+3	-	[24,31,32]
Hred	1	+2	+2	$HredH^+$	[4,17,25,33–38]
Hred'	1	+1	+3	H'red', Hred	[37–39]
Hsred	2	+1	+2	$HsredH^+$	[36,38,40,46]
Hhyd	2	+1	+4	-	[41–43]
Hox-CO	0	+2	+4	-	[24,29,44,45]

site are still under debate.[4,17,25,33–38] Recently Hred', a one electron reduced state that carries the electron at the [4Fe-4S] cluster was reported.[37–39] The diiron site stays oxidized and the IR signature indicates structural similarity to Hox. As redox states reduced by two electrons, Hsred and Hhyd are reported. Hsred features a reduced diiron site and a reduced [4Fe-4S] cluster. Like in Hred, the structure and ligand arrangement of the reduced diiron site is under debate.[36,40] In Hhyd, the two electrons are "stored" in binding a terminal hydride at the vacancy of Fe_d. The diiron side appears to be further oxidized to Hox (+4) and the [4Fe-4S] cluster was found to be reduced (+1). Hhyd was only observed in amino acid or cofactor variants.[41–43] An oxidized, CO inhibited state (Hox-CO) has been shown to bind an additional CO ligand.[24,29,44,45]

1.4 Scope of the thesis

[FeFe]-hydrogenases release H_2 with outstanding efficiency. Understanding the molecular events that lead to hydrogen turnover is required to suggest the design of synthetic, biomimetic catalysts that are able to compete with the natural paragon.

The aim of this thesis is the identification of catalytically relevant redox states and determination of their structure. Hydrogen turnover involves protons and electrons but molecular details of reduction/ protonation dynamics at the H-cluster remain unclear. Reduction and protonation of the H-cluster, function of a conserved proton transfer path, and the role of amino acids surrounding the H-cluster are analyzed by ATR-FTIR spectroscopy. The ATR configuration offers the possibility to access the sample and thereby change experimental parameters *in situ*. IR spectroscopy is sensitive to monitor smallest changes in electron density as for example induced by protonation. Correlation to DFT calculations provides structural information of the redox states observed.

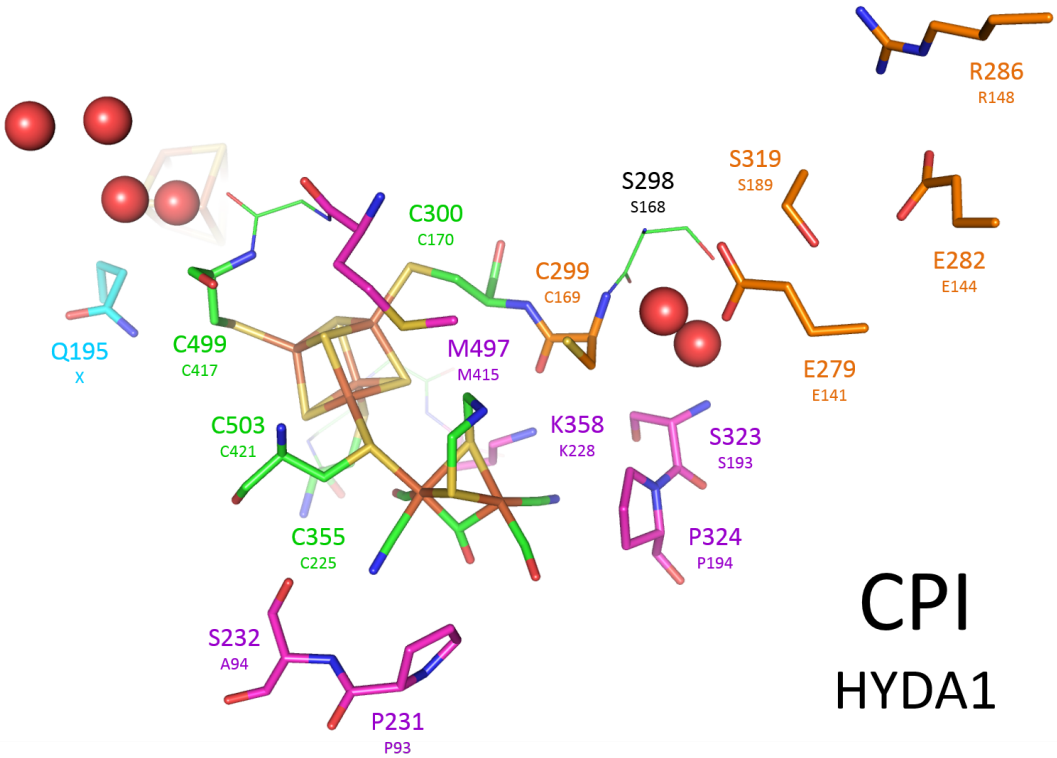

Figure 1.3: H-cluster of [FeFe]-Hydrogenase and surrounding amino acids. Orange residues report on the proton transfer path, green residues are covalently attached to the H-cluster, magenta amino acids are possible H-bond donors to the diiron site and red spheres represent crystal water molecules. Amino acid numbering for CpI in large numbers and for HydA1 in small numbers. (Structure according to PDB 4XDC[47])

Chapter 2

Materials and Methods

2.1 Vibrational Spectroscopy

2.1.1 Molecular Vibrations

Vibrational spectroscopy probes vibrational transitions within a molecule. The simplest approximation is a molecule that consists of two atoms that can be described by two mass points (m_1, m_2) connected by a spring with spring constant k as harmonic oscillator. Its vibrational frequency ω can be written with μ as the reduced mass:

$$\omega = \frac{1}{2\pi}\sqrt{k\left(\frac{1}{m_1}+\frac{1}{m_2}\right)} = \frac{1}{2\pi}\sqrt{\frac{k}{\mu}} \tag{2.1}$$

The Schrödinger equation of this system can be solved using Hermite polynomials. This introduces the quantification of energy levels (with ν as vibrational quantum number and $\hbar$ as reduced Planck constant).

$$E_\nu = \left(\nu + \frac{1}{2}\right)\hbar\omega \tag{2.2}$$

Equation 2.2 implies the lowest energy level $E_0 = \frac{1}{2}\hbar\omega$ for $\nu = 0$. In the harmonic potential the energy levels are equidistant and the maximal distance between the mass point rises until infinity. While low energy levels are well characterized by the harmonic potential molecule dissoziation with increasing distance between its atoms (high energy levels) contradicts this description. To implement molecule dissociation the Morse potential can be used:

$$V(r) = E_D\left(1 - e^{-\alpha(r-r_0)}\right)^2 \tag{2.3}$$

This potential includes the dissociation energy (E_D), the distance between the atoms (r), the equilibrium bond distance (r_0) and $\alpha = \sqrt{k/2E_D}$. It allows for exact solution of Schrödinger equation.

$$E_\nu = \hbar\omega\left(\nu + \frac{1}{2}\right) - \frac{\hbar^2\omega^2}{4E_D}\left(\nu + \frac{1}{2}\right)^2 \tag{2.4}$$

Now, the energy levels are not equidistant. Instead the energy difference decreases with increasing vibrational quantum numbers. Note even if the energy difference is decreasing there are still a finite number of energy levels until dissociation.[48,49]

2.1.2 IR Spectroscopy

Infrared radiation interacts with molecules that change their dipolmoment when their atoms oscillate. If such a molecule is hit by infrared light it can absorb a photon corresponding to the transition energy to a higher vibrational level. The transmittance is given by:

$$T = \frac{I}{I_0} \tag{2.5}$$

were I_0 is the initial light intensity and I the light intensity after passing the absorbing media. The absorption A is defined as:

$$A = -lg(T) = -lg\left(\frac{I}{I_0}\right) \tag{2.6}$$

To get an absorption (A) spectrum the intensity of the emitted light (I_0) to the intensity of the transmitted light (I) is compared. With the help of Beer-Lambert Law (2.7) it is possible to quantify the measured sample absorbance.

$$A = -lg\left(\frac{I}{I_0}\right) = \epsilon_\lambda cd \tag{2.7}$$

ϵ_λ represents the extinction coefficient of the absorbing media, c the concentration and d the path length of the absorbing media. For a given wavelength, e.g. by a monochromator, background intensity (emitted light) and sample intensity (transmitted light) has to be recorded. In order to get a spectrum, this process has to be repeated across the desired energy interval with a given spectral resolution.[50]

2.1.3 Fourier Transform Infrared Spectroscopy

In Fourier Transform Infrared Spectroscopy (FTIR) broadband Infrared (IR) radiation is sent through Michelson Interferometer that consists of a beam splitter, a fixed mirror and a movable mirror. The beam splitter reflects half of the incoming beam to the fixed mirror and transmits the other half to the movable mirror. The difference in beam path induced by the moving mirror results in interference of the back reflected light at the beam splitter that sends half of the signal back in the direction of the incoming beam and half to the detector. The detector records the intensity of the interferogram in dependency of the mirror position. The mirror position can be monitored by the interference pattern of a

visible laser sent trough the interferometer. This interferogram is the Fourier transformed spectrum created by the interferometer. For monochromatic light with the intensity $I(\tilde{\nu})$ the intensity of the interferogram ($I(p)$) in dependence of mirror position p formulates as the following:

$$I(p) = I(\tilde{\nu})(1 + cos(2\pi\tilde{\nu}p)) \tag{2.8}$$

For polychromatic light all contributions have to be integrated:

$$I(p) = \int_0^\infty I(\tilde{\nu})(1 + cos(2\pi\tilde{\nu}p))d\tilde{\nu} \tag{2.9}$$

Fourier transformation relates the mirror positions back to frequencies

$$I(\tilde{\nu}) = 4\int_0^\infty \left(I(p) - \frac{1}{2}I(0)\right) cos(2\pi\tilde{\nu}p)dp \tag{2.10}$$

and a full spectrum can be obtained.[51] The major advantage of FTIR is that all wavelengths are collected simultaneously so a whole spectrum can be taken. This improves the time resolution, especially relevant for non-repetitive processes. Furthermore the intensity of the IR radiation source in not diminished compared to grid-based IR spectrometers where the slit geometry reduces the probing intensity to a larger extend. High internal wavenumber calibration is granted by the use of the interference pattern of a He-Ne laser to track the mirror position.

2.1.4 Attenuated Total Reflection

When light strikes the interface of two materials that differ in refraction index three different phenomena can be observed. Depending on the angle of the incoming beam and the refractive index, there is either refraction or reflection. The relationship is given by Snells law (2.11) where n_1 and n_2 are the refractive indices and θ_1 and θ_2 the angle of the incoming, respectively refracted/reflected beam to the normal of the interface (Figure: 2.1).

Snells law:

$$n_1 sin(\theta_1) = n_2 sin(\theta_2) \tag{2.11}$$

Refraction happens up to an critical angle(θ_1=θ_C) for which θ_2 equals 90°. The refracted

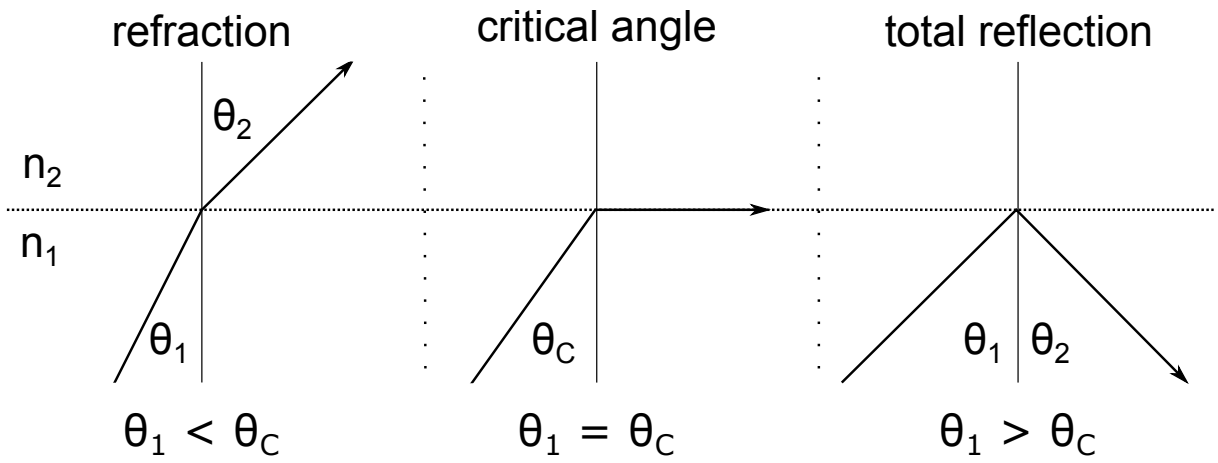

Figure 2.1: Different phenomena that occur at the interface of two media with different optical density. In dependence of the angle θ_1 either refraction($\theta_1 < \theta_C$) or total reflection($\theta_1 > \theta_C$) is observed. The refraction index n_1 is larger than n_2.

beam travels now in the interface of the two media.

$$sin(\theta_1) = \frac{n_2}{n_1} sin(\theta_2) \tag{2.12}$$

for $\theta_2 = 90°$

$$\theta_1 = \theta_C = arcsin\left(\frac{n_2}{n_1}\right) \tag{2.13}$$

For angles larger than θ_C total internal reflection takes place and "the reflection should be total, not 99.9 per cent but 100 per cent".[52] For $\left(\frac{n_2}{n_1}\right) > 1$ arcsin is not defined. No total reflection occurs which means total internal reflection is only possible from a medium with higher refractive index at the interface to a medium with lower refractive index.

In the total reflection process an evanescent wave is formed that penetrates beyond the interface. The transmitted electric field (E_T) can be expressed as follows:

$$\vec{E_T} = \vec{E_0} e^{i(\vec{k_T}\vec{r} - \omega t)} \tag{2.14}$$

with

$$\vec{k_T} = k_T sin(\theta_2)\vec{e_x} + k_T cos(\theta_2)\vec{e_z} \tag{2.15}$$

for a plane wave propagating in x-z direction and with $k_T = \omega n_2/c$ (dispersion relation).

$$sin(\theta_2) = \frac{n_1}{n_2} sin(\theta_1) \tag{2.16}$$

for $n_1 > n_2$ and $\theta_1 > \theta_C$ this results in a complex $cos(\theta_2)$

$$cos(\theta_2) = \sqrt{1 - sin^2(\theta_2)} = i\sqrt{sin^2(\theta_2) - 1} \tag{2.17}$$

with 2.16, 2.17 and the dispersion relation $\vec{k_T}$ gets:

$$\vec{k_T} = \frac{\omega}{c}\left(n_1 sin(\theta_1)\vec{e_x} + n_2 i\sqrt{sin^2(\theta_2) - 1}\vec{e_z}\right) \tag{2.18}$$

Substituting the second term in brackets with relation 2.16 leads to:

$$\vec{k_T} = \frac{\omega}{c}\left(n_1 sin(\theta_1)\vec{e_x} + i\sqrt{n_1^2 sin^2(\theta_1) - n_2^2}\vec{e_z}\right) \tag{2.19}$$

Defining $\vec{k_x}$ and $\vec{k_z}$ as follows:

$$\vec{k_T} = \vec{k_x} + i\vec{k_z} \tag{2.20}$$

Consequently the transmitted electric field can be written as:

$$\vec{E_T} = \vec{E_0} e^{-\vec{k_z}} e^{i(\vec{k_x} - \omega t)} \tag{2.21}$$

with $\vec{k_x}$ and $\vec{k_z}$ exclusively dependent on θ_1, n_1 and n_2. The transmitted electric field has a component in z direction (into the less dense medium) that decays exponentially (evanescent wave) and a component that is parallel to the interface. The total reflected beam looses some energy and is thereby attenuated. The penetration depth of the evanescent wave (in z-direction with wavelength λ) were the amplitude decayed to $\frac{1}{e}$ is described with the help of:

$$|\vec{k_z}| = \frac{\omega}{c}\sqrt{n_1^2 sin^2(\theta_1) - n_2^2} = 1/d \qquad \frac{\omega}{c} = \frac{2\pi}{\lambda} \tag{2.22}$$

$$d = \frac{\lambda}{2\pi\sqrt{n_1^2 sin^2(\theta) - n_2^2}} \tag{2.23}$$

As an example the penetration depth of an evanescent wave at interface of silicon (n=3.4) and a protein film (n = 1.5) with an incoming beam ($\lambda = 5\mu m$ corresponding to 2000 cm^{-1}) at the angle of $\theta = 45°$ is 423 nm.[52,53]

2.1.5 ATR-FTIR Spectroscopy

In Attenuated Total Reflection (ATR)-FTIR spectroscopy the surface of an IR-transparent crystal is probed by the evanescent wave of an IR-beam hitting the crystal surface from beneath. IR-transparent crystals are e.g. Si, Ge, and ZnSe. The evanescent wave penetrates in sub μm range and can probe multiple layers of protein covering the crystal surface. Advantages of this technique are that only small sample volumes are needed and that the protein film is accessible to in principle any treatment e.g.variation in hydration level, gas composition and numerous chemical treatments. Inspired by the "moss cell"[54] modification with gold mesh and a permeable membrane enables also for electrochemical control and measurements in solution. In the described experiments typically 1 μl of 1mM purified enzyme was applied to the ATR crystal. In ATR the z component or evanescent wave interacts with a sample deposited on the less optical dense part and absorption can take place.

2.1.6 Spectrometer and Experimental Environment

If not mentioned otherwise all ATR-FTIR measurements were performed on a Bruker Tensor 27 with an mid-IR globar as radiation source. A liquid nitrogen cooled mercury cadmium telluride detector was used to record the signal. The ATR optics with a two active reflection silicon crystal were manufactured by Smith Detection. The spectrometer was located in a Coy Labs anaerobic glovebox filled with an overpressure atmosphere of nitrogen and up to 1% hydrogen. To avoid any oxygen contaminations paladium catalysts were installed that reduce trace amounds of O_2 to water. The spectrometer was purged by nitrogen as well as the ATR optics compartment. Nitrogen was purified from dry air by a nitrogen generator (Inmatec) to a purity of 4.8-5.0. Spectra were recorded with 1 cm^{-1} resolution and a scanner velocity of 80 kHz.

2.1.7 Aerosol FTIR-ATR Setup

The aerosol ATR-FTIR setup exploits one of the main advantages of ATR spectroscopy: sample accessibility. The ATR optics are placed in the beam path of the FTIR spectrometer. A volume on top of the crystal is sealed by a custom build cell of Polychlorotrifluoroethene. This cell allows for gas exchange via gas interfaces. An optical transparent

window enables for sample illumination or alternative transmission sample preparation. For hydration an aerosol can be created by a gas stream bubbling through a water filled wash bottle and guided into the cell. The sample can interacts with the gas stream that covers its head space above. However no gaseous water is detected by the evanescent wave. The flow rate of gases controlled by a mass flow controller (MFC) and the ratio between dry gas and aerosol allows for control of hydration level of the sample (Section: 3.1.1). In addition to hydration the pH can be adjusted by creation of the aerosol with buffer of desired pH. Thereby pH titrations of hydrated enzyme films can be performed (Section: 3.3). H/D exchange within the enzyme film is facilitated by replacement of of H_2O to D_2O in the wash bottle (Section: 3.3.4). Alteration of the aerosol carrier gas (e.g. N_2, CO, H_2, O_2) can induce different interactions with the sample (Section: 3.1.3). An overview of the aerosol FTIR-ATR setup is given in Figure 2.2. The pH mentioned in aerosol experiments refers always to the buffer pH used to create the aerosol.

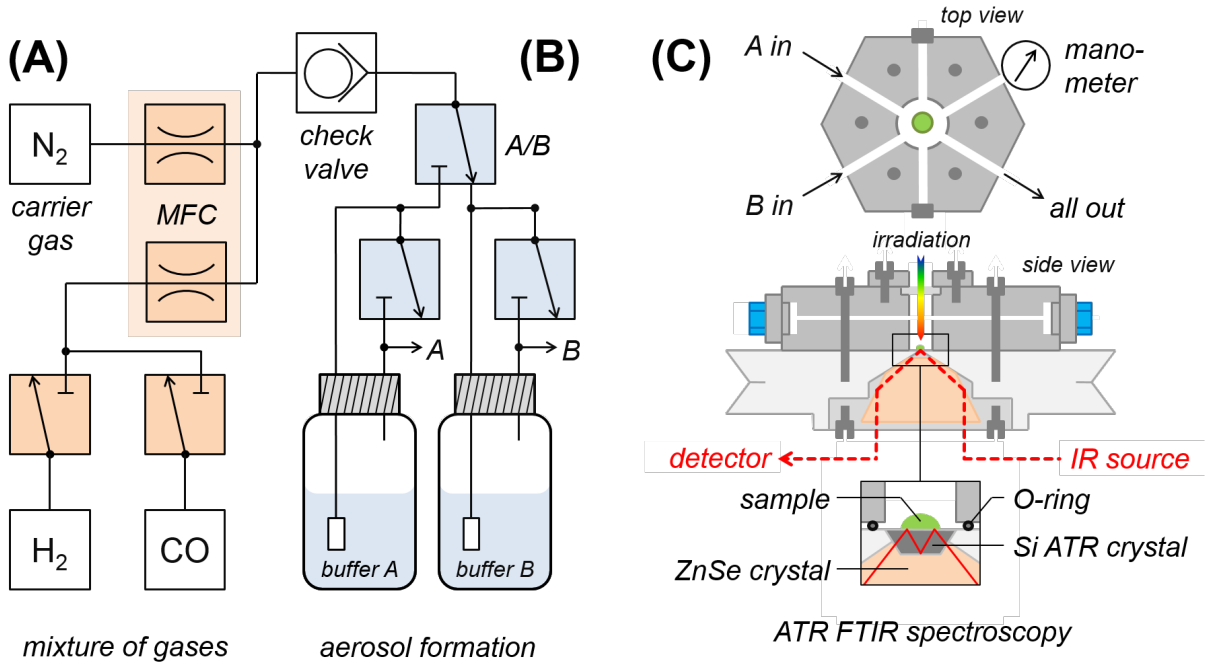

Figure 2.2: Schematic view on the aerosol ATR-FTIR setup. **(A)** N_2 controlled by a mass flow controller (MFC) can be mixed with other gases (e.g. H_2 or CO) that are controlled by a second MFC. **(B)** The eventual gas mixture can now be humidified to create an aerosol via bubbling through one or two wash bottles filled with water/reactants or be guided directly (dry) to the head space volume on top of the sample by a gas inlet in the polychlorotrifluoroethene cell. **(C)** The sample is located on the two active reflection ATR silicon prism were it interacts with the evanescent wave of the IR beam that hits the crystal from below. An optical transparent window that seals top of the cell provides for sample illumination. Gas can leave the head space volume via a gas dump outlet. Figure taken from[IV]

2.1.8 Spectro-electrochemistry using ATR-FTIR spectroscopy

For spectro-electrochemical experiments it is necessary to contact the sample with a electrolyte solvent. The main challenge in performing protein ATR spectroscopy in solution is to keep the protein film close to the crystal surface. For membrane proteins lipid membrane reconstitution can solve this problem. In contrast, a soluble enzyme like [FeFe]-hydrogenase would diffuse away from the crystal surface. To keep the enzyme sample close to the surface a dialysis membrane is used that covers the crystal and the sample beneath it. If the cutoff of the dialysis membrane is smaller than the enzyme molecular weight the sample can get in contact with a solvent without leaving the region of the crystal surface where the evanescent wave still probes.

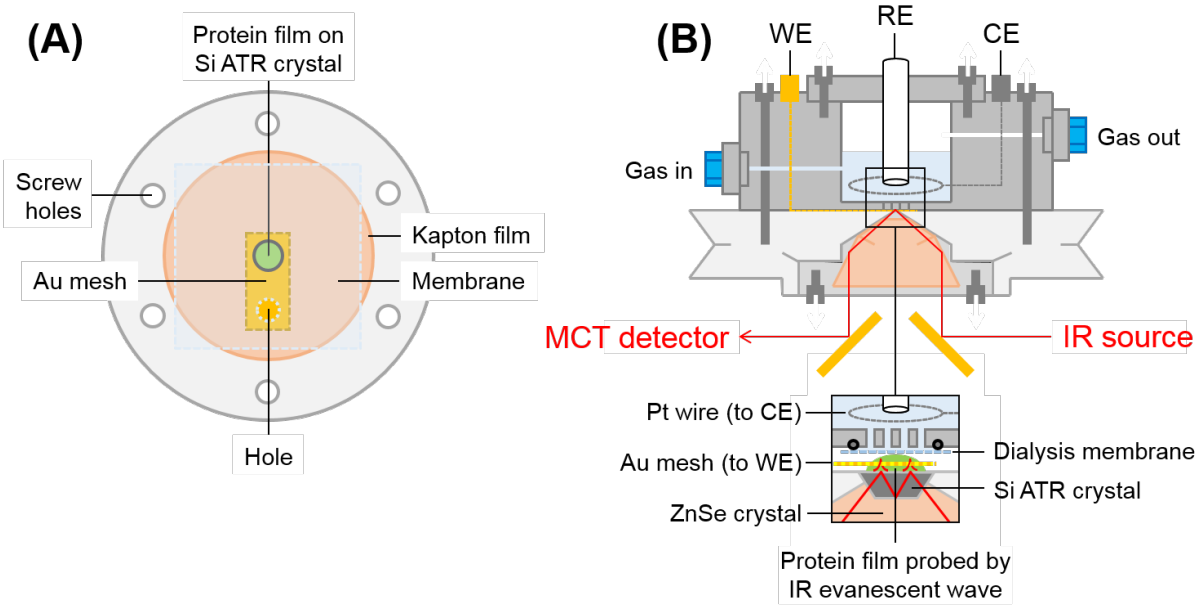

Figure 2.3: Schematic view on the spectro-electrochemisty ATR-FTIR setup. **(A)** Top view on the crystal plate. Kapton tape isolates the crystal plate surface from the gold mesh that covers the crystal surface. Sample is applied beneath a dialysis membrane which features a hole on top of the gold mesh to enable electric contact. **(B)** Side view on the crystal plate with electrochemisty cell. The working electrode is contacted via a copper ring on the bottom of the cell to the gold mesh. A platinum wire serves as counter electrode and the reference electrode is installed from the top. The sample is probed by the IR beam that enters the ATR crystal from the bottom. Figure taken from[III]

A 9 μm gold mesh acts as a working electrode and is placed on the crystal surface of the ATR crystal. The sample is injected into the mesh that is covered by a 8 kDa dialysis membrane. A custom build polychlorotrifluoroethene cell is screwed into the crystal plate and tightens the membrane. The sample get in contact with the solvent if the solvent compartment of the cell was filled with electrolyte buffer. A copper ring fixed beneath

the cell establishes conductive contact to the working electrode (gold mesh). As counter electrode a platinum wire and as reference electrode a Ag/AgCl electrode are used. For electrochemical measurements a potentiostat is connected to three electrodes. Potentials were measured and applied between working and reference electrode while current was detected by working and counter electrode (Figure: 2.3 (A), (B)).

2.2 Density Functional Theory

Density functional theory (DFT) allows for quantum mechanical description of a many body system. This is accomplished by reduction of the 3N spatial coordinates of the wavefunction for N electrons (with N as number of electrons) to N equations one for each electron with only three coordinates, the Kohn-Sham equations (2.24).

$$\left(-\frac{\hbar^2}{2m}\nabla^2 + V_s(\vec{r})\right)\phi_i(\vec{r}) = \epsilon_i\phi_i(\vec{r}) \tag{2.24}$$

Here $V_s(\vec{r})$ is the potential, $\phi_i(\vec{r})$ are the orbitals and $\epsilon_i(\vec{r})$ the corresponding energies. By solving the Kohn-Shan equations it is possible to obtain the electron density for the full system (2.25).

$$n_s(\vec{r}) = \sum_i^N |\phi_i(\vec{r})|^2 \tag{2.25}$$

The particle potential $V_s(\vec{r})$ of equation 2.24 depends on the electron density $n_s(\vec{r})$ and can be written as:

$$V_s(\vec{r}) = V(\vec{r}) + \int \frac{e^2 n_s(\vec{r}')}{|\vec{r} - \vec{r}'|} d^3r' + V_{XC}(n_s(\vec{r})) \tag{2.26}$$

The three terms of the potential $V_s(\vec{r})$ can be separated into external potential, electrostatic interaction and the exchange-correlation potential. Since the potential $V_s(\vec{r})$ needed to solve the Kohn-Sham equations is already dependent on the electron density and the electron density is dependent on $\phi_i(\vec{r})$ and thereby on the solution of the Kohn-Sham equations, an electron density has to be found that solves the set of equations self consistent. Starting with an assumption for the electron density the Kohn-Sham equations (2.24) can be solved. The obtained $\phi_i(\vec{r})$ can be used to refine the electron density (2.25). With this electron density the potential $V_s(\vec{r})$ (2.26) can be recalculated. In this iterative way this potential can be used again to solve the Kohn-Sham equations until the electron density and the potential are not changing anymore.[55]

2.3 Enzyme Expression, Purification and Maturation

Expression, purification and maturation hydrogenase of CpI and HydA1 samples were performed by the working group of Prof. Thomas Happe at Ruhr-Universität Bochum.

Apoenzyme of CpI and HydA1 was expressed in *Escherichia coli* and purified by one-step strep-tactin affinity chromatography under strictly anaerobic conditions. Thus the apoenzyme contains only the [4Fe-4S] cluster of the H-cluster for *in vitro* maturation the apoenzyme was exposed to a 10-fold molar excess of the chemically synthesized diiron site precursor for 30 min.[28] DdH enzyme from *Desulvovibrio desulfuricans* was purified as described previously.[56]

Chapter 3

Results

ATR Spectroscopy on Hydrogenases

Already in 1961 J. Fahrenfort mentioned: "This attenuated total reflection (ATR) technique will be useful in many cases in which normal infra-red techniques fail owing to difficulties in sample preparation.".[53] The ATR technique offers the option to control a large set of conditions crucial for enzyme function like hydration (Section: 3.1.1), gas composition (Section: 3.1.3) and proton concentration (Section: 3.3). Real-time observation of the enzyme response to changes in these conditions can provide insight into enzyme function. For the investigation of the hydrogenase catalytic mechanism the possibility to probe its interaction with its products/educts is crucial. Modification of the ATR setup enables electrochemical control and offers the possibility to control the parameter electron pressure in addition to H_2 and H^+ (Section: 3.3.6 and 3.4).

3.1 ATR-FTIR Spectroscopy on [FeFe]-Hydrogenase

A typical ATR-FTIR spectrum of [FeFe]-Hydrogenase is shown in Figure 3.1. Several bands can be assigned to the protein backbone.[50] The NH stretching vibration of the protein backbone manifests as the Amide A at 3310-3270 cm^{-1} and Amide B band at around 3070 cm^{-1}. The Amide I band arises at around 1650 cm^{-1}. It consists mainly of the C=O stretching vibration that is weakly coupled to the CN out-of-phase stretching, the CCN deformation and the NH in-plane bending vibration. The composition of components forming the Amide I band are sensitive to secondary structure.[50] The out-of-phase combination of the NH in plane bending and the CN stretching vibration forms the Amide II band. It is influenced by the CO in

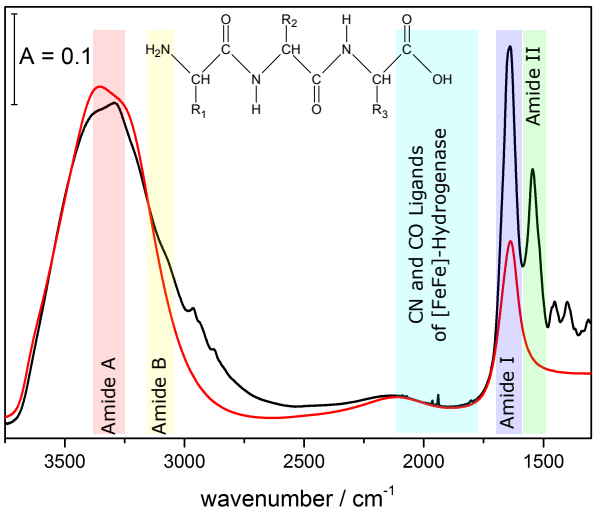

Figure 3.1: ATR FTIR spectrum of [FeFe]-Hydrogenase (black line). The contribution of H_2O is shown (red line). Colored are the Amide A (light red), Amide B (yellow), Amide I (purple) and Amide II (green) regions and the region of the CN and CO H-cluster ligands (cyan) that is well separated from the Amide regions. A chemical representation of a triamine is shown for illustration of the amide vibrations described in the text.

plane bending, the CC stretching and the CN stretching vibration. The Amide II band is also used for secondary structure analysis.[50] Since the protein sample is hydrated bands overlap with the water absorption at around 3400 cm^{-1} (O-H stretching vibration), 2125 cm^{-1} (water association combination band) and 1640 cm^{-1} (H-O-H bending vibration).[57] The region of main interest for hydrogenases in IR spectroscopy is well separated from the Amide bands mentioned above. The CN ligands bound to iron absorb at around 2100 cm^{-1} and the CO ligands when bound to iron absorb in the 1990-1790 cm^{-1} region.[34]

3.1.1 Hydration and Dehydration of Enzyme Films

Since water plays an important role for both enzyme function and the signal in the IR spectrum hydration and dehydration were analyzed in the aerosol setup (described in Section 2.1.7). Even though the main water bands are separated from the CO/CN band region the water content of the enzyme film deposited on the ATR crystal has critical impact on cofactor signal intensity. Hydration leads to swelling of the enzyme film thereby the evanescent wave interacts with less protein and more water molecules due to lower protein density in the probed volume (dilution of the enzyme sample). Dehydration has the opposite effect enhancing the enzyme signal but lowering the reactivity of the film. A typical series of spectra that monitor the dehydration under dry N_2 gas after the liquid sample is deposited on the ATR crystal is shown in Figure: 3.2 (A). Note the nearly complete absence of the Amide II band in the beginning of this process. In the dry film Amide I and Amide II intensity are about equal. Cofactor ligand bands manifest during concentration of the enzyme (drying) (Figure: 3.2 (B)). Rehydration by an humidified aerosol can be seen in Figure: 3.2 (C). Dilution of the film is seen by decreased Amide II band intensity. In Figure:3.2 (D) the cofactor region is shown that points out ∼100% reversibility of this process without loss of the active site signal.

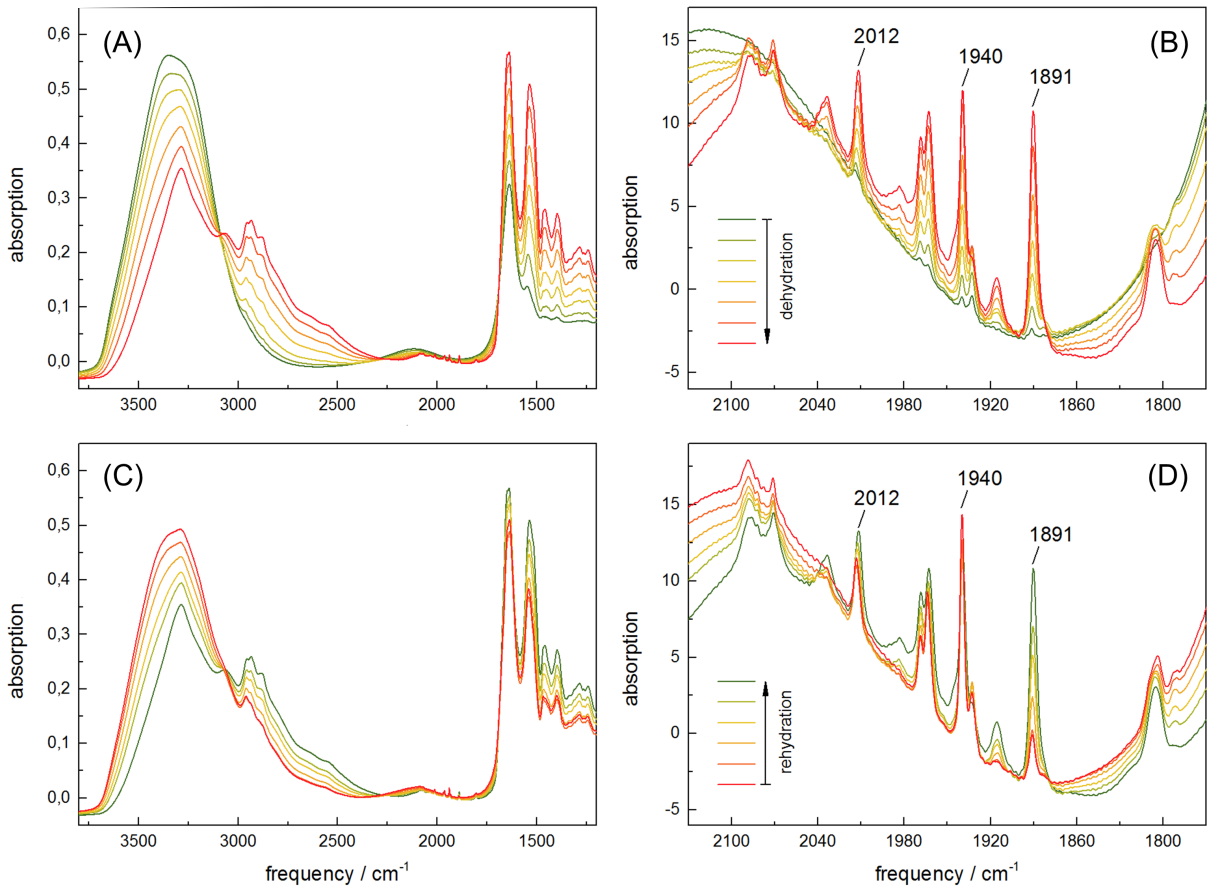

Figure 3.2: Dehydration and rehydration of an exemplary HydA1 enzyme film. Panel (A) displays the drying process from liquid sample as applied to the ATR crystal surface (green spectra) to dry (red spectra). The same process is shown in panel (B) for the cofactor region. Rehydration by a humidified aerosol is displayed in panel (C) (full spectrum) and panel (D) (cofactor region). Figure taken from[I]

3.1.2 Temporal Stability of Enzyme Films

To get an impression for temporal stability of HydA1 enzyme films in the aerosol setup (Section: 2.1.7) the cofactor signals were monitored over time. The enzyme film was equilibrated to semi-dry hydration level and then kept under closed N_2 atmosphere at room temperature. As can be seen in Figure 3.3 no cofactor signal loss was observed for at least eight days. The population of adopted redox states remained constant over the whole time span. The population of Hox, HoxH, Hox-CO and Hred remained constant (Figure: 3.3 right).

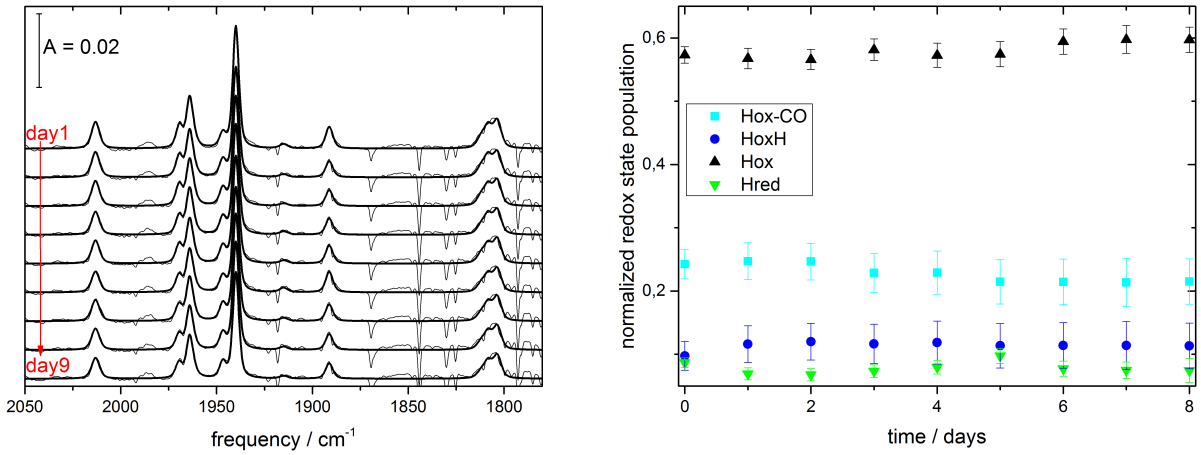

Figure 3.3: Every spectrum of the cofactor region was recorded in time steps of one day. Due to differences in water vapor the spectra were fitted and shown on top of the baseline corrected spectra. Cofactor signal and the adopted redox states stay the same over the whole period.

3.1.3 Overview of Hydrogenase interaction with gases

To get an idea of [FeFe]-hydrogenase interaction with gases like H_2, N_2, CO and O_2 films that consist of 1 μl 1mM HydA1 enzyme were deposited on the ATR crystal surface of the aerosol setup described in Section 2.1.7. The sample was dried and rehydrated by a 1.5 L/min nitrogen stream. Rehydration was carried out with 100mM Tris buffer containing 2mM NaDT at pH 8 (see Section 3.1.1). Sub sequent the sample was exposed to the respective gas. Table 3.1 summarizes the known redox states and their CN/CO band positions from literature.

Table 3.1: Redox states and respective CN and CO band positions from literature.

	CN band positions/cm^{-1}	**CO band positions/cm^{-1}**	**Reference**
Hox	2088, 2070	1964, 1940, 1802	[24,31,32]
Hred	2070, 2033	1962, 1915, 1891	[25,34,38]
Hred'	2084, 2066	1962, 1933, 1792	[37–39]
Hsred	2068, 2026	1951, 1918, 1882	[36,40]
Hox-CO	2091, 2082	2013, 1968, 1962,1808	[24,29,44,45]

Films that consist of 1 μl 1mM HydA1 enzyme were deposited on the ATR crystal surface of the aerosol setup described in Section 2.1.7. The sample was dried and rehydrated by a 1.5 L/min nitrogen stream. Rehydration was carried out with 100mM Tris buffer containing 2mM NaDT at pH 8 (see Section 3.1.1).

Hydrogenase interaction with molecular hydrogen

When the HydA1 enzyme film gets in contact with molecular hydrogen the oxidation of H_2 leads to reduction of the sample. Figure 3.4 shows exemplary the reduction induced by addition of 1% H_2 to the N_2 aerosol stream. The reduction manifests in depopulation of the oxidized state oxidized state (Hox) (black). The one electron reduced states diiron site reduced state (Hred) (green) and [4Fe-4S] reduced state (Hred') (red) are populated as well as the two electron reduced state super reduced state (Hsred) (magenta). The accumulation of the reduced states can be tracked over time and reveals differences in relative population and accumulation velocity(3.4 right). The reduction of the enzyme is reversible if H_2 supply is interrupted and only N_2 acts as a carrier gas for the aerosol. A detailed analysis of these phenomenons will be given in Section 3.3.

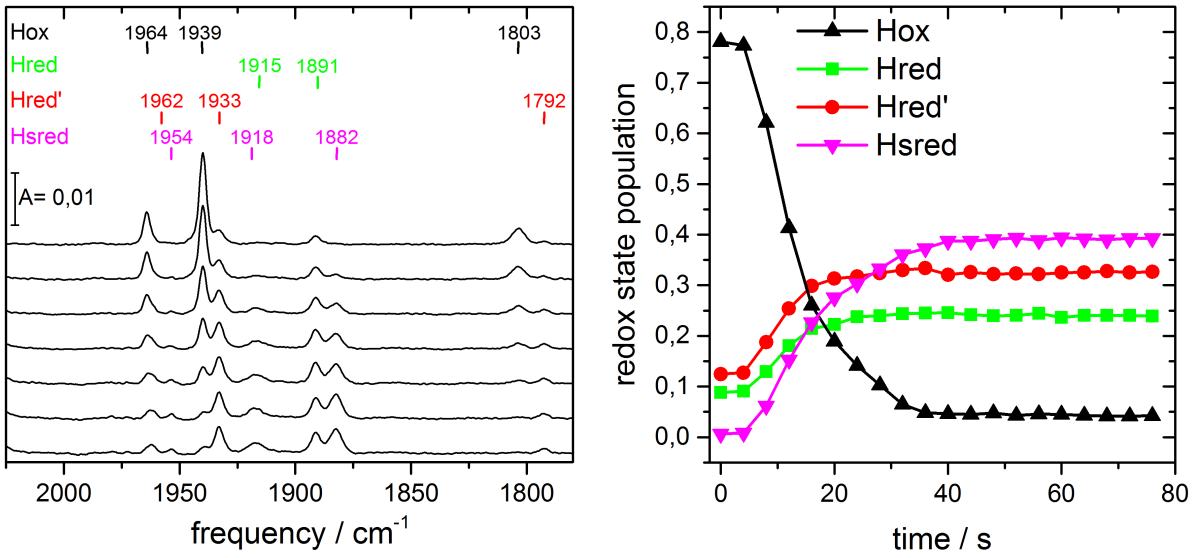

Figure 3.4: Left: Selected spectra that illustrate HydA1 reduction by 1% H_2 (from top to bottom). Hox (black: 1964 cm^{-1}, 1939 cm^{-1}, 1803 cm^{-1}) gets depopulated in favor of the one electron reduced states Hred' (red: 1962 cm^{-1}, 1933 cm^{-1}, 1792 cm^{-1}), Hred (green : 1962 cm^{-1}, 1915 cm^{-1}, 1891 cm^{-1}) and the two electron reduced state Hsred (magenta: 1952 cm^{-1}, 1918 cm^{-1}, 1882 cm^{-1}). **Right:** Timetrace of redox state population that illustrate HydA1 reduction by 1% H_2. Hox (black) gets depopulated in favor of the one electron reduced states Hred' (red) and Hred (green) within 20 seconds. The two electron reduced state Hsred (magenta) is populated within 40 seconds.

Hydrogenase interaction with nitrogen gas

In Figure 3.5 the response of an HydA1 film to N_2 gas is monitored over time. The spectrum shows a mixture of Hox(black), Hred (green) and Hred' (red) with traces of Hsred (magenta). Over time the reduced states bands decrease (3.5 right). The inert gas nitrogen can be used to populate the oxidized state e.g. as a clean starting point before initiating a reaction. All other redox states than Hox are depopulated by N_2. While reduction by H_2 was observed in seconds (3.4) the auto oxidation with N_2 occurs in the time frame of minutes.

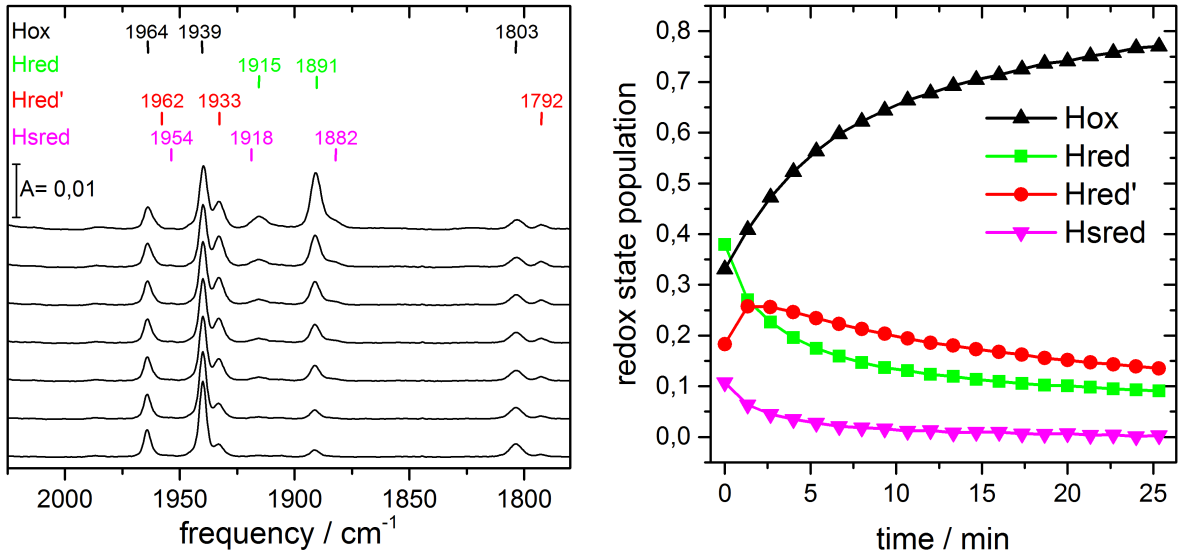

Figure 3.5: Right: Selected spectra that illustrate the response of the HydA1 film to 100% N_2 (from top to bottom). Hox (black: 1964 cm^{-1}, 1939 cm^{-1}, 1803 cm^{-1}) gets populated while the one electron reduced states Hred' (red: 1962 cm^{-1}, 1933 cm^{-1}, 1792 cm^{-1}), Hred (green : 1962 cm^{-1}, 1915 cm^{-1}, 1891 cm^{-1}) and the two electron reduced state Hsred (magenta: 1952 cm^{-1}, 1918 cm^{-1}, 1882 cm^{-1}) get depopulated. **Left:** Timetrace of redox state population that illustrate the response of the HydA1 film to 100% N_2. Hox (black) gets populated while the one electron reduced states Hred' (red) and Hred (green) and the two electron reduced state Hsred (magenta) are depopulated.

Hydrogenase interaction with carbon monooxide gas

[FeFe]-hydrogenase exposed to CO gas gets inhibited by occupation of the open coordination site at Fe_d. A fourth CO ligand can be observed in the IR spectrum of the cofactor region (Figure 3.6 left). CO inhibition occurs with in seconds (Figure 3.6 right) and the fourth CO ligand that blocks the active site can be removed by aerosol treatment either with N_2 in the time frame of hours or H_2 in the time frame of minutes (Figure: 3.7). For a detailed analysis see Section 3.2.

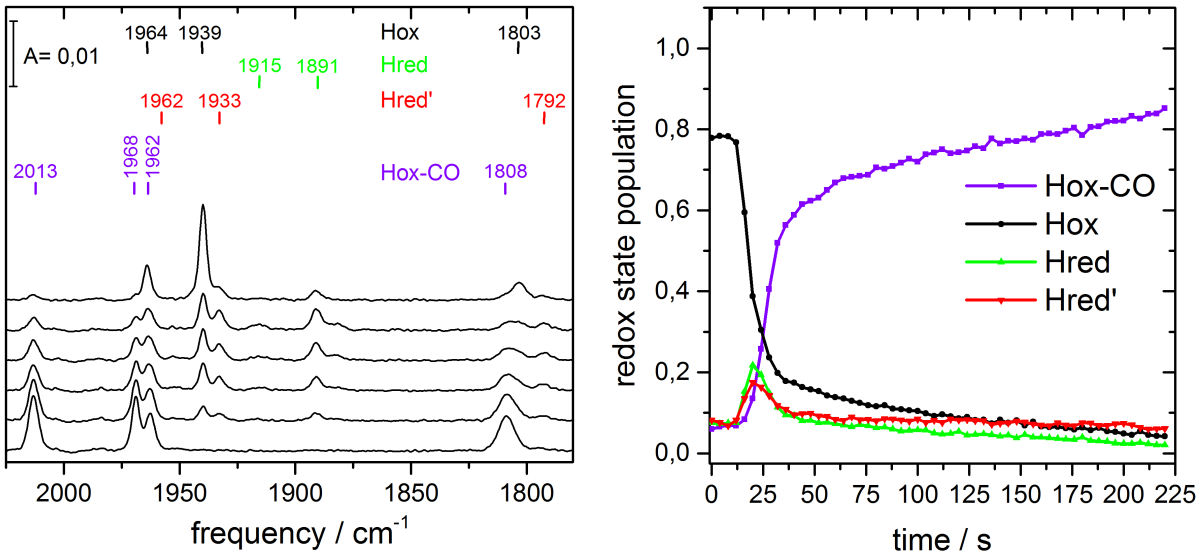

Figure 3.6: Left: Selected spectra that show carbon monoxide inhibition upon 100% CO exposure (from top to bottom). Hox-CO (violet: 2013 cm^{-1}, 1968 cm^{-1}, 1962 cm^{-1}, 1808 cm^{-1}) gets populated while Hox (black:1964 cm^{-1}, 1939 cm^{-1}, 1803 cm^{-1}) and the one electron reduced states Hred' (red: 1962 cm^{-1}, 1933 cm^{-1}, 1792 cm^{-1}) and Hred (green : 1962 cm^{-1}, 1915 cm^{-1}, 1891 cm^{-1}) get depopulated. **Right:** Timetrace of redox state population that illustrate the carbon monooxide inhibition of the HydA1 film upon exposure to 100% CO. Hox-CO (violet) gets populated while Hox (black) and the one electron reduced states Hred' (red) and Hred (green) are depopulated.

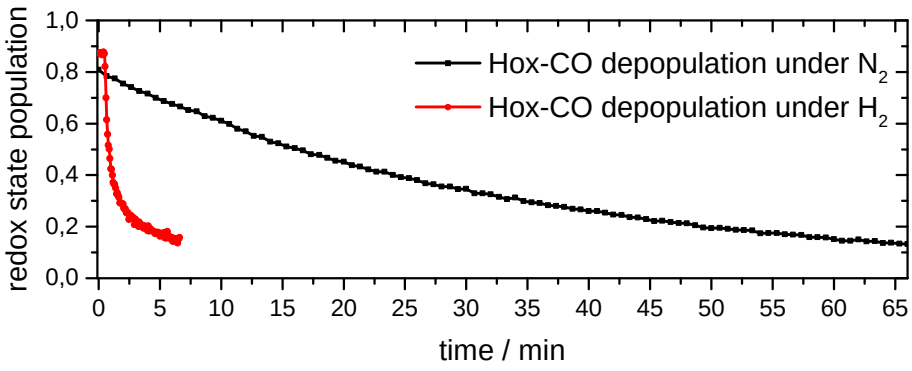

Figure 3.7: Timetrace that highlights the Hox-CO depopulation either in the houre regime treated by a N_2 aerosol (black trace) or in the minutes regime treated by H_2 (red trace).

Hydrogenase interaction with oxygen gas

Exposure of HydA1 to O_2 leads to destruction of the diiron site. Figure 3.8 displays the loss of CO bands during contact to O_2 Bands of Hox (black: 1964 cm^{-1}, 1939 cm^{-1}, 1803 cm^{-1}) vanish while a transient increase in Hox-CO (2012 cm^{-1}, 1968 cm^{-1}, 1962 cm^{-1} and 1808 cm^{-1}) can be observed. Transient Hox-CO population is due to binding of free CO molecules of destroyed diiron sites to intact diiron sites. The IR signature of Hox-CO decays slower than Hox as can be seen in Figure 3.8

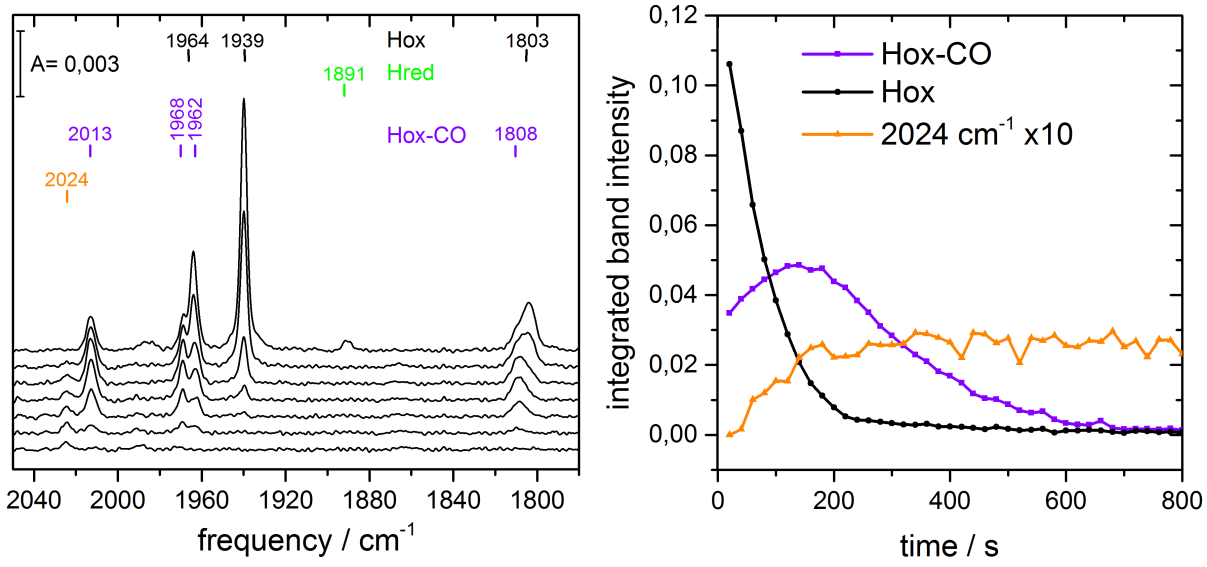

Figure 3.8: Left: Selected spectra that show loss of the CO ligand signal upon O_2 exposure(from top to bottom). Hox (black: 1964 cm^{-1}, 1939 cm^{-1}, 1803 cm^{-1}) gets populated and transient Hox-CO (violet: 2013 cm^{-1}, 1968 cm^{-1}, 1962 cm^{-1}, 1808 cm^{-1}) is enriched due to free CO molecules of disrupted cofactors. An transient band is observed at 2024 cm $^{-1}$ (orange). **Right:** Timetrace of redox state population that illustrate the destruction of the HydA1 film upon exposure to O_2. Hox (black) gets depopulated and transiently Hox-CO (violet) is enriched due to free CO molecules of disrupted cofactors.

3.2 Isotopic editing of Carbonyl ligands

For ^{13}CO isotopic editing experiments typically 1 μl of 1mM HydA1 was applied to the ATR crystal surface. Exposure to ^{12}CO, ^{13}CO and N_2 at different hydration levels and different light qualities was employed to derive pure spectra of all possible permutations of isotopic labeled Hox and Hox-CO. While CO band shift around 44 cm^{-1} upon ^{13}CO replacement the CN ligands are just minor affected by ^{13}CO exchange and shift by circa 1 cm^{-1}. Therefore only the CO bands are discussed here.

The CO ligands were named pCO for the CO ligand bound to Fe$_p$, μCO for the bridging CO ligand and dCO for the CO ligand bound to Fe$_d$. In the case of Hox-CO the former dCO ligand is named d$_1$CO while the new additional CO ligand bound is named d$_2$CO. The accumulation of all possible ^{13}CO isotopameres can be divided into two parts. The first part where the proximal CO ligand remains ^{12}CO (Figure: 3.9) (p^{12}CO, upper cycle)) and the second part where the proximal CO ligand is exchanged for ^{13}CO (Figure: 3.9) (p^{13}CO, lower cycle)). Spectroscopic details of the isotopic editing procedure with unaltered pCO ligand (^{12}CO) and for isotopic edited pCO (^{13}CO) are described in Section 3.2. For both parts the identical experimental procedure was applied besides $^{12/13}$CO treatments were inverted because the starting point of each cycle is either all ^{12}CO labeled Hox-CO or all ^{13}CO labeled Hox-CO (Figure:

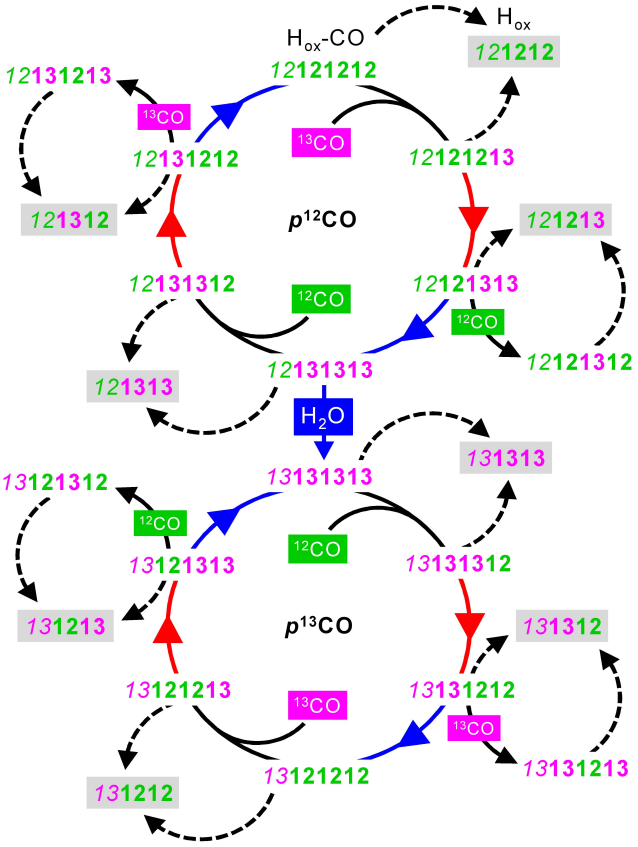

Figure 3.9: Isotopic editing reaction cycle. The labeling pattern is is given by either a green 12 that represents ^{12}CO or a magenta 13 that represents ^{13}CO. The order of numbers for H$_{ox}$CO (4 numbers) from left to right: proximal (pCO), bridging (μCO), first dista l(d$_1$CO), second distal (d$_2$CO) and for H$_{ox}$ (3 numbers) with the order from left to right: pCO, μCO and dCO. Transitions between different states and isotopameres are indicated by lines. Black lines stand for transitions in the dark under either ^{12}CO or ^{13}CO atmosphere. Dashed black lines for dark transitions purging with N_2. Red and blue arrows illustrate transitions that where performed under light with corresponding color. Figure taken from[I]

3.9). The two cycles are connected by the exchange of the proximal CO ligand from ^{12}CO to ^{13}CO and vice versa.

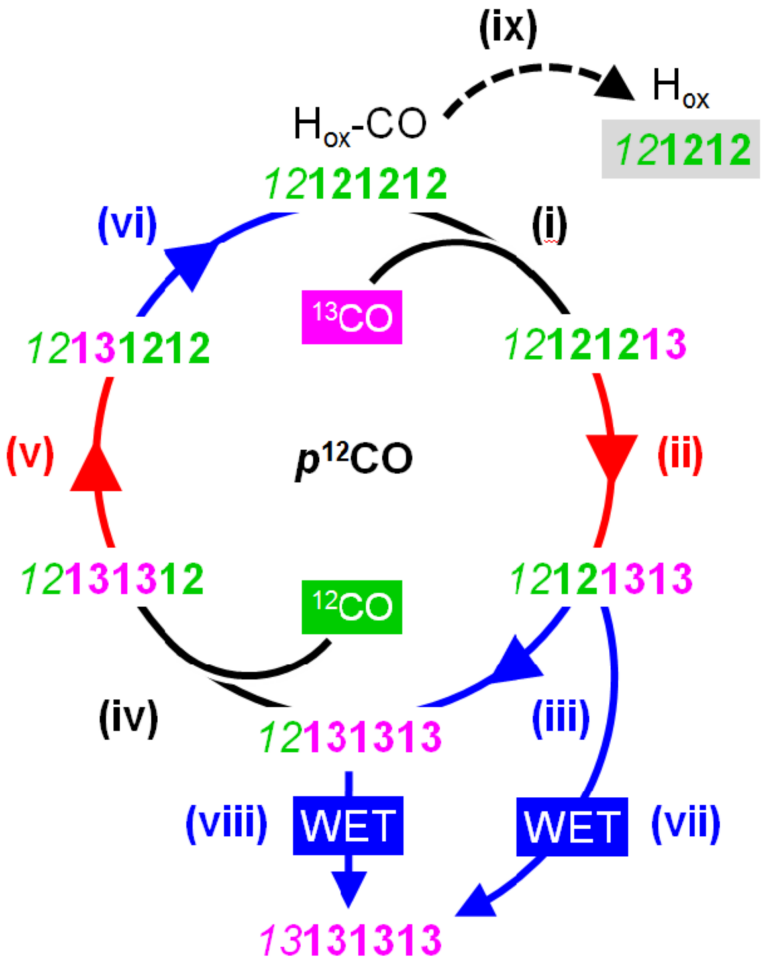

Figure 3.10: Top part of the full isotopic editing reaction cycle (see Figure: 3.9) for which real time ATR-FTIR spectral transitions are presented in Appendix Section B.1. Transitions in the dark, with red light and blue light illumination under $^{12/13}$CO atmosphere build the cycle (i, ii, iii, iv,v, vi). Exchange of pCO under increased hydration conditions is shown in transition vii and viii. A side path transition to obtain active Hox from Hox-CO under N_2 atmosphere is presented (ix). Figure taken from[I]

The starting point for the p^{12}CO cycle is the unlabeled Hox-CO state with all CO ligands composed of ^{12}CO. Upon atmosphere exchange to ^{13}CO the d_2CO ligand is replaced by ^{13}CO (transition (i) in Figure 3.10). Red light illumination under ^{13}CO atmosphere facilitates additional exchange of the d_1CO ligand to ^{13}CO (transition (ii) in Figure 3.10). Depending on hydration level under blue light illumination either only μCO is exchanged to ^{13}CO for less hydrated enzyme films (transition (iii) in Figure 3.10) or μCO and pCO are exchanged at the same time for highly hydrated films leading to completely ^{13}CO edited enzyme (transition (vi) in Figure 3.10). If only μCO was replaced two options to

proceed arose. Increased hydration enables for stepwise replacement of the pCO ligand to fully ^{13}CO edited enzyme under blue light illumination (transition (viii) in Figure 3.10) or exchange of the atmosphere to ^{12}CO in the dark leads to exchange of d_2CO to ^{12}CO (transition (iv) in Figure 3.10). Red light illumination facilitates replacement of d_1CO to ^{12}CO due to the exchanged atmosphere (transition (v) in Figure 3.10). Subsequent blue light illumination substitutes the μCO ligand to ^{12}CO maintaining a completely ^{12}CO edited cofactor once again (transition (vi) in Figure 3.10). At each step of the editing cycle Hox-CO can be transfered into Hox by exchange of the respective atmosphere to N_2 in the dark (e.g. transition (ix) in Figure 3.10). In this process d_2CO is removed(as seen in Figure: 3.7) and isotopic edited active enzyme is obtained.

Isotopomeres with proximal ^{12}CO ligand

In the following the bands of each spectrum are named from low energy to high energy as bands α, β, γ and δ in the case of a fourth band in Hox-CO. Unlabeled Hox-CO (Figure:3.11 (A, xii)) exposed to ^{13}CO resulted in a $\sim$ 20 cm^{-1} down shift of band β and δ. The position of band γ stays nearly the same and the μCO vibration is unchanged (Figure:3.11 (A, ii)). Thus it is likely that a ^{13}CO ligand at the Fe_d was exchanged. An additional down shift of $\sim$ 20 cm^{-1} for band β and δ is observed upon red light illumination. This total (summed) down shift of 40 cm^{-1} suggests an extra ^{13}CO ligand exchanged at Fe_d (Figure:3.11 (A, iii)). Variation of the atmosphere to ^{12}CO resulted in an up shift of band β indicative of ^{13}CO to ^{12}CO ligand exchange at Fe_d (Figure:3.11 (A, v)).

Starting again from species iii (Figure:3.11 (A)) under ^{13}CO atmosphere replacement of the μCO ligand was achieved by irradiation of blue light. Band α undergoes a shift to lower wavenumbers by $\sim$ 40cm^{-1}. All other bands are not influenced highlighting the decoupled character of μCO. By exchange of μCO to ^{13}CO only proximal carbonyl ligand (pCO) remains unlabeled (Figure:3.11 (A, vi)). By changing the atmosphere to ^{12}CO second distal carbonyl ligand (d_2CO) that was occupied by ^{13}CO exchanges to ^{12}CO and thereby only μCO and first distal carbonyl ligand (d_1CO) remain ^{13}CO exchanged. In the spectrum this results in an up shift of band δ by $\sim$ 30 cm^{-1}. Band γ and β are effected by a small shift to higher wavenumbers while the α band stays at its position (Figure:3.11 (A, viii)). Subsequent illumination with red light led to the formation of

a spectra that resembles (Figure: 3.11 (A, xii)) for band δ, γ and β but with band α down shifted by $\sim$ 40 cm^{-1} compared to it. This IR signature hints that only the μCO ligand is exchanged to ^{13}CO (Figure: 3.11 (A, ix)). This species exposed to ^{13}CO induced an exchange of d_2CO to ^{13}CO. The spectra looks similar to (Figure:3.11 (A, ii)) but differs only in the exchanged, down shifted μCO ligand (Figure:3.11 (A, xi)). To obtain the completely unlabeled Hox-CO species (Figure:3.11 (A, xii)) blue light illumination of species (Figure:3.11 (A, ix)) was applied and μCO was switched back to ^{12}CO. All these transitions were monitored in real time and can be found in the Appendix Section B.1.

Isotopomeres with proximal ^{13}CO ligand

In all isotopic edited states described above the proximal CO ligand was not altered. Blue light illumination of the species with all CO ligand replaced by ^{13}CO besides the proximal CO (Figure: 3.11 (A, vi)) at higher hydration levels led to population of a species where all CO ligands were exchanged to ^{13}CO (Figure: 3.11 (B, xii)). The relative intensities of the bands are similar to the all ^{12}CO case (Figure: 3.11 (A, xii)) spectrum but all bands are down shifted by $\sim$38-44 cm^{-1}. Under N_2 atmosphere the all ^{13}CO labeled Hox (Figure:3.11 (B, i)) was accumulated. Taking this state as a starting point all missing isotope permutations with proximal ^{13}CO ligand could be enriched by use of the same protocol (Figure:3.11 (A)).

However since all ligands are now ^{13}CO molecules the replacement starts with ^{12}CO atmosphere instead of ^{13}CO. Under ^{12}CO atmosphere a species with band α at 1768 cm^{-1}, band β at 1918 cm^{-1}, band γ at 1930 cm^{-1} and band δ at 2006 cm^{-1} was obtained that has now a ^{12}CO ligand at the d_2CO position (Figure: 3.11 (B, ii)). Illumination with red light led to an up shift of band γ with small upshifts for band β and δ while band α was not affected (Figure: 3.11 (B, iii)). As before it seems that the second ligand at Fe_d was replaced. Now again three options occur. Either exchange of the atmosphere to N_2 leads to Hox with only distal carbonyl ligand (dCO) replaced by ^{12}CO and bands at 1762 cm^{-1}, 1905 cm^{-1} and 1955 cm^{-1} (Figure: 3.11 (B, iv)). Or substitution of the initial ^{12}CO atmosphere to ^{13}CO atmosphere replaces the d_2CO ligand to ^{13}CO that leads to a down shift of bands γ and δ by $\sim$20 cm^{-1} (Figure:3.11 (B, v)). Or blue light illumination under the initial ^{12}CO atmosphere that yields a species where bands β, γ and δ are not affected

while exclusively the μCO band α shifts up by 40 cm^{-1} (Figure: 3.11 (B, vi)). Species vi (Figure: 3.11 (B)) transfers under N_2 atmosphere into Hox with band α at its original ^{12}CO position at 1802 cm^{-1}, band β at 1905 cm^{-1} and band γ at 1955 cm^{-1}. In analogy to the replacement pattern in Figure: 3.11 (A, vi) now only pCO stays in its initial ^{13}CO configuration while μCO and dCO are replaced by ^{12}CO (Figure: 3.11 (B, vii)). Instead of atmosphere exchange to N_2 exposure to ^{13}CO initiates a down shift of band γ and δ each of $\sim$ 20 cm^{-1} that stands for a ^{13}CO molecule at Fe_d namely d_2CO (Figure: 3.11 (B, viii)). The d_1CO molecule at Fe_d is replaced by ^{13}CO upon red light illumination that manifests in a general down shift of bands β, γ and δ (Figure: 3.11 (B, ix)). Once again three options to proceed arise. First a change to N_2 atmosphere will separate the remove CO ligand and generate Hox. Both bands pCO(γ) and dCO(β) appear at $\sim$ 44 cm^1 downshifted compared to the completely unlabeled Hox state whereas μCO can be found at its initial position (1802 cm^{-1}). This IR signature indicates that pCO and dCO consist of ^{13}CO while μCO is occupied by ^{12}CO (Figure: 3.11 (B, x)). The second option is substitution of the initial ^{13}CO atmosphere to ^{12}CO atmosphere. Thereby the d_2CO ligand is exchanged accordingly from ^{13}CO to ^{12}CO that yields a species that resembles ii (Figure: 3.11 (B)) up to band α (1802 cm^{-1}). The labeling pattern for this species is thought to be as follows: pCO and d_1CO are ^{13}CO ligands while μCO and d_2CO are ^{12}CO ligands (Figure: 3.11 (B, xi)). Third the complete ^{13}CO edited Hox-CO state is populated again when blue light illumination is applied to species ix (Figure: 3.11 (B, xii)) under its initial ^{13}CO atmosphere with its spectroscopic characteristics as described in the beginning of this paragraph.

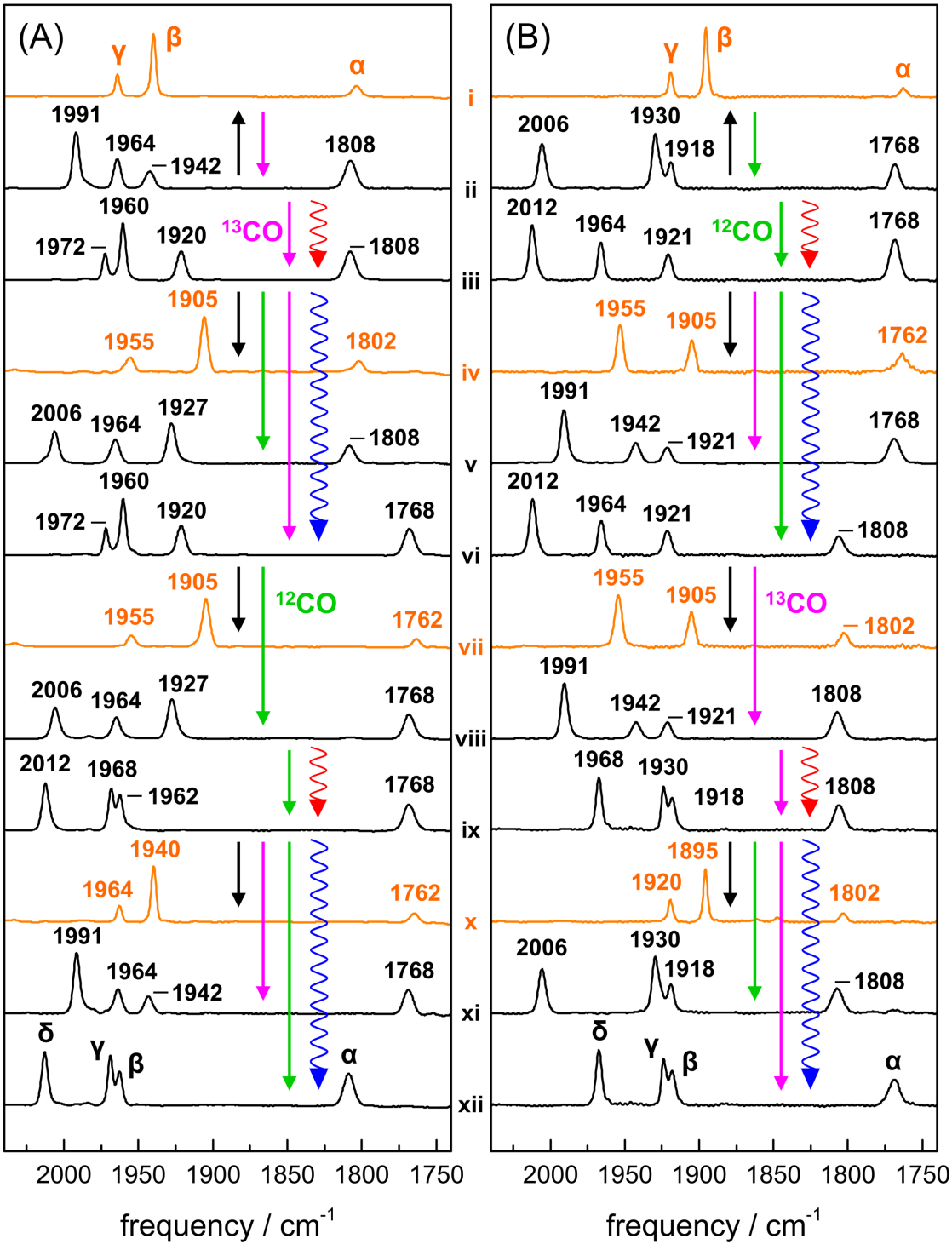

Figure 3.11: Overview of all possible isotopic edited H_{ox} (orange spectra) and H_{ox}-CO states (black spectra). Bands are named from lower to higher wavenumbers α, β, γ and δ. Black arrows indicate transitions under N_2 atmosphere, magenta arrows stand for transitions under ^{13}CO and green arrows for transitions under ^{12}CO atmosphere. Additional light induced transitions are indicated by red or blue arrows depending on the light used for illumination. Panel A shows all isotopic permutations adopted with proximal ^{12}CO and panel B with proximal ^{13}CO. Figure taken from[I]

3.3 pH Titrations

3.3.1 Hox and HoxH

A protein film of native enzyme HydA1 was deposited on the aerosol ATR setup as described in Section 2.1.7. Under nitrogen atmosphere at pH 8 Hox was populated (see Section 3.1.3). Replacement of the aerosol buffer by acidic buffer (pH 4) led to a new band pattern that resembles Hox in relative band intensities but comprises band positions shifted to higher wavenumbers. The CN ligands shift both by four wavenumbers from 2088 cm^{-1} to 2092 cm^{-1} and from 2071 cm^{-1} to 2075 cm^{-1} respectively while pCO and dCO shift by 6 cm^{-1} from 1964 cm^{-1} to 1970 cm^{-1} and from 1940 cm^{-1} to 1946 cm^{-1}. The largest up shift is found for the μCO ligand that shifts by 10 wavenumbers from 1802 cm^{-1} to 1812 cm^{-1} (Figure 3.12). Assuming a protonation the new IR signature was named HoxH. Subsequent buffer exchange back to pH 8 leads to population Hox again. As can be seen in Section 3.7 and B.7 the population of HoxH at acidic pH is conserved for all examined cofactor and amino acid variants. Bacterial enzymes CPI and DDH exhibit this behavior as well (Figure: B.2).

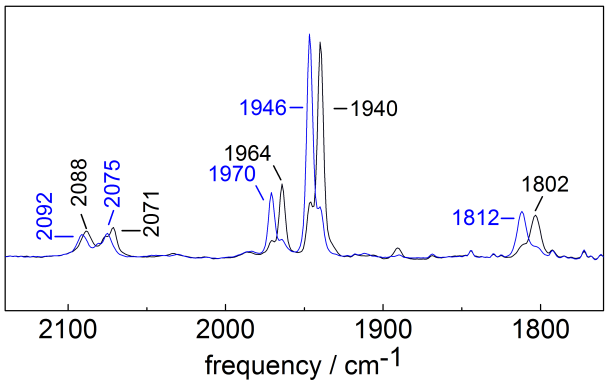

Figure 3.12: Absorption spectra of HydA1 adopted under N_2 atmosphere at pH 8 (black) and pH 4 (blue). At pH 8 Hox (2088 cm^{-1}, 2071 cm^{-1}, 1964 cm^{-1}, 1940 cm^{-1}, 1802 cm^{-1}) accumulates. For pH 4 a similar band pattern appears at up shifted wavenumbers (HoxH (2092 cm^{-1}, 2075 cm^{-1}, 1970 cm^{-1}, 1946 cm^{-1}, 1812 cm^{-1})) Figure taken from[IV]

The transition from Hox to HoxH required the presence of reductant sodium dithionite (DT). To compare the dynamics of this transition for different conditions (e.g. varied pH or DT concentration) the relative population of Hox and HoxH was monitored over time. To obtain relative population first the respective spectra were baseline corrected with the help of a polynomial spline function. The CO/CN ligand bands for each redox state were fitted by Voigt functions (50 % Gaussian and Lorentzian). The obtained peak positions, relative intensities and full width half maximum values for the individual state were kept constant. For spectra that contained multiple redox species the population of each state was given by the fraction of the area of all peaks that belong to a redox state

in respect to the summed peak area. To respect changes in cofactor band intensity the total area of all bands was normalized for each spectrum.

In Figure 3.13 (A) changes in redox state population(from Hox to HoxH) after buffer exchange from pH 8 and 2 mM DT to varying pH that ranged from 8-4 and 10 mM DT are shown over time. Full redox state population conversion from Hox to HoxH is observed for pH 4. For increasing pH the HoxH formation rate and the converted population decreases. At pH 8 no HoxH formation was found. As formation rate the inverse half maximum conversion time given by a sigmoidal fit was used. For a constant DT level (10 mM) the rate increases linear with decreasing pH (Figure: 3.14 (A)).

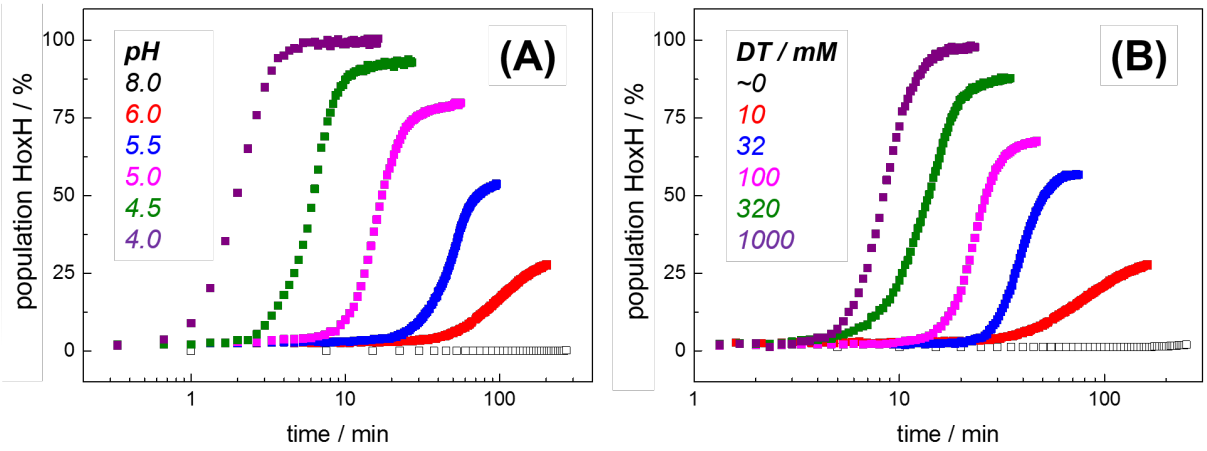

Figure 3.13: Hox to HoxH transitions for different pH and DT concentrations. (A) Population of HoxH for different pH (8-4) with constant DT concentration (10mM). (B) Population of HoxH for different DT concentrations (0-1000 mM)) at pH 6. Figure taken from[IV]

Figure 3.13 (B) monitors the HoxH formation induced by increasing amounts of DT at pH 6. A DT free buffer(pH 6) was exchanged by buffer containing various amounts of DT at pH 6 and changes in populations were tracked over time. With increasing DT concentrations the HoxH formation rate and the converted population co increased (Figure: 3.13 (B)). The formation rate increases linear and saturates for high DT concentrations (Figure: 3.14 (B)).

In Figure 3.14 (C) the final population yield of HoxH is displayed for 10 mM DT and 500 mM DT in dependence of pH. The apparent pK for this reaction is shifted from ca. 5.5 to 7.3 in dependence of the increased DT concentration. Full conversion to HoxH is reached already for pH 5 with 500 mM DT instead of pH 4 with 10 mM DT. HoxH formation can

be detected for larger pH values for increased DT concentration.

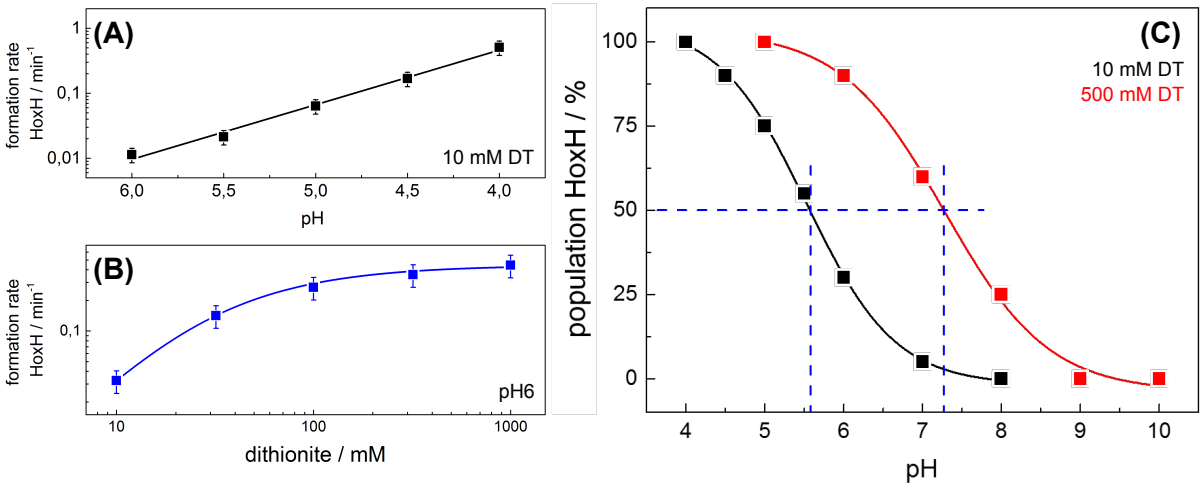

Figure 3.14: Formation rate and yield of HoxH for HydA1. **(A)** Formation rate of HoxH for different pH values at 10mM DT. The formation rate increases with decreasing pH. **(B)** Formation rate of HoxH for different DT concentrations at pH 6. The rate increases linear and saturates for increased DT concentrations. **(C)** HoxH population yield for different pH values for either 10 mM DT(black) or 500 mM DT(red). Apparent pK for this reaction is shifted from ca. 5.5 for 10 mM DT to 7.3 for 500 mM DT. HoxH formation is observed for more alkaline pH values at increased DT level. Figure taken from[IV]

3.3.2 Hox-CO and HoxH-CO

An analogous blue shift upon acidification was observed for the CO inhibited enzyme, Hox-CO. HydA1 was poisoned with 1 % CO and the typical band pattern (see section 3.6) of Hox-CO was observed (Figure: 3.15, purple spectrum). During 60 minutes after exchange from pH 8 to pH 4 in presence of 2 mM DT the population of a novel band pattern with a blue shift of all band besides the band at 2012 cm^{-1} was observed. The μCO band shifts from 1808 cm^{-1} to 1816 cm^{-1} and the two bands at 1962 cm^{-1} and 1968 cm^{-1} shift upwards to 1966 cm^{-1} and 1972 cm^{-1}. The CN bands experience an up shift from 2081 cm^{-1} to 2086 cm^{-1} and from 2091 cm^{-1} to 2094 cm^{-1} respectively. Only the CO band at down shifts by 6 cm^{-1} from 2012 cm^{-1} to 2006 cm^{-1} (Figure: 3.15). This novel state is named oxidized protonated CO inhibited state (HoxH-CO).

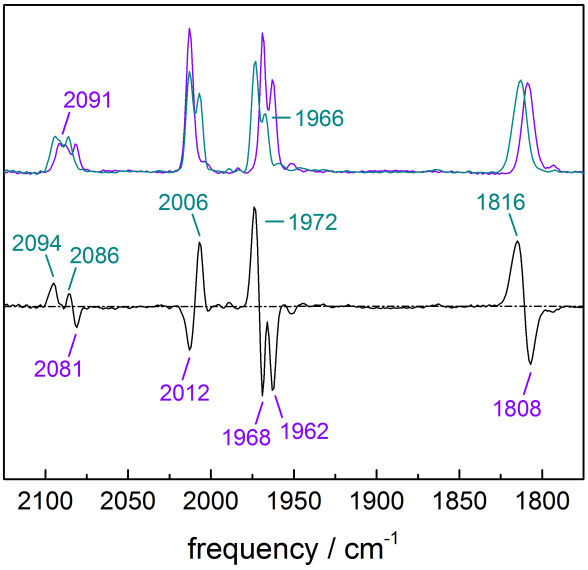

Figure 3.15: Formation of HoxH-CO. HydA1 was poisoned with 1 % CO at pH 8 and the typical band pattern of Hox-CO was observed (purple spectrum). Acidification for 60 minutes with pH 4 buffer containing 2 mM DT led to the population of HoxH-CO (cyan spectrum). All bands are blue shifted by 4-10 cm^{-1} besides the band at 2012 cm^{-1} that down shifts by 6 cm^{-1} to 2006 cm^{-1}. The black spectrum displays the difference spectrum of Hox-CO and HoxH-CO. Figure taken from[IV]

3.3.3 Sulfur/Selenium exchange

To check for direct [4Fe-4S] cluster protonation the sulfur atoms of the [4Fe-4S] cluster were exchanged to selenium atoms for which different characteristics in protonation are expected. For maximal comparability a mixed sample of HydA1 with either a [4Fe-4Se] cluster or a [4Fe-4S] was prepared. Since the IR signatures of the active site in the CO region of HydA1 with a [4Fe-4Se] cluster and with a [4Fe-4S] do not differ significantly[58] the sample fraction that contains the natural [4Fe-4S] cluster was isotopic labeled at distal and bridging position with ^{13}CO (Figure: 3.16 (A), compare Section 3.2 for isotopic editing details). Thereby in the mixed sample the bands for Hox and HoxH of the dCO and μCO ligands for the [4Fe-4S] cluster containing fraction shift down by ca. 40 cm^{-1}

(dCO 1905 cm^{-1} and μCO 1762 cm^{-1}) and are well separated from the bands of the [4Fe-4Se] cluster containing fraction (dCO 1940 cm^{-1} and μCO 1802 cm^{-1}) (Figure: 3.16 (B)). Subsequently the pH was changed from 8 to 4 at 2 mM DT and the Hox to HoxH transition was followed over time. Figure 3.16 (C) shows a series of difference spectra obtained during this transition. The blue shift is clearly visible for the sulfur containing fraction as for the selenium containing fraction. The dCO band of the selenium containing fraction shifts from 1940 cm^{-1} to 1946 cm^{-1} while the ^{13}CO labeled dCO ligand of the sulfur containing fraction shifts fron 1905 cm^{-1} to 1910 cm^{-1}. Analogous the μCO ligand shifts from 1802 cm^{-1} to 1812 cm^{-1} (selenium containing fraction) and 1762 cm^{-1} to 1772 cm^{-1} (sulfur containing fraction). As can be seen in Figure 3.16 (D) the HoxH formation rate for both the [4Fe-4S] and the [4Fe-4Se] containing fraction are similar.

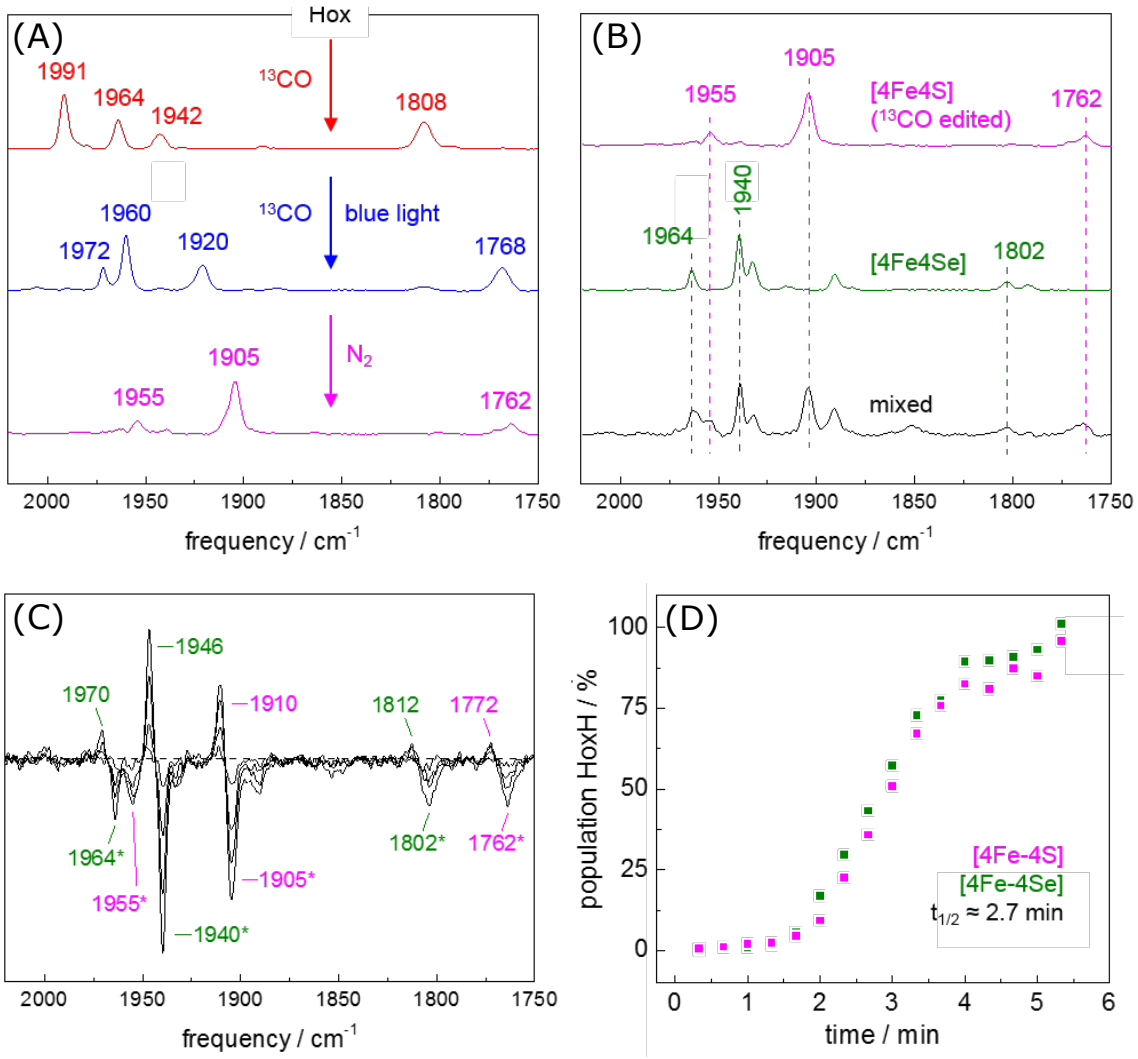

Figure 3.16: Sulfur/Selenium exchange. **(A)** Labeling pattern to exchange dCO and μCO for the [4Fe-4S] containing fraction. ^{13}CO inhibition (red spectrum) followed by subsequent blue light illumination led to exchange of dCO and μCO (blue spectrum). By atmosphere exchange to N_2 Hox was populated (magenta spectrum). **(B)** ^{13}CO edited [4Fe-4S] containing enzyme (magenta spectrum) was mixed with [4Fe-4Se] containing enzyme (green spectrum). The mixed sample (black spectrum) has separated bands for Hox of the [4Fe-4Se] enzyme (dCO 1940 cm^{-1} and μCO 1802 cm^{-1}) compared to the [4Fe-4S] enzyme (dCO 1905 cm^{-1} and μCO 1762 cm^{-1}). **(C)** Difference spectra of the Hox to HoxH transition initiated by pH exchange from pH 8 to pH 4 in presence of 2 mM DT. The dCO band of the [4Fe-4Se] enzyme shifts from 1940 cm^{-1} to 1946 cm^{-1} while the ^{13}CO labeled dCO ligand of the [4Fe-4S] enzyme shifts fron 1905 cm^{-1} to 1910 cm^{-1}. The μCO ligand shifts from 1802 cm^{-1} to 1812 cm^{-1} ([4Fe-4Se] enzyme) and 1762 cm^{-1} to 1772 cm^{-1} ([4Fe-4S] enzyme). **(D)** Population of HoxH for both fractions over time. The halfmax time (ca. 2.7 min) for each fraction is similar. Figure taken from[IV]

3.3.4 H/D exchange

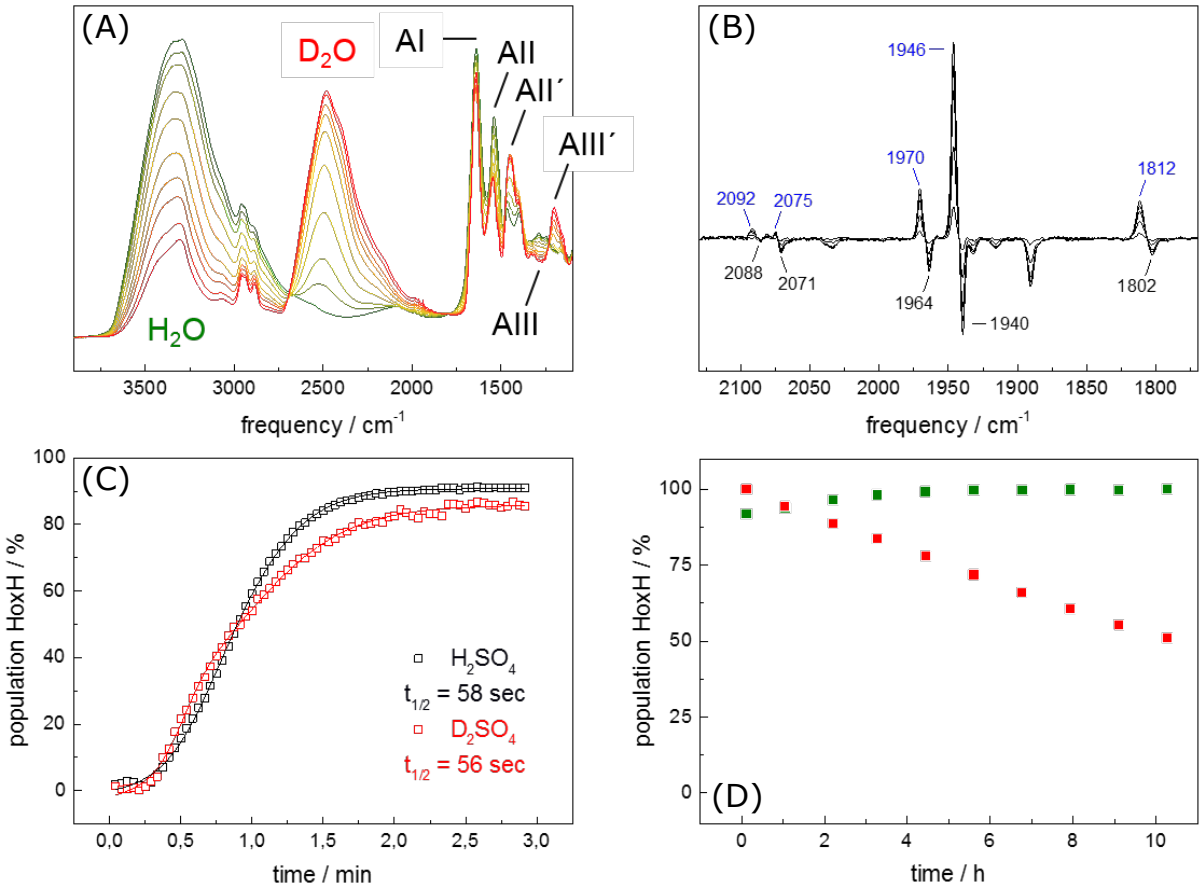

Figure 3.17: **(A)** H_2O to D_2O exchange in the enzyme film via a aerosol of D_2O. Spectra from green to red show that the H_2O band at ca. 3400 cm^{-1} decreases while the D_2O band at ca. 2500 cm^{-1} increases. Amide bands sensitive to H/D exchange shift to lower frequencies (AII to AII‘ and AII to AIII‘). **(B)** Hox to HoxH transition in D_2O of enzyme maturated and purified in D_2O. The transition is induced by 0.5 % D_2SO_4 and 2 mM DT in the aerosol. Hox bands (black, negative peaks at: 2088 cm^{-1}, 2071 cm^{-1}, 1964 cm^{-1}, 1940 cm^{-1}, 1802 cm^{-1}) shift to HoxH (or HoxD) bands (blue, positive peaks at: 2092 cm^{-1}, 2075 cm^{-1}, 1970 cm^{-1}, 1946 cm^{-1}, 1812 cm^{-1}). **(C)** Comparison of the formation of HoxH and HoxD. Formation rates of 58 seconds for H_2SO_4 (black) and 56 seconds for D_2SO_4 (red) are similar within the experimental error. **(D)** Cofactor and enzyme stability at 0.5 % H_2SO_4 and 2 mM DT. The intensity of the cofactor bands and the amide bands is monitored for ten hours. 50 % cofactor band intensity is lost while the amide band intensity remained unchanged. Figure taken from[IV]

In the following the impact of H/D exchange on HoxH is examined. H_2O in the protein film was replaced by an aerosol stream of D_2O. The H_2O band at ca. 3400 cm^{-1} decreases while the D_2O band at ca. 2500 cm^{-1} increases. Amide bands sensitive to H/D exchange shift to lower frequencies (Figure: 3.17 A). In Figure 3.17 B the difference spectrum of the Hox to HoxH (or HoxD) transition is shown. The sample was maturated and purified in D_2O buffer and kept under D_2O aerosol atmosphere. The transition was induced by

acidification with 0.5 % D_2SO_4 and 2 mM DT. Respective Hox bands (negative peaks at: 2088 cm^{-1}, 2071 cm^{-1}, 1964 cm^{-1}, 1940 cm^{-1}, 1802 cm^{-1}) shift to the already observed HoxH (or HoxD) bands (positive peaks at: 2092 cm^{-1}, 2075 cm^{-1}, 1970 cm^{-1}, 1946 cm^{-1}, 1812 cm^{-1}). The formation rate of HoxH for H_2O environment and D_2O environment are comparable with 58 seconds for H_2O and 56 seconds for D_2O environment (transition induced by H_2SO_4 or D_2SO_4) (Figure 3.17 (C)). To monitor the stability of the enzyme and the cofactor at 0.5 % H_2SO_4 (ca. pH 1) and 2 mM DT the intensity of the cofactor bands and the amide bands was analyzed over time. During ten hours 50 % of cofactor intensity was lost in contrast to the amide band intensity that remained constant (Figure 3.17 (D)).

3.3.5 Hred' and Hred

As described in Section 3.1.3 exposure of HydA1 to H_2 leads to reduction of the enzyme. In Figure 3.18 the reduction of an N_2 equilibrated sample(Hox) is shown. Negative bands are attributed to Hox while positive bands at 1933 cm^{-1}, 1915 cm^{-1}, 1891 cm^{-1} and 1792 cm^{-1} represent reduced species. To assign these bands ^{13}CO isotopic editing was applied as described above in Section 3.2 and 3.3.3. Again dCO and μCO were exchanged by ^{13}CO and reduction of an oxidized sample by H_2 was induced (Figure: 3.18 lower difference spectrum). The difference spectrum was compared to the non labeled case. Isotopic shifts of ca. 40 cm^{-1} that relate the bands to either dCO or μCO were observed for the 1933 cm^{-1} band(1893 cm^{-1}), the 1891 cm^{-1} band (1851 cm^{-1}) and the 1792 cm^{-1} band (1752 cm^{-1}). The band at 1915 cm^{-1} shifts only minor to 1910 cm^{-1}.

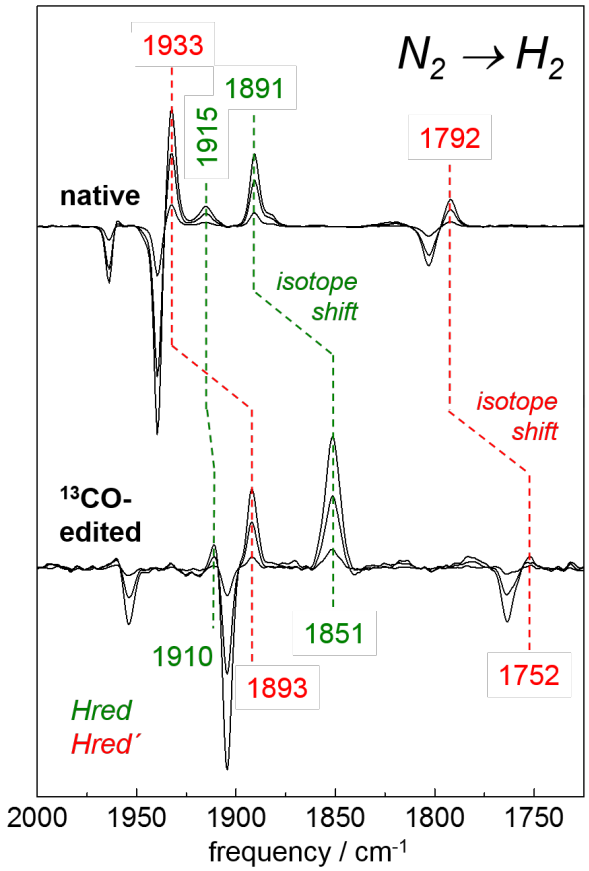

Figure 3.18: Assignment of reduced states. Difference spectra that show the reduction induced by 10% H_2 for native (top) and ^{13}CO edited HydA1 (bottom). Hox (negative bands) gets depopulated while positve bands for Hred (green) and Hred' (red) appear. Isotopic replacement of dCO and μCO by ^{13}CO lead to a down shift of ca. 40 cm^{-1} for the respective bands in Hox, Hred and Hred'. The shift of both bands, 1933 cm^{-1} to 1893 cm^{-1} and 1891 cm^{-1} to 1851 cm^{-1} clearly identifies them as dCO originated. Figure taken from[IV]

To clarify the relation of the 1933 cm^{-1}, 1891 cm^{-1} and 1792 cm^{-1} bands a pH titration from pH 8 to pH 6 under 10% H_2 was performed on non isotopic edited enzyme. The 1933 cm^{-1} and the 1792 cm^{-1} band decreases while the 1891cm^{-1} band (and 1915 cm^{-1}) increases. The decreasing bands are assigned to Hred' while the increasing bands are assigned to Hred. Additionally a depopulation of Hsred and population of Hox and hydride state (Hhyd) is observed (Figure 3.19 for absolute spectra see Figure B.3 C). The pH dependent population of Hred and Hred' is analyzed in Figure B.3 A and B. In short

Hred forms at more acidic pH compared to Hred'.

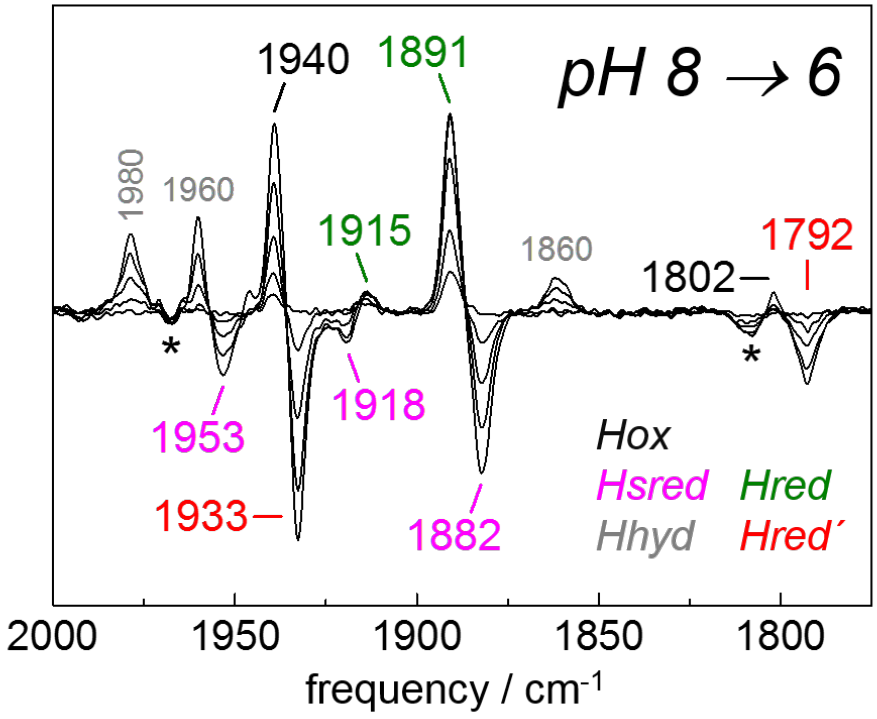

Figure 3.19: Difference spectra that show a pH titration (pH 8 to pH 6) under 10% H_2. Hox (black), Hhyd (gray) and Hred (green) get populated while Hred' (red) and Hsred (magenta) get depopulated. Note the that the 1792 cm^{-1} band correlates with the 1933 cm^{-1} band (Hred') and not with the 1891 cm^{-1} band (Hred). Asterisks mark bands of a Hox-CO getting depopulated. Figure taken from[IV]

3.3.6 Hred' and Hred'H

Aerosol investigation of cofactor variant HydA1pdt

For additional investigation of Hred' in the following the cofactor variant pdt was used. It exclusively forms Hox and Hred' thereby not exhibiting Hred and Hsred. Starting from 100% N_2 (Hox) at pH 8 and 2 mM DT under 100% H_2 Hred' is formed (Figure: 3.20 (A)). The band positions for Hox (black) and Hred' (red) are slightly shifted in comparison to the adt case. The same experiment performed at pH 4 showed the HoxH (blue) to a blue shifted Hred' (named protonated [4Fe-4S reduced state (Hred'H) (orange)) transition (Figure: 3.20 (B)). The band positions of Hred'H lie in between Hox and Hred'. Hred'H was observed in native enzyme too. Figure B.4 shows a DT titration and the correlated redox state population changes. For increasing DT concentrations an increasing Hred'H population was found.

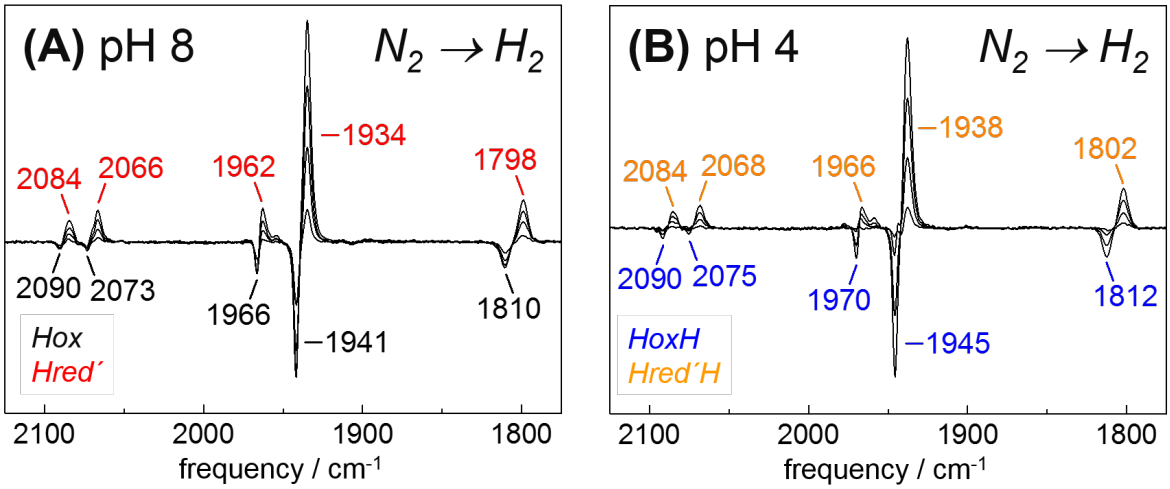

Figure 3.20: Difference spectra of H_2 induced reduction of HydA1pdt. **(A)** Exchange of N_2 to H_2 at pH 8 and 2 mM DT lead to the depopulation of Hox (black, 2090 cm^{-1}, 2073 cm^{-1}, 1966 cm^{-1}, 1941 cm^{-1}, 1810 cm^{-1}) and to the population of Hred' (red, 2084 cm^{-1}, 2066 cm^{-1}, 1962 cm^{-1}, 1934 cm^{-1}, 1798 cm^{-1}). **(B)** At pH 4 the HoxH population (blue, 2090 cm^{-1}, 2075 cm^{-1}, 1970 cm^{-1}, 1945 cm^{-1} and 1812 cm^{-1}) is converted into Hred'H (orange, 2084 cm^{-1}, 2068 cm^{-1}, 1966 cm^{-1}, 1938 cm^{-1}, 1802 cm^{-1}). Figure taken from[IV]

Dilution of HydA1pdt with Bovine serum albumin protein (BSA) in the film effected the formation rate and the total observed population of Hred' upon H_2 exposure. The formation rate drops to ca. 50% when diluted to a concentration of 40 % HydA1pdt in the film. Below a concentration of 20% HydA1pdt no Hred' formation was observed (Figure B.5 (A) and (C)). In contrast the population of HoxH was minor effected by dilution with BSA. Even at a total concentration of 6.25% complete HoxH formation was observed and the formation rate dropped only by ca. 25% (Figure B.5 (B) and (C)).

Spectro-electrochemical investigation of cofactor variant HydA1pdt

To further investigate the pdt cofactor variant spectro-electrochemistry in ATR configuration was applied (Setup 2.1.8). The absence of Hred and Hsred in cofactor variant pdt was exploited to focus on the Hox to Hred' transition. Equilibrated at -200 mV vs. standard hydrogen electrode (SHE) the pdt variant adopted either Hox or HoxH or a mixture of both depending on buffer pH. Buffer contained 10 mM DT but no reduced species were observed at open circuit potential. Buffer pH was changed from 7.5 to 5.0 in steps of half a pH unit. For sightly alkaline pH values (pH 7.5 to 7.0) the sample showed mainly population of Hox, for pH value of 6.5 to 6.0 a mixed population of Hox and HoxH was observed and for more acidic pH values (pH 5.5 to 5.0) mainly HoxH was populated. The potential was changed to more reducing values in steps of 50mV. Depopulation of oxidized

redox species Hox or/and HoxH was observed associated with population of reduced redox species Hred' or/and Hred'.

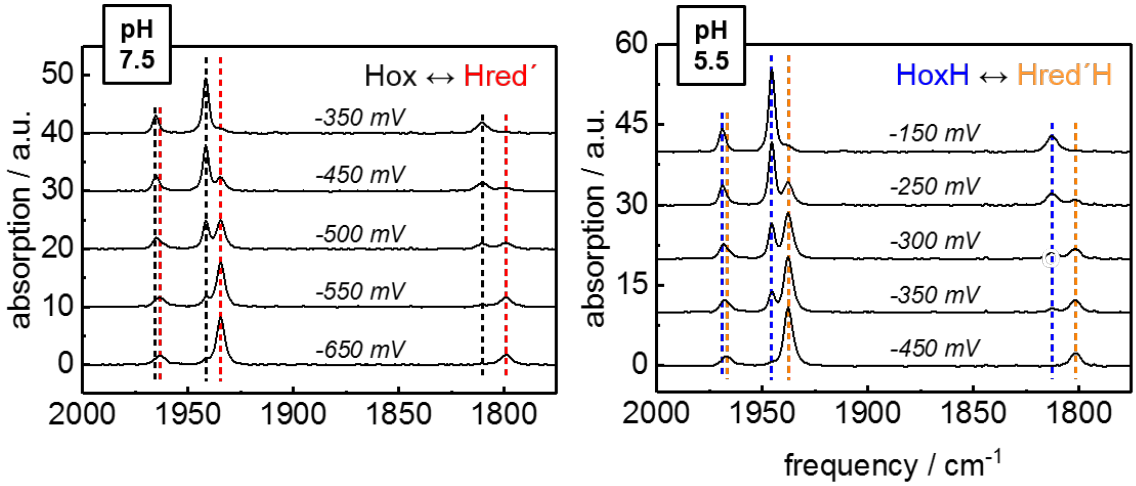

Figure 3.21: IR spectra of cofactor variant pdt of HydA1 at different potential and pH. At pH 7.5 Hox gets depopulated for reducing potentials and Hred' gets populated. For pH 5.5 starting from HoxH Hred'H gets populated during reduction. Figure taken from[VI]

Figure 3.21 shows exemplary IR spectra for a redox titration at pH 7.5 and pH 5.5. The individual redox state population was quantified as described in Section 3.3. The midpoint potential (Em) for the Hox to Hred' and the HoxH to Hred'H transition was determined by fitting the obtained changes in redox state population over potential with a Nerstian behavior for one electron (Figure: 3.22). The obtained Em for the respective transition is shown for each tested pH value in a Pourbaix diagram (Figure: 3.23). A linear pH dependency of the Em was found for both transitions. Linear fit resulted in slopes of 55 ± 5 mV/pH for the Hox to Hred' transition and 50 ±3 mV/pH for the HoxH to Hred'H transition. While the Hox to Hred' transition follows the reference values of the H^+ to H_2 transition the HoxH to Hred'H transition is offset by ca. 50 mV to more oxidizing potentials.

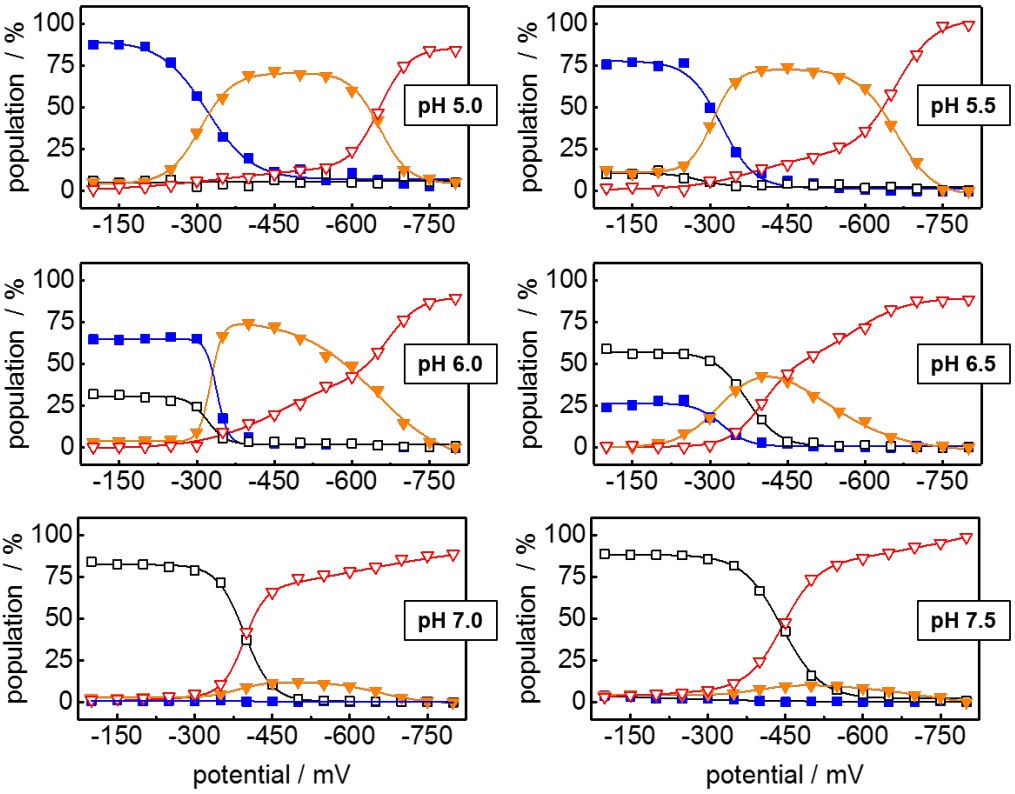

Figure 3.22: Redox state populations at pH values that range from 5.0 to 7.5 in dependence of applied potential. For acidic pH values(pH 5.0 to 5.5) mainly the HoxH (blue squares) to Hred'H (orange triangles) transition is observed. For pH values from 6.0 to 6.5 the Hox to Hred' and the HoxH to Hred'H transition appears simultaneously but note at different potentials. pH values of 7.0 to 7.5 show nearly pure the Hox (black squares) to Hred' (red triangles) transition. Figure taken from[VI]

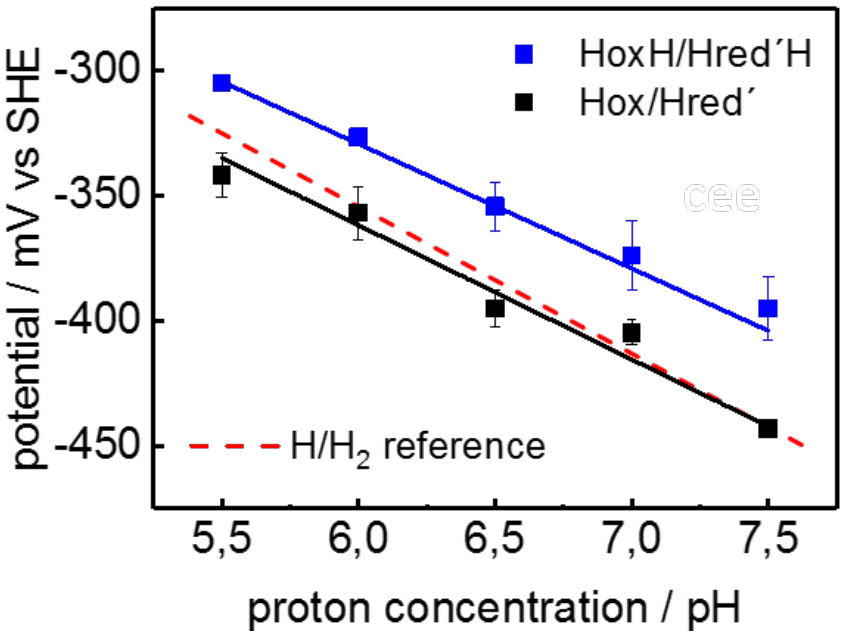

Figure 3.23: Pourbaix diagram that displays the midpoint potential of the Hox to Hred' and the HoxH to Hred'H transition in dependence of pH. Linear fit revealed slopes of 55 ± 5 mV/pH for the Hox to Hred' transition and 50 ± 3 mV/pH for the HoxH to Hred'H transition. While the Em of the Hox to Hred' transition follows the H/H_2 reference potential the Em of the HoxH to Hred'H transition is offset by ca. 50 mV to more oxidative potentials. Figure taken from[VI]

3.4 Hred and Hsred

Spectro-electrochemistry in ATR configuration (Setup: 2.1.8) was applied to native HydA1 enzyme to separate the reduced states that were accumulated in mixed populations by aerosol experiments under H_2 (Section: 3.1.3). Figure 3.24 shows redox states accumulated at different potentials. At -200 mV mainly Hox is populated (black), at -400 mV Hred (green) with traces of Hox accumulates, at -750 mV Hred' (red) is observed while at -900 mV mainly Hsred (magenta) is populated. All potentials are given vs. SHE. In Hred compared to Hox the most intense CO band shifts down ca. 40 cm^{-1} as expected for one electron reduction at the diiron site. The same holds true for Hred' compared to Hsred. The former μCO band experiences an up shift of ca. 150 cm^{-1} indicative of an conformational rearrangement without bridging CO (Figure: 3.24 and B.6 (A)). The CN ligand bands are down shifted as well and the separation of these two bands increase for the reduced states (Hred, Hsred) in comparison to Hox (Figure: 3.24 and B.6 (B)).

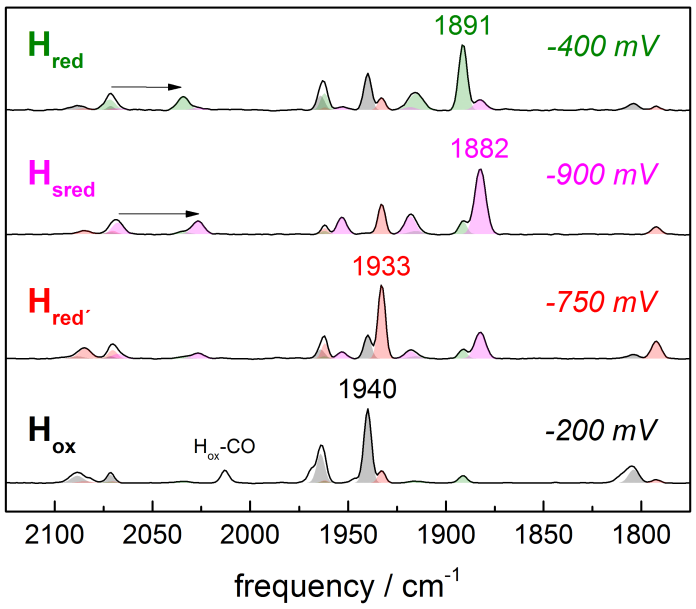

Figure 3.24: IR spectra of redox states equilibrated at different potentials. At -200 mV Hox (black), at -400 mV Hred (green), at -750 mV Hred' (red) and at -900 mV Hsred (magenta) accumulates. The most intense dCO marker band shifts down significantly for Hred and Hsred. Separation of CN ligand band positions for Hred and Hsred is indicated by black arrows. Figure taken from[VIII]

Hred was electrochemically enriched for different ^{13}CO isotopic edited enzymes (Figure: 3.25). Isotopic editing was performed as described in Section 3.2. Independent of ^{13}CO editing the CN ligand bands were observed at 2072 cm^{-1} and 2033 cm^{-1}. Hred CO bands for unaltered cofactor were found at 1961 cm^{-1}, 1915 cm^{-1} and 1891 cm^{-1} (Figure: 3.25 (A)). Enrichment of Hred out of an isotopomere with ^{13}CO edited μCO in Hox resulted in a down shift of the 1961 cm^{-1} band to 1938 cm^{-1}. The two other CO bands are only minor effected and shift 1912 cm^{-1} and 1889 cm^{-1} respectively (Figure: 3.25 (B)). When only

dCO was replaced band positions at 1964 cm^{-1}, 1910 cm^{-1} and 1855 cm^{-1} were found for Hred (Figure: 3.25 (C)). Replacement of μCO and dCO resulted in bands at 1928 cm^{-1}, 1910 cm^{-1} and 1851 cm^{-1} (Figure: 3.25 (D)). Band positions at 1918 cm^{-1}, 1872 cm^{-1} and 1847 cm^{-1} were observed when all CO ligands were substituted by ^{13}CO (Figure: 3.25 (E)). Band positions for Hsred of these isotopomeres were obtained by difference spectra of Hsred minus Hred and are shown in Appendix Figure B.7.

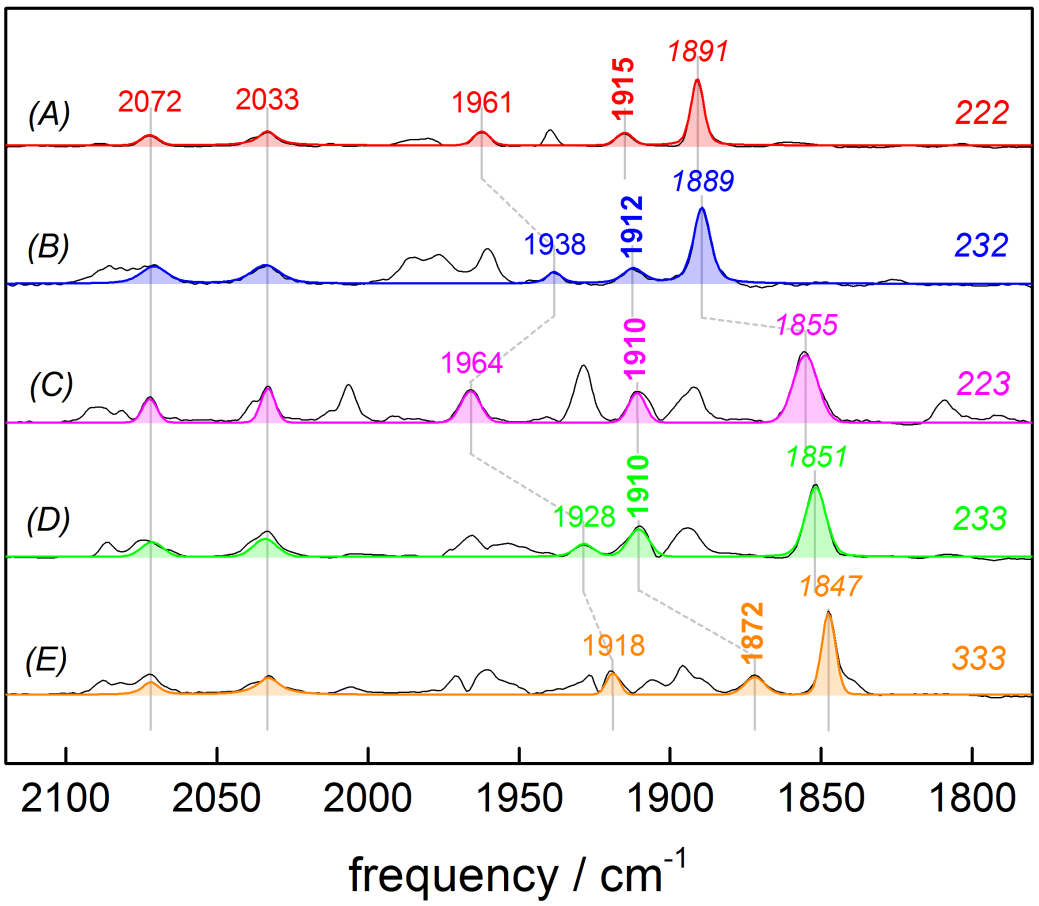

Figure 3.25: IR spectra of Hred for ^{13}CO edited isotopameres. The order of numbers reports on the labeling pattern starting from pCO, μCO to dCO(2 stands for ^{12}CO and 3 for ^{13}CO). CN ligand bands were unaffected by CO ligand editing. Gray lines indicate the shift of respective CO ligand bands. **(A)** Hred for unaltered enzyme with bands at 1961 cm^{-1}, 1915 cm^{-1} and 1891 cm^{-1}. **(B)** Hred for enzyme with substituted former μCO ligand (1938 cm^{-1}, 1912 cm^{-1} and 1889 cm^{-1}). **(C)** Hred for enzyme with replaced dCO ligand (1964 cm^{-1}, 1910 cm^{-1} and 1855 cm^{-1}). **(D)** Hred for enzyme with former μCO and dCO exchanged for ^{13}CO (1928 cm^{-1}, 1910 cm^{-1} and 1851 cm^{-1}) **(E)** Hred for completely ^{13}CO edited enzyme with bands at 1918 cm^{-1}, 1872 cm^{-1} and 1847 cm^{-1}. Figure taken from[VIII]

3.5 The hydride state (Hhyd)

The following experiments were performed in the aerosol ATR setup as described in Section 2.1.7. A sample of 1 μl 1mM HydA1 was equilibrated with pH 8 buffer under a constant steam of humidified N_2. Hox was populated(see Section 3.1.3). The aerosol stream was exchanged to H_2 at the same pH and population of Hred and Hsred was observed (see Section 3.1.3). Difference spectra that monitor the transition from N_2 to H_2 are shown in Figure 3.26 (top). Hox gets depopulated (negative bands) while Hred and Hsred get populated (positive bands). Additionally to Hred' traces of a band pattern with peaks at 1978 cm^{-1}, 1960 cm^{-1} and 1860 cm^{-1} arise. Subsequent exchange of the carrier gas of the aerosol back to N_2 lead to population of Hox again.

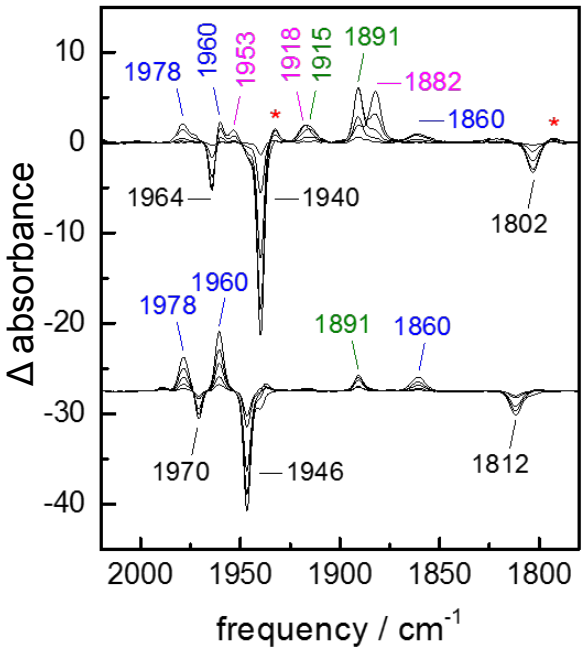

Figure 3.26: Difference spectra of N_2 to H_2 exchange experiments performed at pH 8 and pH 4. Top: Carrier gas exchange to H_2 at pH 8 lead to depopulation of Hox (negative bands, 1965 cm^{-1}, 1940 cm^{-1} and 1802 cm^{-1}) and population of Hred (green positive bands, 1915 cm^{-1}, 1891 cm^{-1}) and Hsred (purple positive bands, 1953 cm^{-1}, 1918 cm^{-1}, 1882 cm^{-1}). Traces of Hhyd (gray positive bands, 1978 cm^{-1}, 1960 cm^{-1} and 1860 cm^{-1}) and Hred' (red asterisks) were detected. Bottom: Carrier gas exchange to H_2 at pH 4 lead to depopulation of HoxH (negative bands, 1970 cm^{-1}, 1946 cm^{-1}, 1812 cm^{-1}) and population of Hhyd (gray positive bands, 1978 cm^{-1}, 1960 cm^{-1}, 1860 cm^{-1}). Hred (green positive band 1891 cm^{-1}) is only present in traces. Figure taken from[VII]

As seen in Section 3.3 exposure of the enzyme film to a aerosol stream evolved of pH 4 buffer lead to the population of HoxH. Once again the carrier gas was exchanged from N_2 to H_2 and difference spectra were taken (Figure 3.26 (bottom)). Depopulation of HoxH was observed (negative bands). In contrast to the experiment at pH 8 population of Hred is only seen in traces while the band pattern with peaks at 1978 cm^{-1}, 1960 cm^{-1} and 1860 cm^{-1} is now the predominantly populated species. The new species is called Hhyd. Population and depopulation of Hhyd was found to be reversible for variation of pH under H_2 atmosphere. For example in presence of H_2 Hhyd is formed in expense of Hred and Hsred as a function of pH value (Figure:

B.8 (A), (C)). Reversibility was also found for exchange of carrier gas at constant acidic pH. Exchange of N_2 to H_2 lead to depopulation of HoxH and population of Hhyd while switching back to N_2 lead to depopulation of Hhyd in favor of HoxH (Figure: B.8 (B)). For more acidic pH values than pH 4 destruction of cofactor ligand bands was observed within minutes (Figure: B.8 D).

Population of Hhyd induced by D_2 instead of H_2 lead to a specific change in the observed band pattern. The μCO band was down shifted by 5 cm^{-1} to 1855 cm^{-1} while all other band positions remained unchanged(Figure: 3.27). Similar behavior was found for variant C169A of HydA1(Figure: B.10 (A)), for variant E279A of CpI(Figure: B.10 (B)) and cofactor variant odt of HydA1(Figure: B.10 (C)).

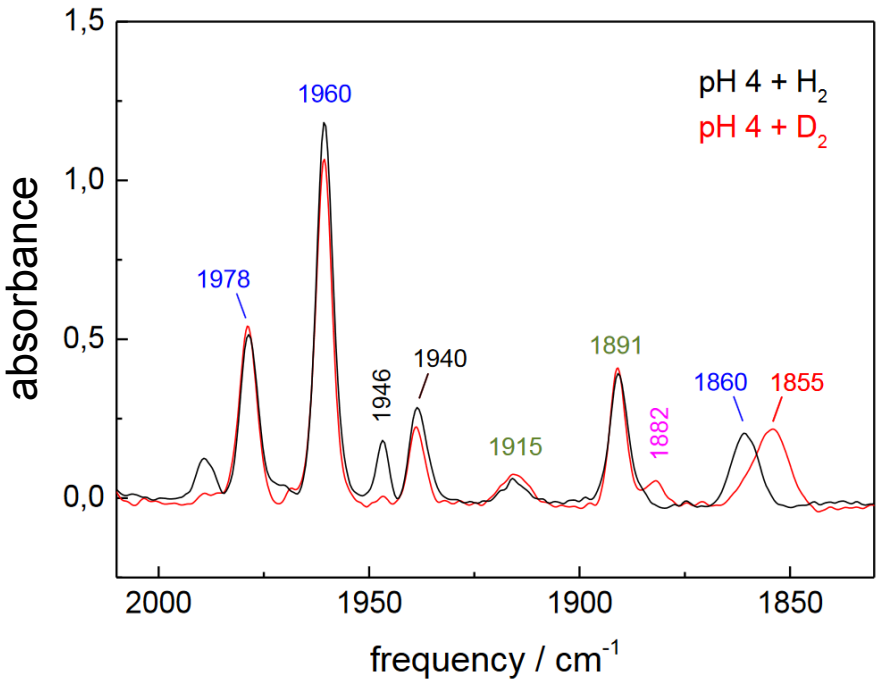

Figure 3.27: Absolute spectra of Hhyd in HydA1 induced by H_2 or D_2. The black spectrum shows mainly Hhyd with its characteristic CO bands at 1978 cm^{-1}, 1960 cm^{-1} and 1860 cm^{-1} induced by H_2. In red the spectrum of Hhyd induced by D_2 is shown. The μCO band is down shifted by 5 cm^{-1} from 1860 cm^{-1} to 1855 cm^{-1} most likely due to trans coupling with an apical bound hydride/deuteride species. Figure taken from[VII]

At the same conditions as reported for HydA1 above the population of Hhyd was observed for [FeFe]-hydrogenase CpI and DDH. Gas exchange of N_2 to H_2 at pH 4 lead to depopulation of HoxH and population of Hhyd (Figure: B.9 left). It has to be noted that dehydration of a HydA1 film at pH 8 under H_2 lead to subsequent depopulation of Hred and Hsred and population of Hhyd (Figure: B.9 right).

3.6 O_2 inactivation (Hox-O_2)

Proton path variant C169A of HydA1 was exposed to 20% O_2 at pH 8 and conversion of Hox into a novel state named Hox-O_2 was observed. In native enzyme the cofactor was disintegrated and cofactor bands were lost upon exposure to O_2 (for native enzyme see Section: 3.1.3). Figure 3.28 shows the IR spectra of Hox and Hox-O_2. All peaks of Hox-O_2 are blue shifted to Hox. The largest shift is found for the μCO band that moves ca. 60 cm^{-1} from 1804 cm^{-1} to 1862 cm^{-1}. The dCO band of Hox experiences an up shift of ca. 50 cm^{-1} from 1939 cm^{-1} to 1990 cm^{-1} and the pCO band shifts from 1964 cm^{-1} to 2007 cm^{-1}. CN bands are blue shifted by ca. 15 cm^{-1} in average.

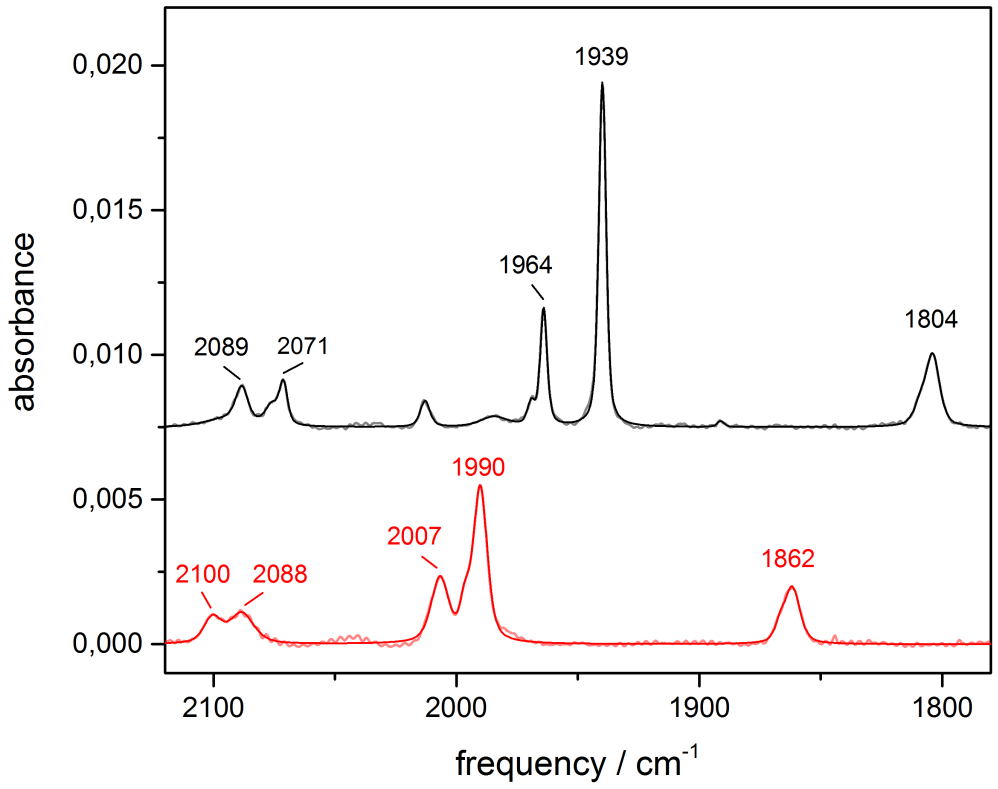

Figure 3.28: IR spectra of Hox and Hox-O_2. Top black spectrum shows Hox with its CO/CN ligand bands at 2089 cm^{-1}, 2071 cm^{-1}, 1964 cm^{-1}, 1939 cm^{-1} and 1804 cm^{-1}. Bottom red spectrum shows Hox-O_2 with blue shifted bands compared to Hox at 2100 cm^{-1}, 2088 cm^{-1}, 2007 cm^{-1}, 1990 cm^{-1} and 1862 cm^{-1}. Figure taken from[V]

3.7 CpI, Cofactor Variants and Amino Acid Variants

In addition to HydA1 from *Chlamydomonas reinhardtii* [FeFe]-hydrogenase CpI from *Clostridium pasteurianum* was analyzed (Appendix Section: B.6). While HydA1 is the "minimal version" of [FeFe]-hydrogenase CpI harbors four additional [FeS]-clusters. Comparisons of these two hydrogenases were performed to scan for common features and differences. Since HydA1 and CpI are artificial maturated[27,28,47] it is possible to vary the diiron site composition, especially the bridging atom of the catalytically important azadithiolate (adt) bridge. The replacement of the bridging nitrogen atom by a methyl group (pdt), an oxygen atom (odt), a sulfur atom (sdt), or edt that lacks the bridging atom was analyzed. Individual analysis of these cofactor variants can be found in Appendix Section B.7. Amino acid variants of HydA1 and CpI for the proposed PTP were screened to verify their involvement in proton transport (Section: 3.7). The two different hydrogenases, cofactor variants and amino acid variants were compared to native HydA1 especially by their response to N_2, H_2 and pH differences. In special cases CO inhibition or exposure to O_2 was analyzed. All experiments where performed in the aerosol ATR setup described in Section 2.1.7.

HydA1 Amino Acid Variants

Several amino acid variants of HydA1 were analyzed to elucidate the involvement in the proton transfer pathway, their effect on the [4Fe-4S]-cluster and on the cofactor ligands. The putative PTP from the enzyme surface to the nitrogen atom of the adt bridge consists of amino acids R148, E144, S189, E141, C169 and a water molecule.[17–22] The involvement of S168 that is close to the water molecule of the PTP, the effect of R277 near the [4Fe-4S] cluster and the influence of A92 and A94 on the cofactor ligands at the Fe_p were examined (Figure: 3.29).

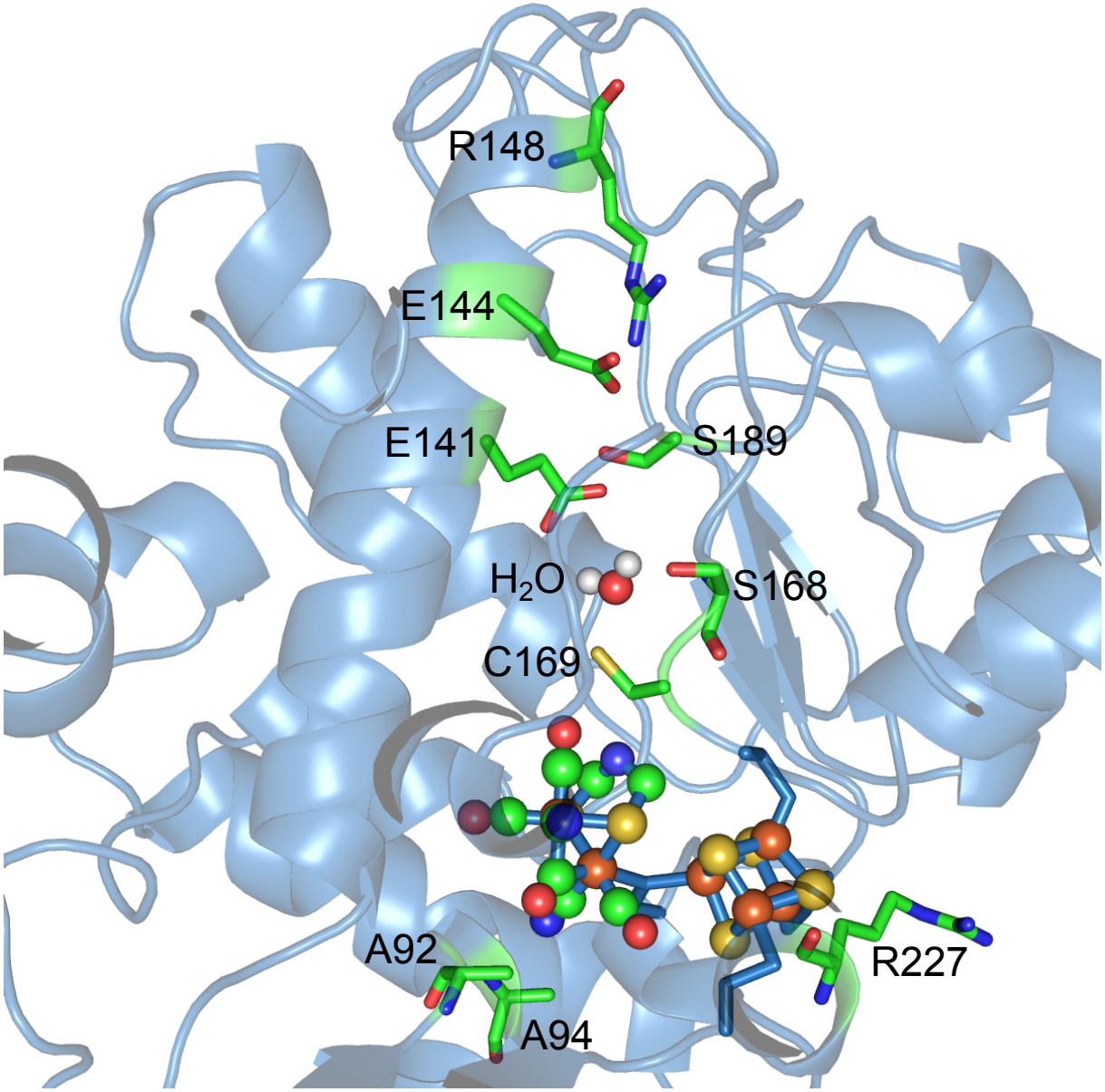

Figure 3.29: Homology model for HydA1 that highlights the varied amino acid positions. From top to the cofactor conserved amino acids and a water molecule form a proton transfer network (R148, E144, S189, E141, H_2O, C169) that is supposed to end at the adt bridge of the diiron site. Serine 168 (S168) was replaced to test the influence on the proton pathway and enzyme behavior. Arginine R227 variation is located near the [4Fe4S]-cluster while alanine A92 and A94 are located close to the proximal iron ligands.

In Figure 3.30 the response to N_2 and H_2 for native enzyme and selected proton path variants at pH 8 is shown. Hox is populated at N_2 atmosphere for all examined variants. Two major types of response can be observed if the atmosphere is changed to H_2. For native enzyme and C169D, S189A and E144D Hsred is populated while C169A, E141A, E141D, E141Q, S189D, E144A and E144Q mainly expose the spectral features of Hhyd. R148A adopts both redox states in nearly similar amounts. Exposure to N_2 at pH 4 lead to population of HoxH for all examined variants (Figure: B.39). Only small differences in band positions between native enzyme and variants are detected.

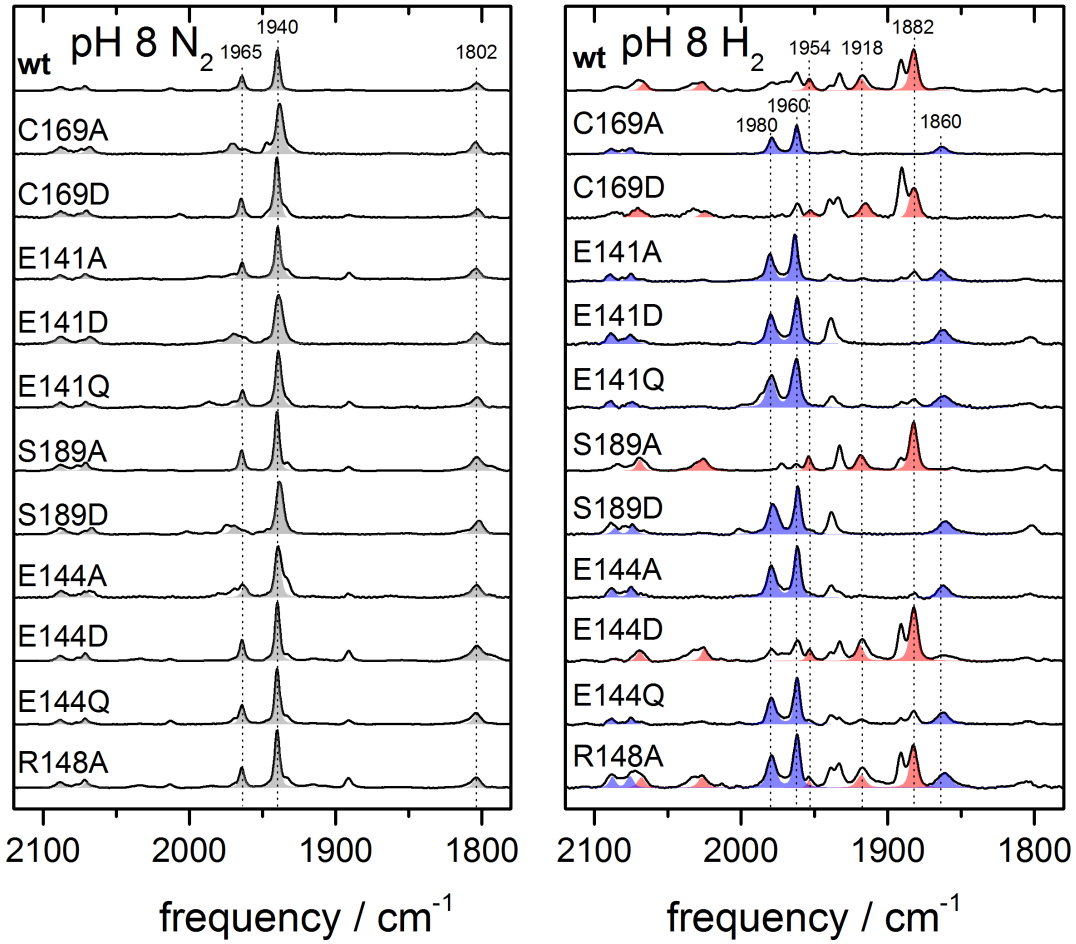

Figure 3.30: Overview of cofactor band patterns adopted for N_2 and H_2 for native enzyme and selected proton path variants at pH 8. Upon N_2 exposure Hox is populated for all variants like in native enzyme (gray, 1965cm^{-1}, 1940cm^{-1} and 1802cm^{-1}). Exchange to H_2 leads to population of two main redox species either native enzyme like Hsred(red, 1954cm^{-1}, 1918cm^{-1} and 1882cm^{-1}) or Hhyd (blue, 1980cm^{-1}, 1960cm^{-1} and 1860cm^{-1}).

S189A and E144D exhibit native enzyme characteristics at H_2 and pH 8. At pH 4 these two variants adopt as well Hhyd like native enzyme (B.40). An individual analysis of all variants can be found in Appendix Section B.8.

3.8 Correlation to DFT model structures and frequency calculations

All DFT calculations were performed by Dr. Stefan Mebs (Freie Universität, AG Dau, Dr. Haumann working group) using Gaussian. To evaluate the correlation of experimental and calculated vibrational frequency the root mean square deviation (RMSD) was employed. RMSD was calculated by the following equation:

$$RMSD = \sqrt{\sum_{i-n}^{n}(F_i^{cal} - F_i^{exp})^2/n} \tag{3.1}$$

with n as the number of CO bands, F_i^{cal} as the calculated frequency of a specific CO band and F_i^{exp} as the experimental frequency of a specific CO band.

3.8.1 Hox and Hox-CO

All possible permutations of ^{12}CO and ^{13}CO ligands for Hox and Hox-CO were analyzed by DFT calculations to obtain theoretical IR spectra for comparison with experimental data. Up to six isotopomers were compared to include alternations of the diiron site ligation geometry. Three models with increasing H-cluster coordination sphere were analyzed to account for effects of the protein environment. As a starting structure for DFT calculations on the H-cluster the crystal structure of CO-inhibited [FeFe]-hydrogenase of CpI (PDB 1C4C)[59] was taken. The smallest model of ca. 50 atoms was build of the atoms forming the H-cluster and additional S-CH_3 molecules that replace the cysteines from the protein fold coordinating the [4Fe4S]-cluster of the H-cluster (Figure B.11(A)). By addition of amino acid fragments in the vicinity of the diiron site the medium sized model (ca. 140 atoms) was obtained (Figure B.11(B)). The largest model features even more amino acids and parts of the protein backbone with ca. 330 atoms (Figure B.12). The full set of all possible permutations of ^{12}CO and ^{13}CO isotopic labels and all possible rotational isomers of CO/CN ligands were calculated for Hox and Hox-CO with the small H-cluster model. For bigger models only specific isotopic labeled species and selected isomers were analyzed.

The iron atoms of the [4Fe4S]-cluster were handled as anti ferromagnetic coupled prior

to geometry optimization. For small models the position of the carbon atoms of the S-CH_3 molecules that ligate the [4Fe4S]-cluster and the position of Fe_p were fixed during structural relaxation. In medium sized models only the position of the carbon atoms of the S-CH_3 molecules were kept constant while in the large model these positions were replaced by cysteines whose CH_2 groups were also part of the optimization. All positions of atoms of amino acids besides hydrogen atoms were kept constant in the optimization process. Only relaxed molecular geometries were used for vibrational frequency calculation. The BP86/TZVP functional/basis-set combination was applied for all models and the TPSSh/TZVP functional/basis-set combination only on selected models to check for functional/basis-set influence. The CO ligands were named pCO for the CO ligand bound to Fe_p, μCO for the bridging CO ligand and dCO for the CO ligand bound to Fe_d. In the case of Hox-CO the former dCO ligand is named d_1CO while the new additional CO ligand bound is named d_2CO.

The oxidized state is adopted under N_2 gas (Section: 3.1.3). Comparison with calculated frequencies for rotamers with equatorial CO/CN^- led to a RMSD of around 10 cm^{-1}. Resembling results were obtained for a Hox rotamer with distal cyanide ligand (dCN) in a rotated position (Figure: 3.31, top) whereas a ligation geometry where the dCN is in complete apical position was less fitting the experimental band pattern.

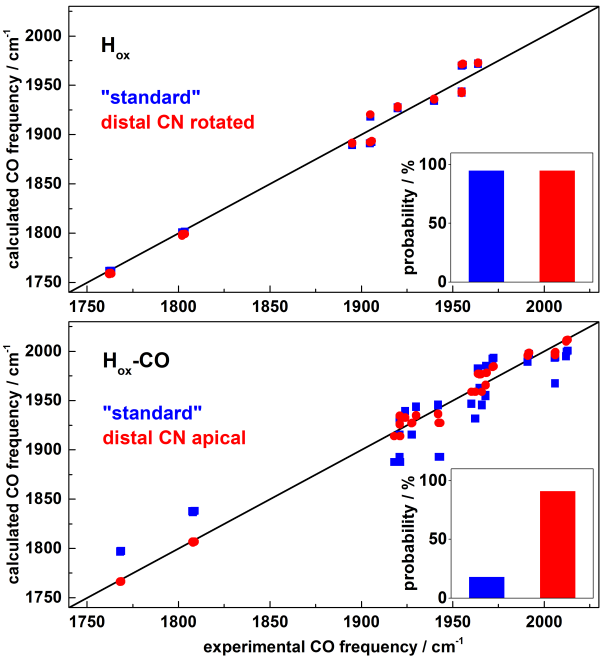

Figure 3.31: Correlation of calculated and experimental frequencies for Hox (top) and Hox-CO (bottom). Shown are the CO band positions for all possible isotopameres. **Top:** For Hox the standard (blue) and distal CN rotated (red) cofactor geometry is compared. Both rotameres are equally probable. **Bottom:** For Hox-CO the standard (blue) and the distal CN apical (red) geometry are compared. The distal CN apical geometry is clearly preferred. Figure taken from[I]

Figure 3.32 illustrate the different modes observed for Hox with all CO ligands ^{12}CO or ^{13}CO(Figure: 3.32 (A)) and Hox with a ^{13}CO ligand in proximal position while all other ligands remain unaltered (Figure: 3.32 (B)). For Hox with identical isotopes

as CO ligand its three CO bands are assigned as mainly uncoupled vibrations that originate each from the dCO (γ), the pCO (β) and the μCO ligand (α) (Figure: 3.32 (A)). Only for the ^{13}CO exchanged pCO case the uncoupled character of band β and γ is lost and extensive coupling is found (Figure: 3.32 (B)). Band β originates of an anti symmetric coupled vibration of pCO and dCO while band γ consists of the symmetric coupled vibration of pCO and dCO (Figure: 3.32 (B)). Exposure to ^{12}CO populates the Hox-CO state with its four characteristic bands at 2012 cm^{-1} (δ), 1968cm^{-1} (γ), 1962 cm^{-1} (β) and 1808 cm^{-1} (α). The d_2CO ligand bound led to the appearance of the additional fourth band compared to Hox. For Hox-CO Figure: 3.32 ((C), (D)) shows the coupling patter for

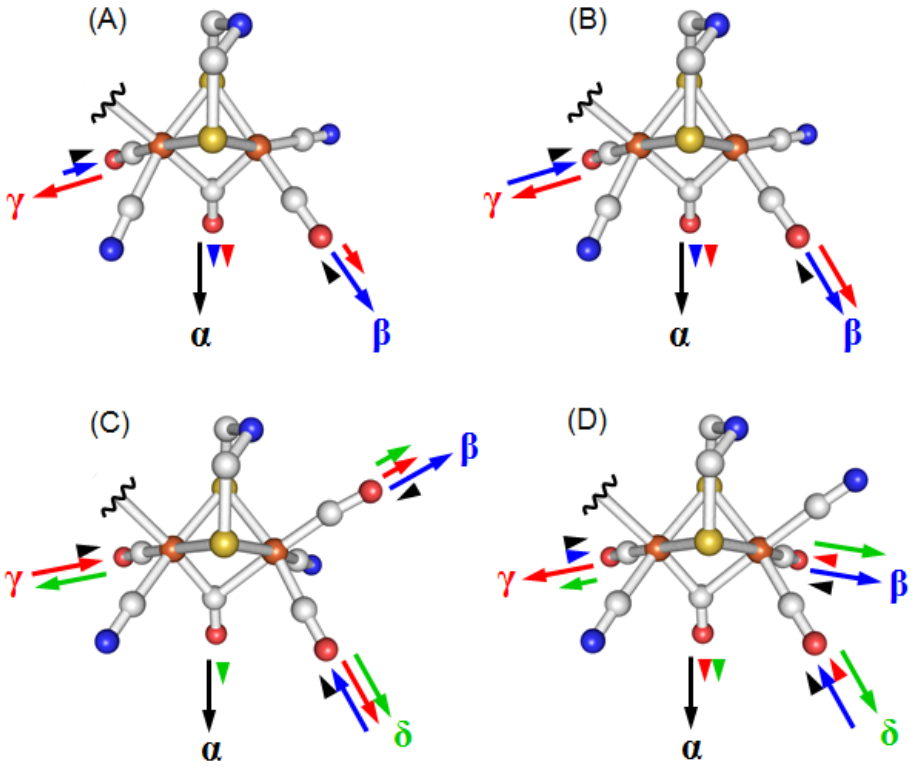

Figure 3.32: Vibrational coupling and contributions of specific CO ligands. Arrows indicate the relative contribution and symmetry character for the CO ligands of each IR band (α, β, γ, δ). Color reports on the IR band, length reports on the relative contribution and the respective orientation on symmetric or antisymmetric vibration. **(A)** Hox with all CO ligands ^{12}CO or ^{13}CO. All bands originate from nearly uncoupled vibrations.. Band α is caused by the μCO vibration (black), band β by the pCO vibration (blue) and band γ by the dCO vibration (red). **(B)** Hox with ^{12}CO as distal CO ligand and ^{13}CO as proximal CO ligand. In contrast to (A) bands β and γ are now largely coupled and represent the anti symmetric (β, blue) and symmetric (γ, red) coupled vibration of pCO and dCO. **(C)** Hox-CO with apical CO ligand. Bands γ (red) and δ (green) consist equally of anti symmetric or symmetric vibrations of pCO and d_1CO respectively. Band α (black) is a uncoupled mode and band β an anti symmetric coupled mode of d_2CO and d_2CO(blue). **(D)** Hox-CO with apical CN. In this geometry band γ (red) is largely uncoupled like seen in experiment. Figure taken from[I]

either the "standard" case with apical d_2CO or the rotamer with both distal CO ligands (d_1CO, d_2CO) in equatorial plane and an apical dCN ligand. The DFT simulations for the four rotameres that feature the additional d_2CO ligand in apical position compared to the experimental frequencies had a RMSD of around 30 cm^{-1}. For a rotamer with d_1CO and d_2CO in equatorial position and an apical dCN a sixfold smaller RMSD was observed (Figure: 3.31, bottom). The α band could be assigned to the μCO stretching vibration for each CO inhibited rotamer. Band β (1962 cm^{-1}) consists of an anti-symmetric coupled stretch vibration with pCO and d_1CO (Figure: 3.32 (C), (D)). A coupled vibration with symmetric contributions of d_1CO and d_2CO and antisymmetric contribution of pCO gives rise to band γ in the apical CO case (Figure: 3.32 (C)). For the apical CN geometry band γ is largely uncoupled (Figure: 3.32 (D)) as seen in experiment Band δ originates from a coupled symmetric mode where all but the μCO ligand are involved with main contributions of pCO and d_1CO for the apical CO case (Figure: 3.32 (C)) and main contributions of d_1 and d_2CO for the apical CN geometry (Figure: 3.32 (D)). Since only band α is an uncoupled mode the assignment of Hox-CO spectra is not that intuitive like in Hox.

3.8.2 Hox and HoxH

To investigate if protonation near the H-cluster could be the origin of the observed blue shift DFT calculations on H-cluster models where performed. A representative model is shown in Figure 3.33. As protonation sites the nitrogen atom of the adt bridge, the μS atoms of the adt bridge (S1-S2), the sulfur atoms of the [4Fe-4S] cluster (S3-S6) and the sulfur atoms of the cysteines that ligate the [4Fe-4S] cluster (S7-S10) were considered. For Hred' and Hred'H additionally reduction of the [4Fe-4S] cluster is modeled.

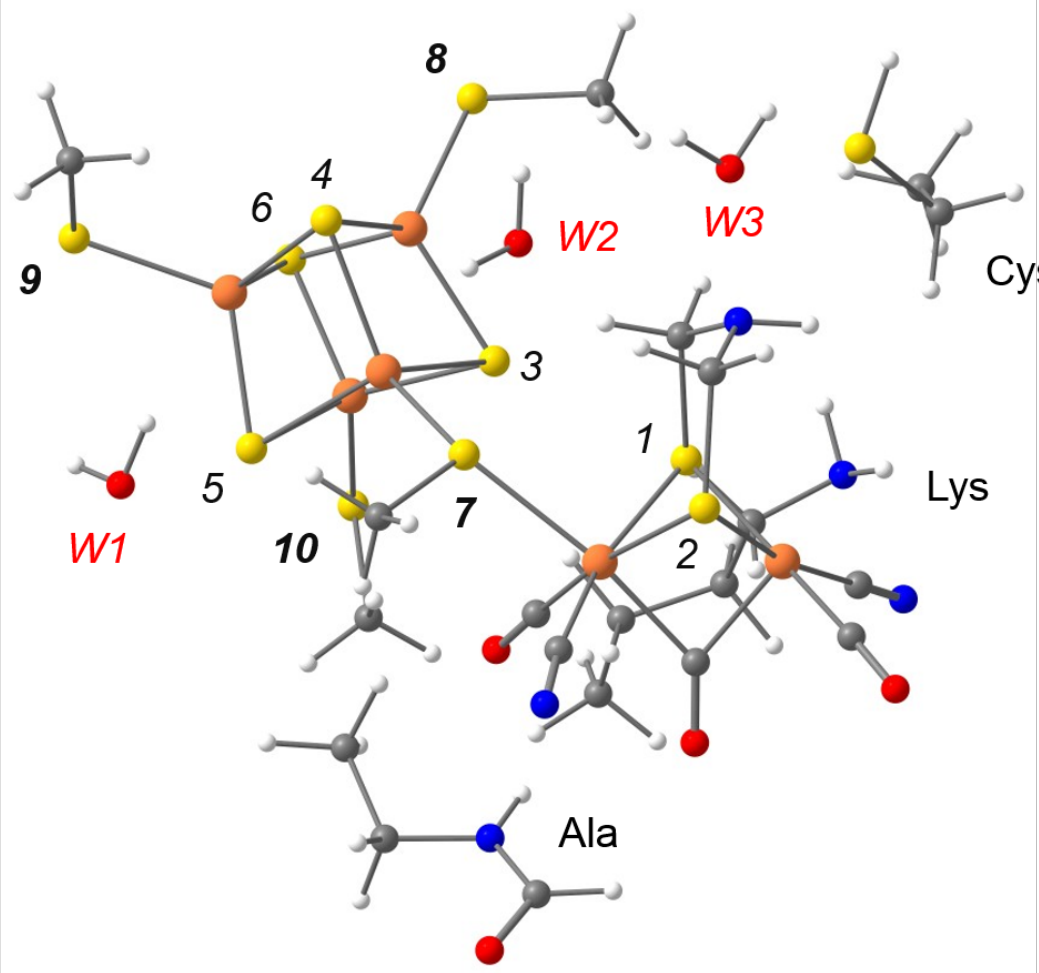

Figure 3.33: DFT model structure and possible protonation sites. Sulfur protonation sites (yellow spheres) are numbered and sulfurs of cysteines that ligate the [4Fe-4S] cluster are printed bold additionally. Water molecules (W1-W3) as extra protonation sites and selected amino acids (Cys, Lys, Ala) were implemented in some calculations. DFT model structure is based on PDB entry 4DXC of CPI. Figure taken from[IV]

Direct protonation of the nitrogen atom of the adt bridge led to frequency up shift of bands ca. 4 times larger than observed for the Hox to HoxH transition. The same holds true for protonation of the sulfur atoms(S1-S2) of the adt bridge (RMSD 15-25 cm^{-1}). Better correlation (RMSD 8-11 cm^{-1}) of experimental and calculated bands was found for

protonation of the μS atoms of the [4Fe-4S] cluster (S3-S6). But the pCO band experiences a down shift when S3 or S5 are protonated and protonation of S4 or S6 led to distortion in the [4Fe-4S] cluster geometry. The down shift of the pCO band is observed for protonation of S10 a sulfur atom of a cysteine that ligates the [4Fe-4S] cluster as well. The protonation of S7 the sulfur atom of the cysteine that connects the diiron site with the [4Fe4S] cluster led to large shifts in IR bands compared to protonation of cysteine sulfurs S8 or S9 that caused a small RMSD of 7 cm^{-1}. Large shifts are observed for protonation of the water molecules (W1-W2). The best match of experimental and calculated band patterns was found for protonation of S9 (Figure 3.34). Deuteration of S9 instead of protonation led to RMSD (less 1 cm^{-1}) of the calculated frequencies. More detailed analysis of IR frequency differences, intensity differences and RMSD for frequency and intensities can be found in Figure B.13.

3.8.3 Hred' and Hred'H

H-cluster models that contain a surplus electron were applied to describe the [4Fe-4S] cluster reduced state Hred'. An model with bridging CO and open apical binding site like in Hox resulted in a down shift of bands by ca. 35 cm^{-1}. Possible protonation at the H-cluster was analysed as a compensation to this large shift. Protonation at the nitrogen atom or the sulfur atoms (S1-S2) of the adt bridge of the reduced active site still displays a large down shift (RMSD 30 cm^{-1}). A large up shift of bands (RMSD 40 cm^{-1}) is observed when an apical hydride is located at the open binding site of Fe_d with a most pronounced up shift of μCO. Protonation of the sulfur atoms of the [4Fe-4S] cluster (S3-S6) in the reduced H-cluster exhibits a down shift in the order of the experiment but in these models geometry of the [4Fe-4S] cluster was disturbed. An intact [4Fe-4S] cluster and good agreement in band pattern was found when the sulfur atoms of the cysteines that ligate the cluster were protonated. Again protonation at S9 was favored to match the spectrum of Hred' (RMSD 9 cm^{-1}, Figure 3.34).

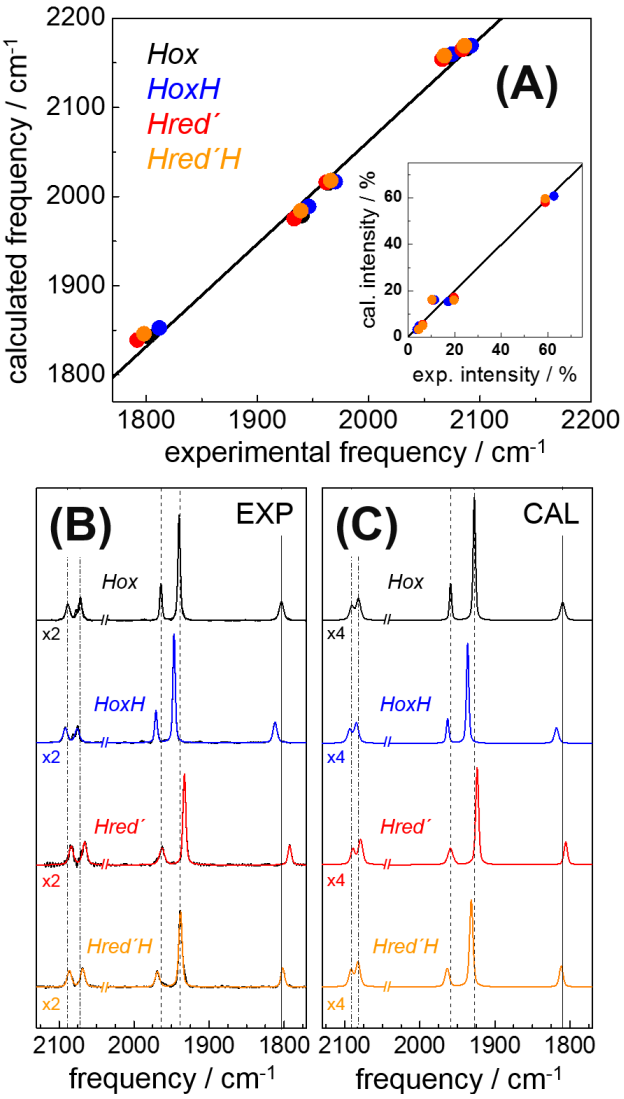

Figure 3.34: Comparison of experimental and calculated spectra for Hox, HoxH, Hred' and Hred'H. **(A)** Correlation plot of experimental and calculated frequencies. **Inset:** Correlation of exp. and calc. intensities. **(B)** Experimental IR spectra of Hox, HoxH, Hred' and Hred'H. **(C)** Calculated IR spectra of Hox, HoxH, Hred' and Hred'H. Figure taken from[IV]

For the Hred'H model an additional protonation to Hred' was assumed. Trends like for HoxH and Hred' were observed regarding structural distortion and band shifts due to reduction and protonation. Best match of experimental and calculated spectrum was

found for protonation of S9 and additional protonation of S8 (Figure: 3.34). Again a more detailed analysis of IR frequency differences, intensity differences and RMSD for frequency and intensities can be found in Figure B.15. The spin and charge distribution of the H-cluster is shown in Figure B.16. At the diiron site the spin density distribution of Fe(I)Fe(II) for all four states is found. For Hred' and Hred'H additional negative charge density on the [4Fe4S] cluster indicates the position of the reductive electron. Only minor charge distribution changes were observed at the diiron site. The vibrational modes of CO and CN are mainly uncoupled for all states.

3.8.4 Hred and Hsred

For Hred and Hsred three structural isomers inspired by literature[36,38,40,41,60–62] were examined that differ in location of a hydrogen atom and CO ligand arrangement. First a structure that features a μCO ligand and an apical hydride or H_2 species bound to Fe_d (Figure: 3.35 I), second a structure that features a "semi bridging" CO ligand bound to Fe_d, a double protonated adt bridge and an open vacancy at Fe_d (Figure:3.35 II) and third a structure that harbors a Fe-Fe bridging hydride (μH) and an apical CO/CN ligand at Fe_d (Figure: 3.35 III).

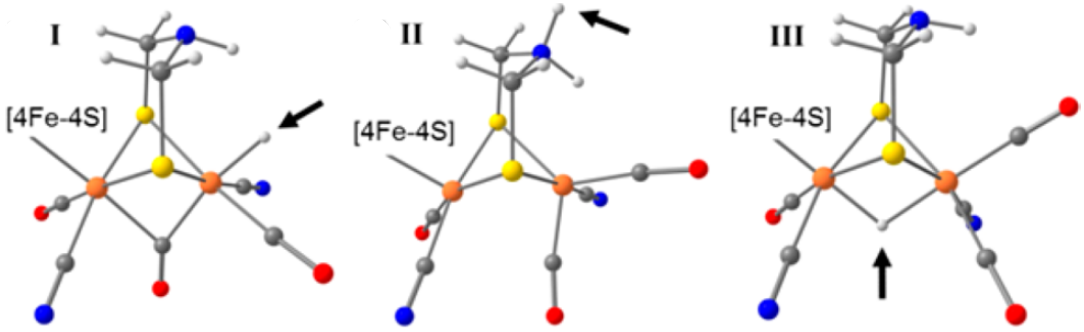

Figure 3.35: Three model structures investigated for Hred and Hsred. **I** bridging CO (μCO) and apical bound hydride or H_2 species at Fe_d. **II** semi open bridging CO ligand bound to Fe_d, double protonated adt bridge and open vacancy at Fe_d. **III** bridging hydride(μH) and apical CO/CN ligand at Fe_d. Arrows indicate the position of the additional proton. Figure taken from[VIII]

Calculated IR band frequencies for each structure model were compared to the experimental frequencies observed in Section 3.4. Calculations were performed with and without selected amino acids that possibly influence cofactor bands. Coupling of CO ligand vibrations varied for each geometry thus the IR bands originate from different vibrational modes among the three models (Figure: B.17). Smallest RMSD was obtained for model

III. For models without surrounding amino acids structures I and II yielded RMSD of 34-67 cm^{-1} and 25-57 cm^{-1} while structure III had two fold smaller RMSD (13-25 cm^{-1}). Here RMSD reports on 6 rotamers to screen for possible permutations of CO/CN ligand arrangement. Models with implemented amino acids Ala 232 and Lys 358 (Figure: B.14) reduced the RMSD for all three structures still favoring modell III. Especially for model III a down shift of CN ligand bands was observed that improved the correlation with experimental band positions. Note the that only model III exhibits the characteristic frequency difference of the CN ligand bands found for Hred and Hsred. Protonation of the [4Fe-4S] cluster for Hsred in model III in analogy to the Hred'/HoxH protonation yielded a minor down shift of 3 cm^{-1}.

Modification of DFT functionals and dielectric constants had no effect on the preference of model III. CO/CN ligand inversion at Fe_p or at Fe_p and Fe_d as introduced in Section 3.2 was disfavored. Discrimination of apical CO or CN ligands in model II and III was investigated. An apical CN in model II improved the RMSD caused by interaction of the adt bridge and the CN ligand. However this model failed to reproduce the specific shifts observed for ^{13}CO isotopic edited Hred/Hsred species as seen in Section 3.4. These characteristic isotopic shifts were only reproduced by model III featuring an apical CO ligand and reproduced best the intensity distribution of the observed bands as well. Correlation of calculated and experimental band frequencies for Hred and Hsred for each of the three models is shown in Figure 3.36. Best correlation is observed for model III.

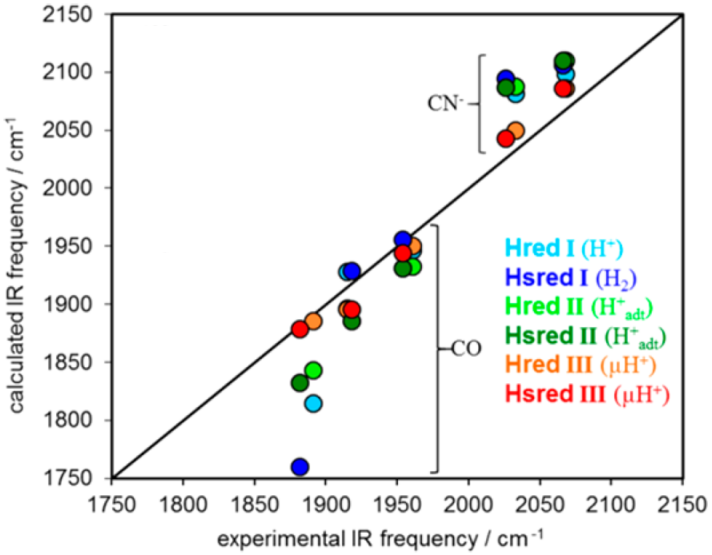

Figure 3.36: Correlation plot of calculated and experimental Hred/Hsred frequencies for models I (blue), II (green) and III (red). Best correlation is found for model III. Figure taken from[VIII]

3.8.5 Hox-O_2 and Hhyd

For Hox-O_2 band frequency calculation the Hox structure with an additional O_2 molecule bound to the apical vacancy at Fe_d was used and yielded a RMSD of ca. 11 cm^{-1} (Figure 3.37). The blue shift of cofactor bands relative to Hox (as seen in Section 3.6) is most likely due to electron density lost at the diiron site caused by formation of a superoxide species (O_2^-). A model with a hydro-peroxo ligand (OOH) at Fe_d was excluded by comparison to experimental data. For the superoxide model the band at 1864 cm^{-1} and at 1990 cm^{-1} could be assigned to an uncoupled μCO and dCO vibration respectively. A coupled mode of dCO and pCO gives rise for the band at 2007 cm^{-1}. Interestingly the order of CN band frequencies were inversed. The dCN ligand band shifts by ca. 30 cm^{-1} compared to Hox while the pCN ligand was nearly not effected.

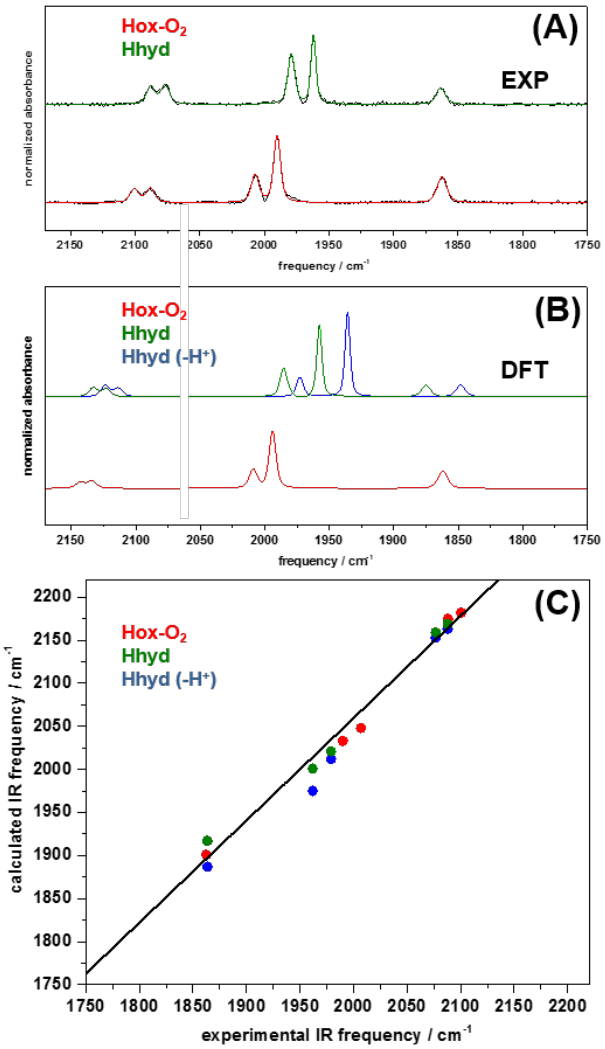

Figure 3.37: Comparison of experimental and calculated spectra for Hhyd and Hox-O_2. **(A)** Experimental spectra of Hhyd (green) and Hox-O_2 (red). **(B)** Calculated spectra of Hhyd (green), Hhyd without protonation(Hhyd(-H^+)) (blue) and Hox-O_2 (red). **(C)** Correlation plot of calculated and experimental frequencies. Good agreement for Hox-O_2 and Hhyd is found. For Hyd(-H^+) the CO bands are not well described. Figure taken from[V]

For Hhyd a structure with a bridging CO ligand(μCO) and a hydride bound at the apical vacancy of Fe_d matched the band pattern of Hhyd. But the large blue shift of CO bands relative to Hox was not reproduced. In analogy to Hred' protonation in vicinity of the H-cluster was checked systematically as described in Section 3.8.2 and Section 3.8.3. Best agreement of calculated and experimental band frequencies was found for protonation of

the very same cysteine (cysteine417 (S9) in Figure 3.33) that ligates the [4Fe4S] cluster (RMSD ca. 11 cm^{-1}). Additionally the intensity of the high energy CO band is better described (Figure: 3.37). An geometry with an apical CN ligand at Fe_d and a hydride in equatorial configuration was ruled out by large up shift of the μCO ligand that does not fit the experimental observed band pattern. For the apical hydride geometry coupling of the hydride to μCO was observed(in accordance with H/D exchange experiments performed in Section 3.5). As for Hox-O_2 the order of CN band frequency was inverted and dCO has and uncoupled mode and an additional coupled mode with pCO at higher energies.

Chapter 4

Discussion

4.1 Hox-CO and Hox

The possibility to control important parameters like gas exposure, illumination, and hydration was exploited to obtain all possible permutations of ^{13}CO isotopic edited Hox-CO and Hox. Thereby spectra of all eight differently labeled Hox and all 16 differently labeled Hox-CO species were identified. This large dataset was compared to DFT calculations to verify the respective edited positions and get insights in vibrational coupling. While the assignment of the mainly uncoupled vibrational modes for Hox was more or less intuitive for Hox-CO increased vibrational coupling was found. An uncoupled CO ligand band shifts 44 cm^{-1} to lower energies when exchanged from ^{12}CO to ^{13}CO.[44,63] For coupled vibrational modes the shift varies and several bands are affected. DFT calculations were used to simulate the coupling characteristics for different isotopic edited cofactor. Since coupling patterns are highly dependent on cofactor ligand arrangement it is possible to obtain structural information by combination of DFT and FTIR spectroscopy.

An apical CN ligand at Fe$_d$ is favored for Hox-CO For all differently edited isotopologues correlation of experimental and calculated ligand band positions was poor for standard Hox-CO structures[59,64] with apical CO ligand at Fe$_d$. In contrast structures featuring an apical CN ligand showed good correlation and reproduced several properties observed in experimental spectra (Figure: 4.1 on the facing page C, D). For example the vibrationally uncoupled pCO mode[25,44] or inverted band intensities for some isotopologues. Irrespective of native maturation for DDH or artificial maturation for HydA1 and CpI[16,36,65–67] this trend was conserved. Thereby the preference for an apical CN at Fe$_d$ is not due to rotamer formation in artificial maturation. An apical CN ligand for Hox-CO was proposed in earlier DFT/IR studies but without isotopic editing only a single spectrum was available for correlation with experiment.[64,68,69] Facilitated by a broad set of experimental data to compare the enhanced statistics support the apical CN ligand arrangement in every case. At Fe$_p$ the standard ligand arrangement was confirmed like proposed for crystal structures before.[9,14,47] In these structures the CN/CO ligand arrangement was modeled by possible hydrogen bonds to CN ligands by surrounding amino acids.[9,17,19,29,70] Discrimination of CO and CN ligands is not given at protein crystal structure resolution. An interaction of dCN and to surrounding amino acids was proposed by an EPR investigation[71] but this interaction was not confirmed in a later EPR

study.[67] In apical CN ligand geometry arrangement the adt nitogen base slightly interacts with the CN ligand by hydrogen bonding. This arrangement was found to be favored before.[64] Note for hydrogen uptake hydrogen bonding to the adt bridge is suggested as well.[29,41,70,72] Independent of CO/CN ligand arrangement at Fe_d the isotopic editing process can be described by the cycles shown in Section 3.2 on page 31.

Structural flexibility in Hox For Hox the standard and a rotated CN ligand arrangement can not be discriminated since both show good correlation with experimental data. Besides this CO/CN ligand arrangement as suggested for respective crystal structures is confirmed.[9,14,29,47] It is possible that at cryogenic temperatures as applied for crystal

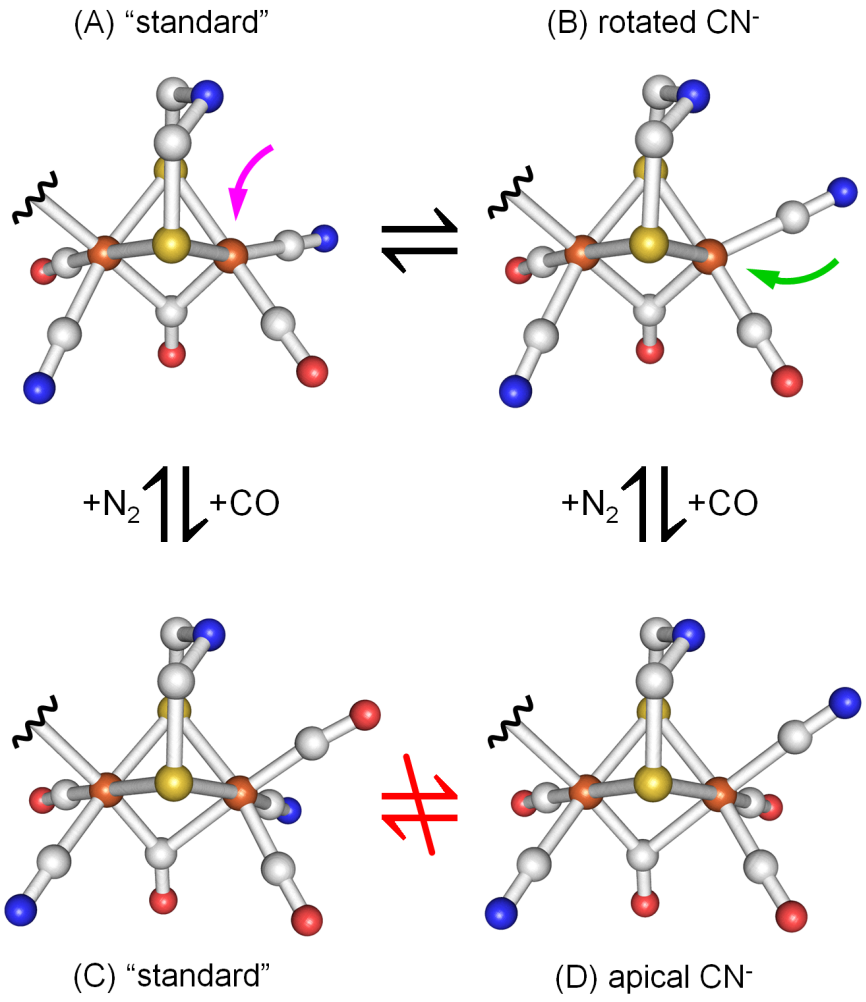

Figure 4.1: Rotamer structures for Hox and Hox-CO. Hox in standard geometry (A) exposed to CO binds apical the new CO ligand(magenta arrow) and forms Hox-CO standard (C). Hox with rotated CN geometry (B) enables equatorial binding of CO(green arrow) and forms Hox-CO with apical CN ligand (D). Interconversion of Hox in standard and rotated geometry is thought to be possible while the octahedral coordination of Fe_d in Hox-CO should prevent the transition between standard and apical CN geometry. Figure taken from[I]

structure determination, Hox in standard arrangement is the prevailing geometry while at room temperature as used for FTIR experiments an equilibrium of Hox in standard and rotated CN geometry might be possible (Figure: 4.1 on the preceding page A, B). Equilibria like this were observed for model compounds before.[73–75] Further indication of ligand flexibility is given by a molecular dynamics study were distal ligand rotation was related to amino acid side chain movement.[61] For Hox with rotated CN ligand arrangement CO could possibly bind in equatorial position and give rise to Hox-CO with apical CN ligand weakly hydrogen bonded to the nitrogen atom of the adt bridge. This ligand flexibility can be thought to have an influence on ligand binding like H_2 for example.

4.2 Hred and Hsred

Hred and Hsred cofactor structure For [FeFe]-hydrogenases Hred and Hsred are the two redox states which are reduced at the diiron site. While Hred is only reduced at the diiron site Hsred is additional reduced at the [4Fe-4S] cluster. By combination of spectro electrochemistry (Section: 2.1.8 on page 17) and isotopic editing (Section: 3.2 on page 31) band positions for Hred and Hsred for five differently isotopic edited H-clusters were obtained (Section: 3.4 on page 50). These band positions were compared to DFT calculations of different structures to gain insights in coupling of CO ligands and cofactor geometry. Out of the large variety of structures proposed for Hred and Hsred[36,38,40,41,60–62] three major model structures were set up and analyzed by DFT. The set of model structures comprises: a model with bridging CO ligand and a proton/H_2 bound to Fe_d, a model with additional protonation at the adt bridge, "semi bridging" CO bridge and open vacancy at Fe_d, a model with bridging hydride and apical CO/CN ligand at Fe_d. Preference was found for the structure that features a bridging hydride (μH) and an apical CO ligand at Fe_d. The discrimination between apical CN or CO ligand was enabled by enrichment of isotopic edited Hred and Hsred species. Only a model with apical CO could reproduce the coupling patterns found. Additional protonation at the reduced [4Fe-4S] cluster for Hsred as found for Hred' and HoxH (Section: 3.8.2 on page 62 and 3.8.3 on page 64) did not improve the RMSD significantly. Implementation of cofactor surrounding amino acids yielded better agreement with experiment especially for the CN ligand band positions. It seems that for diiron site reduced states (Hred, Hsred) the interaction with the enzyme surrounding is more pronounced than for example for Hox-CO or Hox where only insignificant effects were observed for inclusion of surrounding amino acids.

Experimental separation of Hred and Hred' Exposure to H_2 populatesredox states Hred, Hsred and Hred'. Both Hred and Hred' are reduced by one electron compared to Hox. The location of the reducing electron is the [4Fe4S] cluster for Hred'[37,38] or the diiron site for Hred.[24] The IR signature of Hred was incorrectly assigned for a long time and in multiple studies for HydA1[4,17,35–37] while for [FeFe]-hydrogenase DdH, Hred was known.[24,25,33] Misassignment was due to mixture and simultaneous population of Hred and Hred' in HydA1. Hred' was not known at this stage, most likely because significant enrichment was not observed in [FeFe]-hydrogenases that bind additional FeS

clusters.[24,25,33,45,63] Disentangling of these states was achieved by isotopic edited CO ligands and pH titrations under reducing conditions.

To identify the dCO ligand of Hred and Hred' the ligand was exchanged to ^{13}CO as described before (Section: 3.2 on page 31). After population of Hox under N_2 subsequent exposure to H_2 enriched both Hred and Hred'. As reported in Section 3.3.5 on page 45 in the resulting difference spectrum the natural band positions of two bands are shifted by 40 cm^{-1}. First the band at 1891 cm^{-1} that was assigned for Hred in DdH before[24,25,33] shifts down to 1851 cm^{-1} and is thereby assigned to the dCO vibration of Hred in HydA1 as well. If only one CO ligand is exchanged (in this case dCO) the other bands of Hred should shift only minor. The band at 1933 cm^{-1} shifts down 40 cm^{-1} as well and has therefore to be assigned to a separate state, the dCO vibration of Hred'. The band at 1792 cm^{-1} was assigned as μCO by isotopic replacement and the related down shift of 40 cm^{-1} as expected for ^{13}CO replacement. To correlate the 1792 cm^{-1} band either to Hred or Hred' a pH titration of unaltered enzyme under reducing conditions gave clear evidence. Decreasing pH led to population of the 1891 cm^{-1} band while the 1933 cm^{-1} band depopulates. Depopulation of the 1792 cm^{-1} band in the same process correlates it to the 1933 cm^{-1} reduced state, namely Hred'. Hred' is thereby associated with a μCO ligand while the absence of a μCO bands suggest no bridging CO ligand for Hred. This was already indicated by comparison to DFT calculations above (Section: 4.2 on the preceding page).

4.3 HoxH

Location of the proton for HoxH Under N_2 at acidic pH and in the presence of DT Hox was converted to HoxH. The small frequency up shift observed for HoxH compared to Hox is unlikely due to further one electron oxidation of the diiron site where larger shifts are expected.[76] A protonation event in the vicinity of the H-cluster that decreases electron density and leads to partial "oxidation" is proposed for HoxH due to its formation at low pH values. No population of HoxH was found if DT was absent and in DT titration experiments the apparent pK of HoxH formation shifted. This contradicts protonation of an amino acid residue that should be independent of reductant concentration. The ap-

pearance of the blue shifted version of Hox-CO in which the vacancy at Fe_d is occupied by a CN ligand as or either way a CO ligand disagrees with direct protonation at Fe_d. This finding is supported by H/D exchange experiments. A deuterium species bound to Fe_d would induce coupling of the μCO ligand vibration located trans to the Fe-D vibration as seen for Hhyd.[41,43] No such effect is observed for HoxH (HoxD). Furthermore the identical band pattern of HoxH (HoxD) in D_2O disfavors protonation of the sulfur atoms of the adt bridge as well. The sulfur deuterium vibration would be down shifted in the region of the CO ligands[77] and vibrational coupling could be expected as suggested by DFT calculations. Additional protonation of the nitrogen atom of the adt bridge was disproven by HoxH formation in cofactor variants odt, sdt, edt and pdt. The cysteine that connects the PTP to the adt bridge C169 was ruled out as a protonation site. For amino acid exchange to aspartic acid (C169D) or alanine (C169A) variants still show HoxH formation. C169D acts similar as native enzyme but interestingly C169A has a slower HoxH formation rate. The slower HoxH formation rate for C169A indicates involvement of the PTP to the di-iron site and thereby catalysis in HoxH formation. Artificial maturation can be excluded as a reason because [FeFe]-hydrogenases CpI and DDH show HoxH formation as well . These experimental findings (Section: 3.3 on page 37) and correlation of the respective IR spectra to DFT calculations (Section: 3.8.2 on page 62) suggest the sulfur atom of C417 at the [4Fe-4S] cluster as protonation site.

HoxH formation involves turnover The Hox to HoxH conversion follows over time a sigmoidal function. Thereby the involvement of two processes for HoxH formation is most likely. Moreover the compelling need for DT indicates that a reduction event proceeds the HoxH formation but no reduced species were observed in HoxH formation from Hox. This is in discrepancy to earlier experiments where reduced species are reported for DT exposure.[36,62] Most likely the reduced species decay much faster than they are formed by for example H_2 evolution. In this scenario HoxH would emerge as a result of protonation at the [4Fe-4S] cluster during the H_2 evolution process. The pdt cofactor variant is reported to be less active in hydrogen evolution[27] and had a 20 times slower HoxH formation rate that hints again to involvement of reduction steps and H_2 evolution for HoxH formation. Hindered proton supply would slow down H_2 evolution and thereby HoxH formation as observed for C169A. The HoxH to Hox back-transition appears to be more or less independent of pH and DT and follows an exponential function. The deprotonation event seems thereby not to be mandatory connected to turnover.

Intermolecular electron transfer enables H_2 uptake in cofactor variant pdt Further investigation was performed on cofactor variant pdt. For this variant population of Hox and Hred' were the only redox states reported earlier.[37] Since the pdt variant shows HoxH formation Hred' is a likely intermediate for the Hox to HoxH transition. In contrast to low H_2 uptake that was found in former studies,[27] exposure to H_2 led to the reversible population of Hred'. While low H_2 uptake activity in diluted solution assays on the one hand on the other hand Hred' population in rehydrated concentrated enzyme in the ATR setup was observed. To investigate this discrepancy dilution of enzyme films was performed. Studies on pdt films diluted with BSA (Section: 3.3.6 on page 46) revealed that the Hox to Hred' formation rate upon exposure to H_2 was strongly dependent on the relative concentration of pdt enzyme. For more diluted enzyme films the Hred' formation rate dropped significantly. Intermolecular electron transfer would be a likely explanation for this dependency as no two-electron reduced species were observed. Possibly successful H_2 uptake for variant pdt requires fast removal of the first electron for example to a nearby enzyme while the second electron can be stored at the [4Fe-4S] cluster by Hred' formation. If this holds true the low H_2 uptake activity reported could be due to inefficient intermolecular electron transfer in diluted solution assays. Interestingly the HoxH

formation rate was only minor effected by dilution indicating that intermolecular electron transfer is not predominantly involved in this process. This observation fits the theory that HoxH originates from protonation connected to one electron reduction by DT during H_2 evolution.

Hred' as an intermediate in HoxH formation cycle At proton concentrations of maximal H_2 evolution[78] the formation of Hred' is favored over Hred. In cofactor variant pdt Hred' is the only reduced state known. Regarding these points Hred' is proposed as intermediate in formation of HoxH from Hox. Especially the concept of charge compensation favors Hred'. Most likely due to the reduction of the [4Fe-4S] cluster a proton is bound nearby. After the second reduction step and subsequent H_2 evolution the proton is still bound. If deprotonation is hindered by an already protonated proton acceptor (low pH) HoxH accumulates while Hox is regained at more alkaline pH values. As proton donor/acceptor H_2O molecules either from bulk solution for HydA1 or conserved, "crystal" water molecules as observed for CpI and DDH[9,47,79] can be considered (Figure: 4.2).

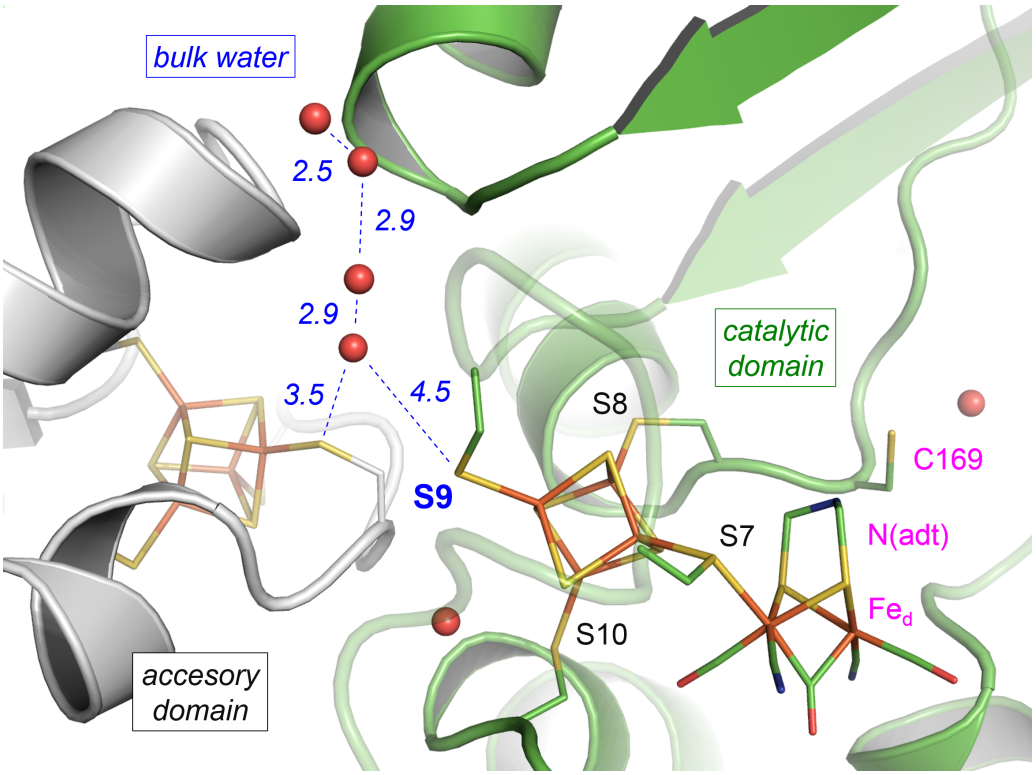

Figure 4.2: Chain of water molecules observed in crystal structures of CpI and DDH[9,47,79] (PDB 4XDC). Water molecules (red spheres) form a path from the bulk to sulfur atom S9 of cysteine417 at the [4Fe-4S] cluster (regulatory proton transfer path). Blue numbers report on the oxygen to oxygen distance of the water molecules. In magenta part of the catalytic proton transfer path is shown. Figure taken from[IV].

4.4 Hred' and Hred'H

Hred' and Hred'H in cofactor variant HydA1pdt Native HydA1 exposed to H_2 adopts the reduced states Hred', Hred and Hsred simultaneously. To focus on Hred' cofactor variant pdt was analyzed in more detail. This variant exclusively adopts Hred' upon H_2 exposure. In analogy to the native enzyme population of HoxH under N_2 was observed when the pH was lowered in presence of DT. Instead of population of Hhyd or known reduced states (e.g. Hred, Hsred, Hred') exposure to H_2 at low pH resulted in a new band pattern with band positions between those of Hred' and Hox. The intensity distribution of cofactor bands resembles Hox and Hred' as well suggesting similar ligand arrangement. The new species was called Hred'H in analogy to the Hox/HoxH notation and due to the comparable frequency up shift with respect to Hred' (Section: 3.3.6 on page 46). As a reason for the upshift additional protonation is suggested by DFT calculations and confirmed by spectro-electrochemical experiments described in the next paragraph. Hred'H can be observed in native enzyme (adt) as well. However the dCO marker band at 1938 cm^{-1} of Hred'H overlaps with the main band of Hox at 1940 cm^{-1} and is therefore difficult to discriminate. Additionally simultaneous population of HoxH, Hhyd, Hred and Hsred in native enzyme complicates the characterization of Hred'H.

Reduction at the [4Fe4S] cluster is associated with a protonation event Electrochemical investigation at varied pH values for the Hox to Hred' and the HoxH to Hred'H transition revealed linear correlation between Em and pH (Section: 3.3.6 on page 47). Solution of the Nernst equation for room temperatur and one electron and one proton proposes a slope of ca. 59 mV per pH unit. The slopes of 55 mV/pH and 50 mV/pH directly suggest that one proton is involved in each of these one electron redox transitions. In formation of Hred' from Hox one proton is involved and in the transition from the already protonated HoxH to Hred'H an additional proton is bound. Hred'H is thereby double protonated and Hred' single protonated compared to Hox as seen in DFT calculations too. The location of the proton associated with Hred' was identified as for HoxH. The best agreement between experimental and calculated IR spectra of Hred' hints to protonation of a sulfur atom that belongs to a cysteine that ligates the [4Fe-4S] cluster. This site, cysteine 417(S9) is the most likely protonation site for HoxH and Hred'H as well. For Hred'H protonation of an additional cysteine(C170(S8)) at the [4Fe-4S] cluster

is assumed (Section: 3.8.3 on page 64). The spin density distribution obtained by DFT calculations revealed conserved charge distribution at the diiron site while the location of the reducing electron was found to be the [4Fe-4S] cluster. The offset of the Em for the Hox to Hred' and the HoxH to Hred'H transition shows that protonation at the [4Fe-4S] cluster modulates the redox potential and elevates the Em by ca. 50 mV to less reducing potentials in favor of the HoxH to Hred'H transition.

Reduction at the diiron site vs. reduction at the [4Fe-4S] cluster In pH and DT titrations four states were identified that share a similar spectral vibrational fingerprint(Hox, HoxH, Hred', Hred'H). Redox and protonation state differs between these states. The cofactor geometry of Hox was shown to feature a bridging CO ligand an an apical vacancy at Fe_d in crystal structures,[9,47,79] FTIR studies[25,29,34,44,45,59,62] and DFT calculations.[33,61,68] In our DFT analysis this cofactor geometry was found for Hox/ HoxH and Hred'/ Hred'H. Hox and HoxH share the same redox state with a $[4Fe\text{-}4S]^{2+}$-FeFe(I,II) H-cluster configuration[24,31,32] while Hred' and Hred'H are reduced at the [4Fe-4S] cluster and have $[4Fe\text{-}4S]^{1+}$-FeFe(I,II) H-cluster configuration.[37] The oxidized diiron site is the major difference to Hred and Hsred that adopt FeFe(I,I) configuration at the diiron site. The location of a reducing electron at the H-cluster seems to be linked to protonation. For Hred reduction at the diiron site was proposed to be associated with a additional protonation of the nitrogen atom of the adt bridge.[36,38,40,42] However no evidence of a double protonated nitrogen atom in the adt bridge was shown. The comparison of isotopic edited HydA1 spectra for Hred and Hsred to DFT calculations rather suggests that the proton is bound as a bridging hydride (Section: 3.8.4 on page 65). For reduction at the diiron site the μCO ligand flips to the apical vacancy at Fe_d and the proton occupies the Fe-Fe bridging position. In this new arrangement the distance between Fe_p and Fe_d increases and the vacancy at Fe_d is occupied. Either way reduction at the diiron site is accompanied by protonation at the diiron site.

The observed pH dependency of Hred' formation suggests that a protonation event is involved in [4Fe-4S] cluster reduction as well. DFT calculations show that the small shift to lower wavenumbers (Hox to Hred) is exclusively reproduced if protonation compensates for the reduction event at the [4Fe-4S] cluster. In contrast to Hred for Hred' reduction

and protonation at the [4Fe-4S] cluster preserves the conservative diiron site geometry (Section: 3.8.3 on page 64) that features a open apical vacancy at Fe_d.[9,47,79]

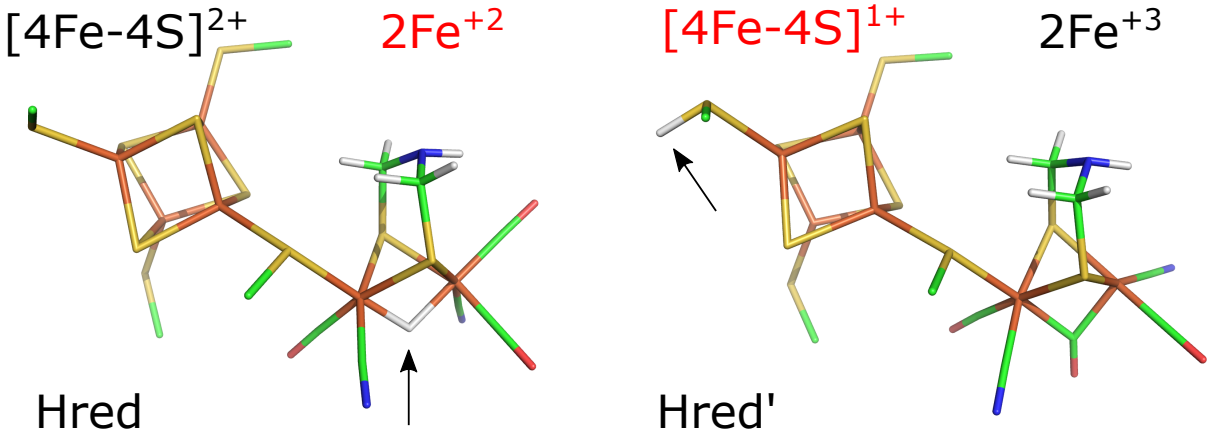

Figure 4.3: Stick representation of cofactor structures obtained by DFT calculations. **Left:** Hred with reduced diiron site (2Fe) and bridging hydride (arrow). **Right:** Hred' with reduced [4Fe-4S] cluster, protonation at the ligating cysteine (arrow), and conserved diiron site geometry.

Proton pathways Exchange of the adt bridge or amino acids that are part of the PTP resulted did not abolish formation of protonated redox states HoxH, Hred' and Hred'H. Therefore the catalytic proton path[17–22] is not involved in [4Fe-4S] cluster protonation. The absence of reduced states that feature a μH (namely Hred and Hsred) in for example cofactor variant pdt enzyme supports the blockage of the PTP.[37] The catalytic pathway seems to be unable to deliver protons to form the μH for stable population of Hred and Hsred at the diiron site. Besides their function in electron transfer [4Fe-4S] clusters are reported to be involved in proton transfer.[80,81] In HydA1 the [4Fe-4S] cluster is exposed to the surrounding bulk.[82] For larger [FeFe]-hydrogenases the [4Fe-4S] cluster of the H-cluster is not located at the surface of the enzymes. Here conserved water molecules form a possible proton pathway from the protein surface to the [4Fe-4S] cluster.[9,47,79] Instead of the catalytic pathway that leads to the apical vacancy at Fe_d most likely this alternative proton pathway, the regulatory pathway, is responsible for [4Fe-4S] cluster protonation (compare Figure: 4.2 on page 77).

4.5 The hydride state Hhyd

Exposure to H_2 at pH 8 lead to population of Hred and Hsred[36] as described in Section 3.5 on page 52. The new band pattern Hhyd observed at pH 4 and under H_2 resembles mostly Htrans in DDH enzyme.[25] However the reversibility of Hhyd population and depopulation upon gas or pH exchange contradicts with this assignment. In contradiction to reduction of the diiron site by H_2 as observed for pH 8 the strongly blue shifted band positions hint to a formally more oxidized diiron site compared to Hox.[76] This super oxidized redox species looks similar to spectra observed for DT treated C169S variant of HydA1. These spectra were computed to originate from a redox state with super oxidized diiron site, reduced [4Fe-4S] cluster and a terminal apical hydride bound at Fe_d.[17,42] Indeed comparison of experimental and DFT calculated spectra confirm this configuration and suggest additionally protonation at cysteine 417(S9) like in Hred' and HoxH. H/D exchange experiments and DFT calculations showed that the μCO band down shifts for deuteride binding.[41,43] The H/D exchange experiments performed reproduce the shift of the μCO ligand band position for native enzyme of HydA1, CpI and DDH. The downshift of the μCO band is due to less intense trans coupling of the Fe-D vibration ad Fe_d with the μCO vibration.[83] Additional measurements on cofactor variant odt of HydA1 and amino acid variants C169A of HydA1 and E279A of CpI confirm this behavior and indicate the apical hydride as a common feature of the hydride state. Acidic pH was not mandatory for Hhyd population for all varied enzymes investigated in contrast to native enzymes. All variations were at locations of the enzymes that are part of the catalytic proton pathway.[16–22] Hindered proton transport from the H-cluster to the enzyme surface after H_2 oxidation is a likely reason for the stabilization of the terminal hydride. Population of Hhyd in native enzyme at low pH is probably due to the increased proton pressure that prevents or slows down efficient release of protons via the PTP. Hhyd formation for dehydration under H_2 atmosphere likely be caused by the same reason.

4.6 Hox-O_2

[FeFe]-hydrogenases are extreamly sensitive to O_2. In native enzyme the H-cluster is destroyed when exposed to oxygen.[23] CO inhibition by former CO ligands released upon disruption is observed probably due to the densely packed enzyme film in the ATR setup. A similar observation, called cannibalization, was made by Albracht et al. for disrupted cofactor upon illumination.[25] In this process released CO ligands are "captured" by still intact cofactors forming Hox-CO. Transiently a band at 2024 cm^{-1} was observed that was in a former study related to oxygen attacking the diiron site.[84] A novel stable IR signature was observed upon exposure to O_2 when the PTP was blocked by C169 variation to alanine (C169A). The novel spectrum exhibits a large blue shift of all bands compared to Hox. A DFT model resembling Hox with a O_2 molecule bound to the apical vacancy at Fe_d could reproduce the spectral features thus the new redox species is named Hox-O_2. The diiron site gets partially oxidized by binding of O_2 giving rise to the observed blue shift.

Lyophilization of HydA1 was reported to protect from O_2 induced cofactor destruction.[85] Interestingly dehydration under H_2 lead to the formation of Hhyd due to inefficient proton transfer as supposed above. This suggests that inefficient proton transfer stabilizes Hox-O_2 by preventing protonation of the O_2 molecule bound. This presumption is further supported since an already protonated hydro-peroxo ligand (OOH) modeled at Fe_d was not reproducing the experimental band pattern. Proton transfer has been reported before to be involved in cofactor destruction by O_2.[86,87] Thereby most likely due to blockage of the PTP in HydA1, the initial step of O_2 binding to the H-cluster could be stabilized and further cofactor destruction was prevented.

4.7 The catalytic cycle

In Table 4.1 all known redox states observed for HydA1 are compared by occupancy of the apical vacancy at Fe_d, Fe-Fe bridging ligand, location of a possible protonation, and oxidation state of diiron site and [4Fe-4S] cluster. For hydrogen turnover the CO inhibited states Hox-CO/ HoxH-CO and Hox-O_2 are not considered. The involvement for the remaining redox states has to be verified.

Table 4.1: Electronic configuration and alternative annotations of different redox states. μH refers to protonation of the diiron site resulting in a bridging hydride ligand and [4Fe-4S] refers to protonation of cysteines that ligate the [4Fe-4S] cluster.

	apical / μ	**protonation**	**[4Fe-4S]**	**diiron site**	**reference**
Hox	open / CO	none	+2	+3	[24,31,32] this work^{I}
HoxH	open / CO	[4Fe-4S]	+2	+3	this work^{IV}
Hred'	open / CO	[4Fe-4S]	+1	+3	[37–39] this work^{VI,VI}
Hred'H	open / CO	2x [4Fe-4S]	+1	+3	this work^{VI,VI}
Hhyd	H / CO	[4Fe-4S]	+1	+4	[41–43] this work^{IV,V}
Hred	CO / H	diiron site	+2	+2	[25,34,38] this work^{VIII}
Hsred	CO / H	diiron site	+1	+2	[36,40] this work^{VIII}
Hox-CO	CN / CO	none	+2	+3	[24,29,44,45] this work^{I}
HoxH-CO	CN / CO	[4Fe-4S]	+2	+3	this work^{IV}
Hox-O_2	O_2 / CO	none	+2	+4	this work^{V}

Catalytic cycle In comparison to Hox the μH geometry for Hred and Hsred disfavors an involvement of the latter in hydrogen turnover. The bridging hydride ligand would have to "flip" twice for one hydrogen turnover cycle. This μH geometry was found to be energetically favored[88] and is for this reason "too stable" to intervene in hydrogen turnover. While for Hred reduction and protonation at the diiron site alternates the cofactor geometry, for Hred' the μCO geometry is conserved by protonation and reduction at the [4Fe-4S] cluster. The mixed valence diiron site is preserved.

In principle, Hred' resembles Hox with one electron stored at the H-cluster and the redox potential difference induced by reduction compensated by protonation at the [4Fe-4S] cluster. The observed redox potential modulation of ca. 50 mV to less reducing potentials

induced by protonation of the [4Fe-4S] cluster may facilitate fast and efficient hydrogen catalysis. In vivo two electrons have to be accepted from an one electron donor, for example ferredoxin.[89,90] Protonation at the [4Fe-4S] cluster can balance its redox potential after the first reduction step to enhance the probability of the second reduction step. The two electron reduced species Hhyd features a μCO ligand and a terminally bound hydride at the apical coordination site of Fe_d. This terminal hydride is already in position to combine with a proton offered by the PTP via the adt bridge. For Hhyd protontion at the [4Fe-4S] cluster was found as well.

Due to the altered cofactor geometry and the stability of the μCO configuration, an involvement of Hred and Hsred in the fast hydrogen evolution cycle of [FeFe]-hydrogenases is hardly probable. Hred' and Hhyd in contrast preserve cofactor geometry and protonation at the [4Fe-4S] cluster levels redox potential.

The catalytic cycle can be wrapped up as in Figure 4.4 on the next page. Starting from Hox in a proton coupled electron transfer (PCET) fashion protonation and reduction of the [4Fe-4S] cluster leads to population of Hred'. The proton bound is not used for catalysis but acts as a regulatory proton at the [4Fe-4S] cluster. In a subsequent PCET step an additional electron and a proton are uptaken to form Hhyd. The proton binds trans to the μCO ligand at the apical vacancy at Fe_d and forms the terminal hydride. With an additional proton offered by the PTP the hydride combines to molecular hydrogen and HoxH is formed since the regulatory proton at the [4Fe-4S] cluster is still bound. Upon release of the regulatory proton Hox is recovered again. Reduction of HoxH should lead directly to Hred' without de- and reprotonation at the [4Fe-4S] cluster but was not observed in experiments. the involvement of Hox and/ or HoxH is under debate.

Formation of Hred is thought to succeed Hred' since electron injection happens via the [4Fe-4S] cluster.[19,89,91,92] For this transition the regulatory proton has to dissociate from the [4Fe-4S] cluster and a catalytic proton delivered by the PTP has to flip in bridging position. The former bridging CO ligand flips in terminal position. The location of the electron changes from [4Fe-4S] cluster to the diiron site. Conversion into Hsred is facilitated by reduction of the [4Fe-4S] cluster. A possible formation of Hhyd with the

terminal, reactive hydride would include again flipping of the bridging hydride species into terminal position and simultaneously reverse flip of the former terminal CO ligand. This process was found to be incompatible with the fast H_2 evolution observed for [FeFe]-hydrogenases.[61,64,93,94]

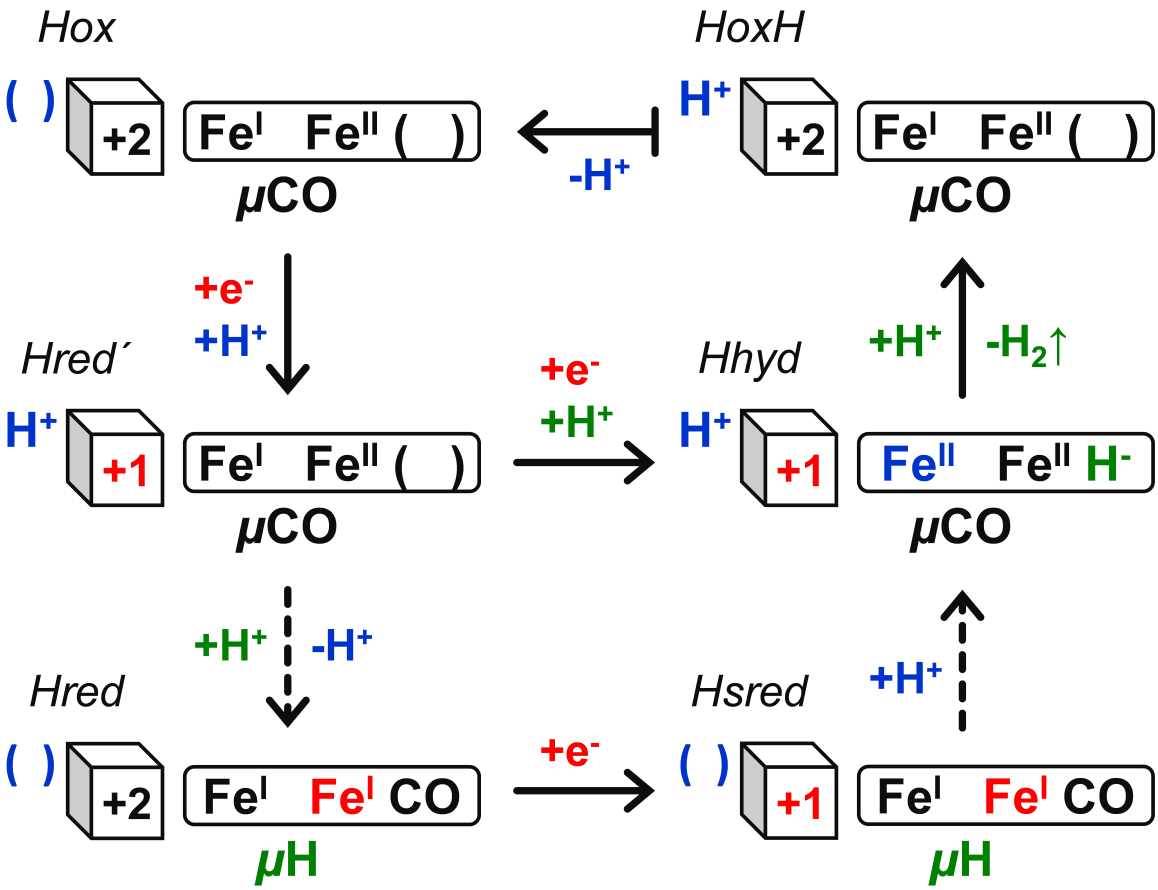

Figure 4.4: Proposed catalytic cycle. Location of reducing electrons are highlighted in red, location of catalytic protons in green and protonation of the [4Fe-4S] cluster by a regulatory proton in blue. Protonation and reduction of Hox (top left) forms Hred' (middle left) with the regulatory proton bound at the reduced [4Fe-4S] cluster. Additional protonation and reduction creates Hhyd (middle right) with the catalytic proton terminally bound as a hydride at Fe_d. Upon addition of another catalytic proton combination with the hydride leads to molecular hydrogen evolution and formation of HoxH (top right). Subsequent release of the regulatory proton recovers Hox. Direct reduction of HoxH to Hred' was not observed in experiments. Dashed arrows from Hred' to Hred (bottom left) and from Hsred (bottom right) to Hhyd indicate t/μ flip of H/CO ligands unfavored for fast catalysis. Figure taken from[VI]

Chapter 5

Conclusion

[FeFe]-hydrogenases catalyze hydrogen turnover with high efficiency. Reaction intermediates, the role of proton- and electron transfer, and the influence of the protein fold on catalysis were investigated. Characterization of [FeFe]-hydrogenases in an ATR-FTIR setup was performed under biologically relevant conditions, i.e. at room temperature, ambient pressure, and in presence of water. A novel aerosol technique exploits sample accessibility and allows observing spectral differences induced by changes in hydration, pH and/ or gas composition. Electrochemical control enables redox titrations superior to former experiments performed in transmission without sample accessibility.[16,36–38]

Several new redox states were identified. A selective enrichment was achieved by disturbing the equilibrium of product/ educt concentrations. For increased levels of reductant and at acidic pH, the educts of H_2 evolution, HoxH could be stabilized^{VI}. Titrations of reductant and pH, amino acid side chain variations and correlation with DFT calculations identified a protonation at cysteine 417 as major difference to Hox. Additional exposure to H_2 lead to the enrichment of Hhyd, a proposed catalytic intermediate featuring a terminal hydride^{IV}. For heterolytic H_2 formation the hydride bound terminal at Fe_d is thought to be mandatory to react with a proton provided from the proton transfer path via the adt group. Before cofactor destruction, an O_2 bound intermediate is trapped in amino acid variant with focus on the proposed catalytic proton transfer path[17–22] and lead to identification of Hox-O_2^{VII}. Insufficient proton transfer to the active side prevents formation of a reactive peroxo species and slows down cofactor degradation. Variation of the adt ligand to pdt was exploited to suppress population of Hred and Hsred and facilitated a direct characterization of Hred' and Hred'H^{VI,VIII}.

A protocol for selective ^{13}CO isotopic cofactor ligand editing in native enzyme that exploits light sensitivity of Fe-carbonyl complexes was developed to discriminate simultaneously populated redox states^{I}. For HydA1 the two reduced states Hred and Hred' were incorrectly assigned as a single state before.[4,17,35–37] Both are reduced by one electron but at different locations either at the diiron site or the [4Fe-4S] cluster. Reduction of enzyme with isotopic edited cofactor gives clear evidence for the spectroscopic separation of these states^{VI}.

Correlation of experimentally observed IR signatures and calculated DFT patterns revealed coupling. Isotopic editing was used to enlarge the experimental data set for correlation. This increased the accuracy of discrimination. Isotopomeres that exhibit characteristic vibrational coupling patterns are strongly dependent of cofactor ligand arrangement and granted structural insight of the cofactor. By this analysis novel structural features for Hox, Hox-CO, Hred, Hsred, Hred' and Hhyd were found not accessible before due to missing sensitivity to protonation and lack of selective, quantitative enrichment of specific redox states in alternative techniques as X-ray crystallography[9,47,79] or EPR spectroscopy.[24,67]

Hred and Hsred were former reported to feature a "semi bridging" CO ligand and have been suggested to be involved in H_2 turnover.[4,17,35–37] In contrast, a bridging hydride geometry was favored by correlation to DFT calculations. Due to the stability of the μH geometry[88] that hinders fast H_2 turnover[61,64,93,94] Hred and Hsred must be considered rather improbable intermediates in H_2 turnover.

Alternative to Hred the second one-electron reduced state Hred' was investigated. As Hred was proposed to be associated with protonation of the diiron site in previous reports,[36–38,46] electrochemical and pH titrations gave evidence for a protonation event involved in formation of Hred' as well[VI,VIII]. Protonation site-selective experiments and DFT calculations suggested cysteine 417 at the [4Fe-4S] cluster as most probable protonation site[VI]. A cofactor geometry that resembles Hox is preserved that favors Hred' as first reduced state in H_2 formation. Electrochemical investigations verified that a protonation step is involved in the transition of Hox to Hred'[VIII]. Analysis of the Hox/ Hred' and HoxH/ Hred'H transition midpoint potentials indicate that the additional protonation in HoxH/ Hred'H modulates the redox potential of the [4Fe-4S] cluster to less reducing potentials. Since two electrons have to be accepted from the one-electron donor ferredoxin in vivo[89,90] redox potential modulation may be necessary for efficient hydrogen turnover.

After all, protonation/ reduction dynamics, structural information and thermodynamic considerations were fused to formulate a reaction cycle for H_2 turnover. It is based on redox states featuring a conserved geometry exclusively, as for Hred' and Hhyd stabilized

by protonation/ reduction dynamics found at the [4Fe-4S] cluster. A second reduction is facilitated by modulation of the redox potential accompanied with this protonation. The μH geometry found for Hred and Hsred disfavors their catalytic relevance concerning stability of this configuration.[93,95,96] In design of synthetic catalysts protonable ligands offer the possibility to avoid μH geometry and to maintain conserved rotated cofactor structure.

To further validate the involvement of redox states in H_2 release sub-turnover time-resolved IR spectroscopy can be applied. First measurements (Appendix Section: B.9 on page 137) prove the feasibility of this approach. Future research on the catalytic cycle of [FeFe]-hydrogenase may focus on the direct observation of the H_2 turnover process alternative to stabilization of possible reaction intermediates.

Bibliography

[1] D. A. King, "Environment - Climate change science: Adapt, mitigate, or ignore?," *Science*, vol. 303, no. 5655, pp. 176–177, 2004.

[2] D. Abbott, "Is Nuclear Power Globally Scalable?," *Proceedings of the Ieee*, vol. 99, no. 10, pp. 1611–1617, 2011.

[3] P. P. Edwards, V. L. Kuznetsov, W. I. F. David, and N. P. Brandon, "Hydrogen and fuel cells: Towards a sustainable energy future," *Energy Policy*, vol. 36, no. 12, pp. 4356–4362, 2008.

[4] W. Lubitz, H. Ogata, O. Rudiger, and E. Reijerse, "Hydrogenases," *Chem Rev*, vol. 114, no. 8, pp. 4081–148, 2014.

[5] A. Volbeda, M. H. Charon, C. Piras, E. C. Hatchikian, M. Frey, and J. C. Fontecilla-camps, "Crystal-Structure of the Nickel-Iron Hydrogenase from Desulfovibrio-Gigas," *Nature*, vol. 373, no. 6515, pp. 580–587, 1995.

[6] S. Shima and U. Ermler, "Structure and Function of [Fe]-Hydrogenase and its Iron-Guanylylpyridinol (FeGP) Cofactor," *European Journal of Inorganic Chemistry*, no. 7, pp. 963–972, 2011.

[7] J. C. Fontecilla-Camps, A. Volbeda, C. Cavazza, and Y. Nicolet, "Structure/function relationships of [NiFe]- and [FeFe]-hydrogenases (vol 107, pg 4273, 2007)," *Chemical Reviews*, vol. 107, no. 11, pp. 5411–5411, 2007.

[8] P. M. Vignais and B. Billoud, "Occurrence, classification, and biological function of hydrogenases: An overview," *Chemical Reviews*, vol. 107, no. 10, pp. 4206–4272, 2007.

[9] J. W. Peters, W. N. Lanzilotta, B. J. Lemon, and L. C. Seefeldt, "X-ray crystal structure of the Fe-only hydrogenase (Cpl) from Clostridium pasteurianum to 1.8 angstrom resolution," *Science*, vol. 282, no. 5395, pp. 1853–1858, 1998.

[10] C. Madden, M. D. Vaughn, I. Diez-Perez, K. A. Brown, P. W. King, D. Gust, A. L. Moore, and T. A. Moore, "Catalytic turnover of [FeFe]-hydrogenase based on single-molecule imaging," *J Am Chem Soc*, vol. 134, no. 3, pp. 1577–82, 2012.

[11] M. Winkler, S. Kawelke, and T. Happe, "Light driven hydrogen production in protein based semi-artificial systems," *Bioresource Technology*, vol. 102, no. 18, pp. 8493–8500, 2011.

[12] K. A. Vincent, A. Parkin, and F. A. Armstrong, "Investigating and exploiting the electrocatalytic properties of hydrogenases," *Chemical Reviews*, vol. 107, no. 10, pp. 4366–4413, 2007.

[13] J. Fritsch, O. Lenz, and B. Friedrich, "Structure, function and biosynthesis of O-2-tolerant hydrogenases," *Nature Reviews Microbiology*, vol. 11, no. 2, pp. 106–114, 2013.

[14] Y. Nicolet, C. Piras, P. Legrand, C. E. Hatchikian, and J. C. Fontecilla-Camps, "Desulfovibrio desulfuricans iron hydrogenase: the structure shows unusual coordination to an active site Fe binuclear center," *Structure with Folding Design*, vol. 7, no. 1, pp. 13–23, 1999.

[15] G. Berggren, A. Adamska, C. Lambertz, T. R. Simmons, J. Esselborn, M. Atta, S. Gambarelli, J. M. Mouesca, E. Reijerse, W. Lubitz, T. Happe, V. Artero, and M. Fontecave, "Biomimetic assembly and activation of [FeFe]-hydrogenases," *Nature*, vol. 499, no. 7456, pp. 66–+, 2013.

[16] A. Silakov, B. Wenk, E. Reijerse, and W. Lubitz, "N-14 HYSCORE investigation of the H-cluster of [FeFe] hydrogenase: evidence for a nitrogen in the dithiol bridge," *Physical Chemistry Chemical Physics*, vol. 11, no. 31, pp. 6592–6599, 2009.

[17] P. Knorzer, A. Silakov, C. E. Foster, F. A. Armstrong, W. Lubitz, and T. Happe, "Importance of the Protein Framework for Catalytic Activity of [FeFe]-Hydrogenases," *Journal of Biological Chemistry*, vol. 287, no. 2, pp. 1489–1499, 2012.

[18] S. Morra, A. Giraudo, G. Di Nardo, P. W. King, G. Gilardi, and F. Valetti, "Site Saturation Mutagenesis Demonstrates a Central Role for Cysteine 298 as Proton Donor to the Catalytic Site in CaHydA [FeFe]-Hydrogenase," *Plos One*, vol. 7, no. 10, 2012.

[19] M. Winkler, J. Esselborn, and T. Happe, "Molecular basis of [FeFe]-hydrogenase function An insight into the complex interplay between protein and catalytic cofactor," *Biochimica Et Biophysica Acta-Bioenergetics*, vol. 1827, no. 8-9, pp. 974–985, 2013.

[20] A. J. Cornish, K. Gartner, H. Yang, J. W. Peters, and E. L. Hegg, "Mechanism of Proton Transfer in [FeFe]-Hydrogenase from Clostridium pasteurianum," *Journal of Biological Chemistry*, vol. 286, no. 44, pp. 38341–38347, 2011.

[21] B. Ginovska-Pangovska, M. H. Ho, J. C. Linehan, Y. H. Cheng, M. Dupuis, S. Raugei, and W. J. Shaw, "Molecular dynamics study of the proposed proton transport pathways in [FeFe]-hydrogenase," *Biochimica Et Biophysica Acta-Bioenergetics*, vol. 1837, no. 1, pp. 131–138, 2014.

[22] A. J. Comish, B. Ginovska, A. Thelen, J. C. S. da Silva, T. A. Soares, S. Raugei, M. Dupuis, W. J. Shaw, and E. L. Hegg, "Single-Amino Acid Modifications Reveal Additional Controls on the Proton Pathway of [FeFe]-Hydrogenase," *Biochemistry*, vol. 55, no. 22, pp. 3165–3173, 2016.

[23] S. T. Stripp, G. Goldet, C. Brandmayr, O. Sanganas, K. A. Vincent, M. Haumann, F. A. Armstrong, and T. Happe, "How oxygen attacks [FeFe] hydrogenases from photosynthetic organisms," *Proc Natl Acad Sci U S A*, vol. 106, no. 41, pp. 17331–6, 2009.

[24] S. P. J. Albracht, W. Roseboom, and E. C. Hatchikian, "The active site of the [FeFe]-hydrogenase from Desulfovibrio desulfuricans. 1. Light sensitivity and magnetic hyperfine interactions as observed by electron paramagnetic resonance," *Journal of Biological Inorganic Chemistry*, vol. 11, no. 1, pp. 88–101, 2006.

[25] W. Roseboom, A. L. De Lacey, V. M. Fernandez, E. C. Hatchikian, and S. P. J. Albracht, "The active site of the [FeFe]-hydrogenase from Desulfovibrio desulfuricans. II. Redox properties, light sensitivity and CO-ligand exchange as observed by infrared spectroscopy," *Journal of Biological Inorganic Chemistry*, vol. 11, no. 1, pp. 102–118, 2006.

[26] J. A. Birrell, K. Wrede, K. Pawlak, P. Rodriguez-Macia, O. Rudiger, E. J. Reijerse, and W. Lubitz, "Artificial Maturation of the Highly Active Heterodimeric [FeFe] Hydrogenase from Desulfovibrio desulfuricans ATCC 7757," *Israel Journal of Chemistry*, vol. 56, no. 9-10, pp. 852–863, 2016.

[27] J. F. Siebel, A. Adamska-Venkatesh, K. Weber, S. Rumpel, E. Reijerse, and W. Lubitz, "Hybrid [FeFe]-Hydrogenases with Modified Active Sites Show Remarkable Residual Enzymatic Activity," *Biochemistry*, vol. 54, no. 7, pp. 1474–1483, 2015.

[28] J. Esselborn, C. Lambertz, A. Adamska-Venkatesh, T. Simmons', G. Berggren, J. Nothl, J. Siebel, A. Hemschemeier, V. Artero, E. Reijerse, M. Fontecave, W. Lubitz, and T. Happe, "Spontaneous activation of [FeFe]-hydrogenases by an inorganic [2Fe] active site mimic," *Nature Chemical Biology*, vol. 9, no. 10, pp. 607–609, 2013.

[29] Y. Nicolet, A. L. de Lacey, X. Vernede, V. M. Fernandez, E. C. Hatchikian, and J. C. Fontecilla-Camps, "Crystallographic and FTIR spectroscopic evidence of changes in Fe coordination upon reduction of the active site of the Fe-only hydrogenase from Desulfovibrio desulfuricans," *Journal of the American Chemical Society*, vol. 123, no. 8, pp. 1596–1601, 2001.

[30] A. S. Pereira, P. Tavares, I. Moura, J. J. G. Moura, and B. H. Huynh, "Mossbauer characterization of the iron-sulfur clusters in Desulfovibrio vulgaris hydrogenase," *Journal of the American Chemical Society*, vol. 123, no. 12, pp. 2771–2782, 2001.

[31] C. Kamp, A. Silakov, M. Winkler, E. J. Reijerse, W. Lubitz, and T. Happe, "Isolation and first EPR characterization of the [FeFe]-hydrogenases from green algae," *Biochimica Et Biophysica Acta-Bioenergetics*, vol. 1777, no. 5, pp. 410–416, 2008.

[32] B. Bennett, B. J. Lemon, and J. W. Peters, "Reversible carbon monoxide binding and inhibition at the active site of the Fe-only hydrogenase," *Biochemistry*, vol. 39, no. 25, pp. 7455–7460, 2000.

[33] T. M. VanderSpek, A. F. Arendsen, R. P. Happe, S. Y. Yun, K. A. Bagley, D. J. Stufkens, W. R. Hagen, and S. P. J. Albracht, "Similarities in the architecture of the active sites of Ni-hydrogenases and Fe-hydrogenases detected by means of infrared spectroscopy," *European Journal of Biochemistry*, vol. 237, no. 3, pp. 629–634, 1996.

[34] A. J. Pierik, M. Hulstein, W. R. Hagen, and S. P. J. Albracht, "A low-spin iron with CN and CO as intrinsic ligands forms the core of the active site in [Fe]-hydrogenases," *European Journal of Biochemistry*, vol. 258, no. 2, pp. 572–578, 1998.

[35] A. Silakov, C. Kamp, E. Reijerse, T. Happe, and W. Lubitz, "Spectroelectrochemical Characterization of the Active Site of the [FeFe] Hydrogenase HydA1 from Chlamydomonas reinhardtii," *Biochemistry*, vol. 48, no. 33, pp. 7780–7786, 2009.

[36] A. Adamska, A. Silakov, C. Lambertz, O. Rudiger, T. Happe, E. Reijerse, and W. Lubitz, "Identification and Characterization of the "Super-Reduced" State of the H-Cluster in [FeFe] Hydrogenase: A New Building Block for the Catalytic Cycle?," *Angewandte Chemie-International Edition*, vol. 51, no. 46, pp. 11458–11462, 2012.

[37] A. Adamska-Venkatesh, D. Krawietz, J. Siebel, K. Weber, T. Happe, E. Reijerse, and W. Lubitz, "New Redox States Observed in [FeFe] Hydrogenases Reveal Redox Coupling Within the H-Cluster," *Journal of the American Chemical Society*, vol. 136, no. 32, pp. 11339–11346, 2014.

[38] C. Sommer, A. Adamska-Venkatesh, K. Pawlak, J. A. Birrell, O. Rudiger, E. J. Reijerse, and W. Lubitz, "Proton Coupled Electronic Rearrangement within the H-Cluster as an Essential Step in the Catalytic Cycle of [FeFe] Hydrogenases," *Journal of the American Chemical Society*, vol. 139, no. 4, pp. 1440–1443, 2017.

[39] S. Katz, J. Noth, M. Horch, H. S. Shafaat, T. Happe, P. Hildebrandt, and I. Zebger, "Vibrational spectroscopy reveals the initial steps of biological hydrogen evolution," *Chemical Science*, vol. 7, no. 11, pp. 6746–6752, 2016.

[40] P. Chernev, C. Lambertz, A. Brunje, N. Leidel, K. G. V. Sigfridsson, R. Kositzki, C. H. Hsieh, S. L. Yao, R. Schiwon, M. Driess, C. Limberg, T. Happe, and M. Haumann, "Hydride Binding to the Active Site of [FeFe]-Hydrogenase," *Inorganic Chemistry*, vol. 53, no. 22, pp. 12164–12177, 2014.

[41] D. W. Mulder, M. W. Ratzloff, M. Bruschi, C. Greco, E. Koonce, J. W. Peters, and P. W. King, "Investigations on the Role of Proton-Coupled Electron Transfer in Hydrogen Activation by [FeFe]-Hydrogenase," *Journal of the American Chemical Society*, vol. 136, no. 43, pp. 15394–15402, 2014.

[42] D. W. Mulder, Y. S. Guo, M. W. Ratzloff, and P. W. King, "Identification of a Catalytic Iron-Hydride at the H-Cluster of [FeFe]-Hydrogenase," *Journal of the American Chemical Society*, vol. 139, no. 1, pp. 83–86, 2017.

[43] E. J. Reijerse, C. C. Pham, V. Pelmenschikov, R. Gilbert-Wilson, A. Adamska-Venkatesh, J. F. Siebel, L. B. Gee, Y. Yoda, K. Tamasaku, W. Lubitz, T. B. Rauchfuss, and S. P. Cramer, "Direct Observation of an Iron-Bound Terminal Hydride in [FeFe]-Hydrogenase by Nuclear Resonance Vibrational Spectroscopy," *Journal of the American Chemical Society*, vol. 139, no. 12, pp. 4306–4309, 2017.

[44] A. L. De Lacey, C. Stadler, C. Cavazza, E. C. Hatchikian, and V. M. Fernandez, "FTIR characterization of the active site of the Fe-hydrogenase from Desulfovibrio desulfuricans," *Journal of the American Chemical Society*, vol. 122, no. 45, pp. 11232–11233, 2000.

[45] Z. J. Chen, B. J. Lemon, S. Huang, D. J. Swartz, J. W. Peters, and K. A. Bagley, "Infrared studies of the CO-inhibited form of the Fe-only hydrogenase from Clostridium pasteurianum I: Examination of its light sensitivity at cryogenic temperatures," *Biochemistry*, vol. 41, no. 6, pp. 2036–2043, 2002.

[46] P. Rodriguez-Macia, K. Pawlak, O. Rudiger, E. J. Reijerse, W. Lubitz, and J. A. Birrell, "Inter-cluster Redox Coupling Influences Protonation at the H-cluster in [FeFe] Hydrogenases," *J Am Chem Soc*, 2017.

[47] J. Esselborn, N. Muraki, K. Klein, V. Engelbrecht, N. Metzler-Nolte, U. P. Apfel, E. Hofmann, G. Kurisu, and T. Happe, "A structural view of synthetic cofactor integration into [FeFe]-hydrogenases," *Chemical Science*, vol. 7, no. 2, pp. 959–968, 2016.

[48] W. Demtröder, *Experimentalphysik 3: Atome, Moleküle und Festkörper*. Springer, 2005.

[49] J. P. Dahl and M. Springborg, "The Morse Oscillator in Position-Space, Momentum Space, and Phase-Space," *Journal of Chemical Physics*, vol. 88, no. 7, pp. 4535–4547, 1988.

[50] A. Barth, "Infrared spectroscopy of proteins," *Biochimica Et Biophysica Acta-Bioenergetics*, vol. 1767, no. 9, pp. 1073–1101, 2007.

[51] P. R. Griffiths and J. A. de Haseth, *Introduction to Vibrational Spectroscopy*, pp. 1–18. 2006.

[52] N. J. Harrick, "Total Internal Reflection and Its Application to Surface Studies," *Annals of the New York Academy of Sciences*, vol. 101, no. 3, p. 928, 1963.

[53] J. Fahrenfort, "Attenuated Total Reflection - a New Principle for the Production of Useful Infra-Red Reflection Spectra of Organic Compounds," *Spectrochimica Acta*, vol. 17, no. 7, p. 698, 1961.

[54] D. Moss, E. Nabedryk, J. Breton, and W. Mantele, "Redox-Linked Conformational-Changes in Proteins Detected by a Combination of Infrared-Spectroscopy and Protein Electrochemistry - Evaluation of the Technique with Cytochrome-C," *European Journal of Biochemistry*, vol. 187, no. 3, pp. 565–572, 1990.

[55] W. Kohn, "Nobel Lecture: Electronic structure of matter-wave functions and density functionals," *Reviews of Modern Physics*, vol. 71, no. 5, pp. 1253–1266, 1999.

[56] E. C. Hatchikian, N. Forget, V. M. Fernandez, R. Williams, and R. Cammack, "Further Characterization of the [Fe]-Hydrogenase from Desulfovibrio-Desulfuricans Atcc-7757," *European Journal of Biochemistry*, vol. 209, no. 1, pp. 357–365, 1992.

[57] A. Bouhekka and T. Burgi, "In situ ATR-IR spectroscopy study of adsorbed protein: Visible light denaturation of bovine serum albumin on TiO2," *Applied Surface Science*, vol. 261, pp. 369–374, 2012.

[58] J. Noth, J. Esselborn, J. Guldenhaupt, A. Brunje, A. Sawyer, U. P. Apfel, K. Gerwert, E. Hofmann, M. Winkler, and T. Happe, "[FeFe]-Hydrogenase with Chalcogenide Substitutions at the H-Cluster Maintains Full H-2 Evolution Activity," *Angewandte Chemie-International Edition*, vol. 55, no. 29, pp. 8396–8400, 2016.

[59] B. J. Lemon and J. W. Peters, "Binding of exogenously added carbon monoxide at the active site of the iron-only hydrogenase (CpI) from Clostridium pasteurianum," *Biochemistry*, vol. 38, no. 40, pp. 12969–12973, 1999.

[60] C. Lambertz, P. Chernev, K. Klingan, N. Leidel, K. G. V. Sigfridsson, T. Happe, and M. Haumann, "Electronic and molecular structures of the active-site H-cluster in [FeFe]-hydrogenase determined by site-selective X-ray spectroscopy and quantum chemical calculations," *Chemical Science*, vol. 5, no. 3, pp. 1187–1203, 2014.

[61] V. Fourmond, C. Greco, K. Sybirna, C. Baffert, P. H. Wang, P. Ezanno, M. Montefiori, M. Bruschi, I. Meynial-Salles, P. Soucaille, J. Blumberger, H. Bottin, L. De Gioia, and C. Leger, "The oxidative inactivation of FeFe hydrogenase reveals the flexibility of the H-cluster," *Nature Chemistry*, vol. 6, no. 4, pp. 336–342, 2014.

[62] D. W. Mulder, M. W. Ratzloff, E. M. Shepard, A. S. Byer, S. M. Noone, J. W. Peters, J. B. Broderick, and P. W. King, "EPR and FTIR Analysis of the Mechanism of H-2 Activation by [FeFe]-Hydrogenase HydA1 from Chlamydomonas reinhardtii," *Journal of the American Chemical Society*, vol. 135, no. 18, pp. 6921–6929, 2013.

[63] J. M. Kuchenreuther, S. J. George, C. S. Grady-Smith, S. P. Cramer, and J. R. Swartz, "Cell-free H-cluster Synthesis and [FeFe] Hydrogenase Activation: All Five CO and CN-Ligands Derive from Tyrosine," *Plos One*, vol. 6, no. 5, 2011.

[64] C. Greco, M. Bruschi, L. De Gioia, and U. Ryde, "A QM/MM investigation of the activation and catalytic mechanism of Fe-only hydrogenases," *Inorganic Chemistry*, vol. 46, no. 15, pp. 5911–5921, 2007.

[65] R. Gilbert-Wilson, J. F. Siebel, A. Adamska-Venkatesh, C. C. Pham, E. Reijerse, H. X. Wang, S. P. Cramer, W. Lubitz, and T. B. Rauchfuss, "Spectroscopic Investigations of [FeFe] Hydrogenase Maturated with [Fe-57(2)(adt)(CN)(2)(CO)(4)](2-)," *Journal of the American Chemical Society*, vol. 137, no. 28, pp. 8998–9005, 2015.

[66] A. Adamska-Venkatesh, S. Roy, J. F. Siebel, T. R. Simmons, M. Fontecave, V. Artero, E. Reijerse, and W. Lubitz, "Spectroscopic Characterization of the Bridging Amine in the Active Site of [FeFe] Hydrogenase Using lsotopologues of the H-Cluster," *Journal of the American Chemical Society*, vol. 137, no. 40, pp. 12744–12747, 2015.

[67] A. Adamska-Venkatesh, T. R. Simmons, J. F. Siebel, V. Artero, M. Fontecave, E. Reijerse, and W. Lubitz, "Artificially maturated [FeFe] hydrogenase from Chlamydomonas reinhardtii: a HYSCORE and ENDOR study of a non-natural H-cluster," *Physical Chemistry Chemical Physics*, vol. 17, no. 7, pp. 5421–5430, 2015.

[68] L. Yu, C. Greco, M. Bruschi, U. Ryde, L. De Gioia, and M. Reiheet, "Targeting Intermediates of [FeFe]-Hydrogenase by CO and CN Vibrational Signatures," *Inorganic Chemistry*, vol. 50, no. 9, pp. 3888–3900, 2011.

[69] S. Zilberman, E. I. Stiefel, M. H. Cohen, and R. Car, "Resolving the CO/CN ligand arrangement in CO-inactivated [FeFe] hydrogenase by first principles density functional theory calculations," *Inorganic Chemistry*, vol. 45, no. 15, pp. 5715–5717, 2006.

[70] M. Bruschi, C. Greco, M. Kaukonen, P. Fantucci, U. Ryde, and L. De Gioia, "Influence of the [2Fe](H) Subcluster Environment on the Properties of Key Intermediates in the Catalytic Cycle of [FeFe] Hydrogenases: Hints for the Rational Design of Synthetic Catalysts," *Angewandte Chemie-International Edition*, vol. 48, no. 19, pp. 3503–3506, 2009.

[71] A. Silakov, E. J. Reijerse, S. P. J. Albracht, E. C. Hatchikian, and W. Lubitz, "The electronic structure of the H-cluster in the [FeFe]-hydrogenase from Desulfovibrio desulfuricans: A Q-band Fe-57-ENDOR and HYSCORE study," *Journal of the American Chemical Society*, vol. 129, no. 37, pp. 11447–11458, 2007.

[72] T. B. Rauchfuss, "Diiron Azadithiolates as Models for the [FeFe]-Hydrogenase Active Site and Paradigm for the Role of the Second Coordination Sphere," *Accounts of Chemical Research*, vol. 48, no. 7, pp. 2107–2116, 2015.

[73] N. Leidel, P. Chernev, K. G. V. Havelius, L. Schwartz, S. Ott, and M. Haumann, "Electronic Structure of an [FeFe] Hydrogenase Model Complex in Solution Revealed by X-ray Absorption Spectroscopy Using Narrow-Band Emission Detection," *Journal of the American Chemical Society*, vol. 134, no. 34, pp. 14142–14157, 2012.

[74] R. D. Bethel, D. J. Crouthers, C. H. Hsieh, J. A. Denny, M. B. Hall, and M. Y. Darensbourg, "Regioselectivity in Ligand Substitution Reactions on Diiron Complexes Governed by Nucleophilic and Electrophilic Ligand Properties," *Inorganic Chemistry*, vol. 54, no. 7, pp. 3523–3535, 2015.

[75] B. E. Barton, G. Zampella, A. K. Justice, L. De Gioia, T. B. Rauchfuss, and S. R. Wilson, "Isomerization of the hydride complexes [HFe2(SR)(2)(PR3)(x)(CO)(6-x)](+) (x=2, 3, 4) relevant to the active site models for the [FeFe]-hydrogenases," *Dalton Transactions*, vol. 39, no. 12, pp. 3011–3019, 2010.

[76] S. Pons, M. Datta, J. F. Mcaleer, and A. S. Hinman, "Infrared Spectroelectrochemistry of the Fe(Cn)6(4-)/Fe(Cn)6(3-) Redox System," *Journal of Electroanalytical Chemistry*, vol. 160, no. 1-2, pp. 369–376, 1984.

[77] J. O. Alben, G. H. Bare, and P. A. Bromberg, "Sulfhydryl Groups as a New Molecular Probe at Alpha1 Beta1 Interface in Hemoglobin Using Fourier-Transform Infrared Spectroscopy," *Nature*, vol. 252, no. 5485, pp. 736–738, 1974.

[78] T. Happe and J. D. Naber, "Isolation, Characterization and N-Terminal Amino-Acid-Sequence of Hydrogenase from the Green-Alga Chlamydomonas-Reinhardtii," *European Journal of Biochemistry*, vol. 214, no. 2, pp. 475–481, 1993.

[79] A. S. Pandey, T. V. Harris, L. J. Giles, J. W. Peters, and R. K. Szilagyi, "Dithiomethylether as a ligand in the hydrogenase H-cluster," *Journal of the American Chemical Society*, vol. 130, no. 13, pp. 4533–4540, 2008.

[80] H. Beinert, R. H. Holm, and E. Munck, "Iron-sulfur clusters: Nature's modular, multipurpose structures," *Science*, vol. 277, no. 5326, pp. 653–659, 1997.

[81] C. T. Saouma, W. D. Morris, J. W. Darcy, and J. M. Mayer, "Protonation and Proton-Coupled Electron Transfer at S-Ligated [4Fe-4S] Clusters," *Chemistry-a European Journal*, vol. 21, no. 25, pp. 9256–9260, 2015.

[82] D. W. Mulder, E. S. Boyd, R. Sarma, R. K. Lange, J. A. Endrizzi, J. B. Broderick, and J. W. Peters, "Stepwise [FeFe]-hydrogenase H-cluster assembly revealed in the structure of HydA(Delta EFG)," *Nature*, vol. 465, no. 7295, pp. 248–U143, 2010.

[83] H. D. Kaesz and R. B. Saillant, "Hydride Complexes of Transition-Metals," *Chemical Reviews*, vol. 72, no. 3, p. 231, 1972.

[84] K. D. Swanson, M. W. Ratzloff, D. W. Mulder, J. H. Artz, S. Ghose, A. Hoffman, S. White, O. A. Zadvornyy, J. B. Broderick, B. Bothner, P. W. King, and J. W. Peters, "[FeFe]-Hydrogenase Oxygen Inactivation Is Initiated at the H Cluster 2Fe Subcluster," *Journal of the American Chemical Society*, vol. 137, no. 5, pp. 1809–1816, 2015.

[85] J. Noth, R. Kositzki, K. Klein, M. Winkler, M. Haumann, and T. Happe, "Lyophilization protects [FeFe]-hydrogenases against O-2-induced H-cluster degradation," *Scientific Reports*, vol. 5, 2015.

[86] M. K. Bruska, M. T. Stiebritz, and M. Reiher, "Regioselectivity of H Cluster Oxidation," *Journal of the American Chemical Society*, vol. 133, no. 50, pp. 20588–20603, 2011.

[87] A. Kubas, C. Orain, D. De Sancho, L. Saujet, M. Sensi, C. Gauquelin, I. Meynial-Salles, P. Soucaille, H. Bottin, C. Baffert, V. Fourmond, R. B. Best, J. Blumberger, and C. Leger, "Mechanism of O-2 diffusion and reduction in FeFe hydrogenases," *Nature Chemistry*, vol. 9, no. 1, pp. 88–95, 2017.

[88] D. Schilter, J. M. Camara, M. T. Huynh, S. Hammes-Schiffer, and T. B. Rauchfuss, "Hydrogenase Enzymes and Their Synthetic Models: The Role of Metal Hydrides," *Chemical Reviews*, vol. 116, no. 15, pp. 8693–8749, 2016.

[89] M. Winkler, A. Hemschemeier, J. Jacobs, S. Stripp, and T. Happe, "Multiple ferredoxin isoforms in Chlamydomonas reinhardtii - Their role under stress conditions and biotechnological implications," *European Journal of Cell Biology*, vol. 89, no. 12, pp. 998–1004, 2010.

[90] K. Fukuyama, "Structure and function of plant-type ferredoxins," *Photosynthesis Research*, vol. 81, no. 3, pp. 289–301, 2004.

[91] C. H. Chang, P. W. King, M. L. Ghirardi, and K. Kim, "Atomic resolution Modeling of the ferredoxin :[FeFe] hydrogenase complex from Chlamydomonas reinhardtii," *Biophysical Journal*, vol. 93, no. 9, pp. 3034–3045, 2007.

[92] A. Sawyer and M. Winkler, "Evolution of Chlamydomonas reinhardtii ferredoxins and their interactions with [FeFe]-hydrogenases," *Photosynth Res*, 2017.

[93] G. Filippi, F. Arrigoni, L. Bertini, L. De Gioia, and G. Zampella, "DFT Dissection of the Reduction Step in H-2 Catalytic Production by [FeFe]-Hydrogenase-Inspired Models: Can the Bridging Hydride Become More Reactive Than the Terminal Isomer?," *Inorganic Chemistry*, vol. 54, no. 19, pp. 9529–9542, 2015.

[94] V. Hajj, C. Baffert, K. Sybirna, I. Meynial-Salles, P. Soucaille, H. Bottin, V. Fourmond, and C. Leger, "FeFe hydrogenase reductive inactivation and implication for catalysis," *Energy and Environmental Science*, vol. 7, no. 2, pp. 715–719, 2014.

[95] G. Zampella, P. Fantucci, and L. De Gioia, "Unveiling How Stereoelectronic Factors Affect Kinetics and Thermodynamics of Protonation Regiochemistry in [FeFe] Hydrogenase Synthetic Models: A DFT Investigation," *Journal of the American Chemical Society*, vol. 131, no. 31, pp. 10909–10917, 2009.

[96] A. Jablonskyte, L. R. Webster, T. R. Simmons, J. A. Wright, and C. J. Pickett, "Electronic Control of the Protonation Rates of Fe-Fe Bonds," *Journal of the American Chemical Society*, vol. 136, no. 37, pp. 13038–13044, 2014.

Anhang A

Selbstständigkeitserklärung

Hiermit versichere ich für diese Dissertation mit dem Titel:

Protonation and Reduction Dynamics in [FeFe]-Hydrogenases

alle Hilfsmittel und Hilfen angegeben zu haben und auf dieser Grundlage die Arbeit selbstständig verfasst zu haben. Ich versichere, dass diese Arbeit nicht schon einmal in einem früheren Promotionsverfahren angenommen oder als ungenügend beurteilt wurde.

Moritz Senger

Appendix B

Supporting Information

B.1 Isotopic editing

Exemplary transitions monitored in real time ATR-FTIR within the isotopic editing reaction cycle are shown here to further illustrate their character. First the transitions under ^{13}CO atmosphere in the dark(Figure: B.1 (i)), under red light illumination(Figure: B.1 (ii)) and blue light illumination(Figure: B.1 (iii)) are displayed(Figure: 3.10(i, ii, iii)). These spectra monitor the stepwise replacement of first d_2CO(Figure: B.1 (i)) than d_1CO(Figure: B.1 (ii)) and finally μCO(Figure: B.1 (iii)). The same transitions under ^{12}CO atmosphere(Figure: B.1 (i-iii)) shows the re exchange from distal CO to μCO by ^{12}CO that leads to the initial starting point of unlabeled Hox-CO(Figure: 3.10(iv, v, vi)). Exchange of pCO is presented in two different ways(Figure: 3.10(vii, viii)). Either replacement of μCO and pCO at the same time(Figure: B.1 (vii)) or exclusive replacement of pCO(Figure: B.1 (viii)). Note that for these transitions an increased hydration level is mandatory. Further more a transition from Hox-CO to Hox under N_2 atmosphere is displayed in Figure: B.1 (ix).

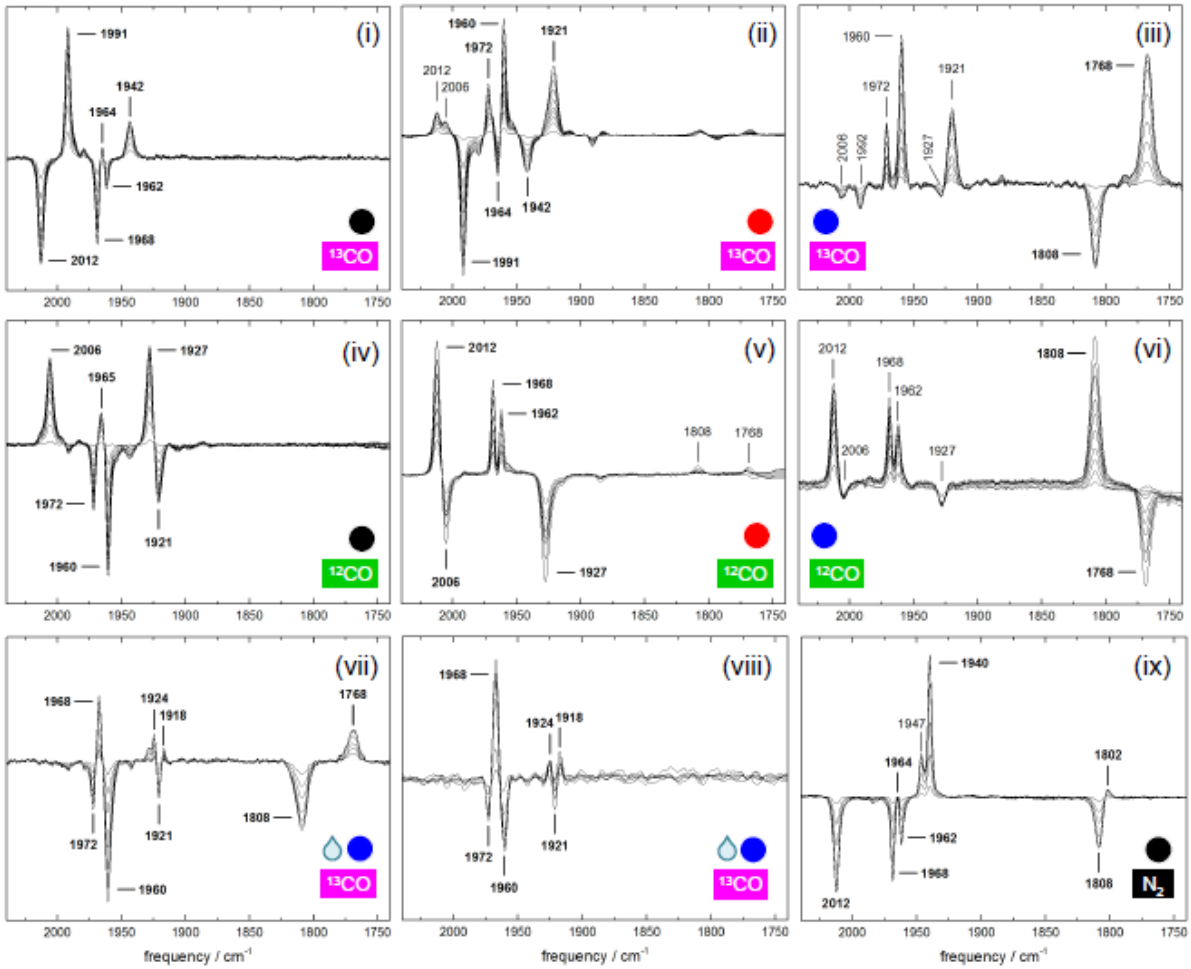

Figure B.1: **(i)** Transition of H_{ox}-CO(12121212) to H_{ox}-CO(12121213) exposed to 100mbar ^{13}CO in the dark. Every spectrum represents 10 seconds. **(ii)** Transition of H_{ox}-CO(12121213) to H_{ox}-CO(12121313) exposed to 100mbar ^{13}CO with red light illumination(640 nm). Every spectrum represents 300 seconds. **(iii)** Transition of H_{ox}-CO(12131313) to H_{ox}-CO(12121313) exposed to 100mbar ^{13}CO with blue light illumination(470 nm). Bands that arise from transition ii increase still due to slight drying of the film.The actual transition manifests in the 1808/1768 cm^{-1} difference band of μCO that has a $\sim$ 5 times smaller extiction coefficient than dCO. Every spectrum represents 60 seconds. **(iv)** Transition of H_{ox}-CO(12131313) to H_{ox}-CO(12131312) exposed to 100mbar ^{12}CO in the dark. Every spectrum represents 10 seconds. **(v)** Transition of H_{ox}-CO(12131312) to H_{ox}-CO(12121212) exposed to 100mbar ^{12}CO with red light illumination(640 nm). Every spectrum represents 300 seconds. **(vi)** Transition of H_{ox}-CO(12131212) to H_{ox}-CO(12121212) exposed to 100mbar ^{13}CO with blue light illumination(470 nm). Bands that arise from transition v increase still due to slight drying of the film.The actual transition manifests in the 1808/1768 cm^{-1} difference band of μCO that has a $\sim$ 5 times smaller extinction coefficient than dCO. Every spectrum represents 60 seconds. **(vii)** Transition of H_{ox}-CO(12121313) to H_{ox}-CO(13131313) exposed to 100mbar ^{13}CO with blue light illumination(470 nm). In this transition the hydration level of the enzyme film was increased. Every spectrum represents 60 seconds. **(viii)** Transition of H_{ox}-CO(12131313) to H_{ox}-CO(13131313) exposed to 100mbar ^{13}CO with blue light illumination(470 nm). In this transition the hydration level of the enzyme film was increased. Every spectrum represents 60 seconds. **(ix)** Transition of H_{ox}-CO(12121212) to H_{ox}(121212) purged with 1 L/min N_2 gas in the dark. This transition took $\sim$ 1 hour. Figure taken from[I]

B.2 pH

Figure B.2: Difference spectra of the Hox to HoxH transition for: **top** CPIadt from *Clostridium pasteurianum* **bottom** DDH from *Desulvovibrio desulfuricans*. Figure taken from[IV]

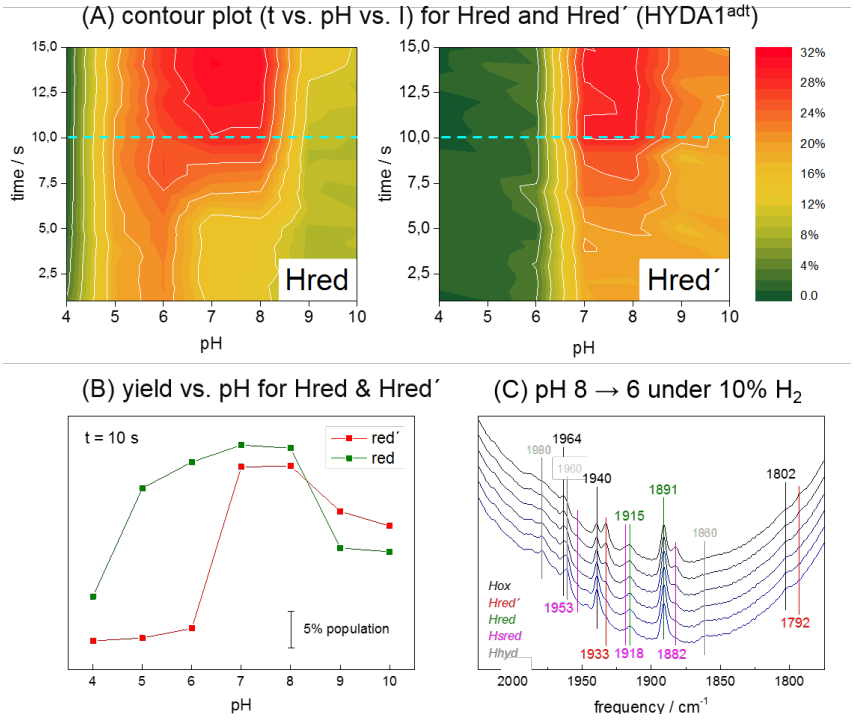

Figure B.3: pH dependence of Hred and Hred'. **(A)** Contour plots that track the formation of Hred (left) and Hred' (right) for different pH upon H_2 exposure. Hred forms predominantly at acidic pH below 7 while Hred' forms at more alkalic pH. **(B)** Yield vs. pH for Hred and Hred'. Up to pH 7.0 nearly no Hred' formation is observed. Hred formation drops at pH 8. **(C)** Absorption spectra of the transition shown in Figure 3.19. Hox (black), Hhyd (gray) and Hred (green) get populated while Hred' (red) and Hsred (magenta) get depopulated. Note the that the 1792 cm^{-1} band correlates with the 1933 cm^{-1} and not with the 1891 cm^{-1} band. Figure taken from[IV]

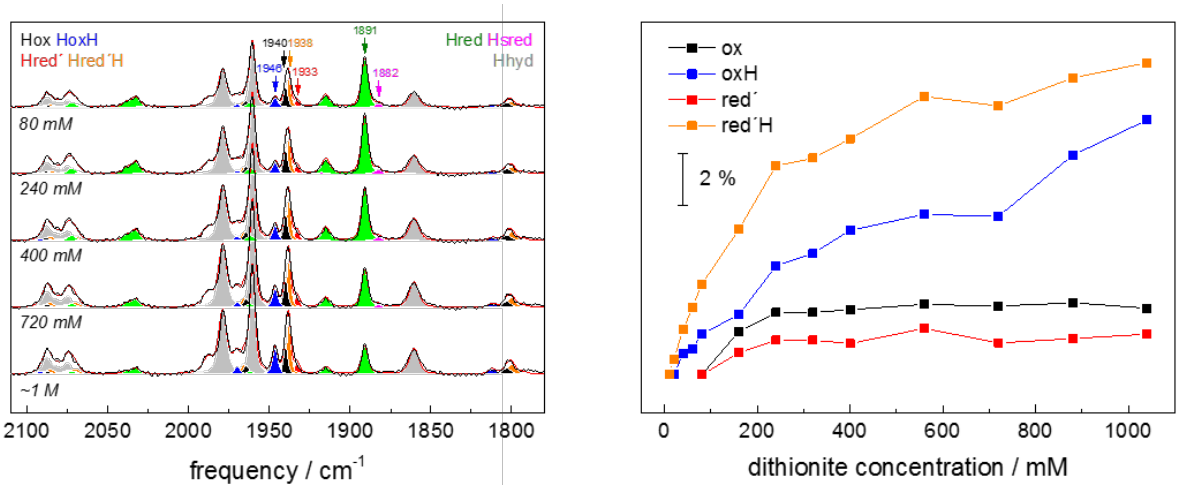

Figure B.4: Hred'H observed in HydA1adt during a DT titration. Hred'H gets populated for increasing DT concentrations. The simultanous population of Hhyd (gray), Hred (green), Hsred (magenta), Hox (black), HoxH (blue)and Hred' (red) complicated the direct observation of Hred'H (orange). Figure taken from[IV]

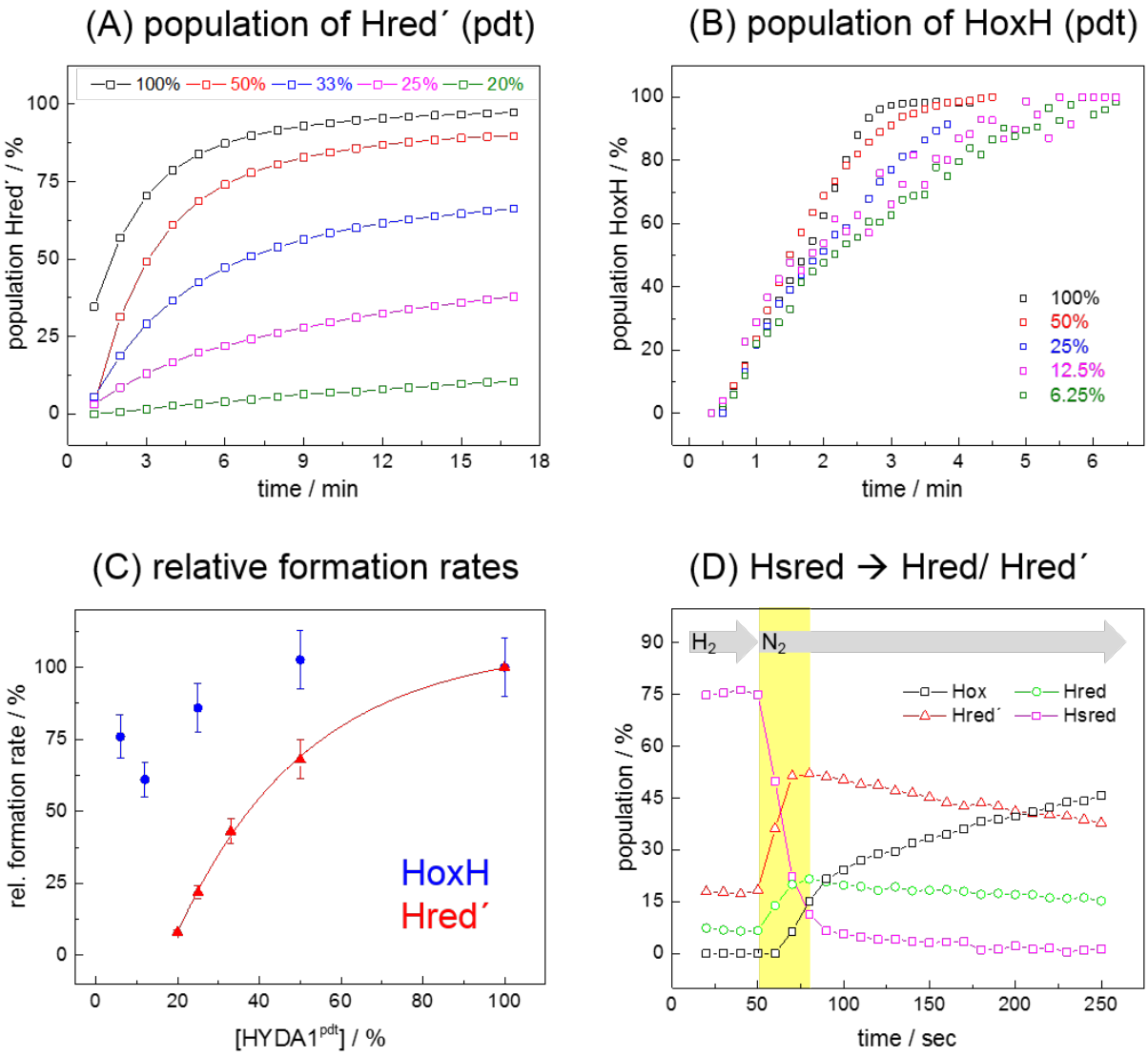

Figure B.5: Intermolecular electron transfer. **(A)** Population of Hred' in HydA1pdt in dependence of dilution by BSA. Formation rate and absolute population decreases with increasing dilution. **(B)** Population of HoxH in HydA1pdt in dependence of dilution by BSA. The absolute population of HoxH remains unaffected and the formation rate drops slightly. **(C)** Comparison of formation rates for HoxH (blue) and Hred' (red) population in dependence of dilution with BSA. The HoxH formation rate is only minor affected while the Hred' formation rate decreases. Below 20% Hyda1pdt concentration no Hred' formation was observed. **(D)** Inter molecular electron transfer in HydA1adt. H_2 atmosphere is exchanged to N_2 and the relative populations of redox states are tracked. Hsred (magenta) depopulates first while Hred (green), Hred' (red) and Hox (black) get populated (yellow area). subsequent Hred and Hred' get depopulated in favor of Hox. Figure taken from[IV]

B.3 Hred and Hsred

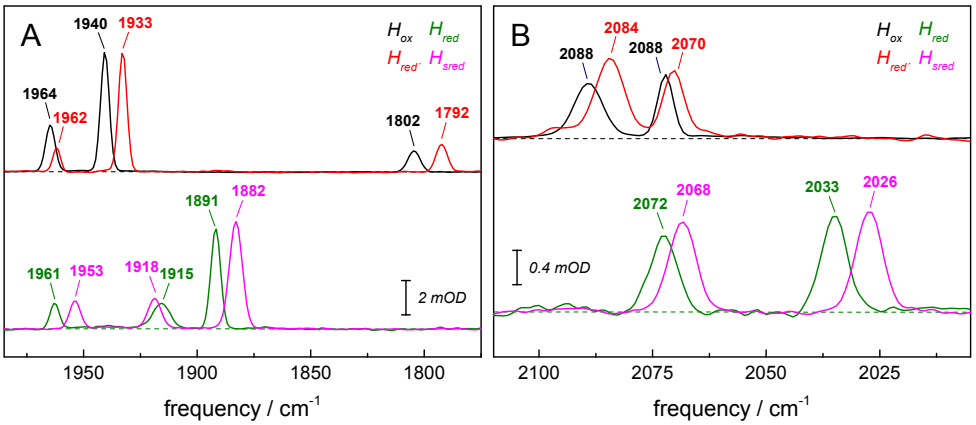

Figure B.6: IR absorption spectra of Hox, Hred', Hred and Hsred. **A** Top: CO band region of Hox (black) and Hred' (red) compared to Hred (green) and Hsred (magenta). Down shift of the dCO ligand upon reduction of the diiiron site and up shift of former μCO ligand band is observed for Hred and Hsred (bottom spectra). **B** CN band region that displays the general down shift of CN bands and the increasing band position difference for Hred and Hsred. Figure taken from[VIII]

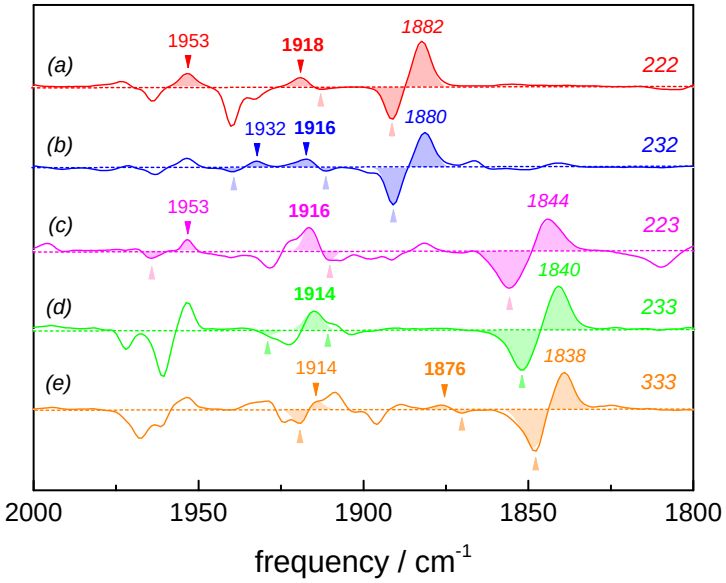

Figure B.7: IR difference spectra of Hsred for ^{13}CO edited isotopameres. The order of numbers reports on the labeling pattern starting from pCO, μCO to dCO (2 stands for ^{12}CO and 3 for ^{13}CO). CN ligand bands were unaffected by CO ligand editing. **(a)** Hsred for unaltered enzyme with bands at 1953 cm^{-1}, 1918 cm^{-1} and 1882 cm^{-1}. **(b)** Hsred for enzyme with substituted μCO ligand(1932 cm^{-1}, 1916 cm^{-1} and 1880 cm^{-1}). **(c)** Hsred for enzyme with replaced dCO ligand (1953 cm^{-1}, 1916 cm^{-1} and 1844 cm^{-1}). **(d)** Hsred for enzyme with μCO and dCO exchanged for ^{13}CO (1922 cm^{-1}, 1914 cm^{-1} and 1840 cm^{-1}) **(e)** Hsred for completely ^{13}CO edited enzyme with bands at 1914 cm^{-1}, 1876 cm^{-1} and 1838 cm^{-1}. Figure taken from[VIII]

B.4 Hydride State

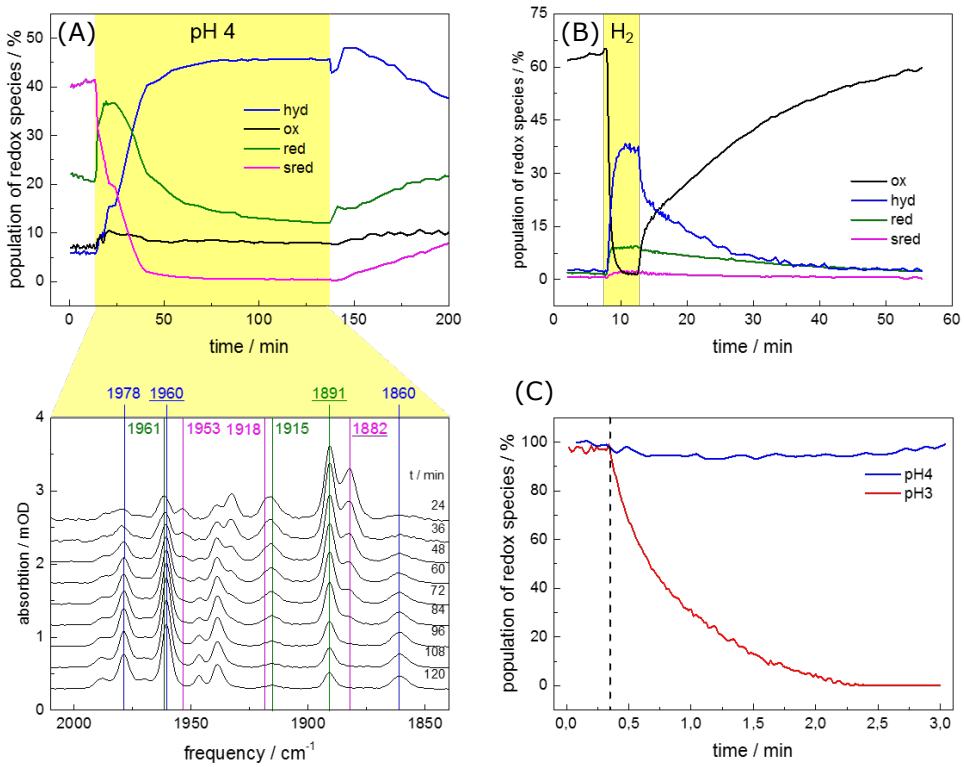

Figure B.8: **(A)** Reversible Hhyd formation on expense of Hsred induced by acidification (yellow region). Top: Respective redox state populations. Bottom: Spectra monitoring the changes. **(B)** Reversible Hhyd formation on expense of Hox induced by carrier gas exchange. N_2 is replaced by H_2 (yellow region) and Hhyd is populated. Under N_2 Hox populates again. **(C)** Normalized cofactor band area over time. At pH 4 the cofactor bands remain constant while at pH 3 the cofactor bands are lost. Figure taken from[VII]

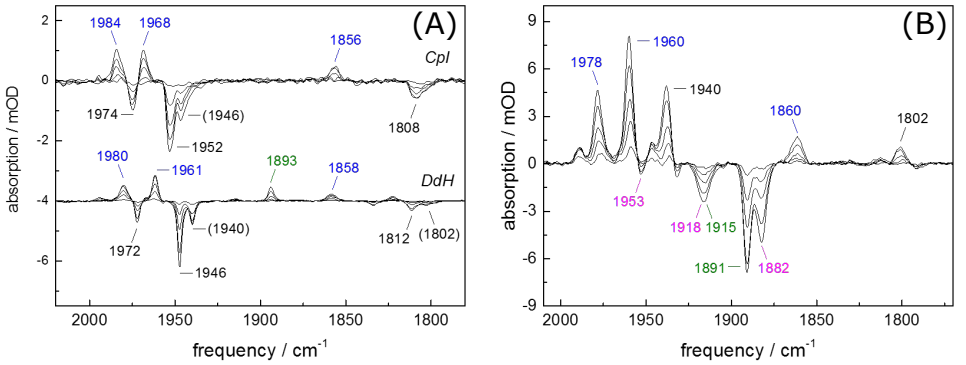

Figure B.9: **(A)** Hydride state formation upon H_2 exposure under acidic conditions for CpI (top) and DdH (bottom). Band positions are slightly shifted with respect to HydA1. **(B)** Difference spectra that show Hhyd formation upon dehydration under H_2 atmosphere. Negative bands for Hred (green) and Hsred (magenta) represent depopulation while positive bands for Hhyd (blue) and Hox (black) stand for redox state enrichment. Figure taken from[VII]

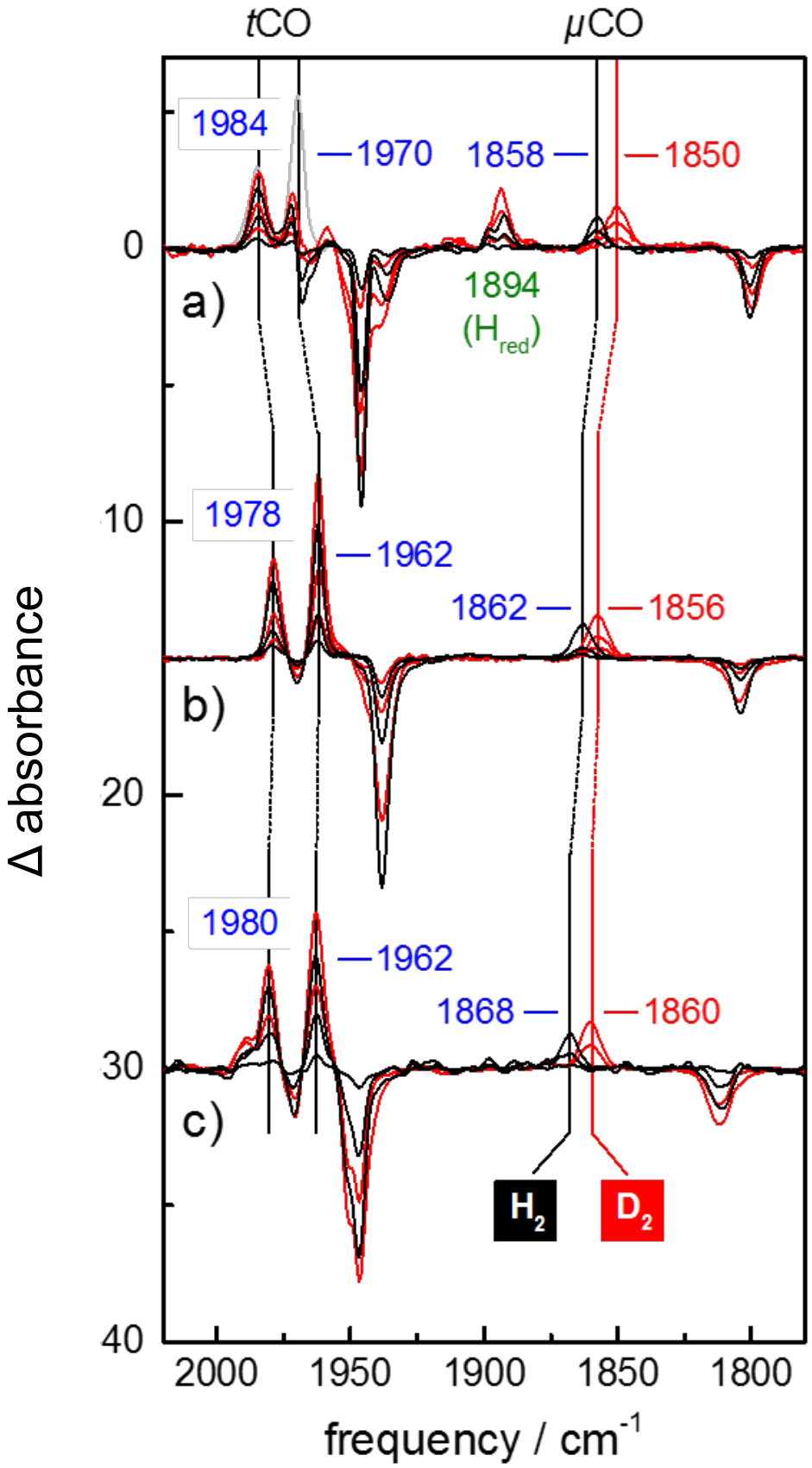

Figure B.10: Hydride state formation upon H_2 exposure under acidic conditions for proton path variant E279A from CpI (**a**), C169A from HydA1 (**b**) and cofactor variant odt from HydA1 (**c**). Band positions are slightly shifted with respect to native HydA1. In red the respective transition induced by D_2 are shown. For all variants the characteristic down shift of μCO due to trans coupling with the apical hydride (deuteride) is observed. Figure taken from[VII]

B.5 DFT

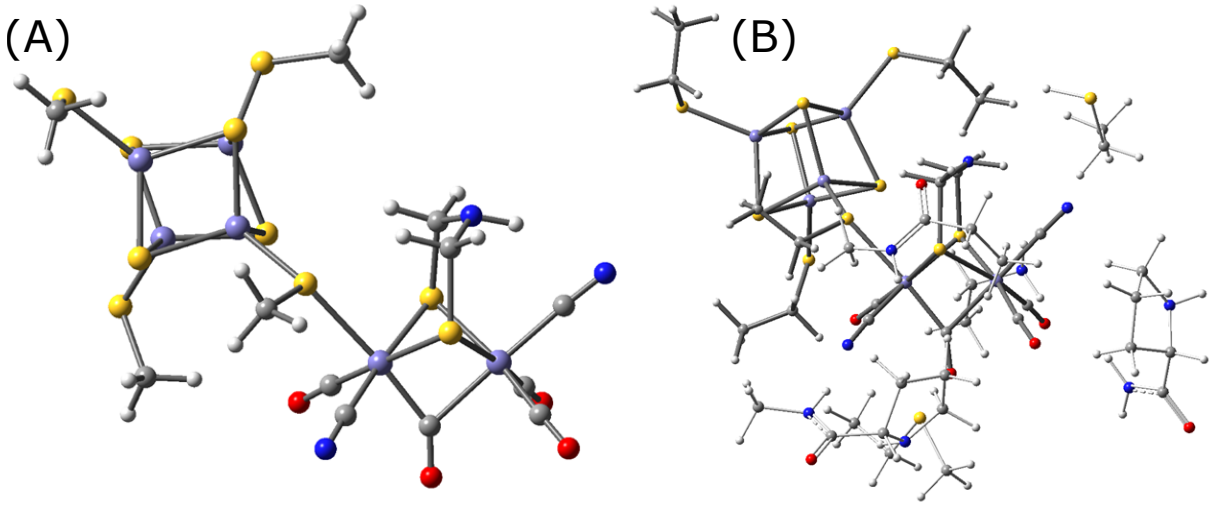

Figure B.11: Small and medium sized model. Small model **(A)** features S-CH_3 molecules that ligate the [4Fe4S]-cluster. The medium sized model **(B)** implements surrounding amino acids and additional flexibility for the ligation of the [4Fe4S]-cluster. Figure taken from[I]

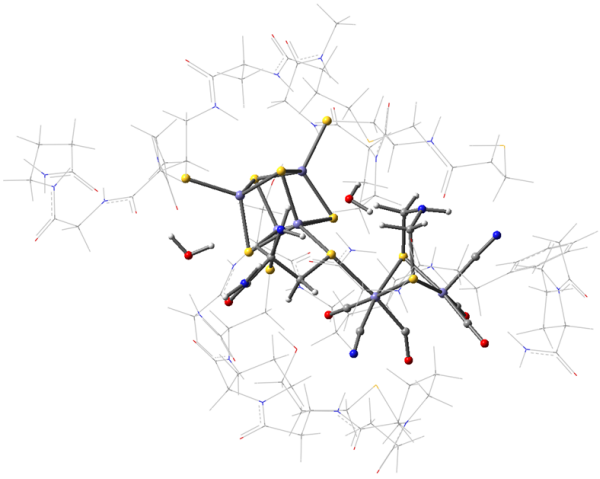

Figure B.12: Large model used for DFT calculations. The model consists of ca. 330 atoms. Figure taken from[I]

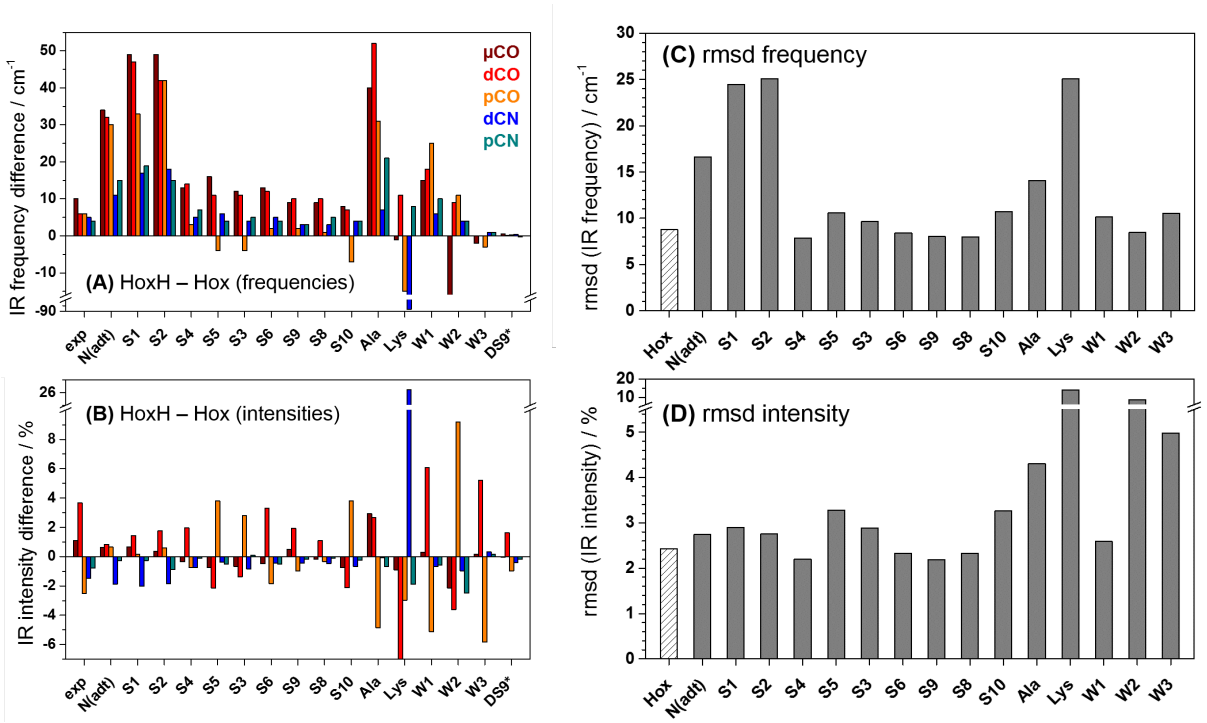

Figure B.13: Top: Experimental and calculated IR frequency differences for the HoxH-Hox transition and different protonation sites. **Bottom:** Experimental and calculated IR intensity differences for the HoxH-Hox transition and different protonation sites. Figure taken from[IV]

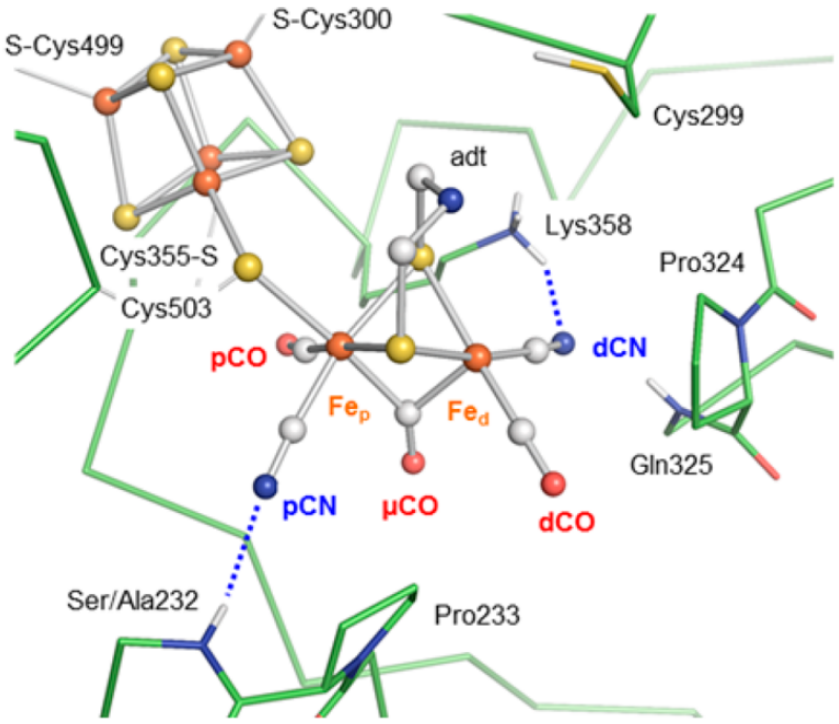

Figure B.14: Crystal structure of CpI(PDB 4XDC) that highlights possible hydrogen bonding interactions with surrounding amino acids. While Lys 358 is conserved Ser232 is replaced by an alanine in HydA1. Figure taken from[VIII]

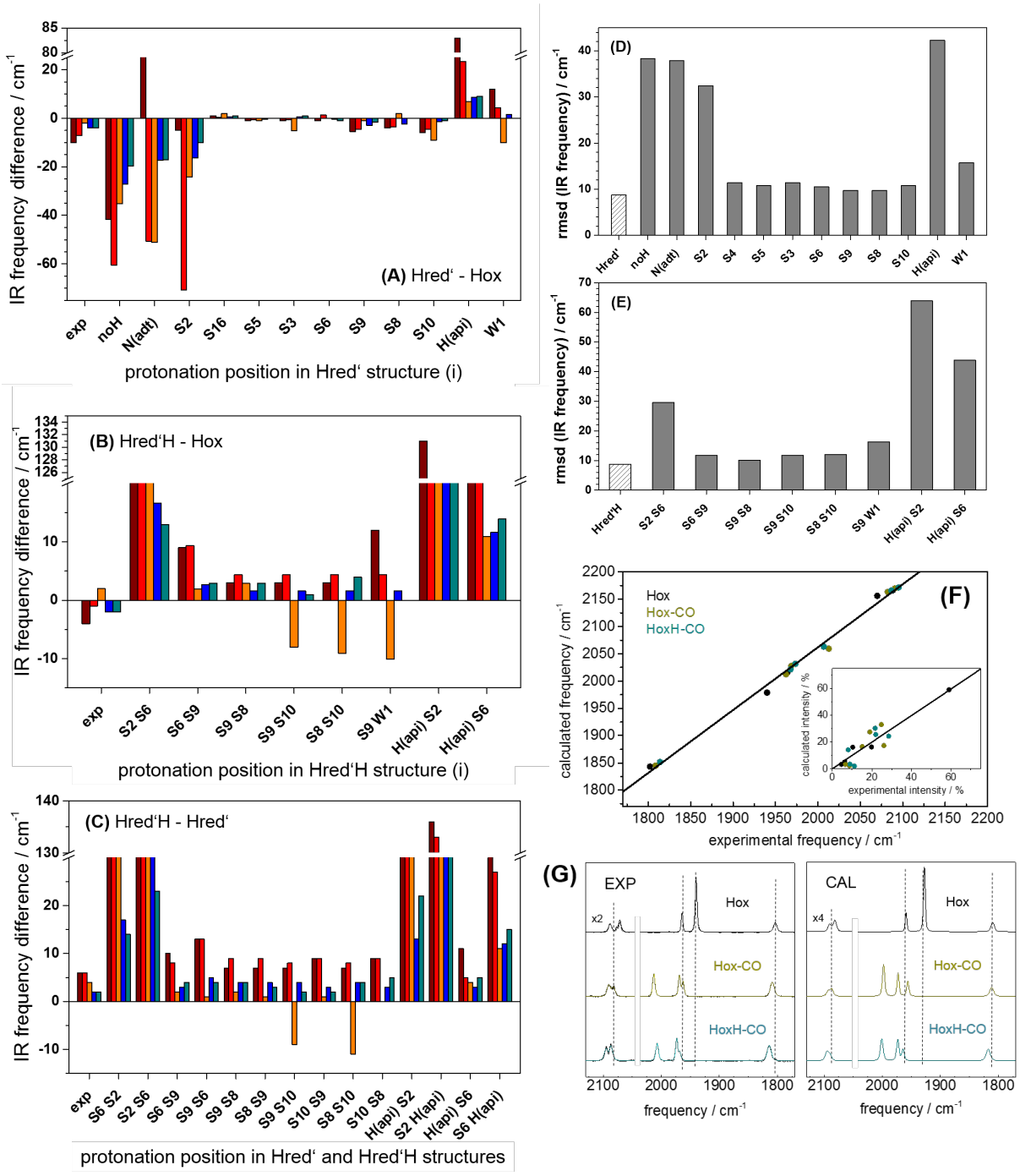

Figure B.15: Top left (A): Experimental and calculated IR frequency differences for the Hred'-Hox transition and different protonation sites. **Middle left (B):** Experimental and calculated IR frequency differences for the Hred'H-Hox transition and different protonation sites. **Bottom left (C):** Experimental and calculated IR frequency differences for the Hred'H-Hred' transition and different protonation sites. **Top right (D):** RMSD of IR frequency for Hred' and different protonation sites. **Middle right (E):** RMSD of IR frequency for Hred'H and different protonation sites. **Bottom right (F) and (G):** Correlation of Hox, Hox-CO and HoxH-CO abnd positions and band intensities. Figure taken from[IV]

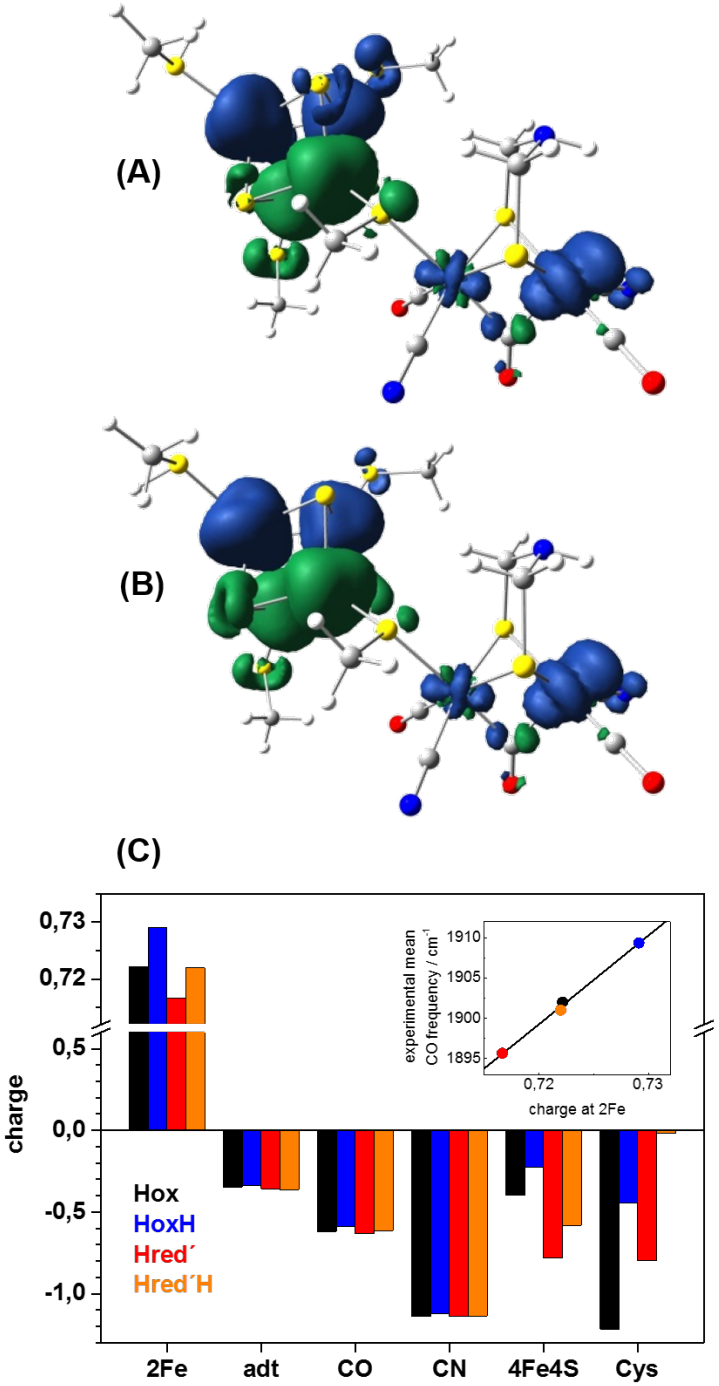

Figure B.16: Spin density and charge **(A)** Spin density of HoxH. **(B)** Spin density of Hred'H. **(C)** Charge distribution for Hox, HoxH, Hred' and Hred'H. Additional charge is found on the [4Fe4S] cluster for Hred' and Hred'H. **inset:** mean experimental frequency and charge at the diiron site correlate linear. Figure taken from[IV]

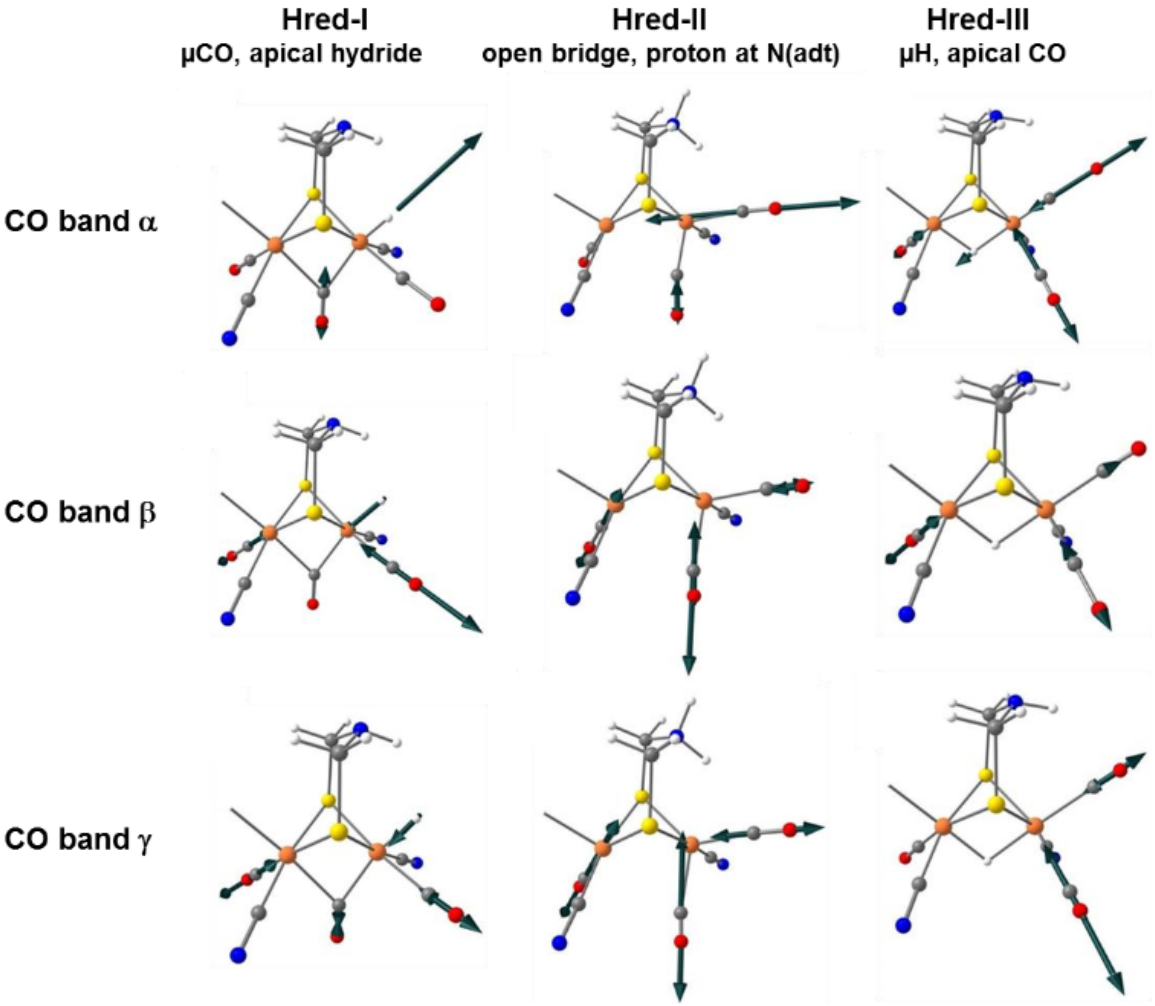

Figure B.17: Coupling patterns for Hred in the three models discussed. Arrows indicate the respective vibrations forming band α, β and γ. Figure taken from[VIII]

B.6 CpI

Figure B.18 on the next page summarizes a typical screening experiment in this case performed on a CpI film. First the CpI film is dried, rehydrated, and equilibrated via aerosol treatment at pH 8 with 100 mM Tris buffer and 100% N_2. Hox is adopted with bands at 1969 cm^{-1} for pCO , 1947 cm^{-1} for dCO and 1801 cm^{-1} for μCO (Figure B.18 on the following page first spectrum). The one electron reduced states Hred' (1962 cm^{-1}, 1938 cm^{-1}, 1789 cm^{-1}), Hred (1962 cm^{-1}, 1914 cm^{-1}, 1899 cm^{-1}) and the two electron reduced state Hsred (1951 cm^{-1}, 1921 cm^{-1}, 1893 cm^{-1}) get depopulated under N_2 (Figure: B.19 on the next page, B.20 on page 115). In a second step the carrier gas of the aerosol is changed to 100% H_2 whereas the pH remains constant. The reduced states get populated due to reduction by H_2 uptake (Figure B.18 on the next page second spectrum). The one electron reduced state Hred' is populated within ca. 100 seconds. Hred and the two electron reduced state Hsred are populated within ca. 250 seconds (Figure: B.21 on page 115, B.22 on page 115). In the presence of N_2 Hox is adopted again like in the first spectrum. Exchange of the buffer to 100mM SSC at pH 4 in the aerosol yielded a blue shifted oxidized state with bands at 1975 cm^{-1} for pCO , 1952 cm^{-1} for dCO and 1810 cm^{-1} for μCO (Figure B.18 on the following page third spectrum). The transition from Hox to the blue shifted species HoxH is shown in Figure B.23 on page 116 and B.24 on page 116. Forth the aerosol carrier gas is changed to H_2 while the buffer remains unchanged at pH 4. Two super-oxidized species compared to Hox are populated instead of the reduced states observed for pH 8 and H_2: Hhyd with bands at 1984 cm^{-1}, 1969 cm^{-1} and 1856 cm^{-1} and HhydH with bands at 1995 cm^{-1}, 1980 cm^{-1} and 1872 cm^{-1} (Figure B.18 on the next page forth spectrum). The transition from Hox to Hhyd and HhydH can be seen in Figure B.25 on page 116 and B.26 on page 117. Replacement of the aerosol composition by N_2 and pH 8 buffer leads again to population of Hox. If N_2 is afterwards replaced by CO Hox-CO with its bands at 2015 cm^{-1}, 1973 cm^{-1},1968 cm^{-1} and 1806 cm^{-1} is formed (Figure B.18 fifth spectrum). Spectra and time traces for CO binding are shown in Figure: B.27 on page 117 and B.28 on page 117.

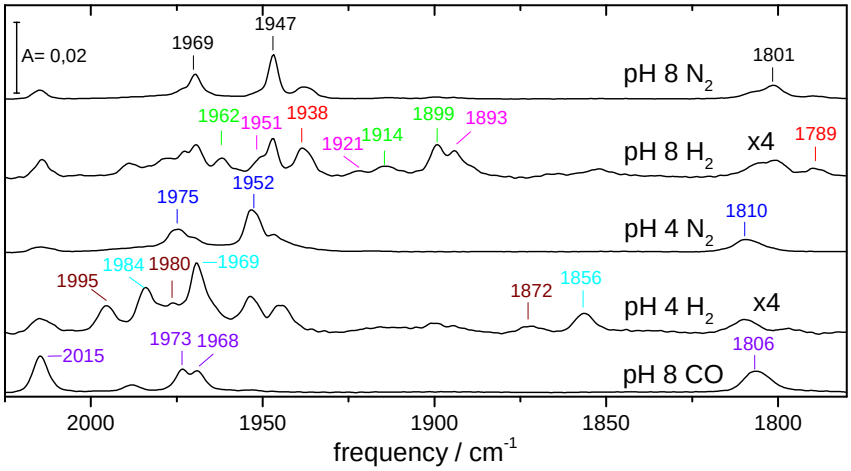

Figure B.18: IR spectra of redox states adopted by a CpI film varying carrier gas and pH of the aerosol stream. The first spectrum (top) displays Hox that is equilibrated with an aerosol of N_2 and pH 8 buffer. An aerosol that consists of H_2 and pH 8 buffer leads to the formation of the reduced states (second spectrum, absorption displayed 4 times increased). The one electron reduced states Hred' (red) 1962 cm^{-1}, 1938 cm^{-1}, 1789 cm^{-1}, Hred (green) 1962 cm^{-1}, 1914 cm^{-1}, 1899 cm^{-1} and the two electron reduced state Hsred (magenta) 1951 cm^{-1}, 1921 cm^{-1}, 1893 cm^{-1} dominate the redox state population. At N_2 and pH 4 HoxH with its bands at 1975 cm^{-1}, 1952 cm^{-1} and 1810 cm^{-1} is populated (third spectrum). If H_2 and pH 4 is applied Hhyd (cyan, 1984 cm^{-1}, 1969 cm^{-1} and 1856 cm^{-1}) and HhydH (brown, 1995 cm^{-1}, 1980 cm^{-1} and 1872 cm^{-1}) can be observed (fourth spectrum, absorption displayed 4 times increased). Exposure to CO at pH 8 leads to the formation of Hox-CO (fifth spectrum) with bands at 2015 cm^{-1}, 1973 cm^{-1},1968 cm^{-1} and 1806 cm^{-1}.

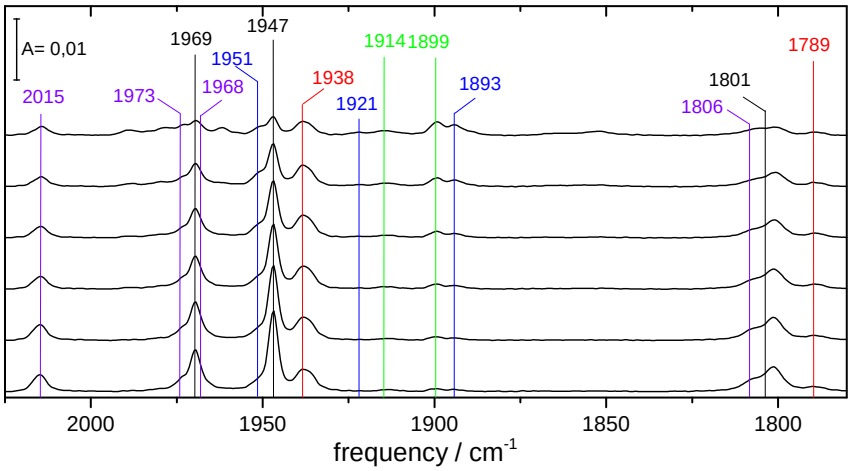

Figure B.19: Selected spectra that illustrate the response of the CpI film to 100% N_2(from top to bottom). Hox(black: 1969 cm^{-1}, 1947 cm^{-1}, 1801 cm^{-1}) gets populated while the one electron reduced states Hred'(red: 1962 cm^{-1}, 1938 cm^{-1}, 1789 cm^{-1}), Hred(green : 1962 cm^{-1}, 1914 cm^{-1}, 1899 cm^{-1}) and the two electron reduced state Hsred(magenta: 1951 cm^{-1}, 1921 cm^{-1}, 1893 cm^{-1}) get depopulated.

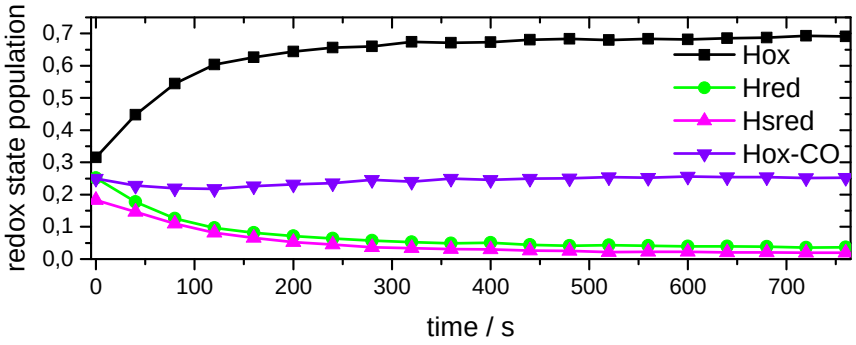

Figure B.20: Timetrace of redox state population that illustrate the response of the CpI film to 100% N_2. Hox(black) gets populated while the one electron reduced states Hred'(red) and Hred(green) and the two electron reduced state Hsred(magenta) are depopulated.

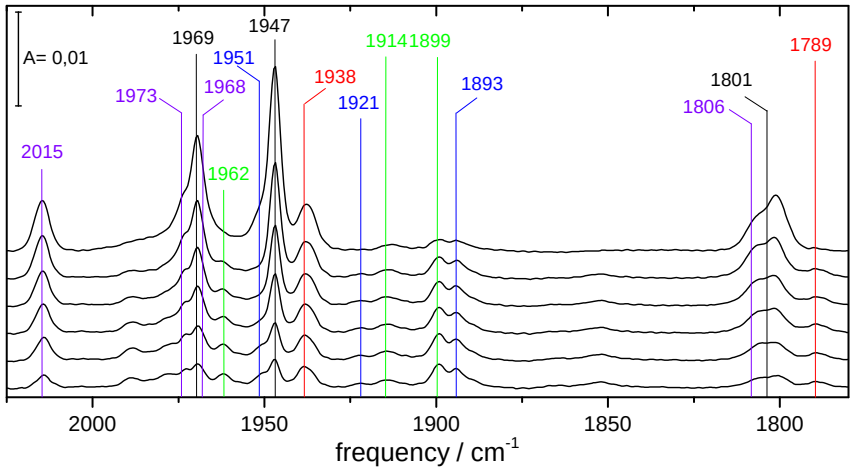

Figure B.21: Selected spectra that illustrate CpI reduction by 100% H_2(from top to bottom). Hox(black: 1969 cm^{-1}, 1947 cm^{-1}, 1801 cm^{-1}) gets depopulated in favor of the one electron reduced states Hred'(red: 1962 cm^{-1}, 1938 cm^{-1}, 1789 cm^{-1}), Hred(green : 1962 cm^{-1}, 1914 cm^{-1}, 1899 cm^{-1}) and the two electron reduced state Hsred(magenta: 1951 cm^{-1}, 1921 cm^{-1}, 1893 cm^{-1}). The CO inhibited state Hox-CO(violet: 2015 cm^{-1}, 1973 cm^{-1}, 1968 cm^{-1}, 1806 cm^{-1}) gets depopulated during reduction.

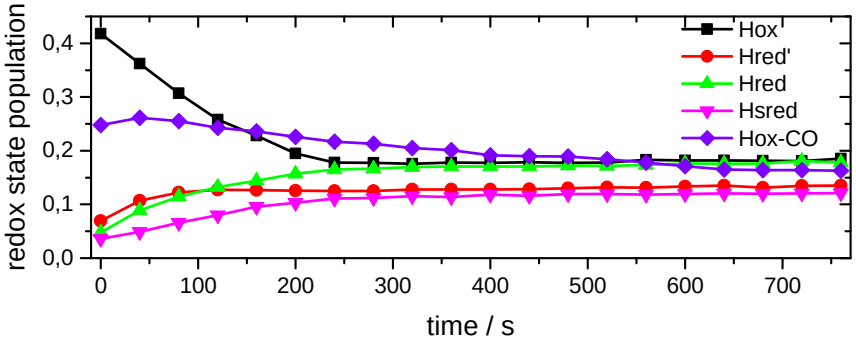

Figure B.22: Timetrace of redox state population that illustrate CpI reduction by 100% H_2. Hox(black) gets depopulated in favor of the one electron reduced state Hred'(red) within 100 seconds. Hred(green) and the two electron reduced state Hsred(magenta) are populated within 250 seconds.

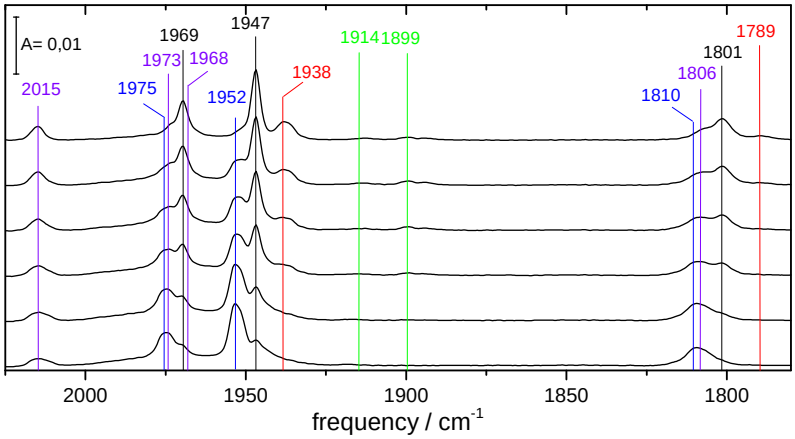

Figure B.23: Selected spectra that illustrate the response of the CpI film to 100% N_2 at pH 4(from top to bottom). Hox (black: 1969 cm^{-1}, 1947 cm^{-1}, 1801 cm^{-1}) and the one electron reduced states Hred' (red: 1962 cm^{-1}, 1938 cm^{-1}, 1789 cm^{-1}) get depopulated while HoxH(blue: 1975 cm^{-1}, 1952 cm^{-1}, 1810 cm^{-1}) gets populated.

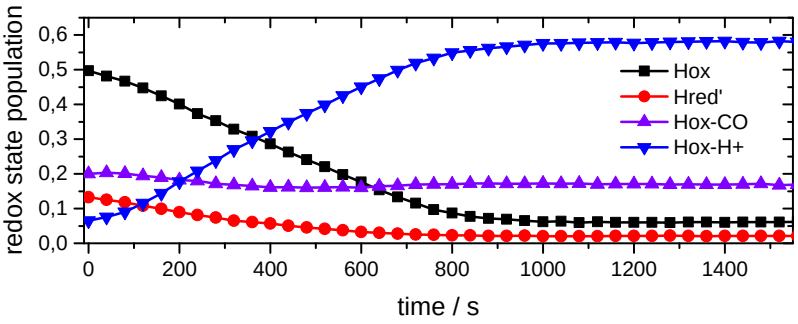

Figure B.24: Timetrace of redox state population that illustrate the response of the CpI film to 100% N_2 at pH 4.Hox(black) and the one electron reduced states Hred'(red) get depopulated while HoxH(blue) gets populated.

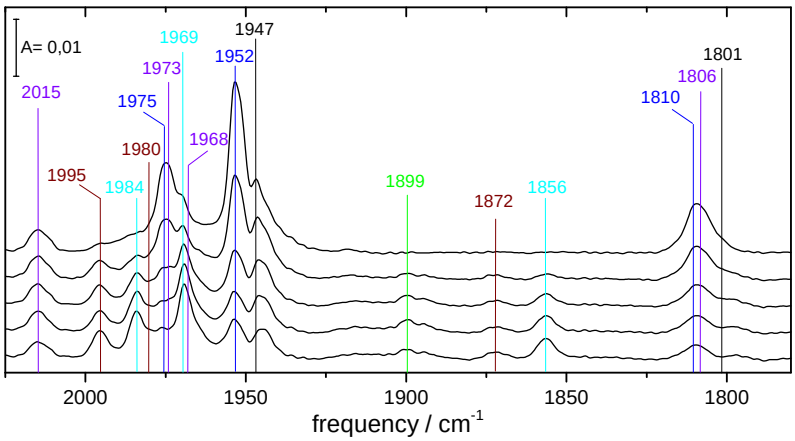

Figure B.25: Selected spectra that illustrate the response of the CpI film to 100% H_2 at pH 4(from top to bottom). HoxH(blue: 1975 cm^{-1}, 1952 cm^{-1}, 1810 cm^{-1}) gets depopulated while Hhyd(cyan, 1984 cm^{-1}, 1969 cm^{-1} and 1856 cm^{-1}) and HhydH(brown, 1995 cm^{-1}, 1980 cm^{-1} and 1872 cm^{-1}) become clearly visible.

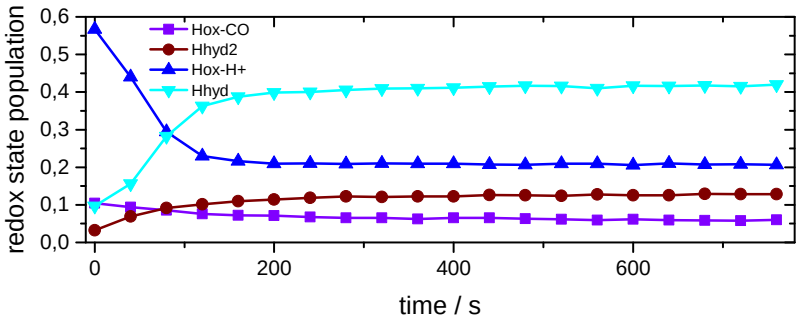

Figure B.26: Timetrace of redox state population that illustrate the response of the CpI film to 100% H_2 at pH 4.HoxH(blue) gets depopulated while Hhyd(cyan) and HhydH(brown) get populated.

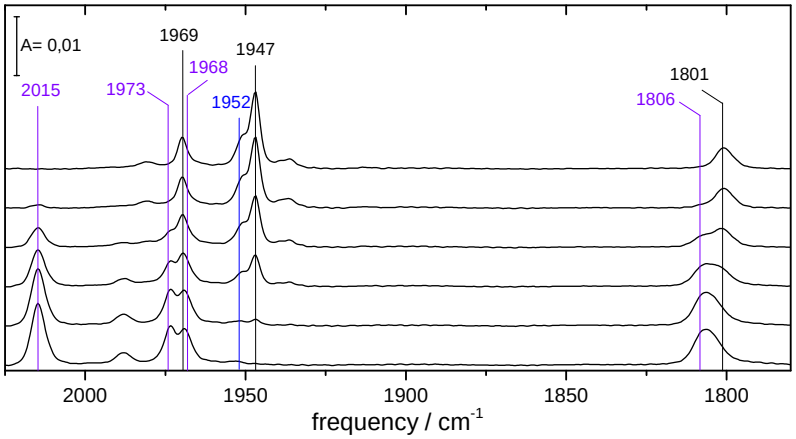

Figure B.27: Selected spectra that show carbon monoxide inhibition upon 100% CO exposure(from top to bottom). Hox-CO(violet: 2015 cm^{-1}, 1973 cm^{-1}, 1968 cm^{-1}, 1806 cm^{-1}) gets populated while Hox(black: 1969 cm^{-1}, 1947 cm^{-1}, 1801 cm^{-1}) gets depopulated.

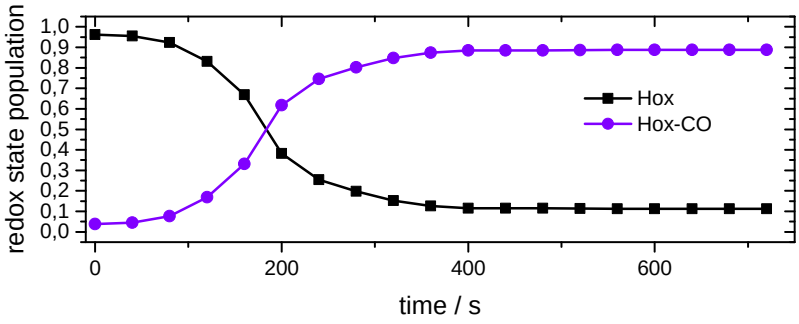

Figure B.28: Timetrace of redox state population that illustrate the carbon monooxide inhibition of the CpI film upon exposure to 100% CO. Hox-CO(violet) gets populated while Hox(black) gets depopulated.

B.7 HydA1 Cofactor Variants

pdt

Replacement of the nitrogen atom in the adt ligand by carbon (propane dithiolate, pdt) shuts off the hydrogen evolution activity however the cofactor still shows the IR signatures of Hox and Hred'. Hred'(1962 cm^{-1}, 1933 cm^{-1}, 1798 cm^{-1}) can be converted into Hox(1965 cm^{-1}, 1941 cm^{-1}, 1810 cm^{-1}) by aerosol treatment at pH 8 with N_2(Figure: B.30, B.31). The same experiment performed at pH 4 leads to a more complex transition that features in addition Hred'H(1966 cm^{-1}, 1938 cm^{-1}, 1802 cm^{-1}) and HoxH(1969 cm^{-1}, 1941 cm^{-1}, 1812 cm^{-1})(Figure: B.29, B.32). Hred'H is populated transient and HoxH is the final redox state. At 100% CO half of the redox state population can be CO inhibited within one minute(Figure: B.33, B.34). Intestingly the depopulation of Hox-CO(2015 cm^{-1}, 1973 cm^{-1}, 1965 cm^{-1}, 1806 cm^{-1}) with N_2 is with 3 minutes about 20 times faster compared to the unaltered enzyme(compare Figure B.35, 3.7).

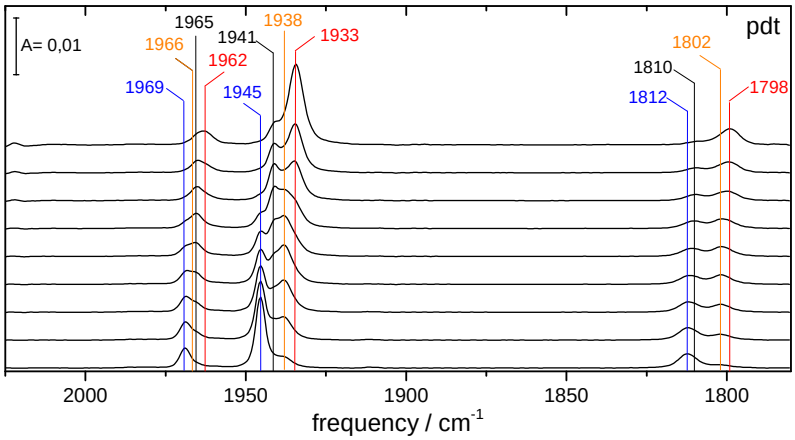

Figure B.29: IR spectra of HydA1pdt that follow the depopulation of Hred'(red, 1962 cm^{-1}, 1933 cm^{-1}, 1798 cm^{-1}) and the population of HoxH(blue, 1969 cm^{-1}, 1941 cm^{-1}, 1812 cm^{-1}) from top to bottom. Hred'H(orange, 1966 cm^{-1}, 1938 cm^{-1}, 1802 cm^{-1}) and Hox(black, 1965 cm^{-1}, 1941 cm^{-1}, 1810 cm^{-1}) get partially populated within this transition.

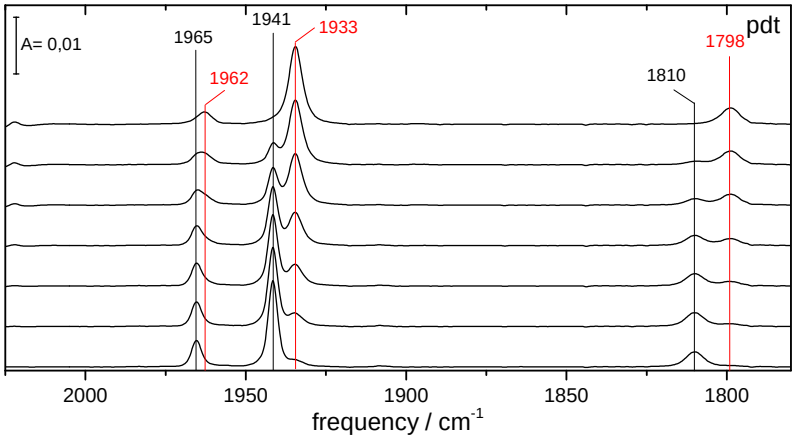

Figure B.30: IR spectra of cofactor variant pdt that follow the depopulation of Hred'(red, 1962 cm^{-1}, 1933 cm^{-1}, 1798 cm^{-1}) and the population of Hox(black, 1965 cm^{-1}, 1941 cm^{-1}, 1810 cm^{-1}) from top to bottom.

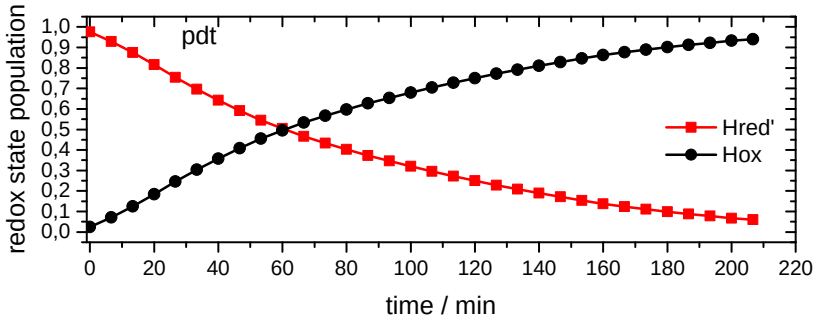

Figure B.31: Time trace that tracks the population of Hox while Hred' gets depopulated. The complete conversion takes about two hours.

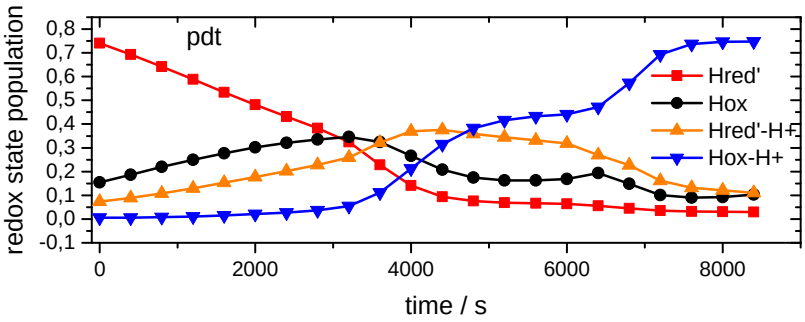

Figure B.32: Time trace that tracks the transition of Hox and Hred' to Hred'H and finally HoxH of cofactor variant pdt. The complete conversion takes about three and a half hours.

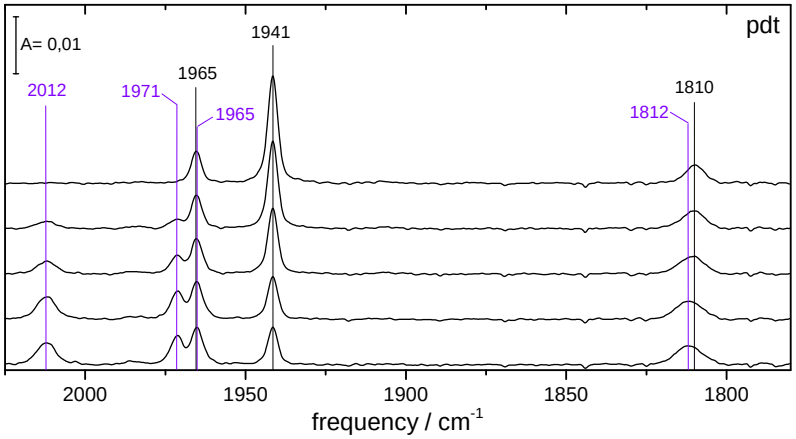

Figure B.33: IR spectra of cofactor variant pdt that follow the depopulation ofHox(black, 1965 cm^{-1}, 1941 cm^{-1}, 1810 cm^{-1}) and the population of Hox-CO(purple, 2012 cm^{-1}, 1971 cm^{-1}, 1965 cm^{-1}, 1812 cm^{-1}) from top to bottom.

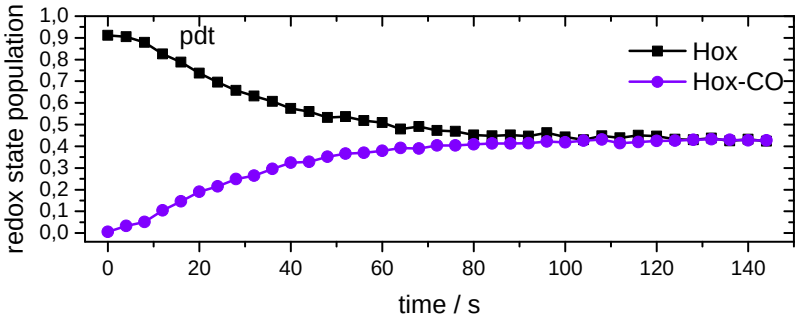

Figure B.34: Time trace that tracks the transition of Hox to Hox-CO of cofactor variant pdt. The complete conversion takes about two and a half hours.

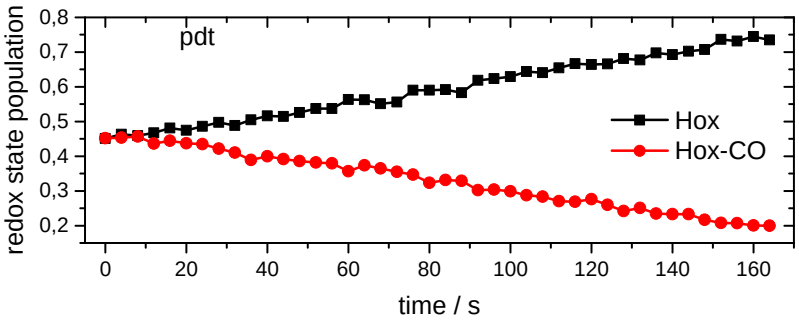

Figure B.35: Time trace that tracks the transition of Hox-CO to Hox of cofactor variant pdt. The conversion is in the order of minutes.

odt

The odt variant is as purified in the Hhyd(1979 cm^{-1}, 1965 cm^{-1}, 1865 cm^{-1}) and Hox(1965 cm^{-1}, 1941 cm^{-1}, 1810 cm^{-1}) state. Here, purging with N_2 populates the H_{ox} state. Acidification reproduced the HoxH(1969 cm^{-1}, 1945 cm^{-1}, 1812 cm^{-1}) state like in wild type enzyme. CO inhibition at pH 4 manifests in a blue shifted Hox-CO(2031 cm^{-1}, 1979 cm^{-1}, 1970 cm^{-1}, 1815 cm^{-1}) compared to the unaltered enzyme(Figure B.36).

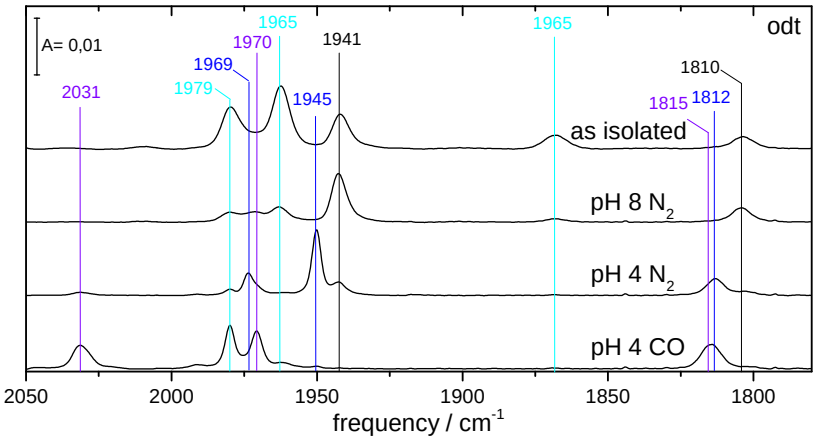

Figure B.36: IR spectra of redox states adopted by a HydA1-odt film varying carrier gas and pH of the aerosol stream. The first spectrum (top) displays a mixture of Hhyd(cyan, 1979 cm^{-1}, 1965 cm^{-1}, 1865 cm^{-1}) and Hox(black, 1965 cm^{-1}, 1941 cm^{-1}, 1810 cm^{-1}) that represents the as isolated state. An aerosol of N_2 and pH 8 buffer populates the H_{ox} state(second spectrum). At N_2 and pH 4 HoxH with its bands at 1969 cm^{-1}, 1945 cm^{-1} and 1812 cm^{-1} is populated(third spectrum). If CO and pH 4 is applied Hox-CO(purple, 2031 cm^{-1}, 1979 cm^{-1}, 1970 cm^{-1}, 1815 cm^{-1}) can be observed(fourth spectrum).

sdt

Upon alteration to sdt (sulfo dithiolate) only Hox and HoxH could be detected. At pH 8 irrespective of the carrier gas(H_2, N_2) Hox is populated. At high proton concentration(pH 4) HoxH gets populated again independent of the used carrier gas(Figure B.37). Neither reduced states nor the hydride state can be observed.

edt

The HydA1-edt variant is as purified in Hred'(1962 cm^{-1}, 1933 cm^{-1}, 1798 cm^{-1}) and remains at pH 8 under N_2 and H_2 in this state. Upon increased proton concentration(pH 4) and N_2 mainly HoxH(1969 cm^{-1}, 1945 cm^{-1}, 1813 cm^{-1}) is adopted, besides Hox(1965 cm^{-1}, 1940 cm^{-1}, 1802 cm^{-1}). Exposure to H_2 under these acidic conditions leads to the enrichment of Hhyd(1976 cm^{-1}, 1958 cm^{-1}, 1865 cm^{-1})(Figure B.38).

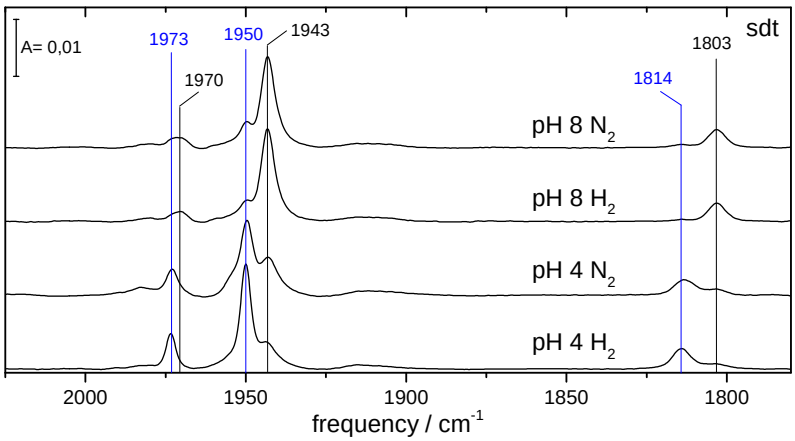

Figure B.37: IR spectra of redox states adopted by a HydA1-sdt film varying carrier gas and pH of the aerosol stream. The first spectrum (top) displays Hox(black, 1970 cm^{-1}, 1943 cm^{-1}, 1803 cm^{-1}) adopted by aerosol of N_2 and pH 8 buffer. The same holds true when the carrier gas is changed to H_2(second spectrum). At N_2 and pH 4 HoxH with its bands at 1973 cm^{-1}, 1950 cm^{-1} and 1814 cm^{-1} is populated(third spectrum)as well as if H_2 and pH 4 is applied(fourth spectrum).

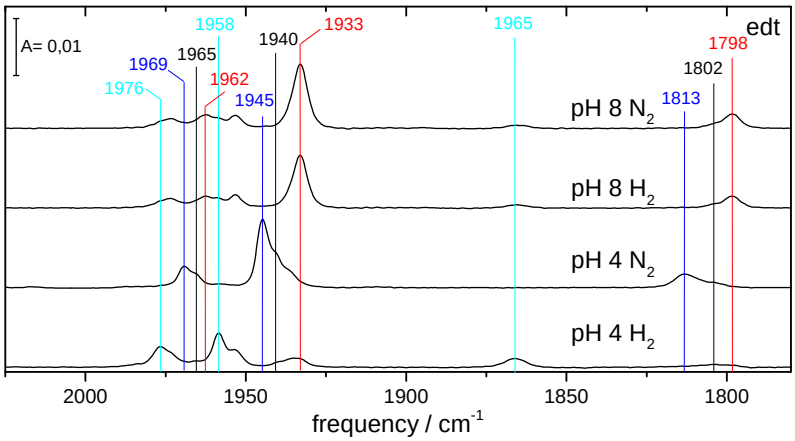

Figure B.38: IR spectra of redox states adopted by a HydA1-edt film varying carrier gas and pH of the aerosol stream. The first spectrum (top) displays Hred'(red, 1962 cm^{-1}, 1933 cm^{-1}, 1798 cm^{-1}) adopted by aerosol of N_2 and pH 8 buffer. The same holds true when the carrier gas is changed to H_2(second spectrum). At N_2 and pH 4 HoxH with its bands at 1969 cm^{-1}, 1945 cm^{-1} and 1813 cm^{-1} is populated(third spectrum)as well as traces of Hox(black, 1965 cm^{-1}, 1940 cm^{-1}, 1802 cm^{-1}). If H_2 and pH 4 is applied the formation of Hhyd(cyan, 1979 cm^{-1}, 1965 cm^{-1}, 1865 cm^{-1}) can be observed(fourth spectrum).

B.8 Proton Path Variants

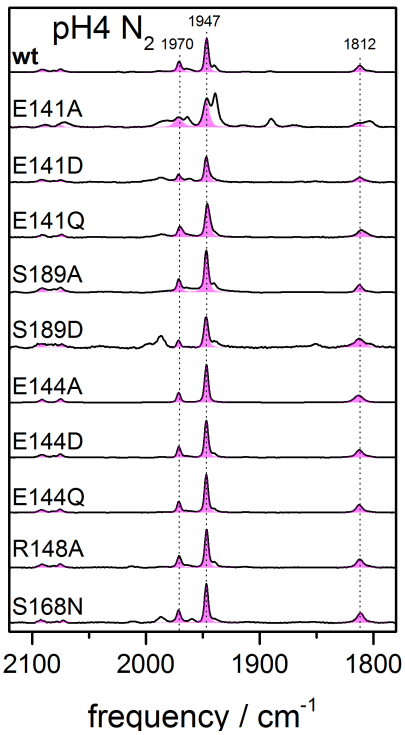

Figure B.39: At pH 4 and under N_2 atmosphere HoxH (magenta, 1970cm^{-1}, 1947cm^{-1} and 1812cm^{-1}) is populated for all variants.

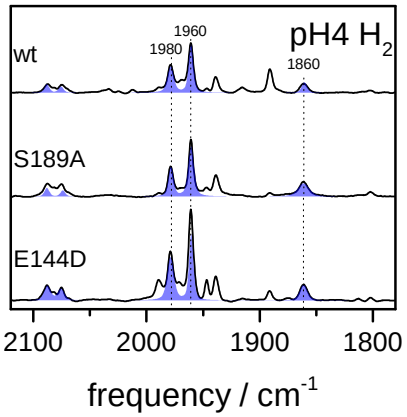

Figure B.40: Overview of cofactor band patterns adopted for N_2 for native enzyme S189A and E144D at pH 4. Upon H_2 exposure Hhyd is populated for all variants like in native enzyme(blue, 1980cm^{-1}, 1960cm^{-1} and 1860cm^{-1}).

C169

The first amino acid in the PTP is cysteine 169. Its sulfur hydrogen residue is located on top of the adt bridge of the diiron site and thereby the first proton donor in case of hydrogen evolution or first proton acceptor in case of hydrogen uptake. This amino acid was exchanged for alanine(C169A), serine(C169S) and aspartic acid(C169D).

C169A

The C169A variant adopts the Hhyd(1978 cm^{-1}, 1962 cm^{-1}, 1863 cm^{-1}) state if exposed to H_2 at pH 8. Purged with an aerosol that consists of N_2 and pH 8 buffer an Hox(1937 cm^{-1}, 1804 cm^{-1}) like redox state is populated where the assignment of the proximal ligand band remains unclear. Exchange of H_2O to D_2O preserves this IR signature. Subsequent exposure to D_2 leads again to population of theHhyd but in this case the band for the μCO ligand is downshifted by 7 wavenumbers from 1863 cm^{-1} to 1856 cm^{-1}(FigureB.41).

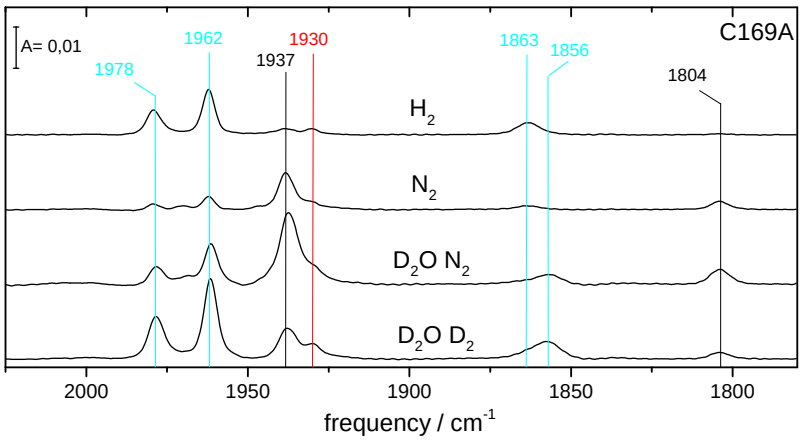

Figure B.41: IR spectra of redox states adopted by a HydA1-C169A film varying carrier gas and pH of the aerosol stream. The first spectrum (top) displays Hhyd(cyan, 1978 cm^{-1}, 1962 cm^{-1}, 1863 cm^{-1}) adopted by aerosol of H_2 and pH 8 buffer. When the carrier gas is changed to N_2 Hox(black, 1937 cm^{-1}, 1804 cm^{-1}) is populated(second spectrum). At N_2 and water exchange to D_2O Hox(black, 1965 cm^{-1}, 1940 cm^{-1}, 1802 cm^{-1}) is populated(third spectrum). If H_2 and D_2O is applied the formation of Hhyd(cyan, 1978 cm^{-1}, 1962 cm^{-1}, 1856 cm^{-1}) can be observed in this case the μCO ligand is downshifted by 9 cm^{-1} from 1863 cm^{-1} to 1856 cm^{-1}(fourth spectrum).

C169S

For C169S a Hred'(1937 cm^{-1}, 1799 cm^{-1}) like IR signature is observed at N_2 atmosphere(FigureB.42, first spectrum). Treatment with 100% H_2 populates two hydride state like IR signatures. One with more native enzyme like band positions(1977 cm^{-1}, 1960 cm^{-1}, 1861 cm^{-1}) and one blue shifted state that resembles HhydH(1983 cm^{-1}, 1967 cm^{-1}, 1867 cm^{-1})(FigureB.43 and FigureB.42, second spectrum). Exposure to an aerosol of N_2 and pH 4 buffer leads to the formation of Hox(1966 cm^{-1}, 1941 cm^{-1}, 1806 cm^{-1})(FigureB.42, third spectrum). Subsequent exchange to H_2 exhibits an IR signature with inverted intensity relation of the "classical" proximal CO band (1964cm^{-1}) and the disztal CO band at 1941 cm^{-1}. The μCO ligand band experiences an downshift to lower wavenumbers by 17 cm^{-1} from 1806 cm^{-1} to 1789 cm^{-1}. During the whole experiment a "dead" species represented by the unchanged band at 1984 cm^{-1} was present.

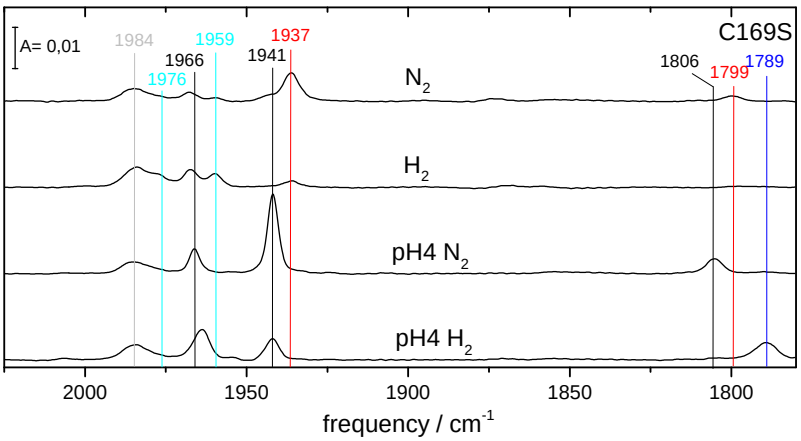

Figure B.42: IR spectra of redox states adopted by a HydA1-C169S film varying carrier gas and pH of the aerosol stream. The first spectrum (top) displays Hred'(red, 1962 cm^{-1}, 1937 cm^{-1}, 1799 cm^{-1}) adopted by aerosol of N_2 and pH 8 buffer. When the carrier gas is changed to N_2 Hhyd(cyan, 1976 cm^{-1}, 1959 cm^{-1} 1859 cm^{-1}) is populated(second spectrum). At N_2 and pH 4 Hox with its bands at 1966 cm^{-1}, 1941 cm^{-1} and 1806 cm^{-1} is populated(third spectrum). Treatment with 100% H_2 at pH 4 populates traces of two hydride state like IR signatures. One with more native enzyme like band positionsHhyd(cyan, 1977 cm^{-1}, 1960 cm^{-1}, 1861 cm^{-1}) and one blue shifted state that resembles HhydH(brown, 1983 cm^{-1}, 1967 cm^{-1}, 1867 cm^{-1})(fourth spectrum, see B.43 for details)

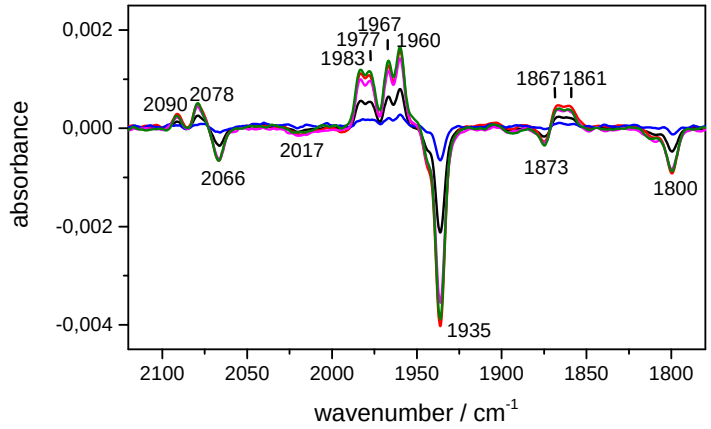

Figure B.43: IR difference spectra of a HydA1-C169S between Hred'(negative bands) and HhydH and Hhyd. Treatment with 100% H_2 at pH 4 populates two hydride state like IR signatures. One with more native enzyme like band positionsHhyd(cyan, 1977 cm^{-1}, 1960 cm^{-1}, 1861 cm^{-1}) and one blue shifted state that resembles HhydH(brown, 1983 cm^{-1}, 1967 cm^{-1}, 1867 cm^{-1})

C169D

The C169D variant exhibits Hred(1962 cm^{-1}, 1915 cm^{-1}, 1891 cm^{-1}), Hred'(1962 cm^{-1}, 1934 cm^{-1}, 1792 cm^{-1}) and Hsred(1954 cm^{-1}, 1918 cm^{-1}, 1882 cm^{-1}) upon contact with H_2(FigureB.44, first spectrum). Atmosphere exchange to N_2 populates Hox(1965 cm^{-1}, 1940 cm^{-1}, 1804 cm^{-1}) (FigureB.44, second spectrum). At pH 4 and N_2 an inverted intensity oxidized state like C169S can be observed. While the bands for most likely proximal and distal CO ligand(1967 cm^{-1}, 1946 cm^{-1}) shift to higher wavenumbers the μCO ligand is again downshifted from 1804 cm^{-1} to 1792 cm^{-1} by 12 cm^{-1}(FigureB.44, third spectrum).

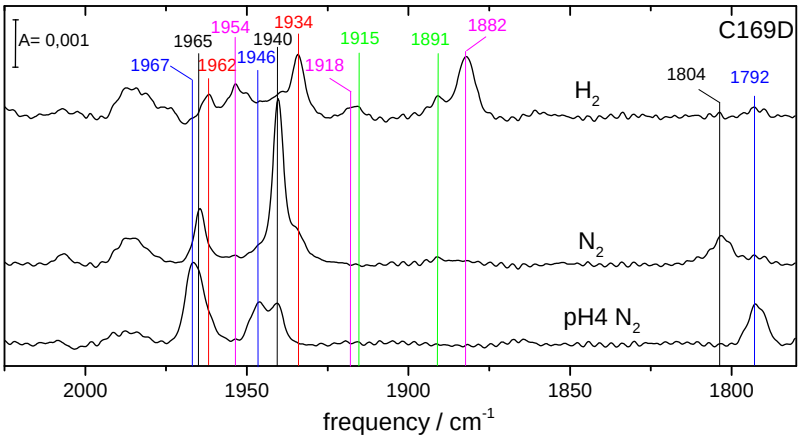

Figure B.44: The IR spectra of the C169D variant exhibits Hred(green, 1962 cm^{-1}, 1915 cm^{-1}, 1891 cm^{-1}), Hred'(red, 1962 cm^{-1}, 1934 cm^{-1}, 1792 cm^{-1}) and Hsred(magenta, 1954 cm^{-1}, 1918 cm^{-1}, 1882 cm^{-1}) upon contact with H_2(first spectrum). Atmosphere exchange to N_2 populates Hox(black, 1965 cm^{-1}, 1940 cm^{-1}, 1804 cm^{-1})(second spectrum). At pH 4 and N_2 an inverted intensity oxidized state like C169S can be observed. While the bands for most likely proximal and distal CO ligand(1967 cm^{-1}, 1946 cm^{-1}) shift to higher wavenumbers the μCO ligand is again downshifted from 1804 cm^{-1} to 1792 cm^{-1} by 12 cm^{-1}(third spectrum, see B.45 main script).

E141

Glutamic acid 141(E141) is the second amino acid in the PTP. It is located between S189 and a water molecule that serves as a connection to C169. This amino acid was altered to alanine(E141A), aspartic acid(E141D) and glutamine(E141Q).

E141A

E141A exposed to H_2 adopts mainly the Hhyd(1980 cm^{-1}, 1963 cm^{-1}, 1863 cm^{-1}) with small fractions of Hred(1962 cm^{-1}, 1915 cm^{-1}, 1891 cm^{-1}), Hred'(1962 cm^{-1}, 1933 cm^{-1}, 1792 cm^{-1}) and Hsred(1954 cm^{-1}, 1918 cm^{-1}, 1881 cm^{-1})(FigureB.45, first spectrum). Under N_2 atmosphere Hox(1964 cm^{-1}, 1939 cm^{-1}, 1803 cm^{-1}) with traces of Hred and Hred' is populated(FigureB.45, second spectrum). The third spectrum of FigureB.45 displays the response to dehydration by N_2. The enrichment of HoxH(1971 cm^{-1}, 1946 cm^{-1}, 1813 cm^{-1}) is clearly visible. Rehydration with D_2O and subsequent exposure to D_2 populates again the Hhyd but with downshifted μCO ligand from 1863 cm^{-1} to 1857 cm^{-1}(FigureB.45, fourth spectrum).

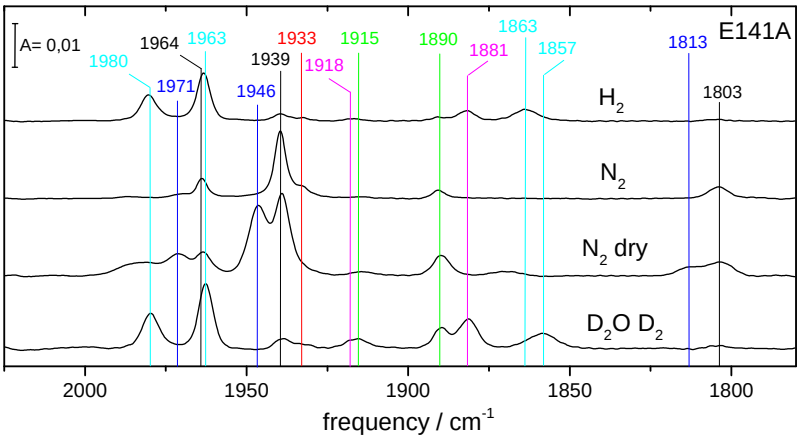

Figure B.45: IR spectra of redox states adopted by a HydA1-E141A film varying carrier gas and pH of the aerosol stream. Exposed to H_2 mainly Hhyd(cyan, 1980 cm^{-1}, 1963 cm^{-1}, 1863 cm^{-1}) with small fractions of Hred(green, 1962 cm^{-1}, 1915 cm^{-1}, 1891 cm^{-1}), Hred'(red, 1962 cm^{-1}, 1933 cm^{-1}, 1792 cm^{-1}) and Hsred(magenta, 1954 cm^{-1}, 1918 cm^{-1}, 1881 cm^{-1} is adopted)(first spectrum). Under N_2 atmosphere Hox(black, 1964 cm^{-1}, 1939 cm^{-1}, 1803 cm^{-1}) with traces of Hred and Hred' is populated(second spectrum). The third spectrum displays the enrichment of HoxH(blue, 1971 cm^{-1}, 1946 cm^{-1}, 1813 cm^{-1}) upon dehydration. Rehydration with D_2O and subsequent exposure to D_2 populates again the Hhyd but with downshifted μCO ligand from 1863 cm^{-1} to 1857 cm^{-1}(fourth spectrum).

E141D

Similar to E141A the variation to aspartic acid adopts the Hhyd state(1979 cm^{-1}, 1961 cm^{-1}, 1863 cm^{-1}) if exposed to H_2 but no reduced states are observed(FigureB.46, first spectrum). Nitrogen atmosphere populates Hox(1964 cm^{-1}, 1939 cm^{-1}, 1803 cm^{-1})(FigureB.46, second spectrum). Replacement of neutral pH buffer in the aerosol by pH 4 buffer leads to the blue shift that is assoziated with HoxH(1971 cm^{-1}, 1946 cm^{-1}, 1813 cm^{-1})(FigureB.46, third spectrum).

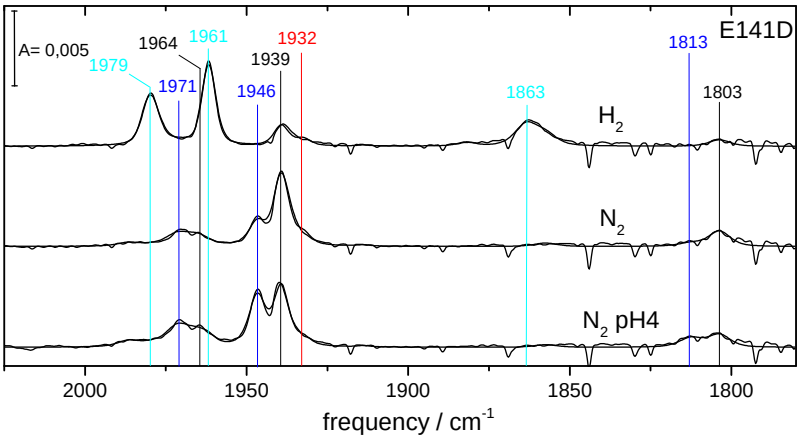

Figure B.46: IR spectra of redox states adopted by a HydA1-E141D film varying carrier gas and pH of the aerosol stream. E141D adopts the Hhyd state(cyan, 1979 cm^{-1}, 1961 cm^{-1}, 1863 cm^{-1}) if exposed to H_2. No reduced states are observed(first spectrum). Nitrogen atmosphere populates Hox(black, 1964 cm^{-1}, 1939 cm^{-1}, 1803 cm^{-1})(second spectrum). Replacement of pH 8 buffer in the aerosol by pH 4 buffer leads to the blue shift that is assoziated with HoxH(blue, 1971 cm^{-1}, 1946 cm^{-1}, 1813 cm^{-1})(third spectrum).

E141Q

E141Q exposed to H_2 adopts mainly the Hhyd(1978 cm^{-1}, 1962 cm^{-1}, 1863 cm^{-1}) with small fractions of Hred(1962 cm^{-1}, 1915 cm^{-1}, 1891 cm^{-1}) and Hsred(1954 cm^{-1}, 1918 cm^{-1}, 1881 cm^{-1})(FigureB.47, first spectrum). Under N_2 atmosphere Hox(1964 cm^{-1}, 1939 cm^{-1}, 1803 cm^{-1}) with traces of Hred is populated(FigureB.47, second spectrum). Replacement of neutral pH buffer in the aerosol by pH 4 buffer leads to the blue shift that is assoziated with HoxH(1970 cm^{-1}, 1946 cm^{-1}, 1808 cm^{-1})(FigureB.47, third spectrum). Exposure to carbon monooxide leads to CO inhibition(Hox-CO(2013 cm^{-1}, 1971 cm^{-1}, 1962 cm^{-1}, 1812 cm^{-1}))(FigureB.47, fourth spectrum).

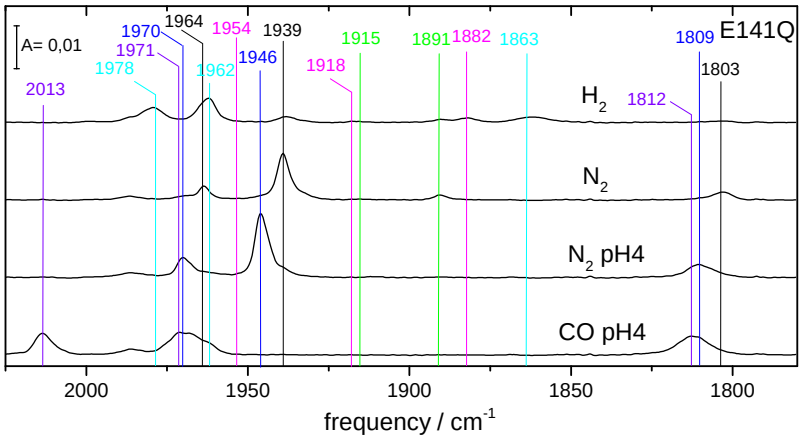

Figure B.47: IR spectra of redox states adopted by a HydA1-E141Q film varying carrier gas and pH of the aerosol stream. E141Q exposed to H_2 adopts mainly the Hhyd(cyan, 1978 cm^{-1}, 1962 cm^{-1}, 1863 cm^{-1}) with small fractions of Hred(green, 1962 cm^{-1}, 1915 cm^{-1}, 1891 cm^{-1}) and Hsred(magenta, 1954 cm^{-1}, 1918 cm^{-1}, 1881 cm^{-1})(first spectrum). Under N_2 atmosphere Hox(black, 1964 cm^{-1}, 1939 cm^{-1}, 1803 cm^{-1}) with traces of Hred is populated(second spectrum). Replacement of neutral pH buffer in the aerosol by pH 4 buffer leads to the blue shift that is assoziated with HoxH(blue, 1970 cm^{-1}, 1946 cm^{-1}, 1808 cm^{-1})(third spectrum). Exposure to carbon monooxide leads to CO inhibition(Hox-CO(purple, 2013 cm^{-1}, 1971 cm^{-1}, 1962 cm^{-1}, 1812 cm^{-1}))(fourth spectrum).

S189

Serin 189(S189) is located inbetween E141 and E144. This amino acid was exchanged for alanine(S189A) and aspartic acid(S189D).

S189A

The alanine to serine variant adopts upon exposure to H_2 Hred(1962 cm^{-1}, 1915 cm^{-1}, 1890 cm^{-1}), Hred'(1962 cm^{-1}, 1933 cm^{-1}, 1792 cm^{-1}) and Hsred(1954 cm^{-1}, 1918 cm^{-1}, 1882 cm^{-1}) (FigureB.48, first spectrum). Under N_2 atmosphere Hox(1964 cm^{-1}, 1940 cm^{-1}, 1803 cm^{-1}) with traces of Hred and Hred' is populated(FigureB.48, second spectrum). Exchange of aerosol buffer to pH 4 leads to a exclusive population of Hox(FigureB.48, third spectrum). Replacement of the carrier gas N_2 by H_2 leads again to population of Hred, Hred' and Hsred(FigureB.48, fourth spectrum).

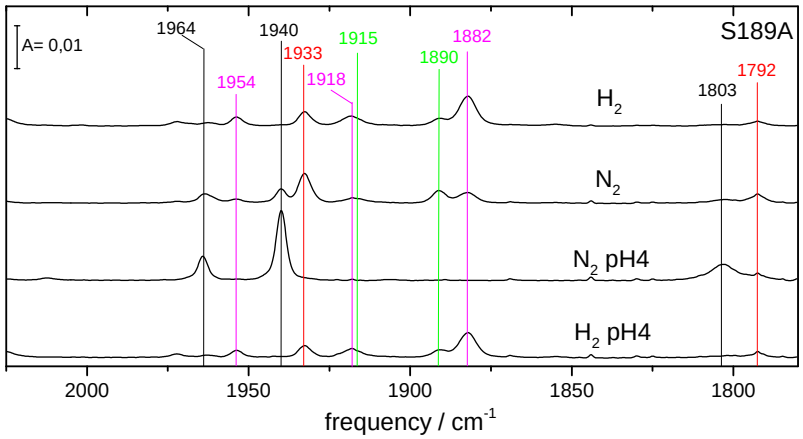

Figure B.48: IR spectra of redox states adopted by a HydA1-S189A film varying carrier gas and pH of the aerosol stream. The alanine to serine variant adopts upon exposure to H_2 Hred(green, 1962 cm^{-1}, 1915 cm^{-1}, 1890 cm^{-1}), Hred'(red, 1962 cm^{-1}, 1933 cm^{-1}, 1792 cm^{-1}) and Hsred(magenta, 1954 cm^{-1}, 1918 cm^{-1}, 1882 cm^{-1}) (first spectrum). Under N_2 atmosphere Hox(black, 1964 cm^{-1}, 1940 cm^{-1}, 1803 cm^{-1}) with traces of Hred and Hred' is populated(second spectrum). Exchange of aerosol buffer to pH 4 leads to a exclusive population of Hox(third spectrum). Replacement of the carrier gas N_2 by H_2 leads again to population of Hred, Hred' and Hsred(fourth spectrum).

S189D

S189D exposed to H_2 adopts the Hhyd(1979 cm^{-1}, 1962 cm^{-1}, 1860 cm^{-1})(FigureB.49, first spectrum). Atmosphere exchange to N_2 populates Hox(1969 cm^{-1}, 1938 cm^{-1}, 1801 cm^{-1}) (FigureB.49, second spectrum). At pH 4 and N_2 the IR signatur of HoxH(1971 cm^{-1}, 1947 cm^{-1}, 1811 cm^{-1}) is observed(FigureB.49, third spectrum). Subsequent exposure to H_2 populates Hhyd again(FigureB.49, fourth spectrum).

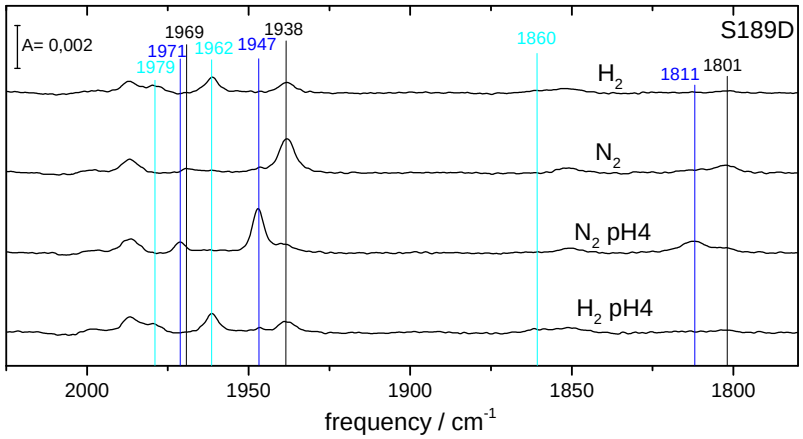

Figure B.49: IR spectra of redox states adopted by a HydA1-S189A film varying carrier gas and pH of the aerosol stream. S189D exposed to H_2 adopts the Hhyd(cyan, 1979 cm^{-1}, 1962 cm^{-1}, 1860 cm^{-1})(first spectrum). Atmosphere exchange to N_2 populates Hox(black, 1969 cm^{-1}, 1938 cm^{-1}, 1801 cm^{-1}) (second spectrum). At pH 4 and N_2 the same IR signatur of Hox is observed(third spectrum). Subsequent exposure to H_2 populates Hhyd again(fourth spectrum).

E144

Glutamic acid 144(E144) is located at the end of the PTP between S189 and R148. This amino acid was altered to alanine(E144A), aspartic acid(E144D) and glutamine(E144Q).

E144A

E144A is as isolated mainly in Hred(1962 cm^{-1}, 1915 cm^{-1}, 1890 cm^{-1}) and Hox(1964 cm^{-1}, 1939 cm^{-1}, 1803 cm^{-1})(FigureB.50, first spectrum). E144A exposed to H_2 adopts Hhyd(1979 cm^{-1}, 1962 cm^{-1}, 1862 cm^{-1})(FigureB.50, second spectrum). Atmosphere exchange to N_2 populates Hox(1964 cm^{-1}, 1939 cm^{-1}, 1803 cm^{-1}) (FigureB.50, third spectrum). Carbon monoxide inhibition manifests in population of Hox-CO(2011 cm^{-1}, 1968 cm^{-1}, 1962 cm^{-1}, 1809 cm^{-1})(FigureB.50, fourth spectrum). At pH 4 and N_2 the IR signatur of HoxH(1970 cm^{-1}, 1947 cm^{-1}, 1812 cm^{-1}) is observed(FigureB.50, fifth spectrum).

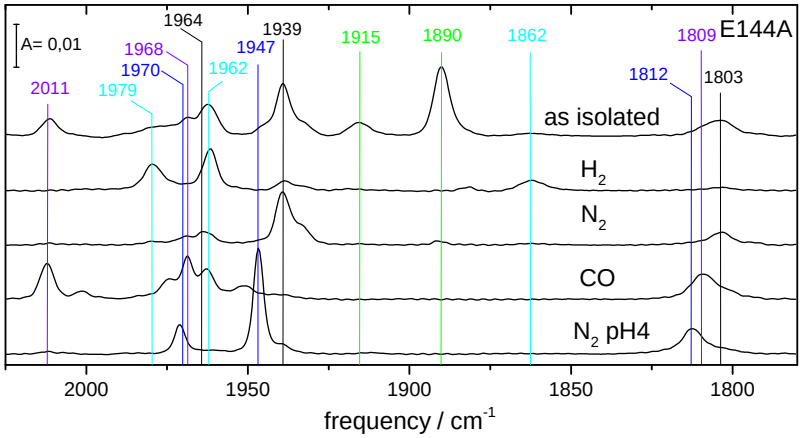

Figure B.50: IR spectra of redox states adopted by a HydA1-E144A film varying carrier gas and pH of the aerosol stream. E144A is as isolated mainly in Hred(green, 1962 cm^{-1}, 1915 cm^{-1}, 1890 cm^{-1}) and Hox(black, 1964 cm^{-1}, 1939 cm^{-1}, 1803 cm^{-1})(first spectrum). E144A exposed to H_2 adopts Hhyd(cyan, 1979 cm^{-1}, 1962 cm^{-1}, 1862 cm^{-1})(second spectrum). Atmosphere exchange to N_2 populates Hox(black, 1964 cm^{-1}, 1939 cm^{-1}, 1803 cm^{-1}) (third spectrum). Carbon monoxide inhibition manifests in population of Hox-CO(purple, 2011 cm^{-1}, 1968 cm^{-1}, 1962 cm^{-1}, 1809 cm^{-1})(fourth spectrum). At pH 4 and N_2 the IR signatur of HoxH(blue, 1970 cm^{-1}, 1947 cm^{-1}, 1812 cm^{-1}) is observed(fifth spectrum).

E144D

E144D adopts upon exposure to H_2 Hred(1962 cm^{-1}, 1915 cm^{-1}, 1890 cm^{-1}) and Hsred(1954 cm^{-1}, 1918 cm^{-1}, 1882 cm^{-1}) (FigureB.51, first spectrum). Under N_2 atmosphere Hox(1964 cm^{-1}, 1939 cm^{-1}, 1803 cm^{-1}) with traces of Hred is populated(FigureB.51, second spectrum). Carbon monoxide inhibition manifests in population of Hox-CO(2011 cm^{-1}, 1968 cm^{-1}, 1962 cm^{-1}, 1809 cm^{-1})(FigureB.51, third spectrum). E144D at pH 4 exposed to D_2 adopts the Hhyd(1979 cm^{-1}, 1961 cm^{-1}, 1860 cm^{-1})(FigureB.51, fourth spectrum).

E144Q

Hox(1964 cm^{-1}, 1940 cm^{-1}, 1803 cm^{-1}) is populated when E144Q is treated with an aerosol at neutral pH and N_2(FigureB.52, first spectrum). Exposed to H_2 adopts the Hhyd(1979 cm^{-1},

1962 cm^{-1}, 1860 cm^{-1})(FigureB.52, second spectrum). With N_2 as carrier gas and pH 4 HoxH(1971 cm^{-1}, 1947 cm^{-1}, 1811 cm^{-1}) is observed(FigureB.52, third spectrum). Exposure to H_2 at pH 4 leads to the formation of Hhyd(1979 cm^{-1}, 1962 cm^{-1}, 1860 cm^{-1})(FigureB.52, fourth spectrum).

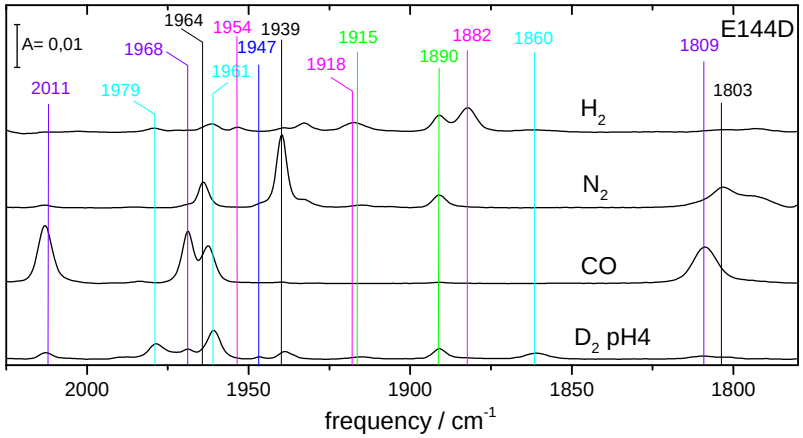

Figure B.51: IR spectra of redox states adopted by a HydA1-E144D film varying carrier gas and pH of the aerosol stream. E144D adopts upon exposure to H_2 Hred(green, 1962 cm^{-1}, 1915 cm^{-1}, 1890 cm^{-1}) and Hsred(magenta, 1954 cm^{-1}, 1918 cm^{-1}, 1882 cm^{-1}) (first spectrum). Under N_2 atmosphere Hox(black, 1964 cm^{-1}, 1939 cm^{-1}, 1803 cm^{-1}) with traces of Hred is populated(second spectrum). Carbon monoxide inhibition manifests in population of Hox-CO(purple, 2011 cm^{-1}, 1968 cm^{-1}, 1962 cm^{-1}, 1809 cm^{-1})(third spectrum). E144D at pH 4 exposed to D_2 adopts the Hhyd(cyan, 1979 cm^{-1}, 1961 cm^{-1}, 1860 cm^{-1})(fourth spectrum).

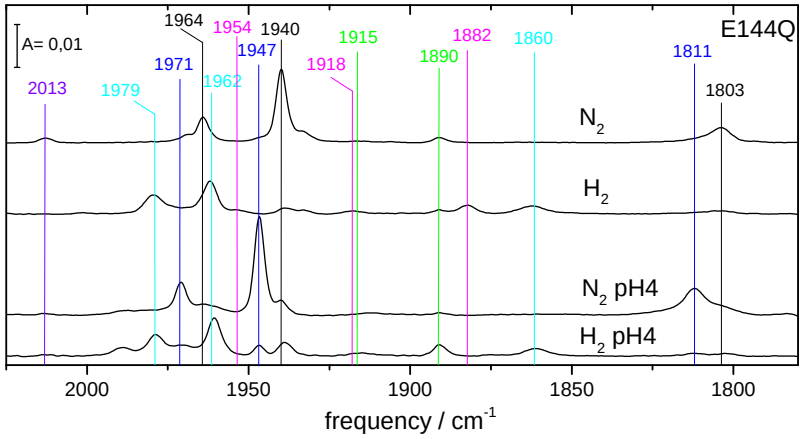

Figure B.52: IR spectra of redox states adopted by a HydA1-E144Q film varying carrier gas and pH of the aerosol stream. Hox(black, 1964 cm^{-1}, 1940 cm^{-1}, 1803 cm^{-1}) is populated when E144Q is treated with an aerosol at neutral pH and N_2(first spectrum). Exposed to H_2 adopts the Hhyd(cyan, 1979 cm^{-1}, 1962 cm^{-1}, 1860 cm^{-1})(second spectrum). With N_2 as carrier gas and pH 4 HoxH(blue, 1971 cm^{-1}, 1947 cm^{-1}, 1811 cm^{-1}) is observed(third spectrum). Exposure to H_2 at pH 4 leads to the formation of Hhyd(cyan, 1979 cm^{-1}, 1962 cm^{-1}, 1860 cm^{-1})(fourth spectrum).

R148

Arginine 148 is located at the end of the PTP. Its effect on the enzyme was tested by exchange to alanine(R148A).

R148A

Upon H_2 exposure R148A exhibits a a mixture of redox states that consists mainly of Hhyd(1979 cm^{-1}, 1962 cm^{-1}, 1860 cm^{-1}) and Hsred(1954 cm^{-1}, 1918 cm^{-1}, 1882 cm^{-1}) but also small fractions of Hred(1962 cm^{-1}, 1915 cm^{-1}, 1890 cm^{-1}) and Hred'(1962 cm^{-1}, 1933 cm^{-1}, 1792 cm^{-1})(FigureB.53, first spectrum). The Hox(1964 cm^{-1}, 1940 cm^{-1}, 1803 cm^{-1}) is populated when R148A is treated with an aerosol at neutral pH and N_2(FigureB.53, second spectrum). Carbon monoxide inhibition manifests in population of Hox-CO(2013 cm^{-1}, 1968 cm^{-1}, 1962 cm^{-1}, 1808 cm^{-1})(FigureB.53, third spectrum). At pH 4 and N_2 the IR signatur of HoxH(1971 cm^{-1}, 1947 cm^{-1}, 1811 cm^{-1}) is observed(FigureB.53, fourth spectrum).

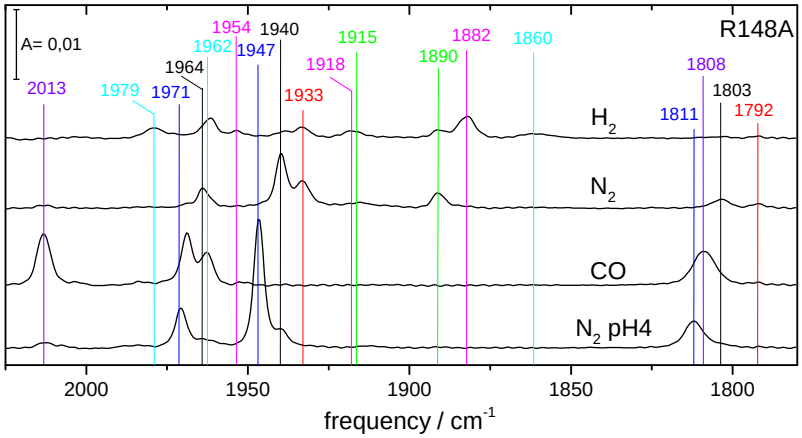

Figure B.53: IR spectra of redox states adopted by a HydA1-R148A film varying carrier gas and pH of the aerosol stream. Upon H_2 exposure R148A exhibits a a mixture of redox states that consists mainly of Hhyd(cyan, 1979 cm^{-1}, 1962 cm^{-1}, 1860 cm^{-1}) and Hsred(magenta, 1954 cm^{-1}, 1918 cm^{-1}, 1882 cm^{-1}) but also small fractions of Hred(green, 1962 cm^{-1}, 1915 cm^{-1}, 1890 cm^{-1}) and Hred'(red, 1962 cm^{-1}, 1933 cm^{-1}, 1792 cm^{-1})(first spectrum). The Hox(black, 1964 cm^{-1}, 1940 cm^{-1}, 1803 cm^{-1}) is populated when R148A is treated with an aerosol at neutral pH and N_2(second spectrum). Carbon monoxide inhibition manifests in population of Hox-CO(purple, 2013 cm^{-1}, 1968 cm^{-1}, 1962 cm^{-1}, 1808 cm^{-1})(third spectrum). At pH 4 and N_2 the IR signatur of HoxH(blue, 1971 cm^{-1}, 1947 cm^{-1}, 1811 cm^{-1}) is observed(fourth spectrum).

S168

Serin168(S168) is located near the water molecule of the PTP. The effect of exchange to asparagine(S168N) and valine(S168V) is analysed here.

S168N

S168N exposed to H_2 adopts mainly the Hhyd(1979 cm^{-1}, 1962 cm^{-1}, 1860 cm^{-1}) with small fractions of Hred(1962 cm^{-1}, 1915 cm^{-1}, 1890 cm^{-1}) and Hsred(1954 cm^{-1}, 1918 cm^{-1}, 1882 cm^{-1})(FigureB.54, first spectrum). Under N_2 atmosphere Hox(1964 cm^{-1}, 1940 cm^{-1}, 1803

cm^{-1}) with traces of Hred is populated(FigureB.54, second spectrum). Replacement of neutral pH buffer in the aerosol by pH 4 buffer leads to the blue shift that is assoziated with HoxH(1971 cm^{-1}, 1947 cm^{-1}, 1811 cm^{-1})(FigureB.54, third spectrum).

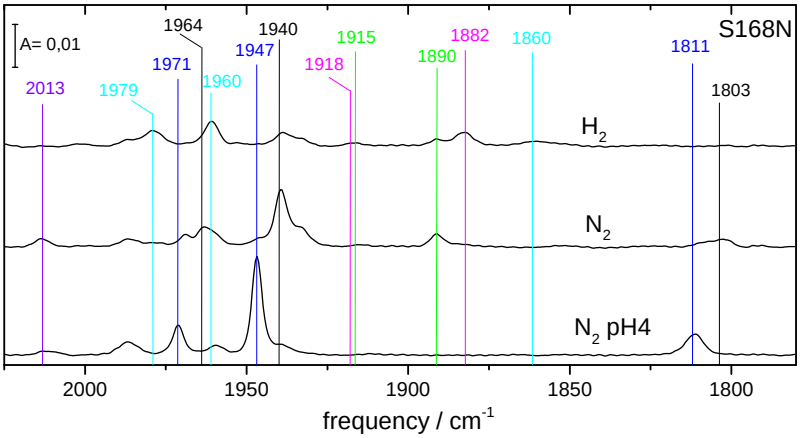

Figure B.54: IR spectra of redox states adopted by a HydA1-S168N film varying carrier gas and pH of the aerosol stream. S168N exposed to H_2 adopts mainly the Hhyd(cyan, 1979 cm^{-1}, 1962 cm^{-1}, 1860 cm^{-1}) with small fractions of Hred(green, 1962 cm^{-1}, 1915 cm^{-1}, 1890 cm^{-1}) and Hsred(magenta, 1954 cm^{-1}, 1918 cm^{-1}, 1882 cm^{-1})(first spectrum). Under N_2 atmosphere Hox(black, 1964 cm^{-1}, 1940 cm^{-1}, 1803 cm^{-1}) with traces of Hred is populated(second spectrum). Replacement of neutral pH buffer in the aerosol by pH 4 buffer leads to the blue shift that is assoziated with HoxH(blue, 1971 cm^{-1}, 1947 cm^{-1}, 1811 cm^{-1})(third spectrum).

S168V

Exposure to H_2 of S168V leads to a small fraction of Hsred(1954 cm^{-1}, 1918 cm^{-1}, 1882 cm^{-1}) but mainly Hox(1964 cm^{-1}, 1940 cm^{-1}, 1803 cm^{-1})(FigureB.55, first spectrum). Exchange to N_2 shows Hox too(FigureB.55, second spectrum). At pH 4 and N_2 the IR signature of HoxH(1971 cm^{-1}, 1947 cm^{-1}, 1811 cm^{-1}) is observed(FigureB.55, third spectrum).

R227

Arginine 227 is located near the [4Fe4S]-cluster at surface exposed site. Replacement by glutamic acid(R227E) introduces a protonable site.

R227E

Under N_2 atmosphere R227E populates the Hox(1964 cm^{-1}, 1940 cm^{-1}, 1803 cm^{-1}). Still there is a fraction of initial Hox-CO(2013 cm^{-1}, 1968 cm^{-1}, 1962 cm^{-1}, 1808 cm^{-1}) observable(FigureB.56, first spectrum). H_2 exposure enriches mostly Hred(1962 cm^{-1}, 1915 cm^{-1}, 1890 cm^{-1}) and in traces Hhyd(1979 cm^{-1}, 1960 cm^{-1}, 1860 cm^{-1})(FigureB.56, second spectrum). HoxH(1971 cm^{-1}, 1947 cm^{-1}, 1811 cm^{-1}) is enriched at pH 4 and N_2 atmosphere(FigureB.56, third spectrum). Exchange of the carrier gas to H_2 at pH 4 leads to population of the blue shifted hydride state(1989 cm^{-1}, 1960 cm^{-1}, 1872 cm^{-1})(FigureB.56, fourth spectrum).

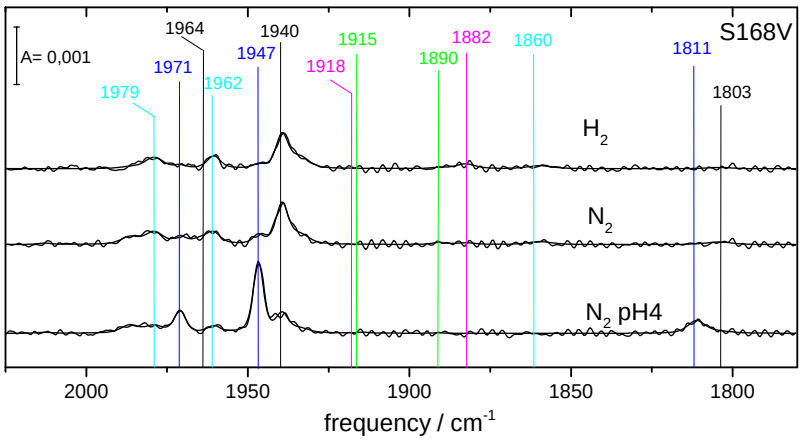

Figure B.55: IR spectra of redox states adopted by a HydA1-S168V film varying carrier gas and pH of the aerosol stream. Exposure to H_2 of S168V leads to a small fraction of Hsred(magenta, 1954 cm^{-1}, 1918 cm^{-1}, 1882 cm^{-1}) but mainly Hox(black, 1964 cm^{-1}, 1940 cm^{-1}, 1803 cm^{-1})(first spectrum). Exchange to N_2 shows Hox too(second spectrum). At pH 4 and N_2 the IR signature of HoxH(blue, 1971 cm^{-1}, 1947 cm^{-1}, 1811 cm^{-1}) is observed(third spectrum).

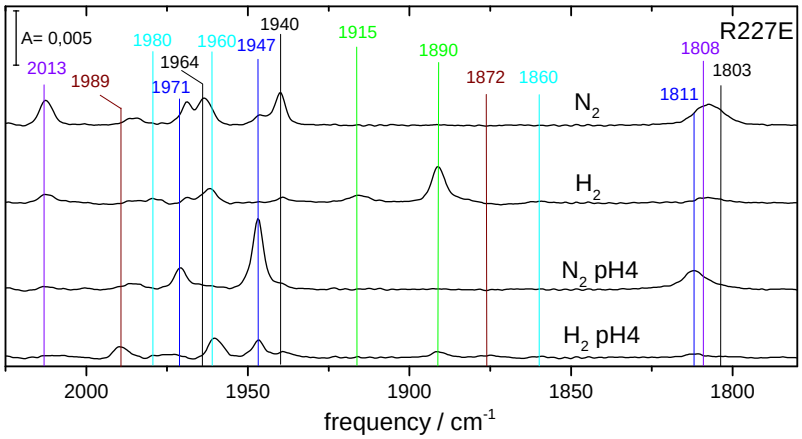

Figure B.56: IR spectra of redox states adopted by a HydA1-R227E film varying carrier gas and pH of the aerosol stream. Under N_2 atmosphere R227E populates the Hox(black, 1964 cm^{-1}, 1940 cm^{-1}, 1803 cm^{-1}). Still there is a fraction of initial Hox-CO(purple, 2013 cm^{-1}, 1968 cm^{-1}, 1962 cm^{-1}, 1808 cm^{-1}) observable(first spectrum). H_2 exposure enriches mostly Hred(green, 1962 cm^{-1}, 1915 cm^{-1}, 1890 cm^{-1}) and in traces Hhyd(cyan, 1979 cm^{-1}, 1960 cm^{-1}, 1860 cm^{-1})(second spectrum). HoxH(blue, 1971 cm^{-1}, 1947 cm^{-1}, 1811 cm^{-1}) is enriched at pH 4 and N_2 atmosphere(third spectrum). Exchange of the carrier gas to H_2 at pH 4 leads to population of the blue shifted hydride state(brown, 1989 cm^{-1}, 1960 cm^{-1}, 1872 cm^{-1})(fourth spectrum).

A92 and A94

Alanine 92 and 94 are located in the vicinity of the proximal iron ion of the H-cluster. They were exchanged each for serine(A92S, A94S).

A92S

A92S exhibits a generally blueshifted redox state pattern while the μCO ligand was red shifted(that resembles CPI band pattern, see B.6). At pH 4 and N_2 the IR signature of HoxH(1974 cm^{-1}, 1951 cm^{-1}, 1803 cm^{-1}) is observed(FigureB.57, first spectrum). H_2 exposure at pH 4 leads to the formation of Hhyd(1981 cm^{-1}, 1965 cm^{-1}, 1854 cm^{-1}) and H_{hyd}-H^+(1991 cm^{-1}, 1867 cm^{-1})(FigureB.57, second spectrum). In contrast at pH 8 and H_2 mostly Hred(1918 cm^{-1}, 1895 cm^{-1}) and Hsred(1922 cm^{-1}, 1886 cm^{-1}) and only traces of Hhyd are populated(FigureB.57, third spectrum). Hox(1968 cm^{-1}, 1945 cm^{-1}, 1795 cm^{-1}) is adopted at pH 8 and N_2 as carrier gas(FigureB.57, fourth spectrum). Exposure to carbon monooxide leads to inhibition and the band pattern associated with Hox-CO(2015 cm^{-1}, 1972 cm^{-1}, 1966 cm^{-1}, 1798 cm^{-1})(FigureB.57, fifth spectrum).

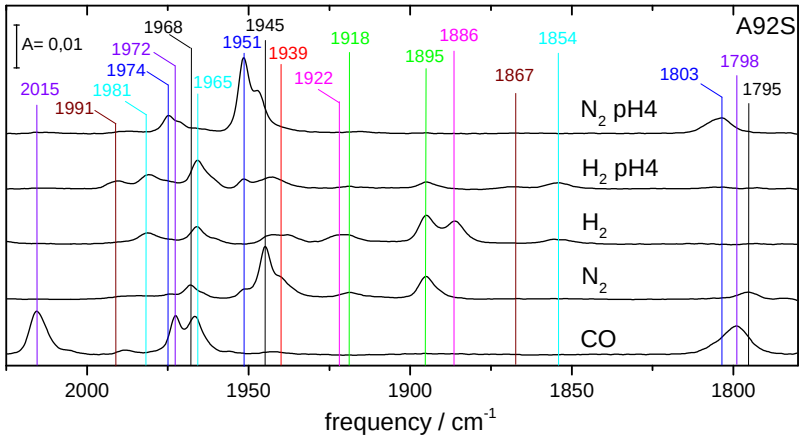

Figure B.57: IR spectra of redox states adopted by a HydA1-A92S film varying carrier gas and pH of the aerosol stream. At pH 4 and N_2 the IR signature of HoxH(blue, 1974 cm^{-1}, 1951 cm^{-1}, 1803 cm^{-1}) is observed(first spectrum). H_2 exposure at pH 4 leads to the formation of Hhyd(cyan, 1981 cm^{-1}, 1965 cm^{-1}, 1854 cm^{-1}) and H_{hyd}-H^+(brown, 1991 cm^{-1}, 1867 cm^{-1})(second spectrum). In contrast at pH 8 and H_2 mostly Hred(green, 1918 cm^{-1}, 1895 cm^{-1}) and Hsred(magenta, 1922 cm^{-1}, 1886 cm^{-1}) and only traces of Hhyd are populated(third spectrum). Hox(black, 1968 cm^{-1}, 1945 cm^{-1}, 1795 cm^{-1}) is adopted at pH 8 and N_2 as carrier gas(fourth spectrum). Exposure to carbon monooxide leads to inhibition and the band pattern assoziated with Hox-CO(purple, 2015 cm^{-1}, 1972 cm^{-1}, 1966 cm^{-1}, 1798 cm^{-1})(fifth spectrum).

A94S

A mixture of Hhyd(1979 cm^{-1}, 1963 cm^{-1}, 1861 cm^{-1}) and Hred(1962 cm^{-1}, 1919 cm^{-1}, 1893 cm^{-1}) is adopted by the A94S variant upon contact with H_2(FigureB.58, first spectrum). Atmosphere exchange to N_2 populates the Hox(1966 cm^{-1}, 1942 cm^{-1}, 1803 cm^{-1})(FigureB.58, second spectrum). Increasing the proton concentration to pH 4 leads to the formation of HoxH(1973 cm^{-1}, 1949 cm^{-1}, 1811 cm^{-1})(FigureB.58, third spectrum). Exposure to H_2 at these conditions leads again to the formation of Hhyd and perhaps H_{hyd}-H^+ with its band at 1991 cm^{-1}(FigureB.58, fourth spectrum). Hox-CO(2015 cm^{-1}, 1972 cm^{-1}, 1966 cm^{-1}, 1798 cm^{-1}) is again observed upon carbon monooxide exposure(FigureB.58, fifth spectrum).

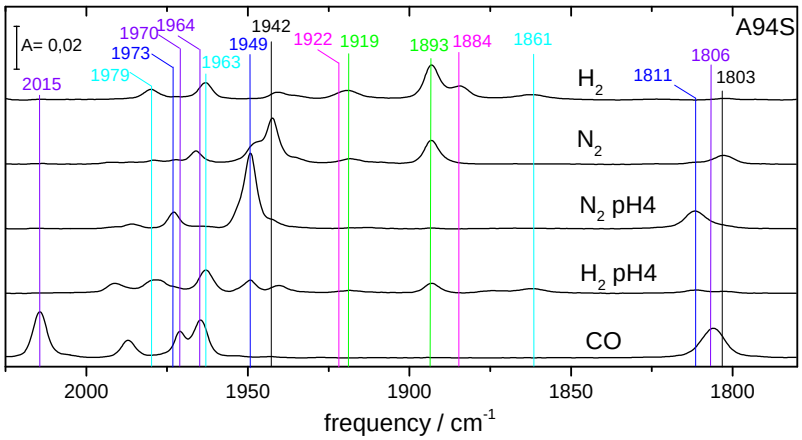

Figure B.58: IR spectra of redox states adopted by a HydA1-A94S film varying carrier gas and pH of the aerosol stream. A mixture of Hhyd(cyan, 1979 cm^{-1}, 1963 cm^{-1}, 1861 cm^{-1}) and Hred(green, 1962 cm^{-1}, 1919 cm^{-1}, 1893 cm^{-1}) is adopted by the A94S variant upon contact with H_2(first spectrum). Atmosphere exchange to N_2 populates the Hox(black, 1966 cm^{-1}, 1942 cm^{-1}, 1803 cm^{-1})(second spectrum). Increasing the proton concentration to pH 4 leads to the formation of HoxH(blue, 1973 cm^{-1}, 1949 cm^{-1}, 1811 cm^{-1})(third spectrum). Exposure to H_2 at these conditions leads again to the formation of Hhyd and perhaps H_{hyd}-H^+(brown) with its band at 1991 cm^{-1}(fourth spectrum). Hox-CO(purple, 2015 cm^{-1}, 1972 cm^{-1}, 1966 cm^{-1}, 1798 cm^{-1}) is again observed upon carbon monooxide exposure(fifth spectrum).

B.9 Time-resolved Studies

In order to obtain further insight into the hydrogenase mechanism time resolved IR spectroscopy was applied. With its hight activity of around 1000 molecules H_2 per second the time frame for one turnover step can be estimated to be 1 millisecond or less. To induce changes in the enzyme fast and synchronized a light pulse e.g. by a laser was used. A nanosecond laser pulse can offer the time resolution needed.

Photoreduction of HydA1 by Zincporphyrin

As a proof of principle on the way to time resolved IR spectroscopy on [FeFe]-hydrogenases sub turnover time regime, photoreduction by visible light was examined. The general idea is to start the hydrogen evolution reaction in all hydrogenase molecules at the same time by a short laser pulse. A photosensitive molecule gets excited and "donates" an electron to the hydrogenase. The provided electrons initiate the hydrogen evolution reaction and the redox state kinetics can be followed over time. Excess of a sacrificial electron donor guarantees fast re-reduction of the photosensitive molecule. Zinc tetraphenylporphyrin (ZnTPPS) acts as photosensitive molecule in the experiment. As sacrificial electron donor triethanolamine (TEA) was used (Figure: B.59).

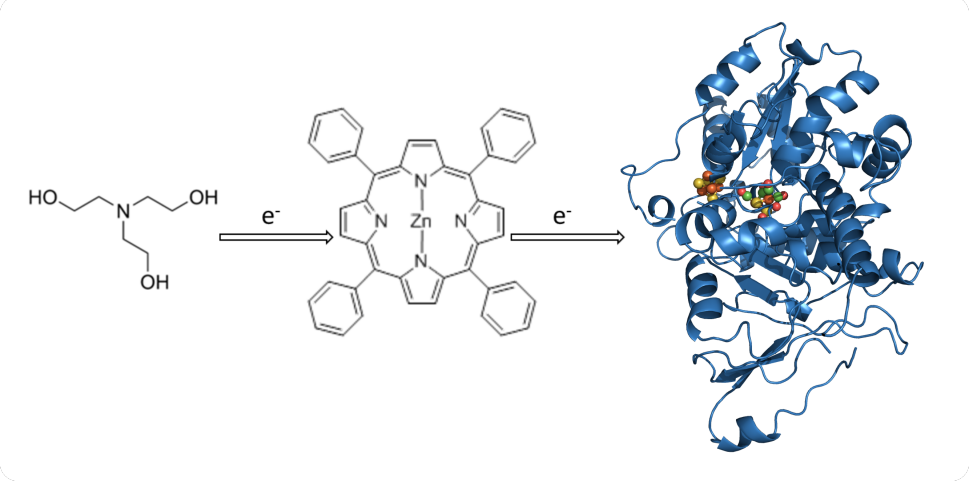

Figure B.59: Simplified scheme that illustrates the principle of photoreduction. The photosensitizer (ZnTPPS) gets excited by a visible light pulse and enables electron injection into the enzyme. ZnTPPS regains the now missing electron from the sacrificial electron donor (TEA) that is present in excess.

At first a continuous illumination experiment was set up to verify light induced reduction. 1.3 μM HydA1 100 mM TEA and 2 mM ZnTPPS in 100 mM tris(hydroxymethyl)aminomethane (Tris) pH 8 were deposited on the ATR crystal. The sample was equilibrated with N_2 at pH 8 to adopt Hox(1964 cm^{-1}, 1939 cm^{-1}, 1803 cm^{-1})(Figure: B.60, first spectrum).

Subsequent illumination by a cold light lamp (KL 1500) equipped with a green bandpass filter (Figure: B.61) leads to photoreduction of the sample within 60 seconds (Figure. B.61). Hred' (1962 cm^{-1}, 1933 cm^{-1}, 1792 cm^{-1}) and Hred (1962 cm^{-1}, 1915 cm^{-1}, 1890 cm^{-1}) were populated while Hox depopulates (FigureB.60, from top to bottom). In red the difference spectrum of Hox (no illumination) and the redox state composition after 60 seconds illumination is shown (FigureB.60, red trace). The accumulation of reduced species and loss of the oxidized species is clearly visible. Only small fractions of Hox-CO (purple, 2013 cm^{-1}, 1968 cm^{-1}, 1962 cm^{-1}, 1808 cm^{-1}) that report on destroyed cofactors due to light induced destruction were detected.

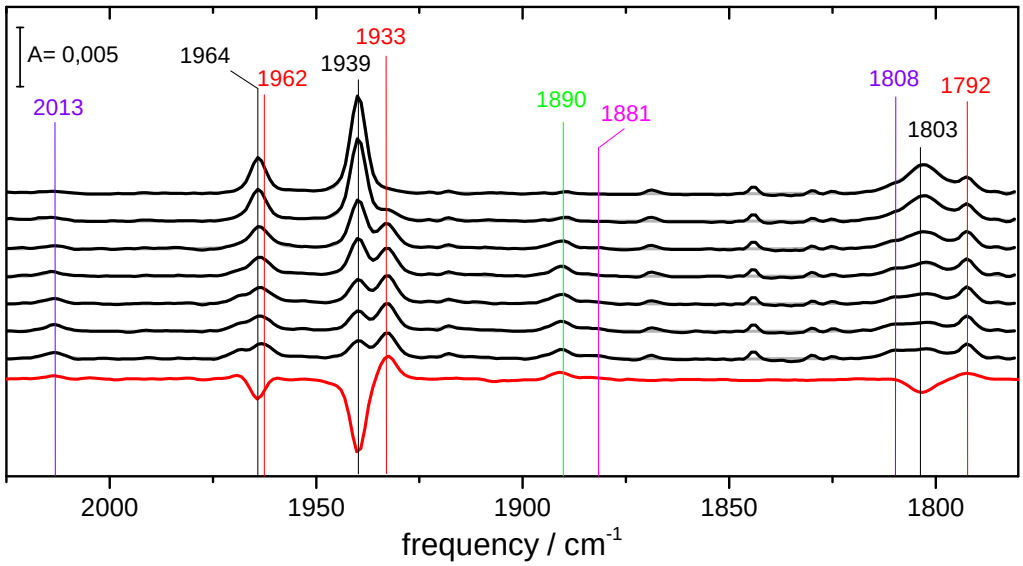

Figure B.60: IR spectra that show the photoreduction induced by continuous illumination with green light (for details see Figure B.61) of 1.3 μM HydA1 by 2 mM ZnTPPS with 100 mM TEA as sacrificial electron donor. The top spectrum represents the Hox (black, 1964 cm^{-1}, 1939 cm^{-1}, 1803 cm^{-1}) equilibrated with N_2 at pH 8. Subsequent illumination leads to the formation of Hred' (red, 1962 cm^{-1}, 1933 cm^{-1}, 1792 cm^{-1}) and Hred (green, 1962 cm^{-1}, 1915 cm^{-1}, 1890 cm^{-1}) (black spectra from top to bottom) within 60 seconds. In red at the bottom the difference spectrum of Hox (negative bands) and Hred' (positive bands) is shown.

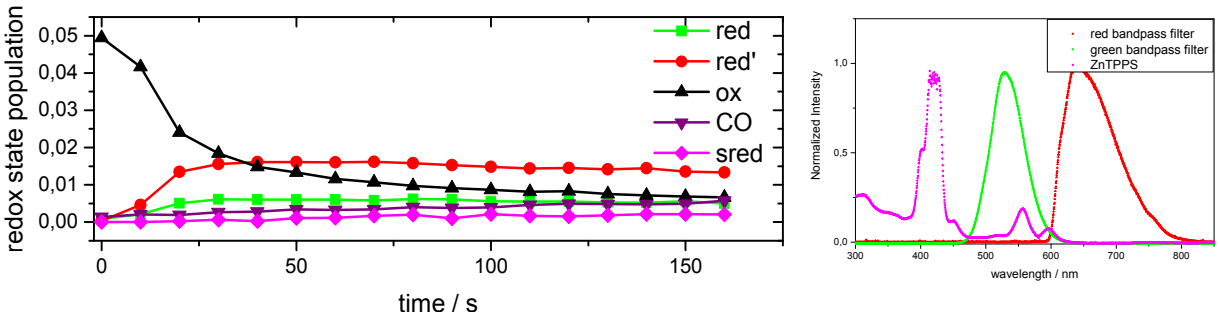

Figure B.61: Left: Timetraces of relative redox state populations upon photoreduction. **Right:** Transmittance of bandpass filters and absorption of ZnTPPS.

Rapid scan

Laser induced reduction was verified by FTIR rapid scan spectroscopy. Instead of continuous illumination a 605nm laser pulse was used to excite ZnTPPS. Figure B.63 gives an overview of the spectral region between 2100-1780 cm^{-1} after laser excitation. The first spectrum was recorded 238 μs after photoreduction. A clear depopulation of Hox (blue negative band at 1940 cm^{-1}) and a simultaneous population of Hred' (red positive band at 1933 cm^{-1}) was observed. In a time frame of 60 seconds the population differences relax back to the initial composition. In Figure B.62 the decay of the photoinduced Hred' (positive band at 1933 cm^{-1}) population and the repopulation of Hox (negative band at 1940 cm^{-1}) is shown. The relatively small difference signal (100μ) decays with a time constant of 1.4 seconds.

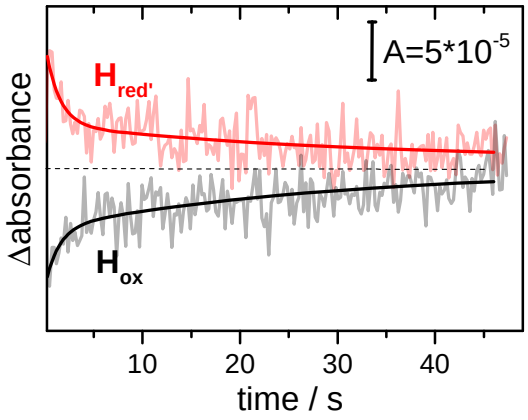

Figure B.62: Timetraces of bands at 1940 cm^{-1} (Hox, black) and 1933cm^{-1} (Hred', red).

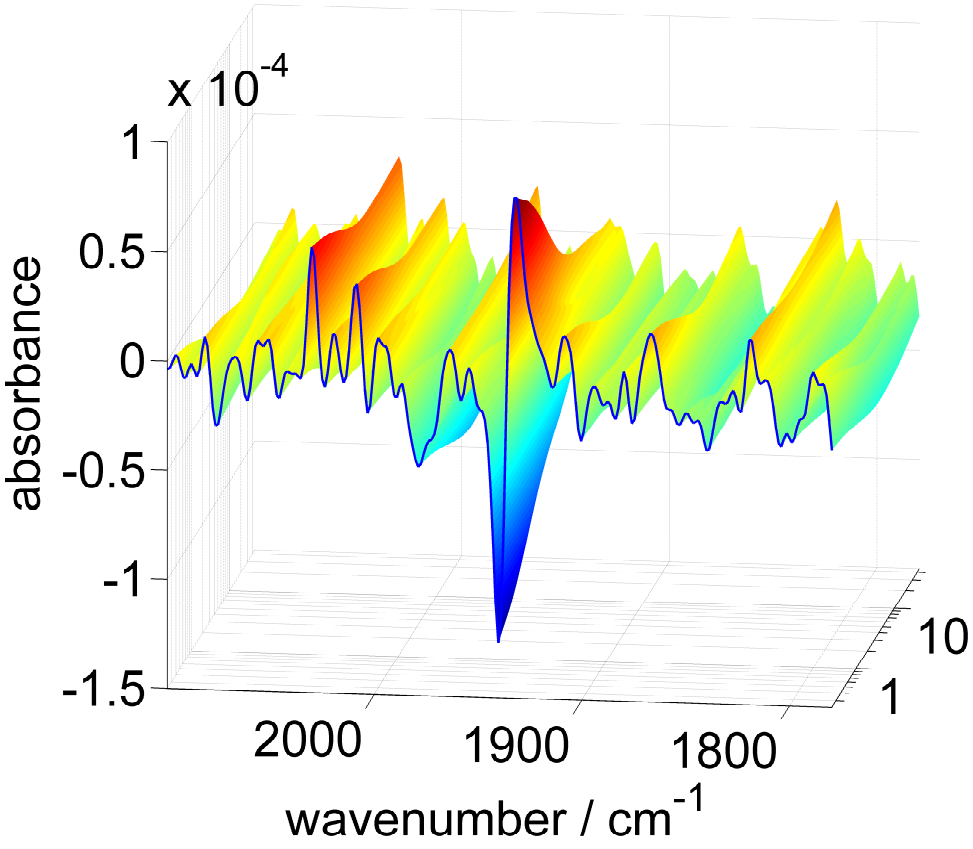

Figure B.63: 3d representation of HydA1 photoreduction by (ZnTPPS) induced by a 605 nm laser pulse. The first spectrum at 238 μs after photoreduction shows a clear depopulation of Hox(blue negative band at 1940 cm^{-1}) and a simultaneous population of Hred' (red positive band at 1933 cm^{-1}). In a timeframe of 60 seconds the population differences relax back to the initial composition. Other bands besides Hox and Hred' are not assigned to any redox state known and exhibit no specific timedepended behavior.

Photo induced CO dissociation

Photo dissociation of the inhibiting CO ligand is another way to explore [FeFe]-hydrogenase in a light induced time resolved manner. A laser pulse can break the bond between the Fe_d and the inhibiting CO ligand of Hox-CO. By the broken bond between the Fe_d and the inhibiting CO ligand the active ready state Hox is formed. CO rebinding that forms Hox-CO again happens in the millisecond time regime.

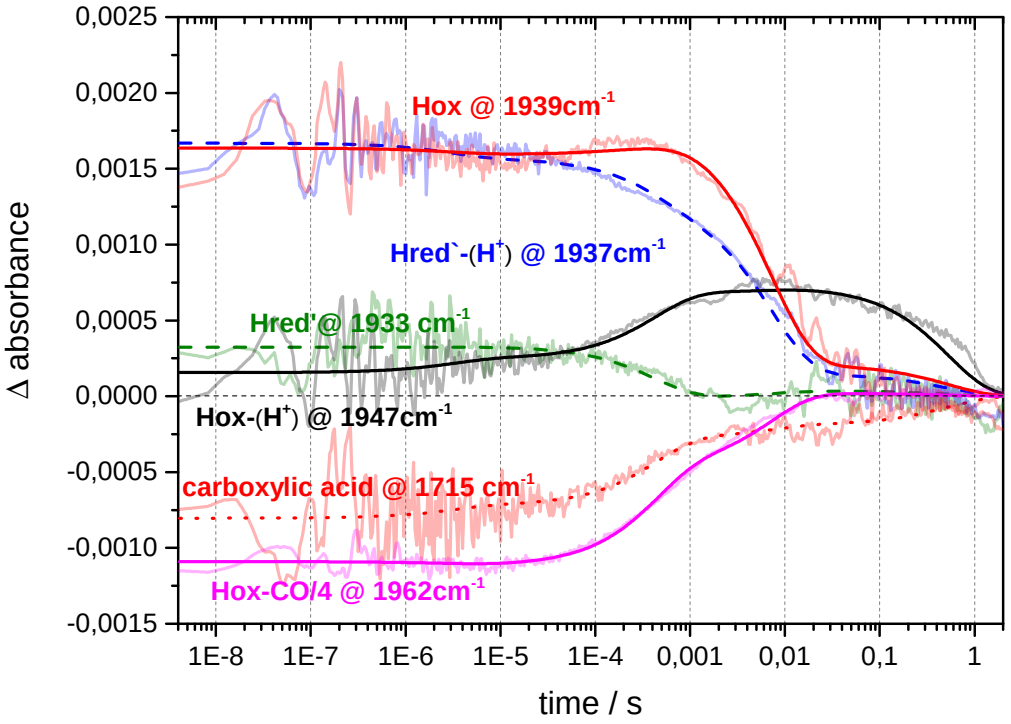

Figure B.64: Kinetic traces of absorbance changes induced by photo dissociation of inhibiting CO. Hox (red) and Hred'H (blue) are populated while Hox-CO (magenta) is bleached. A negative absorbance change in the carboxylic acid band region is observed.